8-13-2024

Physical Properties of Bulk Carbon Nanotube Conductors Impacting Radio Frequency Waveguide Measurements

Samuel J. Boyd
sjb9814@rit.edu

R I T

Physical Properties of Bulk Carbon Nanotube Conductors Impacting Radio Frequency Waveguide Measurements

by

Samuel J. Boyd

A dissertation submitted in partial fulfillment of the requirements for the degree of Doctor of Philosophy in Microsystems Engineering

Microsystems Engineering Program

Kate Gleason College of Engineering

Rochester Institute of Technology

Rochester, New York

August 13th, 2024

ABSTRACT

Kate Gleason College of Engineering
Rochester Institute of Technology

Degree: Doctor of Philosophy **Program:** Microsystems Engineering
Author's Name: Samuel J. Boyd
Advisors' Names: Dr. Brian J. Landi & Dr. Ivan Puchades
Dissertation Title: Physical Properties of Bulk Carbon Nanotube Conductors Impacting Radio Frequency Waveguide Measurements

Recent developments in radio frequency (RF) electronics motivate the interest in developing multi-functional materials which have effective electrical properties with increasing frequency that minimize the conventional skin effect. Carbon nanotubes (CNTs) are emerging as a candidate material due to high direct current (DC) electrical conductivity, flexure tolerance, corrosion resistance, and low density. The DC electrical conductivity of CNT networks is affected by the high resistance junctions between individual or bundled CNTs. Strategies to modify the properties of these junctions have included chemical doping, nano-metal deposition, and physical densification. Alternating current (AC) conductivity measurements of bulk CNT materials to date have shown constant or even increasing values up to 120 GHz. Thus, this dissertation focuses on applying doping and metallization strategies for improving DC electrical properties to altering the AC conductivity of bulk CNTs.

AC conductivity measurements were performed using a rectangular waveguide-based technique up to 40 GHz. Initially, a comparison of purified and $KAuBr_4$-doped commercial MWCNT sheet was made to the as-received material. The as-received MWCNT sheet showed a decrease with frequency, whereas the purified sample (with reduced iron impurities) provided a stable AC conductivity. Laser ablation-based thinning of the purified MWCNT sheet produced increased transmission, which was shown to improve measurement accuracy. The laser-thinned purified MWCNT sheet was subsequently doped with $KAuBr_4$ and demonstrated a 3-4× AC conductivity enhancement. The purified MWCNT sheet was also deposited with varying weight loadings (% w/w) of platinum using a Joule heating-driven chemical vapor deposition (CVD) technique. Platinum overcoating of the MWCNT network was observed, consistent with previous studies, resulting in a 1.4× increase in AC conductivity.

A high frequency modeling technique using the generalized Drude conduction theory was applied to the experimental measurements from purified, $KAuBr_4$-doped, or platinum-deposited MWCNT sheet to better understand the high frequency effects of each process. The fit results showed that inclusion of $KAuBr_4$ or platinum nano-metal to the MWCNT network increased the material's plasma frequency, which is attributed to higher carrier density in the material leading to enhanced AC conductivity. Finally, a demonstration of the enhanced RF properties for CNTs was performed using free-standing thin films to directly measure the EMI shielding effectiveness using the rectangular waveguide setup from 10 GHz to 15 GHz. Thus, the work exhibits a practical application of the CNT conductive materials that combines thin film optical transparency and surface conformability with favorable RF shielding properties.

ACKNOWLEDGEMENTS

First and foremost, I would like to thank my advisors, Drs. Brian Landi and Ivan Puchades. Their guidance and support, as well as their immense patience, has been essential to me over the past four years. The opportunity to draw from their experience has done much to foster my learning and growth as a scientist, a professional, and a person. I am very grateful to have been able to pursue a Ph.D. under their guidance.

I would like to thank my committee members, Dr. Steve Weinstein, Dr. Jayanti Venkataraman, and Dr. Andrew Bucossi. The focus and direction of my research as well as my fundamental knowledge of the subject matter has been shaped by their guidance. I am very grateful for their support of and contributions to my education. I would also like to thank the Microsystems Engineering department head, Dr. Stefan Preble.

Special thanks to Dr. Richard Hailstone for the use of his lab's SEM and EDXS capabilities.

Thank you to my colleagues, fellow students and staff at RIT: Rex Bartolini, Brandon Bogner, Daniel Broderick, Jessica Chatterton, Tristin Del Vecchio, Elizabeth Dugdale, Caitlin Grace, Paul Gregorius, Quintin Hernandez, Ross Hisert, Harris Jilani, Emily Kessler-Lewis, Anthony Leggiero, Connor Levine, Elaine Lewis, Sam Lolly, Lexus Makarowsky, Tomasz Mazur, Dylan McIntyre, Sarah Nadzam, Josh Owens, Amber Palka, Jamie Rossi, Clare Scroger, Karen Soule, Jason Staub, Alex Tomkiewicz, Ricky Wurzer, Lisa Zimmerman, Sami Znati, and any others I haven't listed here. The sense of community and collaboration I received from working with all of you has been invaluable.

Last but not least, I would like to thank all of my family, and especially my parents, for supporting me in my efforts. My drive and motivation have been significantly influenced knowing that I have such a strong base to count on.

ACRONYMS & SYMBOLS

SWCNT, single-walled carbon nanotube

MWCNT, multi-walled carbon nanotube

EDX/EDXS, energy-dispersive x-ray (spectroscopy)

TGA, thermogravimetric analysis

SEM, scanning electron microscopy

$KAuBr_4$, potassium tetrabromoaurate

CVD, chemical vapor deposition

$Pt(acac)_2$, platinum (II) acetylacetonate

Pt-MWCNT, platinum-multiwalled carbon nanotube hybrid

NMP, n-methyl-2-pyrrolidone

RF, radio frequency

VNA, vector network analyzer

TRL, Thru-Reflect-Line

R_{DC}/R_{AC}, direct/alternating current resistance

$R_{s,DC}$/$R_{s,AC}$, direct/alternating current sheet resistance

R/L, resistance-per-length

σ_{DC}/σ_{AC}, direct/alternating current electrical conductivity

ITO, indium tin oxide

MXene, transition metal carbide/carbonitride

SE, shielding effectiveness

SSE/t, specific shielding effectiveness normalized to thickness

Table of Contents

Table of Contents

Table of Contents

Table of Contents

Table of Figures

Table of Figures

Table of Figures

Table of Figures

Table of Figures

1 Introduction

1.1 Background & Rationale

Radio frequency (RF) is a distinction that describes the oscillation of alternating electric currents/voltages (AC) or electromagnetic fields in the frequency range of ~20 kHz to ~300 GHz. The energy from a high frequency AC current within a conductor is able to radiate as a wave, a phenomenon applied in various technologies in use worldwide today. Likely the best known application of RF is the transmission and reception of information through communication devices such as radios, cell phones, computers, and television. Additionally, RF electromagnetic waves are applied for a wide range of non-communication purposes, including but not limited to civilian/military radar, radio frequency identification (RFID), and magnetic resonance imaging (MRI). The performance of the devices used in these technologies depends upon the properties of the conductive materials which are used to transport and manipulate RF signals.

The RF range is the lowest frequency segment of the electromagnetic spectrum, just below the infrared (IR) and ultraviolet (UV) ranges as shown in Figure 1. The upper region of the RF range extends into the microwave (MW) frequencies. Electromagnetic radiation excites different oscillatory responses in a material depending on frequency. In the optical and infrared ranges targeted by techniques like optical absorption and Raman spectroscopies, energies are high enough to raise electrons to excited states or probe the vibrational modes in molecular bonds. In the microwave and upper RF frequencies, the dipole rotation mechanism dominates, while low RF frequencies illicit an ionic conduction polarization response. In dielectric materials the response to an alternating electric field is typically quantified using the complex permittivity ($\varepsilon^* = \varepsilon' - j\varepsilon''$) signifying the polarization (real part) and loss due to heat dissipation (imaginary part). In homogeneous conductor materials, on the other hand, the response is dominated by conduction of free electrons and it is more appropriate to use the

complex conductivity ($\sigma^*=\sigma'+j\sigma''$) to describe resistive losses (real part) and inertial effects (imaginary part). The magnetic field response for both types of materials is similarly described by the complex permeability ($\mu^*=\mu'-j\mu''$). In the case of permittivity/permeability, these are often shown as relative quantities defined with respect to the permittivity ($\varepsilon_0=8.854 \times 10^{-12}$ F/m) and permeability ($\mu_0=1.257 \times 10^{-6}$ H/m) of free space [1].

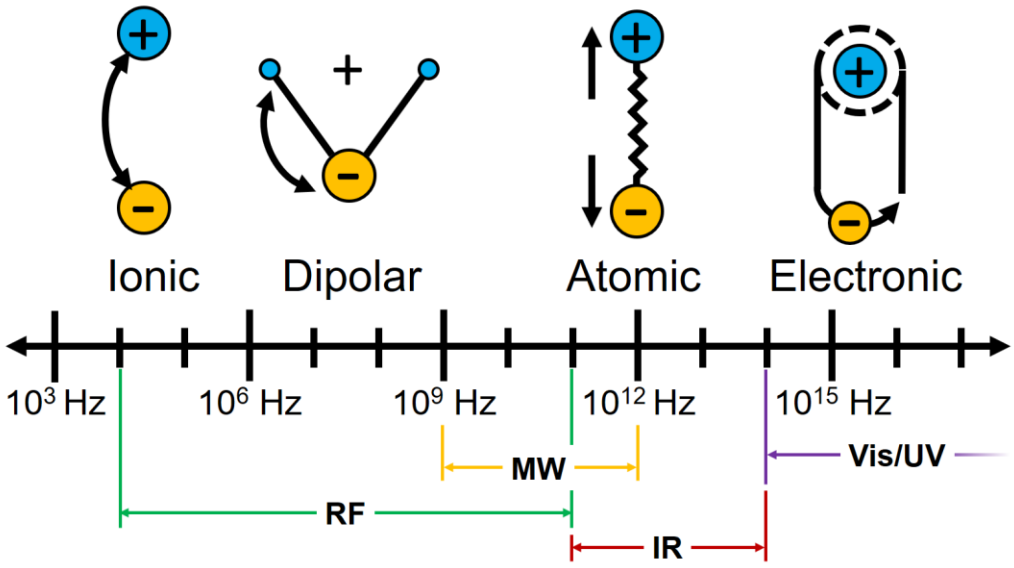

Figure 1. Characteristic excitation mechanisms in a material depending on the frequency of incident electromagnetic waves.

Metals have been the primary conductor materials in electrical applications for decades due to their excellent DC electrical conductivity. However, they suffer in performance when subjected to AC currents due to the oscillating nature of the electromagnetic fields. At very low AC frequencies such as those used in domestic power applications (60 Hz in the United States) metal properties remain significantly better than other options, but they experience much more detrimental effects in the RF range. Although approaches have been developed to mitigate these effects in traditional metal conductors to some extent, there is still substantial interest in investigating materials with alternative frequency-dependent conductive properties for RF applications.

1.2 High Frequency Effects in Conventional Metal Conductors

Metals are the conventional choice for conductive materials in electrical applications due to their high direct current (DC) electrical conductivity (σ_{DC}). The DC electrical conductivity of bulk materials is determined from the conductor cross-sectional area (A_c) and the DC resistance (R_{DC}) over a given length (L) and is governed by the following equation.

$$\sigma_{DC} = \frac{L}{R_{DC}A_c} \tag{1.2-1}$$

Among metals, copper is typically the material of choice due to its advantage in the trade-off of cost and performance over more expensive options such as silver. The DC electrical conductivities and relative magnetic permeabilities (μ_r) of some choice metals are shown in Table 1.

Table 1. DC electrical conductivities and relative magnetic permeabilities of selected metals.

Metal	Elemental Symbol	σ_{DC} (S/m)	μ_r
Copper	Cu	5.8×10^7 [2]	~1*
Silver	Ag	6.15×10^7 [2]	
Aluminum	Al	3.77×10^7 [2]	
Titanium	Ti	1.79×10^6 [3]	
Tungsten	W	1.89×10^7 [2]	
Iron	Fe	1.03×10^7 [2]	5000 [4]

*These metals are non-magnetic.

In a bulk conductor under steady-state DC bias, a constant, unidirectional current flows. Assuming homogeneity, under these conditions the electromagnetic field around the conductor is constant with time and the current flow is uniform throughout the conductor cross section. However, when AC voltage is applied the current alternates direction with a frequency equal to that of the applied bias. The time dependence of voltage, current, and resulting electromagnetic fields leads to a phenomenon in metals known as the skin effect. To summarize the mechanism of this phenomenon in metals, it is convenient to visualize a cylindrical conductor as in Figure 2. The voltage and current

alternate with a frequency f, meaning that charge carrier motion within the conductor involves periodic acceleration and deceleration. This creates an alternating magnetic field $\vec{H}$ within the conductor and inductive effects drive the formation of a similarly alternating electric field. This field opposes the direction of current flow near the conductor center and concurs with the direction of current flow near the conductor surface, visible in Figure 1 in the form of eddy currents I_w. Ultimately, this results in the restriction of net current flow towards the conductor surface [1].

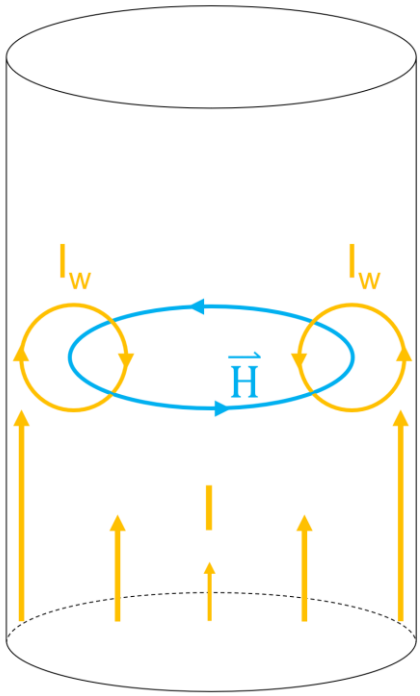

Figure 2. Schematic diagram of the electromagnetic fields resulting in the skin effect in a cylindrical conductor.

The restriction of current flow worsens with increasing frequency, as this opposing electric field increases in strength in accordance with Faraday's law of induction for a time-varying magnetic flux. The skin effect is typically quantified using a parameter known as skin depth (δ) which defines the depth below the conductor surface at which the current density reaches 1/e (~37%) of its surface value. The skin depth for a given metal and frequency is determined by the following equation,

$$\delta = \sqrt{\frac{1}{\pi \sigma_{DC} f \mu_r \mu_0}} \qquad (1.2\text{-}2)$$

where μ_r is the magnetic permeability relative to the permeability of free space, μ_0=1.257x10^{-6} H/m. The formula for skin depth indicates that for metals, approximately 63% of the current will flow in a region which decreases in depth at a rate determined by the square root of the frequency [1].

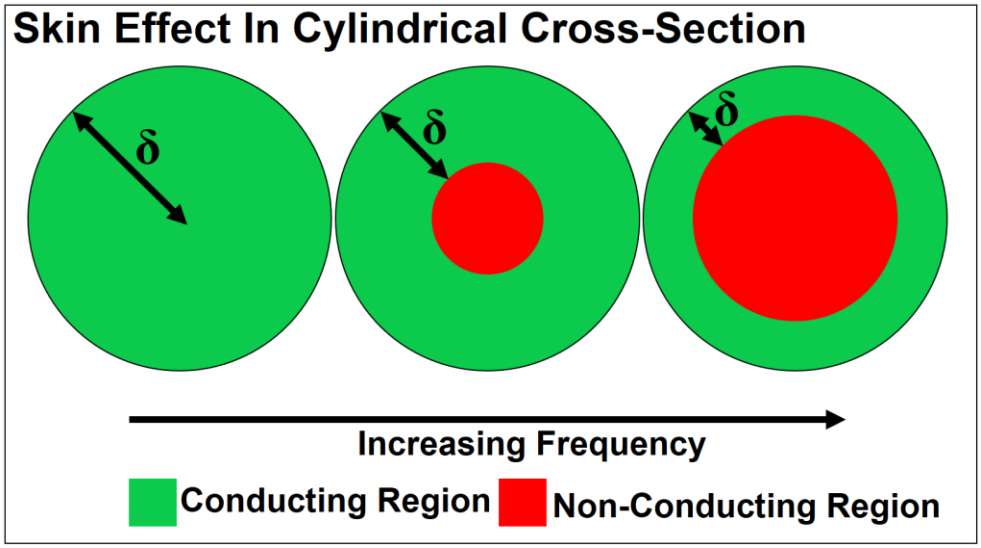

Figure 3. Diagram showing the approximate progression of the skin effect through a decreasing cross-sectional area participating in conduction.

Recalling the tendency of current to flow uniformly in the cross section under DC conditions, it is possible to estimate the AC resistance (R_{AC}) of a cylindrical conductor of radius r at a certain frequency using an annular effective cross sectional area (A_{eff}) which changes with the skin depth, as shown in Figure 3.

$$A_{eff} = \pi[r^2 - (r - \delta)^2] \qquad (1.2\text{-}3)$$

If the skin effect is assumed to occur only when the skin depth becomes smaller than the radius, R_{AC} is calculated using the following formula.

$$R_{AC} = \begin{cases} \frac{L}{\sigma_{DC}\pi r^2} & , \ \delta \geq r \\ \frac{L}{\sigma_{DC}A_{eff}} & , \ \delta < r \end{cases} \quad (1.2\text{-}4)$$

This formula sets R_{AC} equal to R_{DC} when the skin depth is greater than or equal to the conductor radius, as the current flows in the whole cross section. Finally, the effective AC conductivity σ_{AC} of the material can be determined by applying the AC resistance to the actual, physical cross section of the cylinder.

$$\sigma_{AC} = \frac{L}{R_{AC}\pi r^2} \quad (1.2\text{-}5)$$

It is clear from this analysis that the AC conductivity of a metal at a given frequency will be different depending on the physical radius of the cylindrical conductor. The frequency at which σ_{AC} begins to decrease increases with smaller conductor diameter, as shown in Figure 4 for copper.

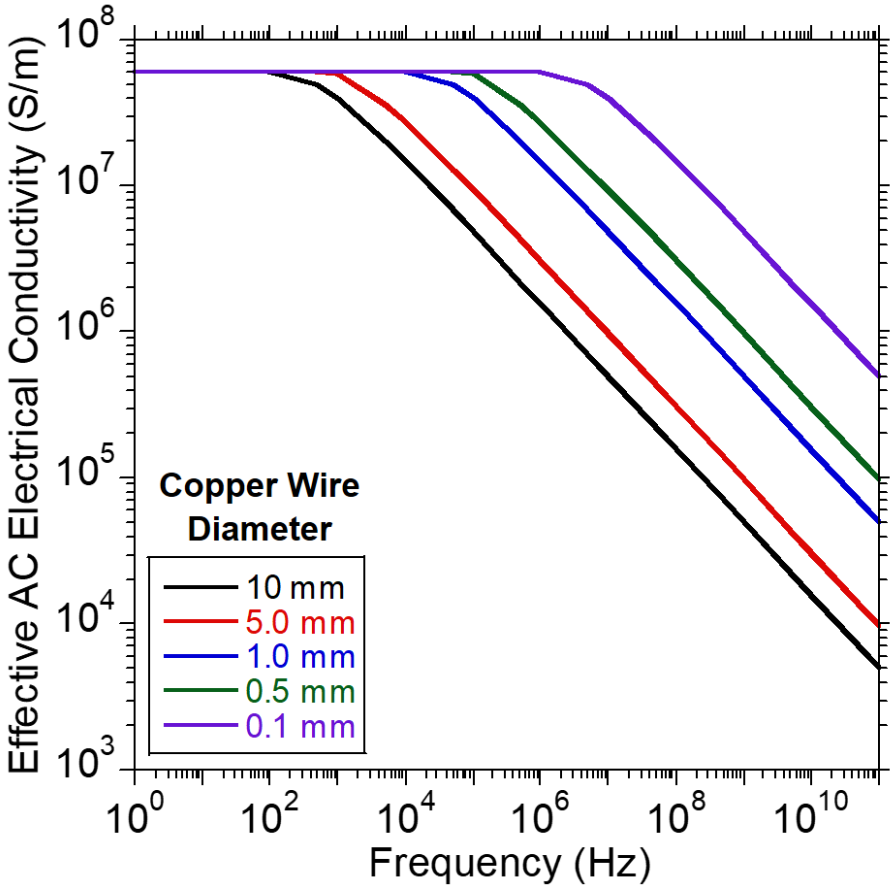

Figure 4. Change in effective AC electrical conductivity of copper wires of various diameters due to the skin effect. Plot has log-log axes.

This shows that for an individual, cylindrical metal conductor, assuming losses only due to the material resistance, reducing the diameter will assist in maintaining conductivity at DC levels at increased frequencies. Figure 4 also demonstrates the consistent rate of decrease due to skin effect regardless of cylinder dimensions. It is important to note that the procedure above only applies to cylindrical conductors, and that other conductor cross sections require alternative cross-sectional area approximations. One such approximation for rectangular conductors determines the effective cross-sectional area based on the relation between the skin depth and the width (w) and thickness (t) of the conductor [5].

$$R_{AC} = \begin{cases} \frac{L}{\delta\sigma_{DC}(2t-4\delta+2w)}, & 2\delta < w \; AND \; 2\delta < t \\ \frac{L}{\sigma_{DC}wt}, & 2\delta \geq w \; AND \; 2\delta \geq t \end{cases} \quad (1.2\text{-}6)$$

It is also informative to consider the skin effect in various different metals. Based on Equation (1.2-2) at a single frequency, increasing DC electrical conductivity causes a corresponding decrease in skin depth. Additionally, in the case of magnetic metals, increasing relative permeability will also decrease the skin depth. Figure 5a shows the skin depth in copper, aluminum, titanium, tungsten, and iron from 1 Hz to 100 GHz. Each metal's skin depth changes with frequency at the same rate, but each begin from different depths at 1 Hz due to their differences in DC conductivity. The skin depth in iron is significantly smaller than the other metals at a given frequency, despite its relatively low DC conductivity, because of its high magnetic permeability (see Table 1). To observe how the skin effect changes the AC conductivity of these metals, cylindrical conductors of 1 mm radius (the dotted black line in Figure 5a) and 1 m length are assumed. The same calculation process as before is used to obtain the plot shown in Figure 5b. It is clear by comparing the two plots that for each metal, the skin effect begins as the skin depth becomes less than the radius of the wire. Each metal's AC conductivity decreases at the same rate, but DC conductivity determines the best performance when all else is equal.

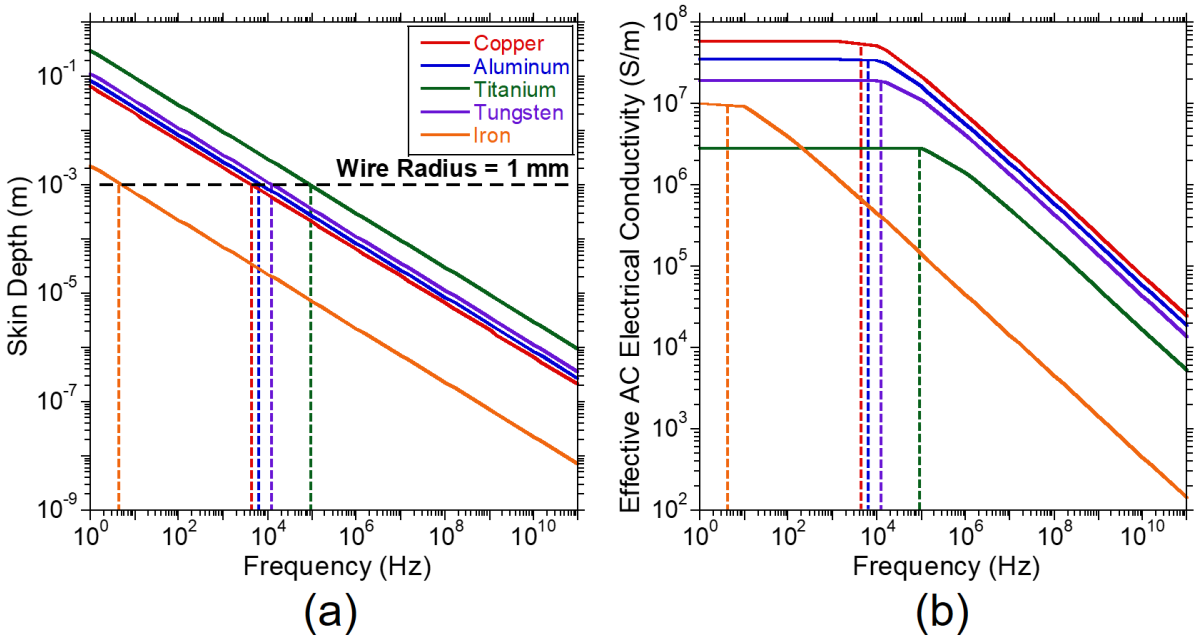

Figure 5. (a) Skin depth vs. frequency for Cu, Al, Ti, W, and Fe metals in comparison to a wire radius of 1 mm from 1 Hz to 100 GHz. (b) AC conductivity vs. frequency for Cu, Al, Ti, W, and Fe metals 1 m in length with a radius of 1 mm from 1 Hz to 100 GHz. The colored dotted lines indicate the onset frequencies of the skin effect for each metal wire. Both plots have log-log axes.

The skin effect at low AC frequencies is not very significant relative to the higher frequencies in use in RF applications. In this range, the current can be restricted into a layer a fraction of a millimeter in thickness and decreasing. Based on knowledge of the variables affecting skin effect, approaches to mitigation in metal conductors have been developed.

1.3 Approaches to Mitigate Skin Effect in Metal Conductors

Several methods have been developed to mitigate the skin effect in metal conductors based on research of the mechanism behind it and the variables that change how it behaves. A common thread between all of these techniques is the changing of the conductor shape and size.

1.3.1 Tubular conductors

A paper by Dwight in 1918 [6] mathematically calculated the skin effect resistance increase with frequency in conductors of several geometries including solid cylinders and hollow tubes. He showed that the rate of resistance increase is suppressed in hollow tubes compared with that of solid wires of

equivalent cross-sectional area, and that the suppression is increased by reducing the thickness/diameter ratio of the tube. Dwight's calculations were found to match with experimental measurements of tubular conductors from some years earlier [7]. Tubular conductors have been used where weight savings or additional mechanical strength is required, in which cases the conductor is left hollow or filled with a stronger material such as steel.

1.3.2 Stranded conductors

Another special concept for which development began in the early 20th century is the use of multiple strand conductors instead of solid wires, in which current is carried by numerous smaller, bundled wires. The hypothesis behind this approach is that each smaller wire would experience less resistance increase due to its dimensions, while the current-carrying capability of the overall conductor would be relatively unaffected. The realization of this result in practice is conditional, and strategies to satisfy the conditions for improved performance were developed. A key conductor type used for this purpose is known as litz wire (derived from the German word "litzendraht" meaning "stranded wire"). It consists of a bundle of wires with dimensions smaller than the skin depth in the range of operation, individually insulated such that the wires do not short to one another. As the electromagnetic field would still vary within the overall conductor cross section in a simple wire bundle, the strands are twisted such that each will occupy every possible position within the cross section to an equal extent throughout the length of the conductor. This equalizes the reactances of the individual wires, causing the current to be uniformly distributed in the cross section [8]. Thus, the influence of skin effect both in the individual wires and in the conductor overall can be greatly reduced. However, this advantage can only be achieved in a specific frequency range (shown in Figure 6) and is limited to the low radio frequencies (<~2 MHz) as higher frequencies simultaneously cause skin effect in the small wires and increase the parasitic capacitances between them [8].

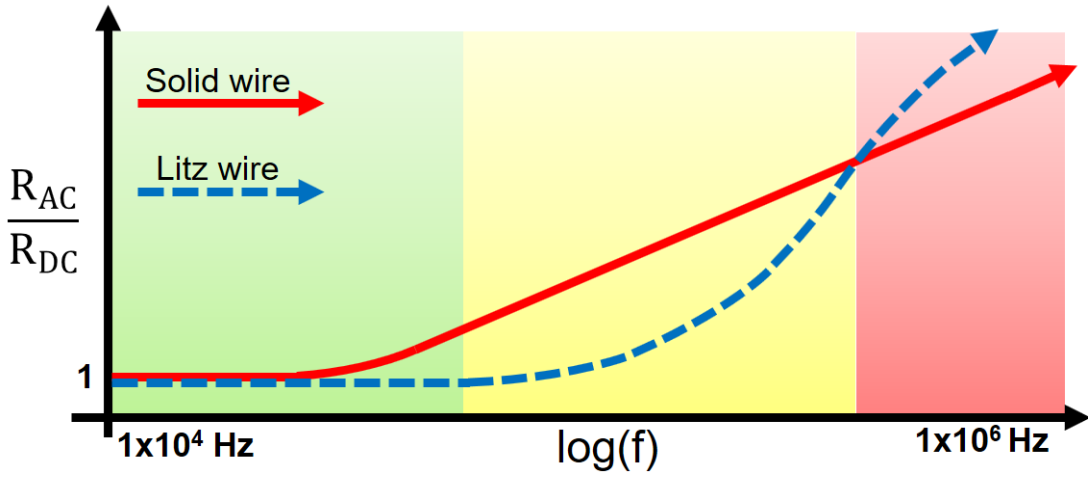

Figure 6. The typical form of the AC to DC resistance ratio vs. log of frequency for a solid wire and a litz wire having similar overall conductor diameter.

In both of the skin effect mitigation approaches described above, the techniques involve reducing or otherwise modifying the internal structure of the conductor. Though this produces a more favorable trend of resistance vs. frequency, both stranded and tubular conductor geometries significantly increase the DC resistance [8].

1.4 DC Conduction in Carbon Nanotubes

More recent research has begun to investigate the novel high frequency transport properties of nanomaterials, which may also offer alternative options to metal conductors. Since their discovery in the 1990s [9], there has been considerable investigation of carbon nanotubes (CNT) owing to their strong attributes in flexibility, corrosion resistance, mechanical, thermal and electrical properties. A CNT can be visualized as a sheet of hexagonally bonded, sp^2 hybridized carbon atoms rolled into a seamless cylinder. A CNT is defined as single-walled (SWCNT), double-walled (DWCNT), or multi-walled (MWCNT) depending on the number of concentric cylinders. This structure gives rise to exceptional properties such as ballistic conduction, whereby the limited energy states available in their 1-D structure allow electrical transport through quantized conduction channels. The record experimentally determined DC conductivity in an individual CNT is 9.7×10^7 S/m [10]. However, this strong conductive mechanism

is significantly affected by structural aspects of single CNTs. For instance, the chirality of the bonding structure influences the band structure of individual SWCNTs, resulting in metallic or semiconducting character [11]. The band structure is further altered when SWCNTs are bundled together, creating induced energy gaps [12]. CNTs tend to favor this bundling and agglomerate due to strong Van der Waals interactions from the delocalized orbitals [13], [14]. Similar interactions take place between the concentric walls of MWCNTs. The axial conduction in CNTs is also known to be significantly affected by defects in the tube bonding structure and adsorbed impurities resulting from synthesis which can act as scattering sites [15], leading to measured resistance per unit length on the order of 6 kΩ/μm for SWCNTs of length 0.4 cm [16].

Scale-up of CNT materials from an individual basis to macroscale arrangements introduces a new gauntlet of challenges for electrical conduction. The primary bottleneck that is encountered is the large number of high resistance junctions that form in a network of interconnected CNTs, greatly limiting the conductivity of the overall material [17], [18], [19], [20]. The past ten years have seen a large focus on improving the DC electrical conductivity of bulk CNT conductors. Areas of investigation have included post-processing techniques to physically enhance the conductivity through improved alignment or gap-bridging [21], [22], and/or modify the local electronic structure using stretching, chemical doping [23], [24], [25], [26], radial, solvent, or planar densification [27], [28], [29], and thermal treatment [30]. Additional exploration using metal-CNT hybrid conductors to compete with the conductivity of metal wires while maintaining the favorable CNT temperature coefficient of resistance has been carried out [31], [32]. In this approach, the gaps between CNTs are selectively bridged with metals in either a single stage process to introduce one conductive metal or a multi-stage process using multiple metals to enhance the conformability of the metallic phase to the CNT phase [33], [34], [35].

Chapter 1 - Introduction

Over the past decades, the promising and unique DC electrical properties of CNTs have driven researchers to extend investigation to their potential electrical benefits at high frequencies.

2 Review of Literature

2.1 Interest in CNTs in RF Devices

The devices or components that are used in RF applications can be broadly categorized as being either passive or active. The latter type requires an external power source in addition to the source of RF signal in order to carry out its function, while the former does not. As the focus of the dissertation work is on the RF properties of conductive materials, analysis of previous study is focused on passive interconnects as they have the most direct relevance. The following discussion therefore references work pertaining to coaxial cables, waveguides, and printed circuit board (PCB) interconnects such as microstrip lines. In addition, examples of existing study of CNT antennas will be discussed.

An intuitive type of passive component is the transmission line, which serves the purpose of guiding RF electromagnetic waves from one point to another in a contained fashion, transmitting energy or information. As RF signals propagate in the form of waves, they are sensitive to discontinuities in their path, caused by impedance mismatch, from which some portion of the wave energy is reflected back. Impedance is a complex quantity that describes the opposition to the flow of an AC electrical current or signal, consisting of a real part (resistance, R) and an imaginary part (reactance, X). The resistance is the conventional opposition to current flow, while the reactance is the opposition manifested by the cyclic storage of energy in magnetic fields (inductance) or electric fields (capacitance). Propagation occurs in various modes, differentiated by the field pattern of the electromagnetic wave. Transmission lines are specified to an ideally length-invariant, frequency independent characteristic impedance, determined by their cross-sectional dimensions, such that these modes can propagate without risk of reflection. In the case of two-conductor lines such as coaxial cables or PCB traces, the fundamental mode is transverse electromagnetic (TEM), while only transverse magnetic (TM) or transverse electric (TE) modes are allowed in single conductor hollow waveguides

[36]. Here, transverse refers to the direction perpendicular to wave propagation. Test equipment for characterization of RF components is primarily designed to Z_0 of 50 Ω or 75 Ω to which any studied transmission line components should be matched.

2.1.1 Coaxial cables

The benefits of CNTs, conductive and otherwise, have already garnered them a significant amount of interest in the fabrication and testing of various types of transmission line. A common transmission line structure is the coaxial cable, in which a center cylindrical conductor is surrounded concentrically by a dielectric separator material and outer conductor layer, as shown in Figure 7. The RF signal is carried on the inner conductor while the outer conductor acts as a shield to contain the resulting electromagnetic waves within the dielectric, as well as to protect from external interference. The characteristic impedance of a coaxial cable depends on the inner conductor diameter (d), the outer conductor diameter (D) and the separator dielectric constant (ε_r) according to the following equation [36].

$$Z_0(coax) = \frac{138 log_{10}(D/d)}{\sqrt{\varepsilon_r}} \quad (2.1\text{-}1)$$

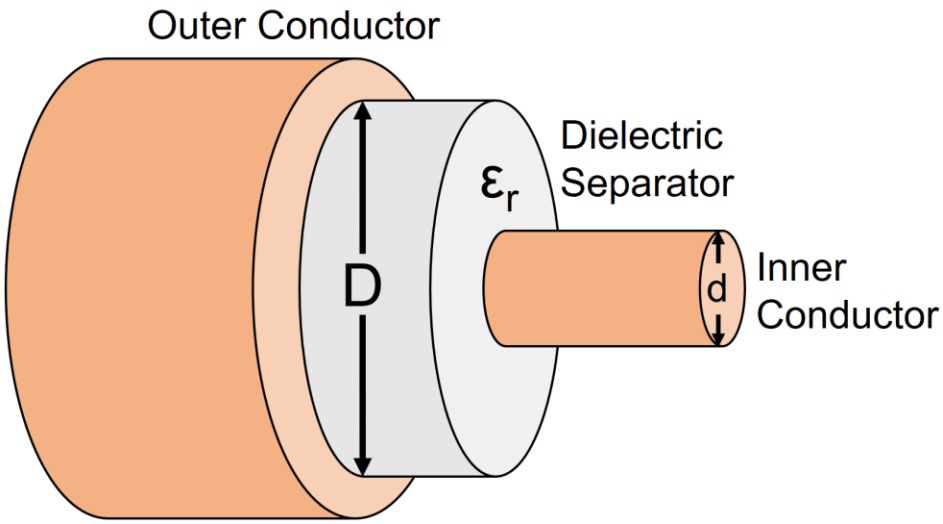

Figure 7. Schematic of a coaxial cable showing parameters used for calculating Z_0 of the line.

A large number of literature examples have been published that focus on the synthesis of nano-coaxial cable structures composed of individual CNTs and other materials [37], [38], [39], [40] with potential appeal for interconnects in nanoscale electronics. Study of the RF performance of these structures as transmission lines is sparse.

Promising work has been published regarding the testing of coaxial cables following standard specifications, where the metal inner and/or outer conductors have been replaced with macroscale CNT assemblies [41], [42], [43], [44]. Studies published by Paul Jarosz and coworkers have reported the successful fabrication of such cables using MWCNT sheets and densified MWCNT wires for the outer and inner conductors, respectively [42], [43]. The cables exhibited attenuation-per-length nearly equivalent to their metal versions up to 3 GHz and demonstrated that potassium tetrabromoaurate ($KAuBr_4$) chemical doping improved performance and reduced the rate of attenuation increase with frequency. A slightly different approach based on this work was utilized by Mirri et al. [44] to replace the coaxial outer conductor by coating the surface of the dielectric separator with a dispersion of CNTs in chlorosulfonic acid (CSA). In both the work by Jarosz et al. and by Mirri et al. it was found that

increasing the CNT layer thickness used in the outer conductor improved attenuation in the cable up to a critical thickness.

2.1.2 Planar transmission lines

In addition to free-standing transmission lines, a category of planar transmission line designs exist that are typically applied as interconnects between components on PCBs. Examples include the microstrip line, stripline, and coplanar waveguide (CPW), shown in Figure 8a, b, and c, respectively. In each case, the transmission line structure consists of a conducting trace to carry the RF signal and one or more ground planes to act as return paths to confine the electromagnetic field, as well as sections of dielectric substrate material. The value of Z_0 for these structures is dependent on various spacings between the components and the properties of the dielectric, depending on the design in question, but all of these must be designed to maintain impedance matching for good performance. In contrast with enclosed coaxial cables and striplines, open structures such as microstrip lines and CPW tend to suffer radiation losses, especially at high frequencies [36].

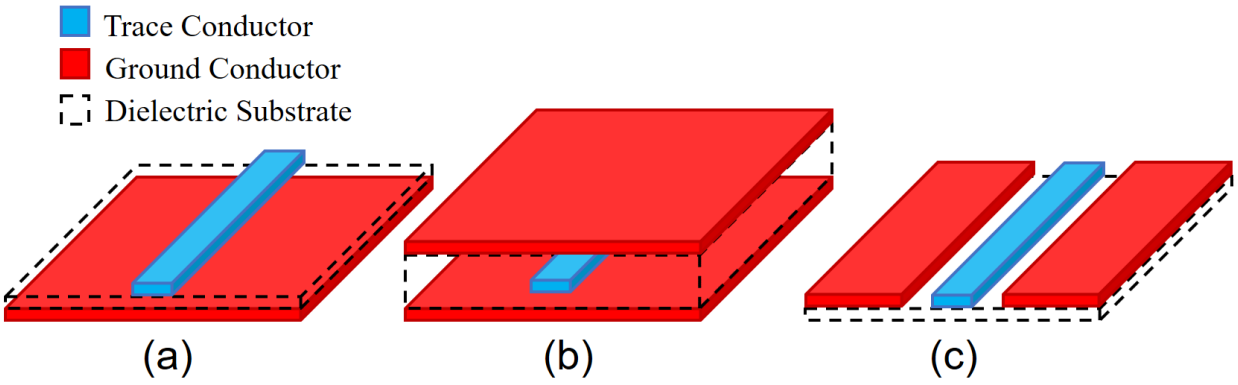

Figure 8. Schematic diagrams of (a) microstrip line, (b) stripline, and (c) coplanar waveguide (CPW) planar transmission line structures. Diagrams show layout of components only and are not scaled to a particular design impedance.

Testing of such planar transmission line structures fabricated from bulk CNT materials is an area of potential development, and only a few examples exist in literature [45], [46]. In the work by El-

Sabbagh et al. [46], loose SWCNT powder was packed into a groove in an alumina substrate and enclosed on top by another alumina piece, with shielding by copper tape to create a stripline geometry. A different structure and approach were utilized by Bulmer et al. [45] in which commercial SWCNT filter paper samples were placed in a gap cut from the trace of a conventional metal microstrip line. In both cases, the well-known equivalent circuit transmission line model based generally on the Telegrapher's equations [47] was used to characterize the transmission line's electrical properties, especially the frequency-dependent resistance of the conductors. This was one approach used to directly probe the frequency-dependent electrical conductivity in CNT sheet materials [45] in which results indicated increasing conductivity with frequency, a diverging trend from that of metals. The details of this study are expanded upon in Section 2.2.3.

2.1.3 Rectangular waveguides

A waveguide, in which an electromagnetic wave is transported inside of a hollow, conductive conduit, is considered to be a special case of transmission line. Due to the use of only one conductor, they are different from typical transmission lines but accomplish the same goal. Rather than the signal being carried on the surfaces of the conductor as in typical transmission lines, it is transported through reflection off of the conduit walls in a zig-zag fashion. For this reason, waveguides are commonly chosen for applications requiring high energy throughput and low loss, as little current flows in the conductor. Waveguides are most often rectangular (Figure 9a) or circular (not shown) in cross section. The lowest order propagation mode in rectangular waveguides is TE_{10}, where the electric field components are transverse to the propagation direction. To facilitate propagation of this mode, the long dimension of the waveguide (A) is made equal to ½ wavelength at the cutoff frequency (f_c) (Figure 9b); this is derived from the general equation for the cutoff frequency of a TE_{mn} mode,

$$f_{c,mn} = \frac{1}{2\pi\sqrt{\mu\varepsilon}}\sqrt{\left(\frac{m\pi}{A}\right)^2 + \left(\frac{n\pi}{B}\right)^2} \quad (2.1\text{-}2)$$

where *m* and *n* are the horizontal and vertical orders of the mode, *A* and *B* are the respective horizontal and vertical dimensions of the waveguide, and μ and ε are the permeability and permittivity of the medium in the waveguide. Because the nature of TE- or TM-mode wave propagation make it impossible to define a unique voltage and current in a rectangular waveguide, the notion of a characteristic impedance is less applicable. Instead, a frequency-dependent quantity called the waveguide impedance or wave impedance is used, which is derived from Maxwell's equations for TEM, TE, or TM waves [36].

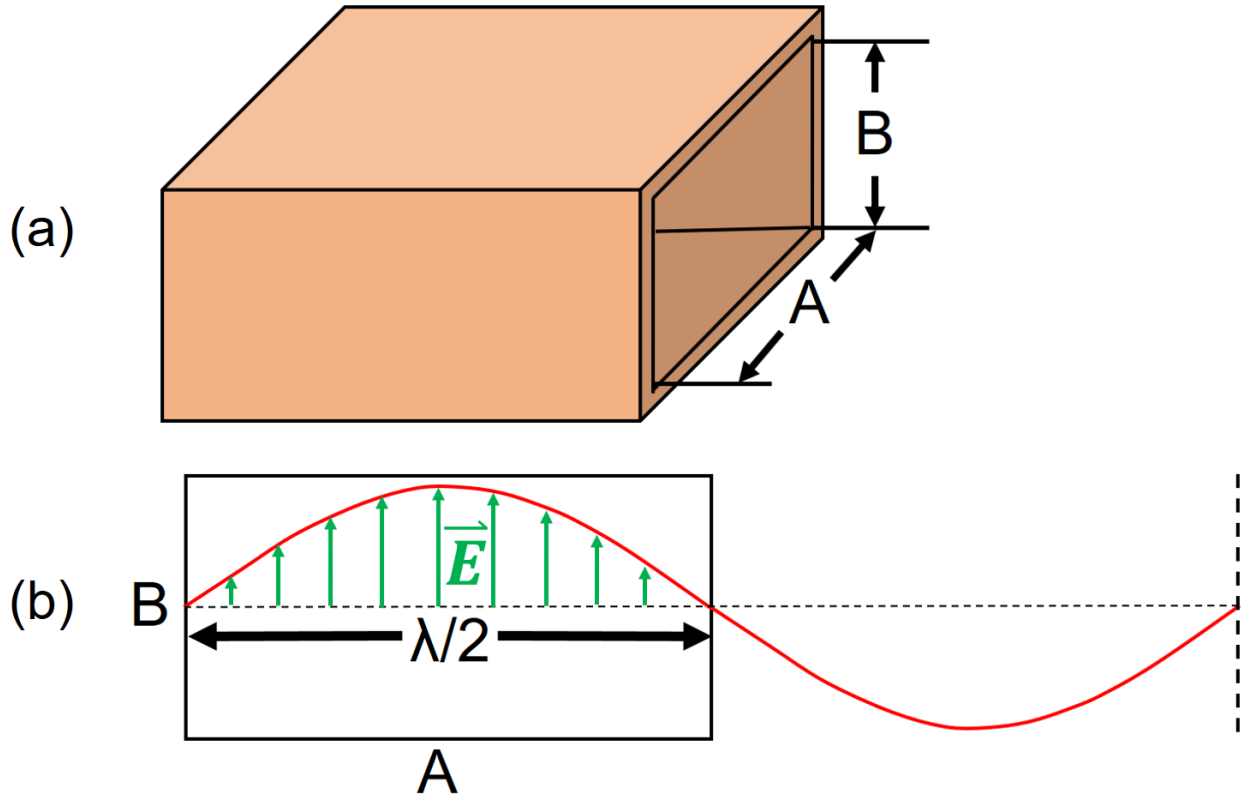

Figure 9. (a) Diagram of a rectangular waveguide showing vertical and horizontal dimensions. (b) The conditions required for the TE_{10} propagation mode in rectangular waveguides.

Investigation in literature as to the use of CNTs to replace the typical metal surfaces fabricated in the interior of waveguides appears to be scarce. CNTs do not appear to have been integrated into

standard rectangular waveguide walls. This may be because the currents flowing in the conductive walls are relatively small such that metals are sufficient even at very high frequencies; this is in part responsible for the ability to use hollow waveguides with metal interiors in high power, high frequency applications. One paper by Cometto and coworkers [48] performed theoretical study of a substrate integrated waveguide (SIW) was simulated with sidewalls constructed of vertical SWCNT bundles, creating a hollow rectangular channel with gold top and bottom plates. In the millimeter-wave regime, it was found that the simulated CNT waveguides performed similarly to counterparts using gold sidewalls. In another study by Gradoni et al. [49] a rectangular waveguide was fabricated from a commercially obtained carbon fiber composite material that was not reported to contain carbon nanotubes. In another vein, several studies [45], [50], [51], [52] have utilized standard metal rectangular waveguides to perform transmission/reflection testing of CNT samples inserted in the waveguide path in order to extract frequency-dependent properties such as permittivity and conductivity. This application is discussed in more detail in Sections 2.2.1 and 2.2.3.

2.1.4 Antennas

RF antennas transfer electromagnetic energy between free space and physical devices through resonant structures. Various types of antenna designs are used in practice, including wire antennas, dipole antennas, and patch antennas, and combinations of multiple antennas can be assembled in arrays to carry out a function in concert. In all cases, the dimensions of the conductive, resonant element(s) of the antennas must be chosen such that an excitation by an RF signal at the desired frequency band creates a standing wave pattern in the resonator. To achieve this, many antenna types target the half-wavelength at the design frequency. For example, a patch antenna (shown in Figure 10) uses a rectangular 2-D patch as its resonant element, fed with a microstrip line, where the length L of the patch is made equal to one half-wavelength at the desired frequency in the composite air-dielectric medium

surrounding the patch. This resonance then results in the radiation of electromagnetic waves from the patch into the surroundings. When the radiated waves are incident on another antenna of the same design frequency, they will also induce a current in that patch by the same mechanism in reverse. Thus, RF antennas use resonance for both the emission and reception of signals [53].

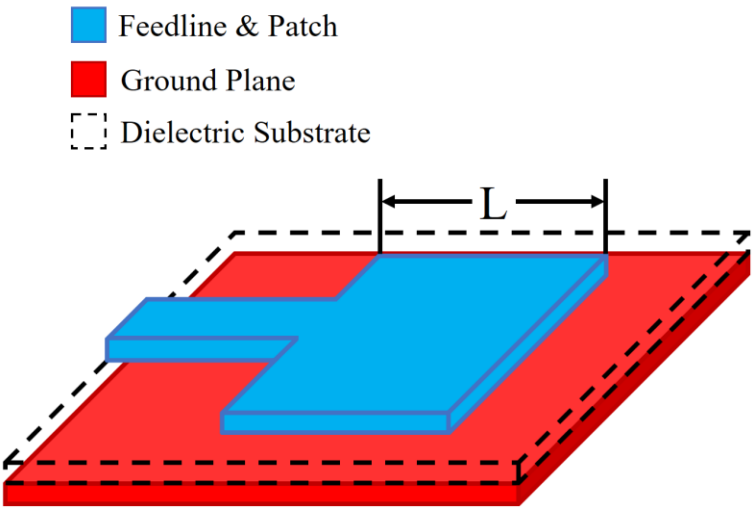

Figure 10. Schematic diagram of a basic patch antenna.

CNTs have garnered significant interest in antenna applications owing to their high corrosion resistance, flexibility/mechanical strength, and low density, in addition to their conductivity. This has led several groups to fabricate and test CNT patch antennas on flexible substrates [54], [55], [56]. Other advances in this area have sought to take advantage of the controllable nanoscale elements of CNT materials, including CNT alignment [57] and chemical doping [58], [59]. These studies have found CNT antennas to consistently and capably achieve resonance at the desired frequencies, while maintaining the advantages provided by the materials over conventional metals as mentioned earlier. These published findings indicate experimental treatments and structural modifications of CNT materials can affect their RF performance. In particular, the alignment of CNTs within a patch antenna was found to produce drastically different gain depending on whether the CNTs were parallel or perpendicular to the E-plane of the antenna [57]. Also, Puchades et al. found that thermally reducing the level of chemical doping in

SWCNT thin films, thereby concurrently reducing their electrical conductivity, proportionally reduced the radiation performance of fabricated inverted-L-type patch antennas [59].

Published literature regarding the application of CNT materials in passive RF components including coaxial and planar transmission lines, hollow waveguides, and antennas have already made significant advancements, indicating a strong interest in these materials as novel RF conductors. The effects of nanostructure variables including CNT alignment and network density, as well as conductivity change using chemical doping on passive components can be observed in evaluation of their performance. Evidently, the understanding of these effects would be bolstered through fundamental study of intrinsic material properties and the mechanisms involved.

2.2 Conductive Property Characterization at High Frequencies

2.2.1 Metals

The skin effect was first theoretically discussed in 1873 by Maxwell [60], and subsequent contributions to understanding of the theory for various metal conductor geometries were made throughout the late 19th century [61], [62], [63], [64], [65], [66], [67], [68], [69]. The early 20th century saw efforts to experimentally measure the AC resistance of metal conductors. One such study was performed by Kennelly & Affel in 1916 [7] in which a radio frequency alternator consisting of a DC motor driving a steel disk rotor was used to generate AC current with frequencies up to 100 kHz, while the resistance of a conductor-under-test placed into a detection circuit was recorded using a voltmeter and ammeter. The researchers found that in addition to the conductor-under-test, compensatory resistors and inductors were required to balance out reactive components which led to measurement inaccuracy if left unchecked. A solid 12 AWG (diameter=0.205 cm) copper wire was measured from DC to 100 kHz. A clear match to the theoretical values for the conductor was observed in the data.

Chapter 2 – Review of Literature

Since the advent of dedicated instruments such as LCR meters and vector network analyzers (VNA), exciting RF signals in test samples and measuring the response has become much more straightforward than during the early studies of skin effect. VNAs in particular are used to evaluate the performance of various RF components and devices in various frequency bands. At their base level, they are capable of measuring the impedance of a connected load. This capability has been used to measure the skin effect in copper wires attached in a loop between the inner and outer conductors of a conventional RF coaxial connector [70]. The impedance of the copper wire as measured was shown to match the data predicted by skin effect theory. Application of this method to metals in literature is limited and studies have only probed up to MHz frequencies [70], [71].

Another method to measure resistance in the RF range is to consider the conductive material used to fabricate transmission lines. In this case, a well-known modeling technique of representing the transmission line as an equivalent circuit may be used. The diagram shown in Figure 11b is one such representation; in this instance it is used for a microstrip line (side view in Figure 11a) as this is the easiest planar transmission line structure to fabricate for testing of various sheet-form conductor materials. The trace and ground conductors together are represented by a series distributed AC resistance (R') and inductance (L'), while the distributed leakage conductance (G') through the dielectric substrate and the distributed capacitance (C') between the conductors are placed in parallel. All four parameters are per unit length. The Telegrapher's equations are derived by considering the voltage and current with respect to position and time and applying Kirchoff's laws over the circuit [47]. They can then be converted to the frequency domain and take the form shown below,

$$-\frac{\partial}{\partial x}V(x) = (R' + j\omega L')I(x) \tag{2.2-1}$$

$$-\frac{\partial}{\partial x}I(x) = (G' + j\omega C')V(x) \tag{2.2-2}$$

where *V(x)* and *I(x)* are the frequency-dependent voltage and current with respect to position along the line. The Telegraph equations can be solved in terms of experimentally measurable transmission and reflection coefficients for the microstrip line, allowing the calculation of AC resistance values from fabricated samples.

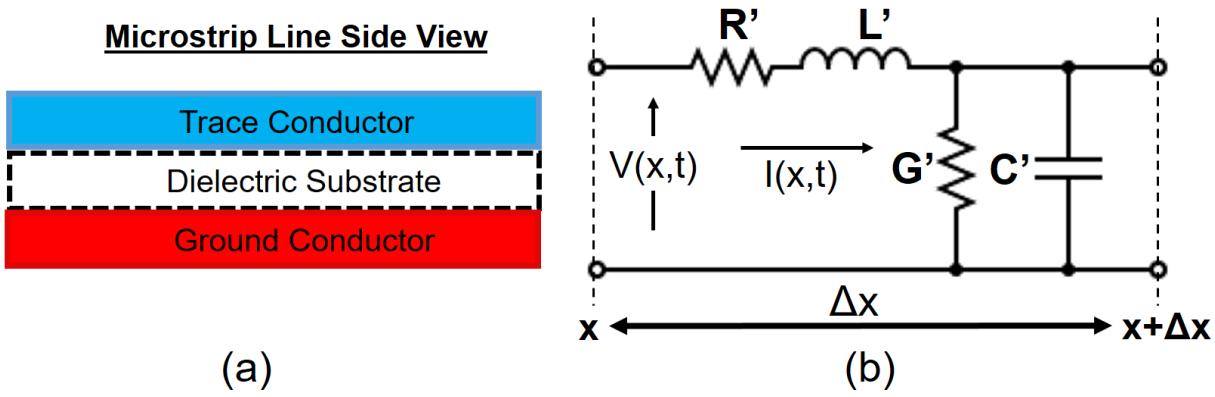

Figure 11. (a) Side view of microstrip line geometry; the direction of propagation is from left to right. (b) Equivalent circuit representation of the microstrip line.

The method described above, while capable of calculating resistance values from measurements of microstrip line conductors, is subject to limitations which may prevent it from accurately characterizing the influence of skin effect in metals. Though in theory the current density in the rectangular conductor of the microstrip should be at the surfaces of the strip and result in AC resistance which agrees with the skin effect prediction, the resistance is typically found to be much higher than expected [72], [73]. This is attributed to two main issues. Firstly, the so-called “edge singularity” effect where surface currents tend to flow closely parallel to sharp edges of a conductor [73] and secondly, the concentration of current towards the bottom of the trace due to the proximity of the ground plane [72]. This results in the cross-sectional distribution of current being more restricted than it would be from skin effect alone, and the measured resistance is thus higher than expected. Additionally, the interfering

effects worsen with increasing frequency. Therefore, the AC resistance of a metal from skin effect may be difficult to measure accurately with this method due to the multiple interfering variables.

Two contactless methods for characterizing materials at radio frequencies are the waveguide and free space transmission/reflection techniques. In these cases, the sample of interest is placed in the path of RF electromagnetic waves carried in hollow waveguides or directed by horn antennas and focusing components. A VNA is used to supply the RF signal and detect the response. The measured data are then used to calculate the sample properties. As horn antennas and waveguides can both be specified to standardized frequency bands, it is possible to assemble a collection of apparatus components to accurately measure a wide range as desired. In general, these methods measure the amount of the incident wave which is reflected and/or transmitted; this data is then correlated to the properties of the sample/material. Several examples in which such a technique was used to measure the frequency-dependent conductive properties of sheet materials exist in literature [45], [50], [51], [74]. However, the sensitivity when measuring metals is limited by the skin effect, as the penetration of high frequency electromagnetic waves into the material is extremely small and decreases with increasing frequency. This results in the entire signal being reflected within all frequency bands of interest [1].

When the thickness of metal films is sufficiently small (on the order of nanometers) RF signals may pass through to some extent, but this is of limited value to characterize the material's bulk properties. This was shown in the work by Poo et al. [74], where gold thin films ranging from 9-20 nm thickness were deposited on polymer film substrates and enclosed in a rectangular waveguide open-terminal apparatus. The sliding short was adjusted to focus the measurement at the substrate/sample interface, allowing the AC conductivity of the gold nanofilms to be calculated from the measured reflection coefficient. The resulting data from 8-12 GHz indicates that the AC conductivity of the films does not change significantly with frequency as would be expected for samples of thickness much

smaller than the skin depth. However, the sample thickness significantly changes the measured conductivity which increases towards the bulk value (4.35×10^7 S/m [2]) as the thickness is increased [74].

The free space version of transmission/reflection measurement is very similar in concept to the version performed in waveguides, in that the signal used for testing is emitted and received using horn antennas, and the signal is directed at the sample using beam focusing components such as dielectric lenses. This has advantages over the waveguide iteration in that it is easier to mount the samples as they are not physically held in place by the probing components. An additional consideration is that the accuracy of the method is sample-size-dependent, as a sample that is too small for the measured frequency band will lead to diffraction or allow signal to leak through in the periphery. Thus, the sample dimensions must be made to properly account for the beam characteristics of the measurement system in a given frequency range. This generally leads to a trend of decreasing required sample dimensions with increasing frequency [75].

2.2.2 Individual CNTs

Due to the excellent electrical properties of individual CNTs at DC level, it is desirable to determine how these properties are affected at radio frequencies. Previous study has sought to investigate this behavior through experimental measurements [76], [77], [78] and theoretical modeling approaches [77], [78], [79]. The theoretical view of single CNT high frequency conduction began with Burke [79], based on the Lüttinger liquid theory. He proposed and developed an equivalent circuit model of an individual SWCNT as a transmission line, consisting of distributed series kinetic inductance and shunt quantum and electrostatic capacitances. The model effectively describes the conduction as taking the form of a 1-D plasmon along the length of the tube. Taking into account the distributed resistance of the tube in real cases, a low resistance does not result in significant plasmon damping and

the impedance behaves as standing waves along the tube. On the other hand, a higher resistance dampens the plasmon waves significantly and two limits corresponding to the DC resistance and the quantum/electrostatic capacitance-limited characteristic impedance at low and high frequencies, respectively are observed [79]. Burke and coworkers went on to experimentally test the resistance of individual SWCNTs in a two-electrode device format up to 10 GHz and found that it decreased with frequency in general agreement with the behavior suggested by the model [76].

Further experimentation was performed by other researchers [77] where an individual SWCNT was aligned between two ground-signal-ground (GSG) probes as shown in Figure 12a. Its RF conduction properties up to 50 GHz were determined by fitting the equivalent circuit model in Figure 12b to VNA measurements. Here R_{CNT} and L_K are the resistance and kinetic inductance of the CNT, respectively, and R_C and C_{el} are the contact resistance and parasitic capacitance, respectively, between the CNT and measurement probes. Based on fitting of the model to measured impedance as shown in Figure 12c, the researchers had two conclusions: first, the shorting of R_C due to C_{el} leads to the reduction of impedance with increasing frequency up to ~6 GHz and second, R_{CNT} remains consistent with the DC value up to 50 GHz at ~34 kΩ. The extracted circuit parameters of the SWCNT were close to those predicted by the earlier theoretical modeling. Further work was performed in this paper to assess the properties of SWCNT bundles using proportionality to the number of CNTs (N) in the bundle. For example, the effective inductance (L_{eff}) of a bundle was found to be proportional to the individual SWCNT inductance (L_k) as $L_{eff}=L_K/N$ [77].

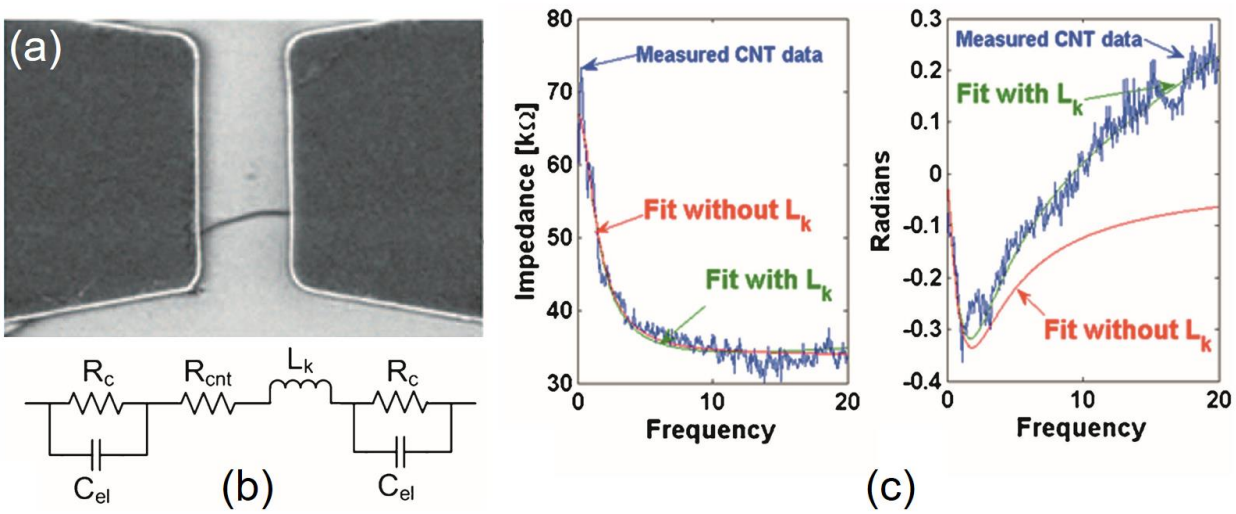

Figure 12. (a) An individual SWCNT suspended between the signal electrodes of a GSG-CPW. (b) The equivalent circuit used to model the SWCNT. (c) The impedance magnitude and phase angle of the SWCNT from DC to 20 GHz. Reprinted with permission from Plombon et al. [77].

A similar experimental procedure was performed in another publication [78] with a suspended MWCNT as shown in Figure 13a. The MWCNT was modeled using a circuit model (Figure 13b) that is nearly identical to that of the SWCNT in [77], but with the addition of a parallel capacitance to represent the multiple concentric walls in the MWCNT. The impedance of the MWCNT in real-imaginary format is shown in Figure 13c. The impedance decreases rapidly with frequency up to 30 GHz, after which the trend tails off; the same response occurs in the extracted resistance of the MWCNT. It was suggested by the authors that this takes place due to inner shells of the MWCNT participating more in conduction as frequency increases until a saturation point, at which the resistance remains constant. The work discussed here has consistent implications that individual CNTs of various types are promising alternatives to metals at high frequencies due to their 1-D nature.

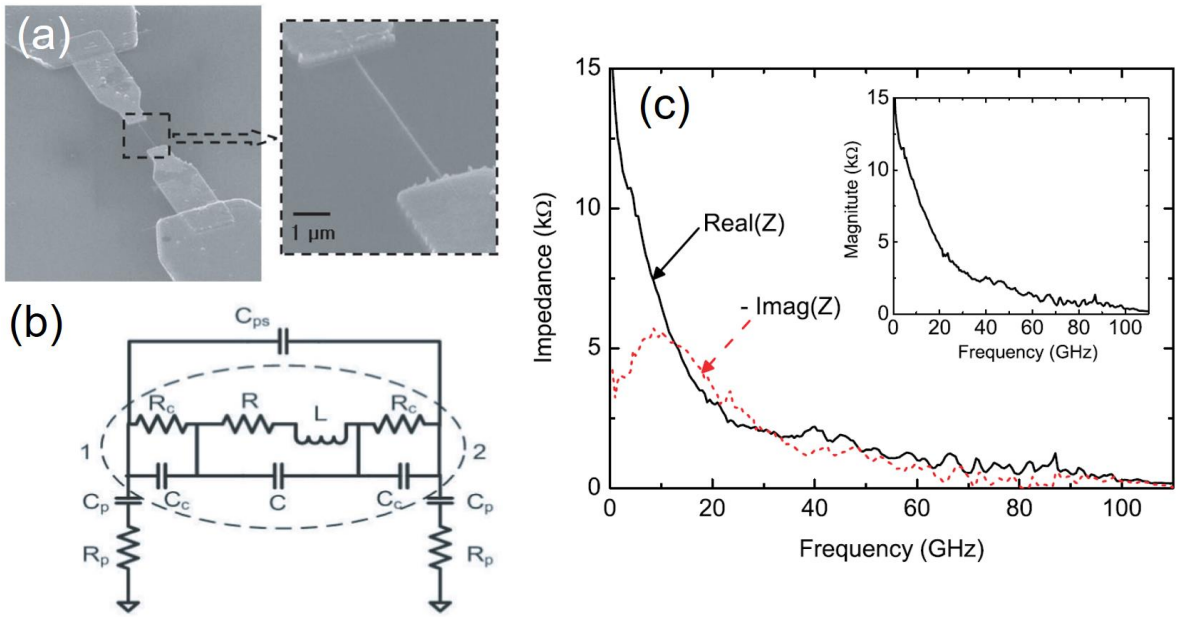

Figure 13. (a) An individual MWCNT suspended between the signal electrodes of a GSG-CPW. (b) The equivalent circuit model of the GSG-CPW with suspended MWCNT (inside of dotted circle). (c) Real and imaginary parts of impedance of the MWCNT (inset is impedance magnitude). Reprinted with permission from [78].

2.2.3 Macroscale or "bulk" CNT materials

Despite early successes in measuring the AC properties of individual CNTs, their high resistances (on the order of kΩ) are expected to cause issues with implementation as interconnects in large-scale integrated circuits [80]. This drove an increase in the study of macroscale CNT assembly RF properties in the first two decades of the 21st century, in part enabled by the development of new production and post-processing techniques to create such samples and control their properties.

Several papers have been published exploring the frequency-dependent conduction in macroscale assemblies of SWCNTs [45], [81], [82], [83], [84], [85], [86], [87], DWCNTs [71], and MWCNTs [50], [88], [89]. Form factors including networks of a few thousand CNTs, CNT thin films, free-standing CNT textiles, and twisted CNT wires have been investigated. Highstrete et al. determined that the assembly of SWCNT networks containing 10^3-10^4 CNTs oriented across the gap between signal and ground of a CPW increased the signal attenuation [82]. In a subsequent study [85], they extracted the

AC conductance of the SWCNT network by modeling the CPW as an equivalent circuit with a shunt admittance (Y, inverse of impedance) between signal and ground. It was found that above a weakly frequency-dependent region, a sharp increase in conductance occurred between 0.1 GHz and 50 GHz.

In a pair of studies published by Xu et al. [83], [84], the AC conductivity of SWCNT films fabricated on polyethylene terephthalate substrates was measured using the Corbino reflectometry method, in which a gold contact pattern deposited on the sample interfaces with a coaxial probe which measures the reflectance of the sample. The impedance $Z_s(\omega)$ was calculated from the measured reflectance data using the following equation,

$$Z_s(\omega) = Z_0 \frac{2\pi}{\ln\left(\frac{b}{a}\right)} \frac{1+S_{11}}{1-S_{11}} \tag{2.2-3}$$

where Z_0 is the coaxial probe characteristic impedance, a and b are the contact pattern's respective outer and inner dimensions, and S_{11} is the complex reflection scattering parameter of the film. In the first study in 2007 [83], the impedance of transfer-printed SWCNT films placed on PET substrates was measured and used to calculate the AC conductivity of the samples from 10 MHz to 30 GHz at various temperatures. In the later 2008 study [84], the impedance of spray-coated SWCNT films on PET substrates was measured and used to calculate the AC conductance from 100 kHz to 50 GHz, with the density of the samples being varied by changing the concentration of the spray-coating solution. AC conductivity data of the transfer printed films from the first study by Xu et al. are shown in Figure 14a, while the AC conductance data of the spray coated films from the second study are shown in Figure 14b.

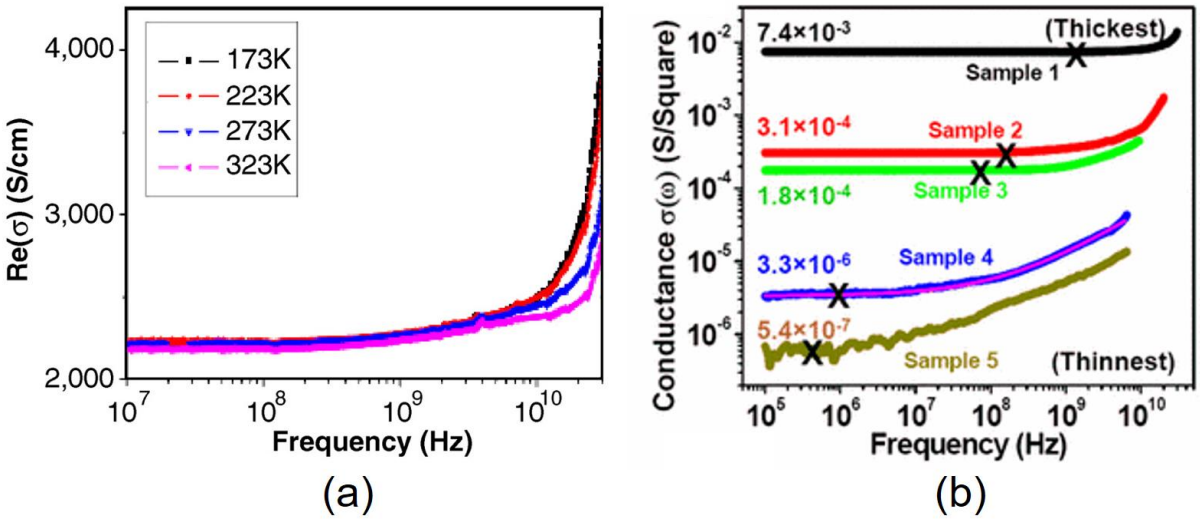

Figure 14. (a) Real AC conductivity data of transfer-printed SWCNT films on PET substrates at four different temperatures. (b) AC conductance data of SWCNT films on PET substrates spray-coated using five successively higher solution concentrations. Reprinted with permission from Xu et al. [83] and [84], respectively.

In both studies, the conductance of the SWCNT films was observed to remain constant at the DC value until a certain onset frequency, after which it began to sharply increase. The films of varying density exhibited increasing DC conductance and higher onset frequencies with increasing sample density. Identical trends were observed by Iqbal et al. when they reproduced this study for proof-of-concept in the potential use of these materials for flexible/transparent electronics [86], [87]. The 2008 work by Xu et al. [84] advanced the understanding of the mechanism resulting in this conductance response. By measuring electric-field-dependent DC conductance of the SWCNT films, they determined the junction-to-junction length scale in the samples and found it matched the half-cycle path length of the charge carriers derived from the AC conductance measurements. This indicated that the conductance increase was due to the reduced number of junctions crossed by charge carriers at higher frequencies, causing the high conductivity of the individual CNT segments to dominate. The higher density SWCNT films were found to have a smaller junction separation, leading to a higher onset frequency, in agreement with previous study of CNT-polymer composites [90].

AC conduction has also been studied for free-standing SWCNT sheet materials [45], [81]. Bulmer et al. [45] studied commercial SWCNT papers fabricated using a surfactant-based dispersion and filtration process. The papers were composed of electronic-type-sorted SWCNTs, with metallic, semiconducting, and unsorted samples. The authors first measured the sheet conductance of small segments of SWCNT paper inserted into a gap in a 50 Ω microstrip line by fitting the resistance using the Telegraph equation-based equivalent circuit model. Though the conductance spectra showed an increasing trend with frequency, the method was deemed inadequate for frequencies higher than 10 GHz due to the self-inductance of the microstrip causing inaccuracy. The researchers switched to the transmission/reflection measurement method in rectangular waveguides to measure the AC conductivity of the sorted and unsorted papers in the bands of 18 GHz to 26 GHz and ~65 GHz to 120 GHz. The Nicolson-Ross-Weir equations were used to extract the complex permittivity of the papers from transmission/reflection measurements and the following relation was used to calculate the AC conductivity (σ(ω)),

$$\sigma(\omega) = -\varepsilon'' \varepsilon_0 \omega \tag{2.2-3}$$

where ε'' is the imaginary part of the relative complex permittivity, ε_0 is the permittivity of free space, and ω is the angular frequency. The results of these measurements are shown in Figure 15.

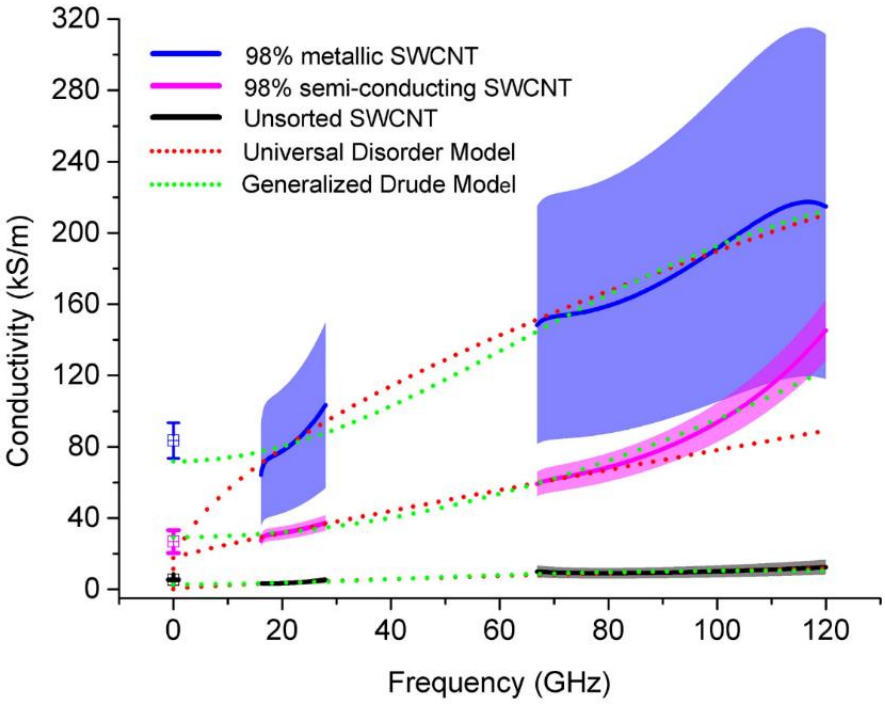

Figure 15. AC conductivity of metallic, semiconducting, and unsorted SWCNT papers measured using rectangular waveguides. The highlighted sections show the error of measured data, while the dotted curves are the fits for each sample of the universal disorder model and the Generalized Drude model. Reprinted with permission from Bulmer et al. [45].

A conductivity increase was observed for all of the SWCNT papers measured up to 120 GHz, the magnitude of which was different for each material. The metallic SWCNTs achieved the highest absolute conductivity owing to their high DC conductivity, but the semiconducting SWCNTs exhibited the greatest increase in conductivity, at 400% of their DC value. The AC conductivity for each sample was modeled using the universal disorder model and the Generalized Drude model (see Chapter 8 for further detail). It was found that the universal disorder model fit well to the metallic and unsorted materials data up to 120 GHz. This was taken to indicate that in addition to metallic composition of the SWCNTs, factors such as defects, junctions, and internal alignment can also affect the frequency-dependent conductivity. Overall, it was noted that the model fitting parameters for other unsorted SWCNTs studied in literature were similar to the ones modeled here, while the same model for higher conductivity films had a lower parameter value. This led the researchers to conclude that longer average CNT length led to higher conductivity and was indicative of lower disorder in the material. As the

behavior of the semiconducting SWCNTs did not follow the universal disorder model above 68 GHz, it was also concluded that a more comprehensive model was needed to describe that material.

In addition to studies on SWCNTs, several papers have been published investigating the high-frequency conductive properties of macroscale arrangements of MWCNTs [50], [88], [89]. Two of the studies [50], [89] focused on free-standing MWCNT papers prepared by dispersion in a solution followed by filtration and drying. In the study by Wang et al., the samples were placed between rectangular waveguides such that the RF signal was incident on the surface in four separate frequency bands from ~8 GHz to 50 GHz. The measured data from the CNT papers was converted to complex permittivity using the Nicolson-Ross-Weir approach and the AC conductivity was extracted from the imaginary part of the permittivity. The conductivity data versus frequency for the MWCNT paper is shown in Figure 16. The conductivity is found to decrease steadily over the frequency ranges measured.

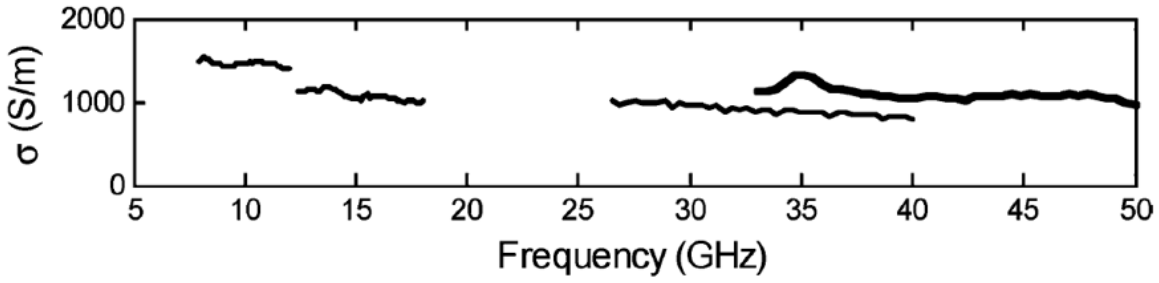

Figure 16. AC conductivity (a) of a MWCNT paper sample in four distinct bands within the limits of ~8 GHz to 50 GHz measured using rectangular waveguides. Reprinted with permission from Wang et al. 2008 [50].

Another group of researchers probed the RF properties of aligned MWCNT sheets drawn from the edge of a CVD-grown array on a silicon substrate [88]. The extracted sheet samples were assembled over the tops of CPWs by wetting and evaporation of alcohol, with the CNTs oriented either parallel or perpendicular to the gaps of the CPW. The shunt conductance Y of the MWCNT samples was extracted by modeling the CPWs with an equivalent circuit model using known resistances and inductances determined from measurements of bare CPWs.

The experimentally measured frequency-dependent conductance of the MWCNT samples was found to increase from DC to 50 GHz for both orientations, with a linear behavior beginning around 20 GHz. The conductance was higher for the case in which the CNTs were oriented across the gap, attributed to their alignment with the electric field component oriented in the same direction. The researchers compared their data with an equivalent circuit model for the MWCNT sample itself, where the sheet is represented by an ideally frequency-independent conductance G_{sheet} in series with a contact capacitance C_{cont}. The contact capacitance is theorized to hinder the shunt conductance at low frequencies, while at high frequencies a reactive shunt conductance due to the polarization within the MWCNTs takes over which is modeled by the frequency-independent capacitance C_{shunt}. The conductance calculated from this model achieved an approximate fit to the measurement data. The model fitting parameters used were found to match the actual values for the system within reason. Due to the lack of inductive effects incorporated in this model and its fit to the data, the conductance measurements of the MWCNT samples were taken to indicate a primarily diffusive scattering mechanism throughout the frequency range, with typical Drude-like inertial behavior absent at high frequencies [88].

Studies of the RF properties of macroscale CNT materials of any type whose properties have been modified using techniques such as chemical doping, mechanical or chemical densification, or metallization to produce hybrid conductors are scarce in the literature. The only example from review of the field is a study where MWCNTs were dispersed in a solvent for electrophoretic deposition (EPD) onto the surface of copper electrodes [91]. The samples were irradiated by a CO_2 laser with various power densities to anneal the MWCNT films, and the AC resistance of the samples was measured using an impedance analyzer from 0.01 MHz to 10 MHz. The AC resistance data for the Cu-CNT conductors were compared with a bare Cu substrate. The resistance of the samples decreased with increasing

applied laser power density. The decrease of resistance with increasing irradiation power density was attributed to the increased crystallinity and better contact of the MWCNTs to the copper surface due to annealing. The contact resistance between the MWCNTs and copper was also measured and found to decrease after annealing, which supports this conclusion. The authors claim based on their AC resistance measurements that the inclusion of MWCNTs at the surface suppressed the skin effect for the hybrid conductors [91].

2.2.4 Bulk CNT materials as EMI shielding materials

Electromagnetic interference (EMI) shielding materials induce a high degree of attenuation in incident electromagnetic waves, either through reflection, absorption, or a combination thereof. The performance of shielding materials is quantified by their shielding effectiveness, a value in decibels (dB) which describes the attenuation of the incident electromagnetic waves. Shielding effectiveness has been measured in previous literature using similar experimental methods to those applied for AC conductivity characterization. CNT composites have seen extensive study as EMI shielding materials [90], [92], [93], [94], [95], [96], [97], [98], [99], [100], [101], [102], [103], [104], [105]. Controllable mass fractions of CNTs of various types and wall counts have been incorporated in composites using a variety of matrix materials, most often polymers. Bulk CNT materials are also emerging as promising materials in this field due to their multi-functional properties combined with high shielding effectiveness [106], [107]. Studies have shown favorable performance characterized by a variety of methods for both SWCNT [83], [106] and MWCNT [107] bulk assemblies. Values of ≥50 dB have been reported, which are generally superior to the properties of previously reported CNT-based composites by several orders of magnitude.

3 Opportunities for Advancement

3.1 Summary & Gap Analysis

Extensive study of beneficial CNT properties including reduced density, high corrosion resistance, and mechanical durability has been performed, but examples in literature that investigate their frequency-dependent conductive properties are comparatively limited. Interest in CNT materials for RF components such as transmission lines and antennas is clear in the literature, but the existing body of work in this area has prioritized comparison of device performance between CNT and metal conductors over investigation of the intrinsic material properties. Individual CNTs have been shown to exhibit a lack of skin effect due to the surface-focused nature of their conduction, but their high intrinsic resistances in the kΩ range limit their applicability for VLSI applications [80]. Bulk CNT conductors in which individual or bundled nanotubes are combined into a network have a wider range of applications. Study of bulk CNT material high frequency properties to date has compared CNTs with different number of walls, electronic type, and alignment. Several studies [45], [81], [82], [83], [84], [85], [86], [87] have shown increasing conductance with frequency in SWCNT thin films and bulk papers, while constant or decreasing conductance with frequency has been observed in MWCNT examples [50], [89]. Also, varying rates of conductance increase were observed in metallic, semiconducting, and unsorted SWCNT papers [45]. Higher conductance was observed when MWCNTs were aligned relative to the direction of high frequency electric fields compared to the misaligned case [88].

The effects of purification, chemical doping, and CVD metallization of bulk CNT materials have been extensively studied with respect to the DC electrical properties. Reduction of the amount of carbonaceous impurities and remnant metal catalyst to increase the CNT network purity is possible via thermal oxidation and acid treatments [108], [109], [110]. Doping with $KAuBr_4$ is known to produce a ~5x DC conductivity increase with high longevity [25], and various effects on the DC properties of

CVD-fabricated metal-CNT hybrids have been observed depending on the deposition metal and its morphology [31], [32], [33], [34], [35]. However, no examples have been found in literature which the high frequency conductive properties of chemically doped or metallized bulk CNT materials have been probed, and the transport mechanisms at high frequencies due to these treatments have not been explored. There is a clear opportunity to study these yet unexplored high frequency aspects of bulk CNT conductive materials which motivated this dissertation work. In addition, the promising application of bulk CNTs as EMI shielding materials can provide a strong practical perspective to the benefits afforded by the fundamental AC electrical properties of these materials. The present work took the opportunity to demonstrate the shielding capabilities of bulk SWCNT and MWCNT materials in the framework of a direct comparison using a single characterization method, which has not been previously done in the existing literature.

3.2 Dissertation Objectives

The research described herein investigated the role of impurities in the AC conduction of CNTs and determined whether the DC benefits of chemical doping of CNTs persist at high frequencies. The effect of platinum overcoating of the CNTs on the RF conduction was interrogated to determine if similar benefits to those observed with DC conductivity could be realized. The EMI shielding effectiveness of bulk SWCNT and MWCNT materials was interrogated to perform a direct comparison of the CNT types in a multi-functional thin film form factor. The main research goals associated with this work were as follows:

Dissertation Objective: Fundamentally understand the effects of impurity content in bulk carbon nanotube (CNT) materials, adsorption of $KAuBr_4$ chemical dopant, and deposited platinum inclusions on RF electrical transport in bulk CNT materials.

Research Goals

1. Establish a suitable and effective method to measure the AC conductivity of bulk CNT conductive sheet materials based on measurement consistency, sample dimensions/mounting requirements, and measurement frequency range.
2. Fabricate purified and $KAuBr_4$-doped bulk MWCNT samples. Perform experimental measurements to determine purity/doping effects on AC conductivity of the MWCNT material.
3. Investigate the effect of platinum deposition using CVD on the AC conductivity of purified MWCNT material by performing experimental measurements on samples containing a variety of metal weight loadings (% w/w).
4. Employ a theoretical model for the AC conductivity previously validated with CNT materials to inform hypotheses regarding the mechanisms affecting the frequency-dependent response of the AC conductivity due to chemical doping with $KAuBr_4$ or platinum metal deposition.
5. Demonstrate a practical application of the CNT materials' favorable RF properties through EMI shielding effectiveness measurements of free-standing CNT thin films with high optical transparency and surface conformability.

4 Experimental Methods

4.1 Characterization of CNT Materials

4.1.1 Bulk CNT materials

Two bulk CNT materials of interest to this work, their sources, general form factors, and properties are summarized in Table 2 below. Miralon MWCNT sheet was procured from Huntsman Corporation, and takes the form of a meter-scale fabric-like sheet with a mass-per-unit-area of 8-12 grams-per-square-meter (GSM) in its as-received state. This material was selected for testing the effect of purification, chemical doping, and metallization via CVD on the RF electrical properties due to the large quantity available, and most importantly, the significant amount of pre-existing knowledge of these treatments' effects on the other properties of the material [23], [25], [29], [31], [32], [33], [34], [35], [111]. Additionally, for studies in which it was desired to compare the properties of MWCNT and SWCNTs, SWCNT papers synthesized and purified in-house using well-studied and developed laser vaporization and acid/thermal treatment procedures [108], [109], [110] were used. Refer to Section 4.2.6 for a detailed description of the procedure used to synthesize the SWCNTs, and to Section 4.2.1 for a detailed description of the purification procedure used for both the MWCNT and SWCNT materials.

Table 2. Characteristics and properties of selected bulk CNT materials.

Material Names	Source	CNT Type	Form/Scale	Characteristics
Miralon® MWCNT sheet (8-12 GSM)	Huntsman Corporation	Multi-walled	Fabric-like sheet/ Several meters	• Little if any CNT alignment. • Fe catalyst remnant and carbonaceous impurities.
RIT SWCNT Paper	Laser vaporization synthesis	Single-walled	Filter paper/centimeter scale	• Little if any CNT alignment. • Co, Ni, and carbonaceous impurities (removed by purification).

4.1.2 Cutting and bonding for CNT sample fabrication

In preparation of CNT samples for various purposes, it is necessary to cut materials into different lengths and shapes. Simple pieces of CNT sheet material can be cut manually using razor blades, while

precise or complex geometries should be defined using computer-controlled tools. In this dissertation work, a Trotec Laser SpeedMarker 700 laser cutter equipped with a 1064 nm 50 W fiber laser was employed. For fabrication of metal components such as electrical contacts, a Cricut Maker 3 blade cutting tool was used.

Use of these tools relies on 2-D patterns which can be created in vector graphic design software or defined in the tool's own software. The blade cutter can be fitted with different attachments as needed, while cut settings with both of the listed laser tools require optimization on a material-specific basis to produce the desired results. Controllable factors include the laser focusing based on z-axis positioning, laser power and movement speed (percent or absolute units), pulse frequency in Hz, and number of laser passes. The range of available power and speed settings for the Trotec SpeedMarker 700 laser system are 1% to 100% of the total 30 W maximum and 1 mm/s to 12000 mm/s, respectively. These ranges offer significant versatility to control the effects of laser cutting on various materials. The Landi group has significant experience in performing parametric studies to obtain optimal cut settings to cleanly define geometries in bulk CNT sheet materials.

CNT sample preparation for various purposes may require a mechanically strong and electrically continuous interface between two separate material pieces. This can be reliably achieved using ultrasonic welding, which can produce a solid state bond between two pieces of material with no adhesives or compounds that may introduce contamination. To create a weld, a work piece to be joined is held under pressure between an anvil and horn and an ultrasonic acoustic vibration is applied at the material interface. The frictional effect produced by the vibration joins the pieces together by inducing plastic deformation and shearing stresses. A Branson-AmTech Ultraweld 40 ultrasonic welder was used in this dissertation work to join metal electrical contacts to CNT sheet samples.

4.1.3 Four-point probe DC electrical measurement

Measurement of DC electrical properties is essential to this work as a point of comparison and verification relative to measured frequency-dependent properties. A four-point probe station is a versatile tool for performing DC electrical measurements on CNT materials. The instrument consists of four probes that are used to pass current and measure resulting voltages in a number of different configurations depending on the characteristics of the sample. For instance, the DC resistance of a linear high aspect ratio sample such as a rectangular CNT strip is measured by supplying current with two outer probes and measuring the voltage between two inner probes separated by a given distance. This setup circumvents measurement errors introduced by the contact resistance of the two outer probes. The conductivity of the material is then correlated from the resistance measurement, the distance between the inner probes, and the cross-sectional area of the conductor using Equation (1.2-1).

Furthermore, a sheet resistance measurement using the van der Pauw configuration may be performed using a four-point probe (Figure 17). This technique places the probes at the corners of a square sample and current is passed along the edges between different sets of probes. The voltage measured along the opposite edge for a given measurement direction is used to calculate the resistance from Ohm's law, and the van der Pauw equation [112] is used to calculate the sample's sheet resistance (R_s) in ohms/square (Ω/□),

$$e^{-\frac{\pi R_{vertical}}{R_S}} + e^{-\frac{\pi R_{horizontal}}{R_S}} = 1 \tag{4.1-1}$$

$$R_{vertical} = \frac{R_{12,34}+R_{34,12}}{2} \qquad R_{horizontal} = \frac{R_{23,41}+R_{41,23}}{2} \tag{4.1-2}$$

where $R_{vertical}$ and $R_{horizontal}$ are the resistances along the vertical and horizontal edges of the sample, respectively, averaged between the forward and reverse biases. The DC conductivity of the material can then be calculated using Equation (4.1-3),

$$\sigma_{DC} = (R_s \cdot t)^{-1} \tag{4.1-3}$$

where t is the material thickness.

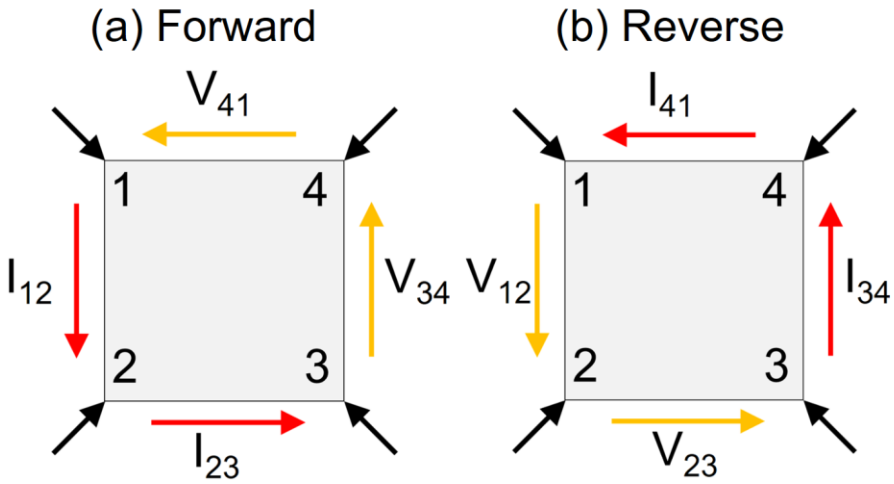

Figure 17. The general sample and probe configuration for the van der Pauw method of measuring sheet resistance in (a) forward direction and (b) reverse direction.

The thickness of the material is an essential parameter to obtain the conductivity of the material from electrical measurements using either of the configurations discussed above. For thicker sheet materials, this value can be obtained by averaging several measurements taken using a digital micrometer, while the thickness of samples for which this is impractical (i.e. thin films) can be obtained through techniques such as optical profilometry, in which the interference patterns produced by light reflected from the film and substrate surfaces are correlated to the film thickness. For this dissertation work, DC electrical measurements were carried out using a four-point probe station connected to a National Instruments (NI) PXI-5652 source/measure unit and an NI PXI-4071 digital multimeter at

room temperature (25°C). Thickness measurements were performed using a CenTech digital micrometer and a Veeco Wyco NT1100 optical profiler using white light interferometry.

4.1.4 Raman spectroscopy

Raman spectroscopy is a valuable technique in the characterization of CNT materials. This technique relies on Raman scattering, where both the energy and direction of photons incident upon the material experience a change due to inelastic interactions with its constituent molecules. This effect is due to the transfer of energy from the photon into the vibrational modes of the molecule in question. Different vibrational modes in a material therefore correspond to characteristic Raman shifts representing the frequency change of the scattered photon from its original state. Raman spectroscopy illuminates the sample of interest with a laser and collects the scattered photons. The distribution of frequency shifts due to the vibrational modes of the material are plotted as a Raman spectrum, and characteristic peaks can be discerned to analyze various aspects of the material.

With respect to CNT materials, Raman spectroscopy can act as a qualitative test for the presence of CNTs in an unknown sample and as a semi-quantitative method of probing specific metrics including CNT diameter distribution, electronic character, defect density, and to a certain extent the purity of a CNT sample. The Raman spectrum of a CNT sample contains three characteristic peaks [113] as shown in Figure 18. The G peak, located at ~1580 cm^{-1}, is characteristic of the pristine graphitic sp^2 bonding structure of CNTs. The D peak, located at ~1350 cm^{-1}, results from the disruption of the regular sp^2 hybridization due to defects such as broken sp^2 bonds or sp^3 bonding from impurities or other surface species. Lastly, the G' peak at ~2700 cm^{-1} represents long range order of the CNT bonding structure, which gives rise to second-order two-phonon scattering.

These three peaks should appear in the Raman spectrum of any CNT material, but there is a fourth, much smaller peak between 100 and 300 cm^{-1} called the radial breathing mode (RBM) peak (inset of Figure 18) arising from the vibrational mode where the CNTs expand and contract radially. This mode is highly damped in MWCNTs by the van der Waals interactions between the walls, and therefore only occurs in SWCNTs. The frequency of this vibration is known to depend on the diameter of a given SWCNT. Typical SWCNT samples will contain a variety of diameters, represented in a Raman spectrum by a composite peak with multiple local maxima.

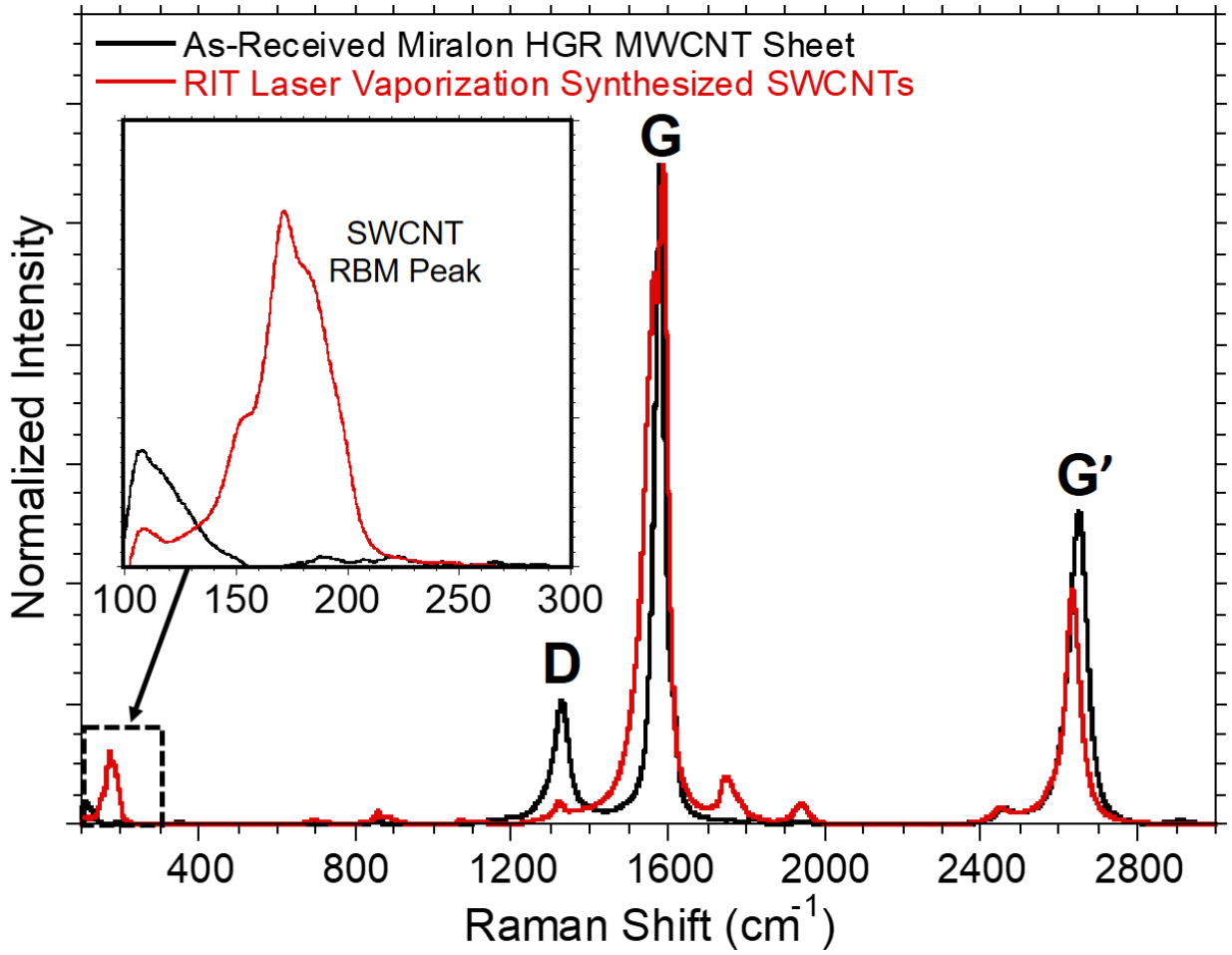

Figure 18. Typical Raman spectra for Miralon HGR MWCNT sheet (black data) and for RIT's laser synthesized SWCNTs (red data) with characteristic peaks labeled. The inset magnifies the region in which the SWCNTs' radial breathing mode peak appears.

Owing to this relationship, the diameter distribution can be determined using the following equation at each local maximum within the RBM peak.

$$\omega_{RBM,SWCNT} = (227.0 cm^{-1} \cdot nm)/d_t \quad (4.1\text{-}4)$$

Here $\omega_{RBM,SWCNT}$ is the Raman shift corresponding to a given maximum and d_t is the related SWCNT diameter. The proportionality constant 227 cm^{-1} nm was determined experimentally [114] through Raman spectroscopic measurements of 197 CVD-grown SWCNTs exhibiting a wide variety of diameters (1-6 nm) and all possible chiralities.

For this dissertation work, a Jobin Yvon (JY) Horiba HR800 LabRam spectrometer (633 nm excitation wavelength) was used for Raman scans on CNT samples in the range of 100-3000 cm^{-1} after an intensity calibration based on the characteristic Raman mode of a Si wafer located at 520.7 cm^{-1}.

4.1.5 Optical absorption spectroscopy

Optical absorption spectroscopy measures the absorption of an incident beam of light by a sample placed in its path. This leads to a spectrum of optical absorbance ($0<A_{opt}<1$) versus the wavelength [nm] or photon energy [eV] of the incident light. The measured absorbance of the sample can then be converted to an optical transmittance (T_{opt}) using the following equation,

$$T_{opt} = 10^{-A_{opt}} \quad (4.1\text{-}5)$$

This technique offers insight into the electronic character of SWCNT samples due to characteristic absorption peaks that are observable for metallic and semiconducting SWCNTs. These absorption bands arise from excitation to the higher energy states at the van Hove singularities in the band structure of SWCNTs [115]. Two peaks appear at ~0.7-0.8 eV and ~1.2 eV for the first and second interband transitions in semiconducting SWCNTs, while a third at ~1.7 eV represents the first interband

transition of metallic SWCNTs [108], [115]. In this work, optical absorption measurements were carried out using a PerkinElmer Lambda 25 optical absorbance spectrometer. CNT thin film samples were measured using a vertical clamp to position the sample normal to the incident beam. Not only can this technique be used to probe electronic type of SWCNTs, but a technique has also been developed to quantify the purity of SWCNT samples based on optical absorbance spectra [108].

4.1.6 Scanning electron microscopy & energy-dispersive x-ray spectroscopy

Scanning electron microscopy (SEM) provides valuable visual information for CNT samples through the interaction of an electron beam with the sample surface. SEM offers much greater magnification and resolution than typical optical microscopy techniques, enabling the nanometer scale surface and network properties of CNTs to be visualized. This capability also enables the examination of impurities or experimentally deposited materials such as metal nanoparticles. An additional, highly useful technique which is often integrated into SEM instruments is energy-dispersive x-ray spectroscopy (EDXS or EDX), which probes the elemental composition of the sample. This technique analyzes the number and energy of x-rays emitted from the sample due to the relaxation of outer shell electrons to lower energy states vacated by electrons excited by the beam of the SEM. The energies of the emitted x-rays are characteristic of the electronic structure of their source elements, which enables rapid identification of a material's elemental contents and composition. For this dissertation work, SEM images were collected in RIT's NanoImaging laboratory (Dr. Richard K. Hailstone) using a Tescan Mira3 FE-SEM employing acceleration voltages of 5-10 kV and a working distance (from sample to polepiece) of 10 mm. EDXS scans were performed using a Bruker XFlash 6|30 detector and accompanying Quantax ESPRIT analysis software.

4.1.7 Thermogravimetric analysis

Thermogravimetric analysis (TGA) provides useful metrics for composition and thermal degradation of CNT samples. In TGA, a sample placed on a weighing pan is gradually heated at a set rate under compressed air flow, and the mass as a function of temperature is measured. Any amorphous carbon impurities in a CNT sample will decompose before the CNTs themselves, which start to break down in air at approximately 560°C [109]. Once the mass decrease stops, only a residual ash containing any oxidized metal catalyst remains. This is useful in the comparison of as-received and purified CNT materials based on the residual impurity content. For this dissertation work, TGA measurements were performed with a consistent ramp rate of 10°C/min to 1000°C under a compressed air sample purge flow rate of 20 mL/min. Two instruments were employed, a Q5000 TGA and a Discovery 5500 TGA, both from TA Instruments.

4.2 Bulk CNT Materials: Synthesis and Property Modification

4.2.1 Purification

As-produced CNT bulk materials may include a variety of undesirable impurities including non-CNT carbonaceous material and metal catalyst particles incorporated during production. Past work has developed a multi-step process for removing these impurities [109], [110]. First, the samples to be purified were characterized to determine their baseline properties such as mass and DC electrical conductivity. The samples were then heated in a tube furnace with flowing air to just below the decomposition temperature of the CNTs (approximately 560°C) at a rate of 10°C/min for 1 hour in order to burn away the less stable amorphous carbon and oxidize the catalyst particles. Next, the samples were submerged in concentrated hydrochloric acid (HCl) for 30 minutes to dissolve the oxidized metal catalyst, and the aforementioned thermal oxidation step was repeated in order to drive off residual HCl and burn away additional impurities exposed in the first two steps [110]. Figure 19 shows Huntsman

Miralon HGR MWCNT sheet before and after purification. It was potentially necessary to repeat this process for an arbitrary number of cycles to compensate for updates in the manufacturing specifications which may have led to increased impurity content in the as-received material.

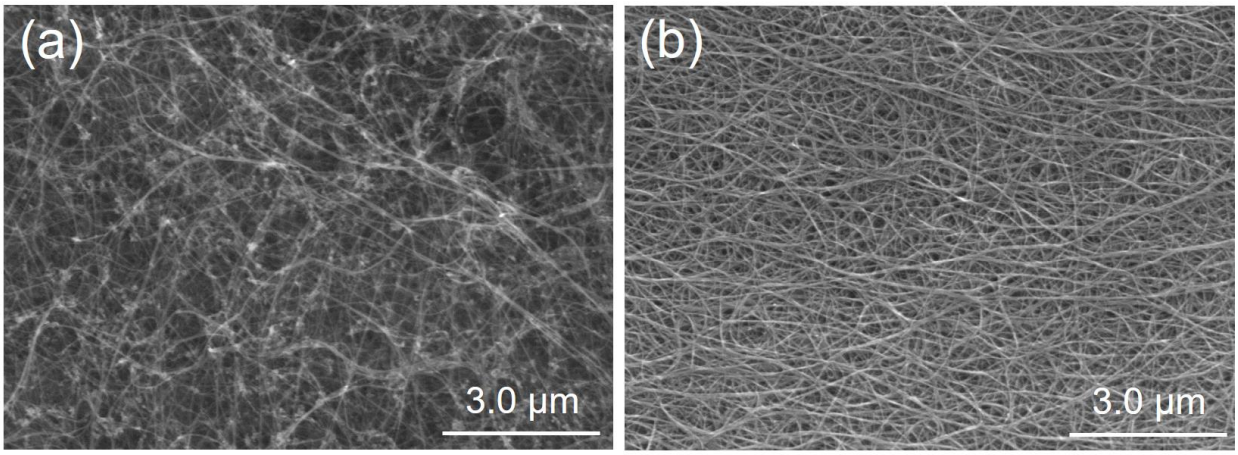

Figure 19. SEM micrographs of Huntsman Miralon MWCNT sheet before (a) and after (b) the purification process.

4.2.2 Chemical doping

The goal of realizing the excellent DC conductive properties of CNTs on an individual level in bulk structures has driven extensive study of the benefits and mechanisms of chemical doping in improving the bulk CNT conductivity. From a broad perspective, the process involves the introduction of dopant molecules to alter the electronic or chemical structure of the material, thereby changing its properties. In existing study of CNTs this has frequently been done by ion implantation of oxygen or nitrogen atoms, but a solution-based process of introducing acidic or halogenated species to CNTs has also been demonstrated [25]. The dopant of choice for conductivity improvement of CNT materials is potassium tetrabromoaurate ($KAuBr_4$) due to combined advantages in conductivity improvement and dopant longevity.

Based on this body of knowledge, the following process was used in this dissertation work to dope CNT materials using $KAuBr_4$. The dopant was obtained as the solid hydrate (99.99%,

CAS#13005-38-4, ThermoScientific) and the required mass for a given volume of solution, targeting a concentration of 5 mM, was measured on an electronic balance. The solid dopant was added to the solution container with the required volume of deionized water and shaken to dissolve the solid. The solution was then agitated in an ultrasonic bath for 30 seconds to ensure total dissolution of the solute. The CNT sample to be doped was prepared as desired and placed in a container appropriate for its size and the volume of dopant solution to be used. The dopant solution was added to the container and it was ensured that the sample was adequately submerged in the solution. The sample was allowed to soak in the solution at room temperature within a fume hood for 1 hour. The sample was removed from the solution and sandwiched between several Kimwipes, where it was dried by passing over the wipe-CNT stack three times with an acrylic roller. The CNT sample was then placed under vacuum at room temperature for 1 hour to fully dry the material.

4.2.3 Solvent-based CNT sheet plying

Portions of the following paragraph were reprinted with permission from (Boyd, S. J. et al., Chemically doped, purified bulk multi-walled carbon nanotube conductors with enhanced AC conductivity to 40 GHz, *Carbon* 226 (2024): 119209). Copyright (2024) Elsevier https://doi.org/10.1016/j.carbon.2024.119209. Previous reports have shown that n-methyl-2-pyrrolidone (NMP) serves as an effective solvent to separate and uniformly disperse CNTs with a high solubility limit [116], [117]. In the present work, this solvent was employed to combine multiple pieces of CNT sheet material together into a cohesive whole. To accomplish this CNT sheet plying, ~1 mL aliquots of NMP (99.5% anhydrous, CAS#872-50-4, Sigma-Aldrich) were dispensed between each sheet. The saturated CNT stack was placed between two 0.13 mm thick polytetrafluoroethylene (PTFE) separators and weighed down with a force per unit area of 0.25 N/m^2. The whole assembly was dried at ~125°C in a vacuum oven (VWR 1400E) for 1 h, using a liquid nitrogen cold trap to recover the waste solvent. The

weight and top PTFE separator were then removed and the resulting sheet assembly was dried with identical conditions in the vacuum oven for an additional 1 h.

4.2.4 Joule heating-driven chemical vapor deposition

Previous work has been performed to develop and optimize a process to produce metal-CNT hybrid conductors by CVD growth of nano-metal seeds throughout the CNT network of bulk materials [31], [32]. A sample was suspended between two electrical contacts inserted through rubber septa inside of a three-neck flask. In an inert gas atmosphere inside a glovebox, a solid organometallic precursor was loaded into the bottom of the flask. Deposition took place via the setup shown in Figure 20. The flask was transferred, sealed with inert gas inside, to a fume hood where it was attached to a Schlenk line to enable the application of vacuum or gas feed. Once all feeds were secure and the reactor was in position, it was insulated using glass wool (omitted for visibility purposes in Figure 20). Vacuum application during the CVD process was classified as active (in which the flask's stopcock was open and the vacuum pump continuously pulled on the reactor) or static (in which the stopcock was closed after the reactor reached a pressure of <100 mTorr). In a typical run, the reactor was first opened to active vacuum and the sample was Joule-heated using a DC power supply. This purge step was carried out for 15 minutes, in which the pre-deposition heating serves to desorb any residual oxygen on the CNT sample. After the purge step, static vacuum was initiated by closing the stopcock while Joule heating was continued, and the heating mantle was simultaneously activated at a set temperature of 200°C to

sublimate the precursor into vapor phase; these conditions were held for 1 hour to perform deposition. The result of this procedure is nano-metal growth throughout the CNT network.

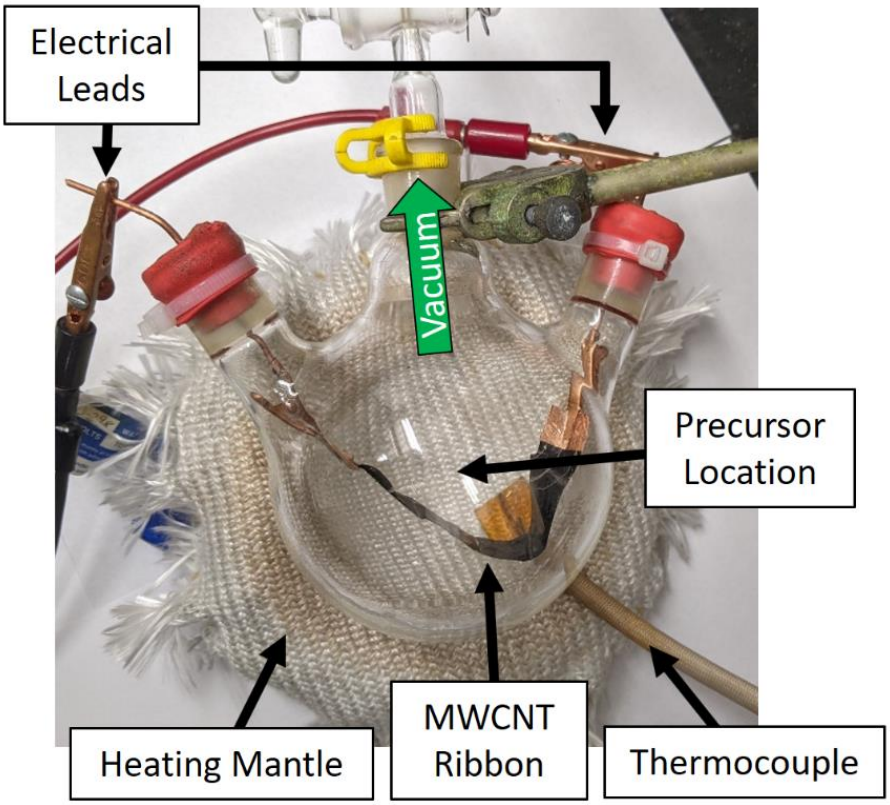

Figure 20. Schematic of the three-neck flask reactor setup used for CVD metallization of bulk CNT materials.

4.2.5 Thermal imaging using an infrared camera

Thermal imaging is a useful technique to perform contactless temperature measurement of samples. This technique is most relevant to the dissertation work discussed herein with respect to the Joule heating-driven CVD process, in which the optimal DC bias to heat samples to a required temperature is determined based on thermal imaging using a forward-looking infrared (FLIR) Ax5 camera. The determination of absolute temperature values within the camera's field of view is based on the emissivity of the material in question, which quantifies how the material surface reflects or radiates thermal energy. An emissivity of 0 corresponds to total reflection, while an emissivity of 1 corresponds

to total radiation of the thermal energy (equivalent to a blackbody radiator). In order to obtain accurate temperature measurement on the CNT materials used in this work, it is necessary to measure the emissivity of the material in question.

In the work discussed herein, a method based on ASTM standard E1933-99a [118] was utilized to measure the emissivity of CNT sheet materials. A hot plate overlaid with a sheet of aluminum foil provides a heat source with a uniform surface temperature, onto which a sample of the material-under-test (MUT), a thermocouple, and a reference sample of electrical tape (known emissivity=0.95[1]) were placed. Thermally conductive paste was used to ensure a proper thermal interface between the test components and the hot plate. The FLIR Ax5 camera was positioned normal to the hot plate surface at a height to the lens edge of ~20 cm, with all test equipment contained inside an acrylic airflow shielding canopy to eliminate the effect of air currents in the laboratory on thermal measurements. The experimental setup used for thermal imaging in the present work is shown in Figure 21a, while the experimental layout for emissivity measurement is shown in Figure 21b.

[1] https://www.flir.com/discover/rd-science/use-low-cost-materials-to-increase-target-emissivity/#:~:text=Most%20high%2Dquality%20electrical%20tape,that%20the%20tape%20is%20opaque.

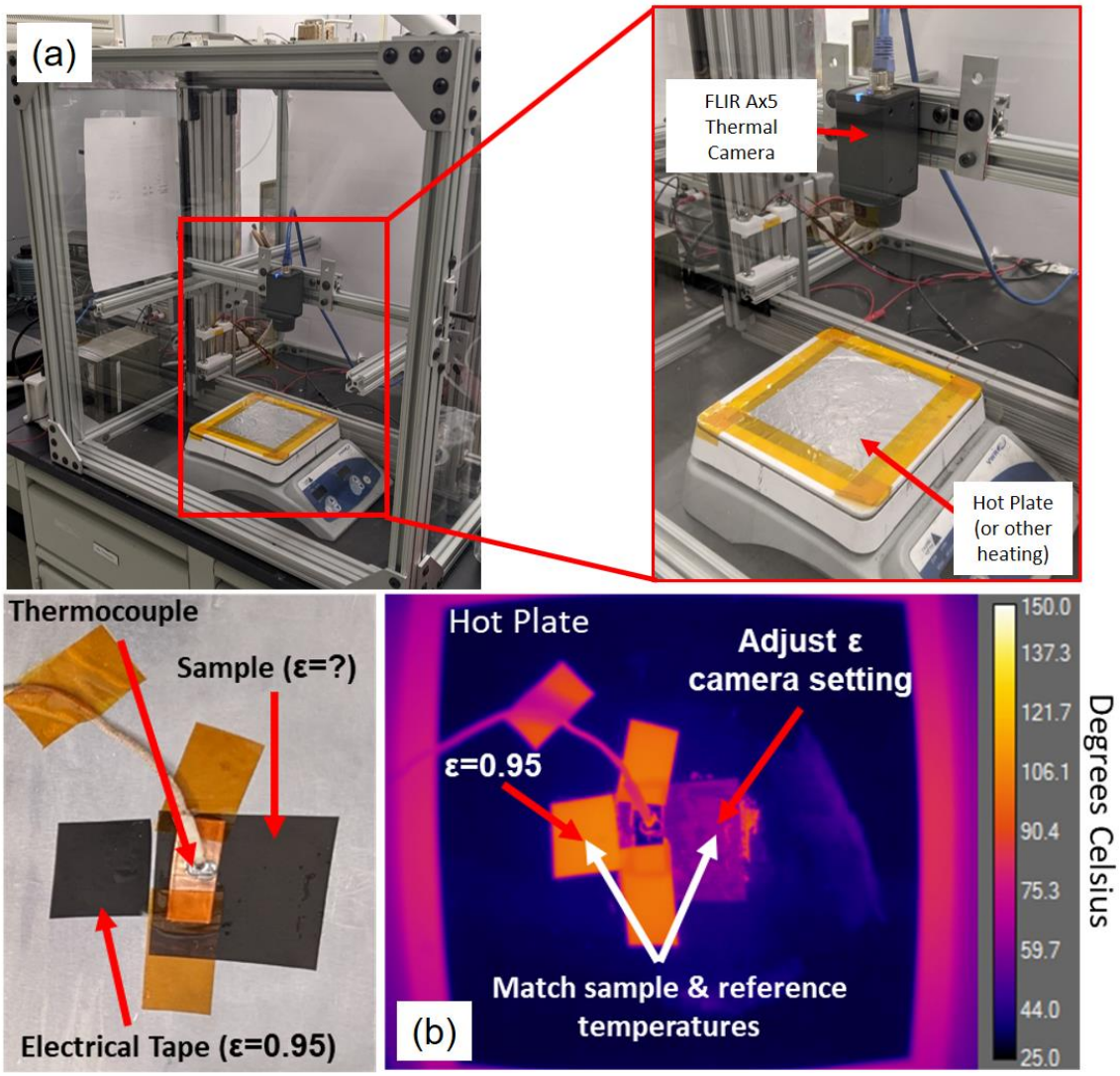

Figure 21. (a) The FLIR Ax5 thermal camera is positioned in 3D space using a three-rail Cartesian mount above the apparatus used for sample heating (a hot plate in the case of emissivity measurements), and the setup is contained within an acrylic airflow shielding enclosure. (b) The experimental setup used for CNT material emissivity measurements (reprinted with permission from Broderick et al. [119])

The hot plate is heated to a temperature set point of 70°C. Regions of interest (ROI) are defined within the FLIR software to measure the average temperatures of the MUT and the electrical tape reference (set to a measurement emissivity of 0.95). The thermocouple is employed as a second reference temperature. Temporal plots of the average temperatures within the MUT and reference ROI are monitored until they reach a steady state. After this condition is met, the measurement emissivity of the MUT ROI is adjusted until the detected temperature matches the electrical tape ROI and

thermocouple readings. The emissivity setting required to achieve a match is taken as the measured emissivity of the MUT. Once the emissivity of a particular material is known, it is possible to image samples of such material with arbitrary shape heated using arbitrary methods, such as ribbons Joule heated using a DC power supply, and obtain accurate temperature readings.

4.2.6 SWCNT laser vaporization synthesis

The Landi group has published significant work on the synthesis of high-purity SWCNT material in a filter paper form factor [108], [109] by the following laser vaporization procedure. A cylindrical graphite target containing 3% by mass each cobalt (1-2 μm) and nickel (submicron) is placed on a stand inside of a quartz tube furnace and subjected to a 5 SCFH argon gas flow. The furnace is heated to 1150°C and a pulsed Alexandrite laser traces across the target surface in a square raster pattern. Laser ablation produces a plume of carbon material which flows downstream to a cooled section where it condenses as loose carbonaceous soot on the quartz tube. During the condensation, carbon atoms diffuse through the metal-carbide eutectic and preferentially organize as either a shell or a tube of sp^2 hybridized carbon. In the latter case the continued condensation of carbon material facilitates the growth of a CNT from the catalyst particle. The produced soot is collected, massed, and acid refluxed in a mixture of deionized water (75% v/v), concentrated hydrochloric acid (7.5% v/v), and concentrated nitric acid (17.5% v/v) for ~14 hours. The reflux solution is vacuum filtered in three aliquots through 1 μm pore size membranes and samples are rinsed with copious amounts of DI water. After discarding the acid filtrate, the resultant SWCNT filter papers are further washed several times with acetone and DI water until the filtrate is clear. The filter paper is released from the membrane and thermally oxidized/HCl washed via the purification procedure described in Section 4.2.1.

4.2.7 CNT thin film preparation

Thin films of CNTs for various test structures are produced using the following procedure. A sample of purified CNT material, either purchased commercially or produced using the Landi group's laser vaporization synthesis reactor, is obtained. A dispersion is prepared of CNTs in chlorosulfonic acid (CSA) by measuring the material on a microbalance (Mettler-Toledo XP-2U), and dispensing the required volume of CSA (99%, CAS# 7790-94-5, Sigma-Aldrich) into a glass scintillation vial along with the CNT sample. The required mass is determined based on a targeted areal density across the filter membrane used to produce the film.

Due to the aggressive reactivity of the CSA, it is dispensed within a sealed glovebox under argon atmosphere and the vial is sealed with a PTFE-lined cap and Parafilm and contained inside of several plastic bags for transport. The dispersion is placed in a resonant acoustic mixer (Resodyn LabRAM) and mixed at an acceleration of 1.15 G (~10.7 m/s^2 or 15% intensity) for 1 hour. Here, the CSA acts to protonate the surface of the CNTs, reducing the van der Waals attractions between them. The acoustic mixing then separates the large aggregates and bundles to create a homogeneous dispersion.

The completed dispersion is then vacuum filtered through an inorganic membrane (Whatman Anodisc, 47 mm dia., 0.2 μm pore size) leaving behind a film of CNTs. The vacuum flask is replaced and the sample is washed with acetone to assist in releasing it from the membrane. The sample is then dried on the filter with the vacuum running for 30 minutes after which the film is floated off of the filter membrane by carefully submerging it into a deionized water bath. The thin film is then transferred onto the desired substrate by scooping it out of the water bath. The substrate may be masked before transfer in order to pattern the thin film or the film may be separated into pieces and refloated to produce several smaller samples. Once the film is in place on its final substrate, it is further dried in an oven heated to above the boiling point of the CSA (~152°C) to remove any remaining acid. The specific temperature of

heating can depend on the stability of the substrate being used, but must be high enough above the stated threshold to remove the CSA. Drying may also be performed in a heated vacuum environment to help mitigate any stability issues.

5 RF Characterization Using Rectangular Waveguides

Task 1 Objectives

- Assess the measurement methods used for AC electrical characterization of bulk CNT materials in previous literature.
- Select and implement one of these methods for use in the present work based on its capabilities, consistency, and suitability to the samples to be measured.

5.1 Evaluation of RF Characterization Measurement Methods

For the present work, a method for characterizing the RF properties of CNTs was needed which fulfilled several criteria used for evaluation. These criteria included:

- Consistency of the probing components
- Sample dimensional requirements
- Sample mounting requirements
- Frequency capabilities

A variety of methods have been used for AC electrical measurements CNTs in previous literature, such as the microstrip [45], coaxial probe [83], [84], and rectangular waveguide [45], [50] methods. The free space method, though not found to be used for this purpose with CNTs in the previous literature, was also considered. Schematics of the experimental setup for each method are presented in Figure 22. These methods were evaluated based on their comparison in the above criteria to select a suitable technique for use in this dissertation work. The evaluated methods are similar in that they determine the AC conductivity by applying a calculation algorithm to the measured S-parameters of the material sample, which describe the reflection and/or transmission of RF electromagnetic waves from the sample. The measurement setup for each technique consists of a sample, emitter, receiver, mounting apparatus, and a

signal processing instrument such as a vector network analyzer (VNA). Table 3 presents the characteristics of each evaluated method and their rating based on the four criteria above in the form of a Chiclets chart. In addition to the qualitative evaluation based on the literature review, the microstrip line method was also tested empirically. Details of this work are given in Appendix B, Section 12.3.

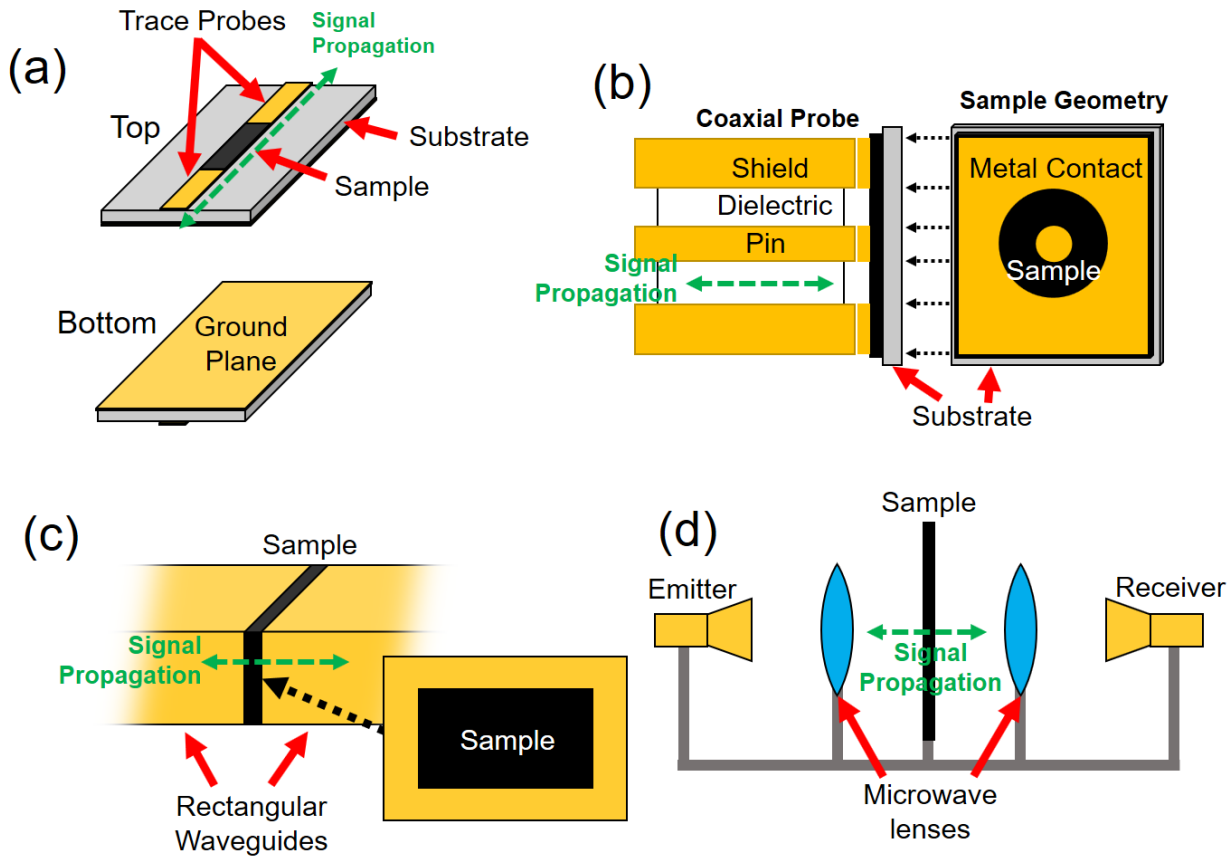

Figure 22. Schematics of the four evaluated RF measurement methods: (a) microstrip line, (b) coaxial probe, (c) rectangular waveguide, and (d) free space.

Table 3. Chiclets chart summarizing the comparison of the four methods considered for RF characterization.

Method	Probing Component	Consistency of Probes	Sample Size	Mounting Requirements	Frequency Capabilities
Microstrip Line	Microstrip trace	• Microstrips can vary based on customer design. • Silver paint interface can be inconsistent.	• Dimensions are cm- to mm-scale. • Depends on trace geometry (impedance matching). • Required dimensions fall within needs of CNT processing.	• Sample must be deposited or adhered onto microstrip substrate. • Adhesive or air gaps could introduce inconsistencies. • Silver paint must be used for electrical contact.	• Radiation and self-inductance limit usage to low frequencies.
Coaxial Probe	Coaxial cable	• Commercial components can be used. • Metal contact geometry adds variability.	• Dimensions are mm-scale. • Required dimensions fall within needs of CNT processing.	• Metal coaxial geometry for continuous electrical contact with probe tip must be deposited by magnetron sputtering. • Contact deposition introduces an additional variable to be optimized.	• Determined by the specifications of the coaxial cable used. • May require multiple specifications to cover desired frequency range.
Rectangular Waveguide	Rectangular waveguide	• Commercial components can be used. • Closed setup blocks external interference.	• Dimensions are cm- to mm-scale. • Sample dimensions are dependent on the waveguide's inner dimensions. • Required dimensions fall within needs of CNT processing.	• Neat, conductive samples can be compressed between the waveguide flanges.	• Determined by the specifications of the waveguide used. • May require multiple specifications to cover desired frequency range.
Free Space	Horn antenna	• Commercial components can be used. • External interference must be accounted for.	• Dimensions are m- to cm- scale. • Sample dimensions must be at least 10λ to prevent leakage, refraction around sample edges. • This exceeds requirements of CVD process.	• Frames or backing substrates are needed to support samples. • Substrates must be characterized accurately to remove their effect on the measurement.	• Determined by the specifications of the antenna used. • May require multiple specifications to cover desired frequency range.

5.1.1 Consistency of probes

In terms of the components used to connect to the sample for the purpose of delivering and receiving signals, the microstrip line method was found to be the least attractive. This was due to the potential variability arising from custom microstrip line circuit boards for testing, as previous efforts [45] had performed this method by designing and ordering commercial fabrication of test articles with gaps in the microstrip trace for the CNT sample. This method required silver paint to be used for electrical contacting between the copper and CNT sections of the strip, which would introduce another level of potential variability. This issue was confirmed through empirical testing (see Appendix B,

Section 12.3). As the remaining three methods could all rely on mass-produced components whose specifications were not unique to this application, they were not ruled out based on physical variability of the probes. The coaxial probe method stands out in its use of a sputtered metal contact on the sample surface [83], [84] which would also represent another factor to be optimized. Between the rectangular waveguide and free space methods, the rectangular waveguide's closed structure was attractive for its ability to prevent external interference from affecting measurements.

5.1.2 Sample dimensional requirements

Primarily due to the physical constraints of the CVD process to fabricate metal-CNT hybrids, the sample dimensions were one of the more important criteria for selecting a measurement method. The present state of the CVD process's development [31], [32], [33], [34], [35] limits its usage to ribbons ~1 cm or less in width due to the size of the 14/20 ground glass fittings on the reactor flask. It was desirable to avoid making excessive modifications to the CVD apparatus to enable the fair comparison of past DC and present AC results. The microstrip line, coaxial probe, and rectangular waveguide methods could all function in theory with samples of this size, while the free space method would be limited at low frequencies where wavelengths become extremely large. This is due to the need for a sample at least ten wavelengths ($10\times\lambda$) in size at the lowest measured frequency in order to avoid signal leakage or diffraction around the sample edges [75].

5.1.3 Sample mounting requirements

The four evaluated methods utilize a variety of mounting strategies. In all cases, it is desirable for the sample to be as flat as possible and be well aligned with the probing components. The microstrip line method, in which the sample is adhered both to the substrate board and the copper strip sections, was the least attractive in this metric. The many potential inconsistencies from adhesives or air gaps at the sample-substrate interface, as well as the aforementioned variability in the silver paint used for

electrical contact with the copper regions, could all contribute to skewed characterization results. This was a potential source of the error in results obtained through empirical testing (Appendix B, Section 12.3). The metal contact geometry used for the coaxial probe method or the frames/substrates needed to suspend a flat sample in the free space method would each present additional variables to be accounted for. Conversely, the rectangular waveguide method provided the most simplistic mounting strategy, in which a conductive sample such as a CNT sheet can be enclosed between the waveguide components without the use of adhesives or other extraneous substances.

5.1.4 Frequency capabilities

The Keysight P9377b VNA used for signal processing in this dissertation work has a frequency capability of 100 kHz to 44 GHz. As the experiments discussed herein benefitted from maximizing the measured frequency within the available capability, a method with broadband capability was desired. Previous reports observed a significant frequency limitation of the microstrip line method which has been attributed to self-inductance [45], as well as edge-singularity [73] and proximity [72] effects due to the geometry of the line. This limitation prevents accurate characterization using this method in a frequency range wide enough for meaningful conclusions to be made. On the other hand, the frequency capabilities of the remaining three evaluated methods all depend on the specifications of the actual coaxial cables/waveguides/antennas used. Though multiple specifications of probing equipment are required to span any significant breadth of the P9377b VNA's frequency capability, this is not a limiting factor of any of the evaluated techniques, and further down-selection was carried out based on the other three criteria.

Based on evaluation of these four methods according to the described criteria, the rectangular waveguide method was selected for use in this dissertation work. It possesses the most suitable characteristics in terms of consistency, simplicity, and applicability to the samples and frequency ranges

of interest. The remainder of this chapter details the characteristics of the specific rectangular waveguide setup employed for the experiments herein.

5.2 Rectangular Waveguide Setup for RF Characterization from 10 GHz to 40 GHz

5.2.1 Rectangular waveguide components

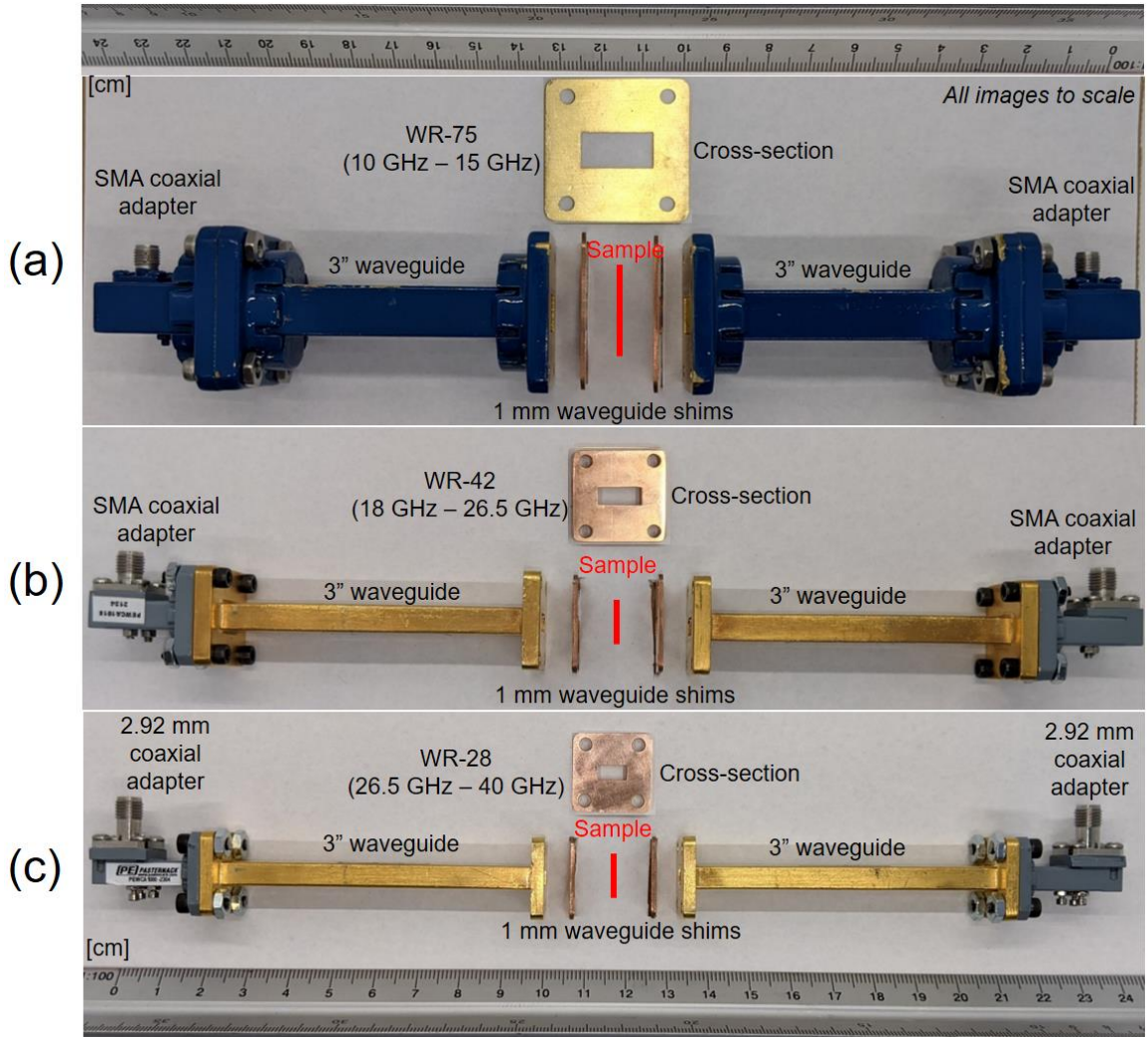

Figure 23. Layout of the rectangular waveguide setup, consisting of a material sample (position within the setup indicated by the red markers) enclosed between 1 mm waveguide shims, flanked on either side by probes consisting of a 3" long waveguide section and a coaxial-to-waveguide adapter. Shown for (a) WR-75 (10 GHz – 15 GHz), (b) WR-42 (18 GHz – 26.5 GHz), and (c) WR-28 (26.5 GHz – 40 GHz) rectangular waveguides. Images are to scale, with dimensions represented in cm by the rulers.

The general layout of the rectangular waveguide setup used for RF characterization is shown in Figure 23. Three waveguide specifications were employed: WR-75 (10 GHz – 15 GHz, Figure 23a),

WR-42 (18 GHz – 26.5 GHz, Figure 23b), and WR-28 (26.5 GHz – 40 GHz, Figure 23c), covering a total frequency range of 10 GHz – 40 GHz with a small discontinuity between 15 and 18 GHz. The selected waveguide specifications provided a wide frequency range for characterization within the capabilities of the Keysight P9377b VNA. All waveguide components were commercially obtained from Pasternack. All connections between these components were made by screws which were secured using a consistent torque of 4.5 N·cm (0.4 in·lb). Figure 24 shows the full configuration used for measurements with the rectangular waveguide setup. The rectangular waveguide setup was secured in a jig with two adjustable clamps, allowing the waveguides to slide on a common rail. The waveguide setup was connected to the ports of the VNA using 2.4 mm coaxial cables. A laptop was used to interface with the VNA, enabling automated frequency sweeping, S-parameter data acquisition, and data processing to obtain the RF properties of samples such as AC conductivity, EMI shielding effectiveness, and complex permittivity/permeability. The measurement setup components were secured onto an optics table to maintain consistent positioning and isolate the setup from mechanical vibrations.

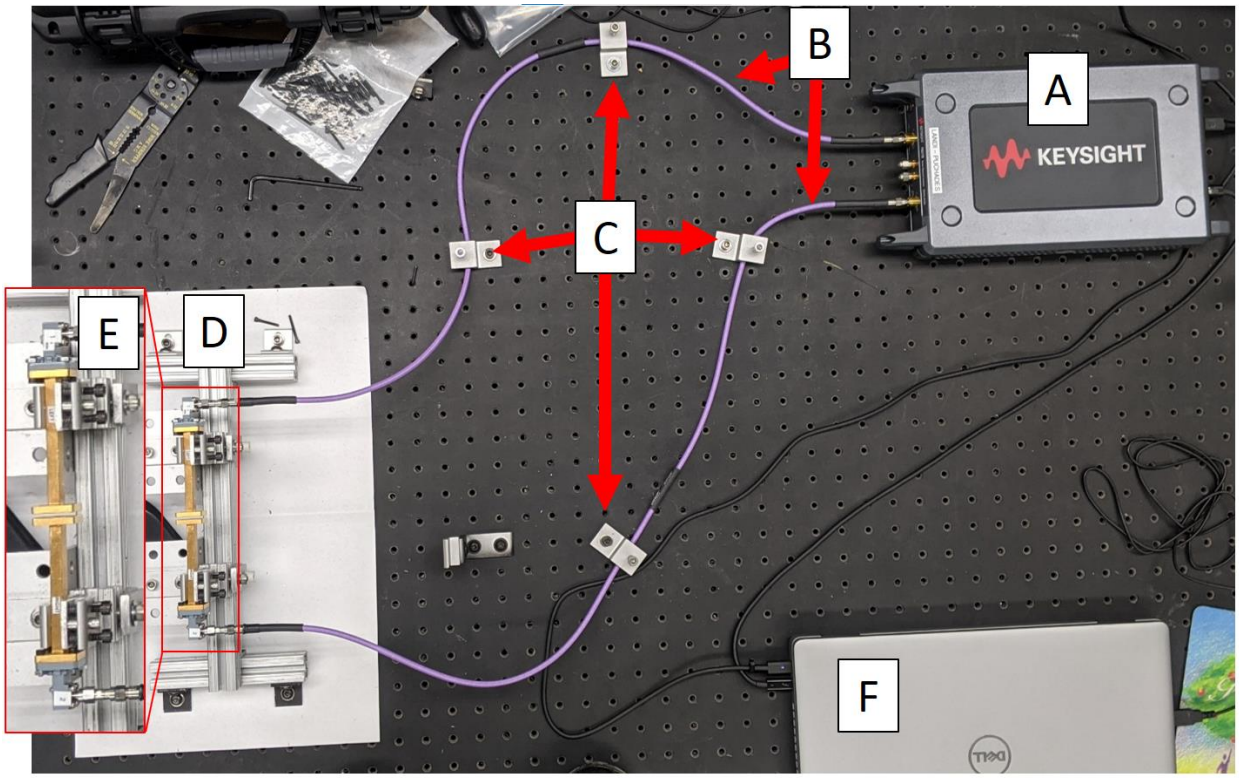

Figure 24. Layout of the components used for data collection and analysis using the rectangular waveguide setup.

5.2.2 S-parameters measurement and analysis

Scattering Parameters (S-Parameters)

Network analysis is the broad term for characterization of devices and components using vector network analyzers (VNA). Modern VNAs combine the functions of signal generation, signal separation for referencing and excitation of the sample-under-test, and reception/analysis to characterize samples with a theoretically arbitrary number of ports. A port is defined as having two terminals in which equivalent current flows into one terminal and out of the other. VNAs are often used with two-port (four-terminal) networks such as the one shown in Figure 25a in order to measure transmission, reflection, or impedance [120].

Chapter 5 – RF Characterization Using Rectangular Waveguides

A matrix of frequency-dependent scattering parameters (S-parameters) is typically used to describe a given network. The S-parameter matrix for a two-port network is shown in Figure 25b. The electromagnetic waves a_1 and a_2 are incident to ports 1 and 2, respectively, while the outgoing electromagnetic waves b_1 and b_2 may be either transmitted from the opposite port or reflected from the same port. For example, the wave transmitted through the network from port 1 as a_1 would leave at port 2 as b_2, while the wave reflected from port 1 as a_1 would return from port 1 as b_1. S-parameters are complex numbers of the form $|S_{mn}|*\exp(j\varphi_{mn})$ with indices m and n in which the magnitude ($|S_{mn}|$) represents the ratio of the electric fields and the phase angle (φ_{mn}) describes the phase shift between the waves. They are always defined relative to a reference impedance (usually Z_0=50 Ω), and can be converted to other parameter sets for two-port networks in order to quantify the impedances of a measured network [36]. The S-parameter magnitudes shown in Figure 25b are defined linearly, but they can also be defined logarithmically with units of dB using the conversion below.

$$|S_{mn}|[dB] = 20log_{10}(|S_{mn}|[linear]) = 20log_{10}\left(\frac{E_{0,out}}{E_{0,in}}\right) \quad (5.2\text{-}1)$$

Figure 26 shows the significance of S-parameters with regard to signal transmission and reflection. An S_{21} or S_{11} magnitude of 0 dB corresponds to 100% signal transmission or 100% signal reflection, respectively. As the S_{21}/S_{11} magnitude becomes more negative, this corresponds to a decreasing percentage of signal transmission or reflection, respectively. The same is true for the reverse direction (S_{12}/S_{22}). An S-parameter magnitude greater than 0 dB is not typically observed for passive components, as it would represent a gain.

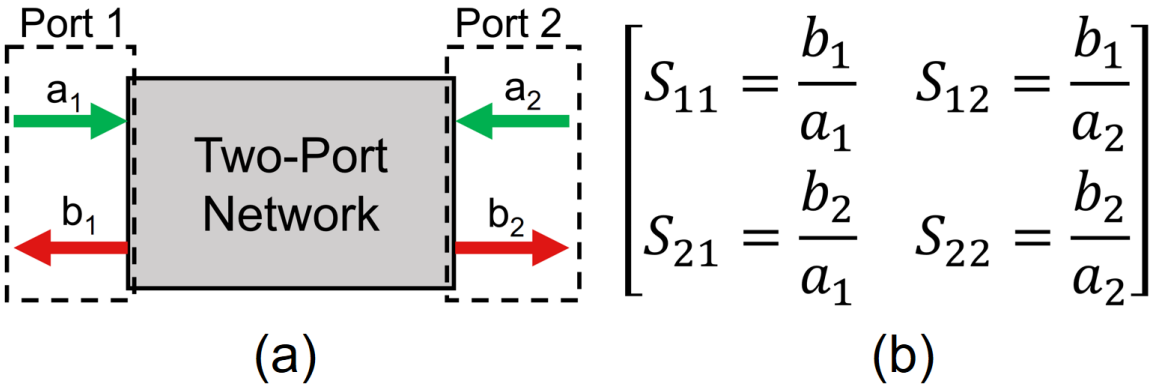

Figure 25. (a) Diagram of a two-port network with incoming waves (a_1, a_2) and outgoing waves (b_1, b_2) at each port. (b) The representative S-matrix for the two-port network.

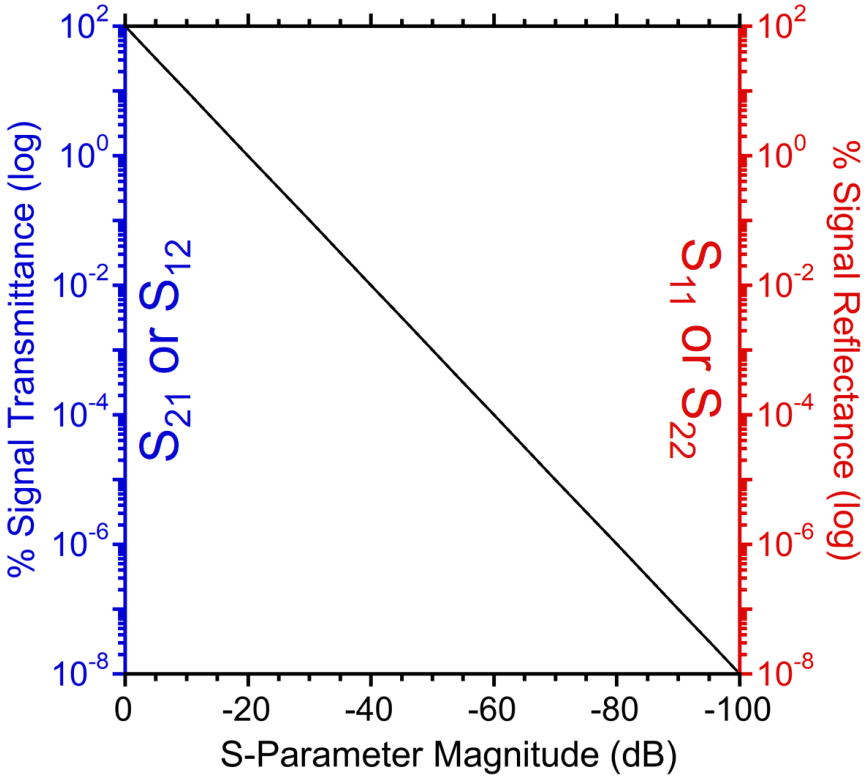

Figure 26. The relationship between S-parameter magnitudes in dB and the percent transmission/reflection of the signal, shown by a log-linear double Y plot.

In the present dissertation work, calculation algorithms are applied to measured S-parameter data in order to obtain several RF material properties as functions of frequency. These properties include the AC conductivity (complex), the reflectance/transmittance (real), and the electromagnetic interference

(EMI) shielding effectiveness (real). The following section summarizes the calculations performed to extract these properties from samples measured using a rectangular waveguide-based setup, but they are for the most part general procedures that could be applied to S-parameter data obtained using other experimental apparatuses.

Accounting for the Wave Impedance of the Rectangular Waveguide

The wave impedance (Z_w) of a rectangular waveguide (as described in Section 2.1.3) is frequency-dependent and describes the opposition to wave propagation along the waveguide at a given frequency. It is determined based on the frequency (f) relative to the waveguide's cutoff frequency (f_c) for the TE_{10} mode, according to the following equation from Pozar [36]:

$$Z_w = \frac{Z_0}{\sqrt{1-(f_c/f)^2}} \tag{5.2-2}$$

where Z_0=377 Ω is the impedance of free space. As the frequency approaches the cutoff frequency from the right, Z_w becomes infinity, indicating propagation is impossible. Increasing the frequency above the cutoff frequency brings the wave impedance asymptotically closer to free space impedance. This indicates that the wavefront propagation velocity increases with frequency, as the wave reflects internally on the waveguide's conductive surfaces. The wave impedance as a function of frequency is used in subsequent calculations herein to subtract this waveguide/frequency specific aspect from the intrinsic material properties. The TE_{10} mode cutoff frequencies of the rectangular waveguides used in this work[2], verified based on Equation (2.1-2), are as follows: 7.869 GHz (WR-75/10 GHz – 15 GHz), 14.051 GHz (WR-42/18 GHz – 26.5 GHz), and 21.077 GHz (WR-28/26.5 GHz – 40 GHz).

AC Electrical Conductivity

[2] "Waveguide Sizes | Dimensions & Cutoff Frequency - everything RF." Accessed: Dec. 20, 2023. [Online]. Available: https://www.everythingrf.com/tech-resources/waveguides-sizes

For this work, the following equation is adapted from J. W. Schultz [75] to calculate the sheet impedance (Z_s) of a resistive sheet from its S_{21} parameter:

$$Z_s = \frac{Z_w}{2}\left(\frac{S_{21}}{1-S_{21}}\right) = R_{s,AC} + jX_s \quad (5.2\text{-}3)$$

Z_w is the frequency-dependent wave impedance in air inside the rectangular waveguide, S_{21} is a complex number, $j = \sqrt{-1}$, and $R_{s,AC}$ and X_s are real parameters representing the respective AC sheet resistance and sheet reactance.

The following equation is then used to calculate the complex-valued AC conductivity, σ_{AC},

$$\sigma_{AC} = \sigma' + j\sigma'' = R_{s,AC}/[t\left(R_{s,AC}^2 + X_s^2\right)] + jX_s/[t(R_{s,AC}^2 + X_s^2)] \quad (5.2\text{-}4)$$

where σ' is the real AC conductivity, σ'' is the imaginary AC conductivity, and t is the average sample thickness.

Reflectance, Transmittance, and EMI Shielding Effectiveness

The following procedure is used to obtain the reflectance, transmittance, and EMI shielding effectiveness as they are interrelated. The RF reflectance and transmittance are determined from the linear magnitudes of S_{11} and S_{21}, respectively. The following equations, which convert S_{11} or S_{21} to impedance, are adapted from J. W. Schultz [75],

$$Z = -\frac{Z_w}{2}\left(\frac{1+S_{11(Z_w)}}{S_{11(Z_w)}}\right) = R_{AC} + jX \quad (5.2\text{-}5)$$

$$Z = \frac{Z_w}{2}\left(\frac{S_{21(Z_w)}}{1-S_{21(Z_w)}}\right) = R_{AC} + jX \quad (5.2\text{-}6)$$

where $S_{11(Zw)}$ and $S_{21(Zw)}$ are the raw, complex-valued S-parameters with Z_w reference impedance, $j = \sqrt{-1}$, and R_{AC} and X are real parameters representing the respective AC resistance and reactance. After

converting the raw S-parameter data into impedances, Equations (5.2-5)-(5.2-6) are inverted and Z_w is replaced with Z_0=377 Ω, producing Equations (5.2-7)-(5.2-8) to convert the impedances into corrected S-parameters with Z_0 reference.

$$S_{11(Z_0)} = -\left(\frac{2Z}{Z_0} + 1\right)^{-1} \tag{5.2-7}$$

$$S_{21(Z_0)} = \frac{2Z}{Z_0}\left(\frac{2Z}{Z_0} + 1\right)^{-1} \tag{5.2-8}$$

The reflectance (R) and transmittance (T) are then determined using Equations (5.2-9)-(5.2-10).

$$R = \left|S_{11(Z_0)}\right|^2 \tag{5.2-9}$$

$$T = \left|S_{21(Z_0)}\right|^2 \tag{5.2-10}$$

where $|S_{mn(Z0)}|$ denotes the linear scale magnitude of the respective corrected S-parameter in absolute units. The EMI shielding effectiveness (SE) in dB is then determined as the sum of reflective (SE_R) and absorptive (SE_A) components calculated from the reflectance and transmittance using Equations (5.2-11)-(5.2-13).

$$SE_R = -10\log(1 - R) \tag{5.2-11}$$

$$SE_A = -10\log\left(\frac{T}{1-R}\right) \tag{5.2-12}$$

$$SE = SE_R + SE_A \tag{5.2-13}$$

5.2.3. Rectangular waveguide measurement procedure

Calibration

Chapter 5 – RF Characterization Using Rectangular Waveguides

Before any samples can be measured, the VNA must be calibrated as attenuation and phase shift from the VNA's internal circuitry, coaxial cables, and rectangular waveguide components will affect the measured S-parameters. The Thru-Reflect-Line (TRL) calibration method [121], [122] was used to achieve this for the present dissertation work. In this technique, three calibration standards (Thru, Reflect, and Line) must be measured. The Thru standard consists of the waveguide setup without a sample, and assumes zero attenuation and phase shift. The Reflect standard is created by placing a solid metal plate at the center of the waveguide setup, producing complete reflection of the signal to both ports. Lastly, the Line standard is similar to the Thru with the addition of waveguide shims to give additional length that corresponds to 90° phase shift ($\lambda/4$) at the center frequency for each waveguide (12.5, 22.25, and 33.25 GHz, respectively). Together, these three standards provide the boundary conditions required to solve for the error terms that describe the aforementioned physical components of the measurement setup. The actual length of the Line standard varies between the three waveguide specifications used in this work. The layout of each standard for each of the waveguides are summarized in Figure 27.

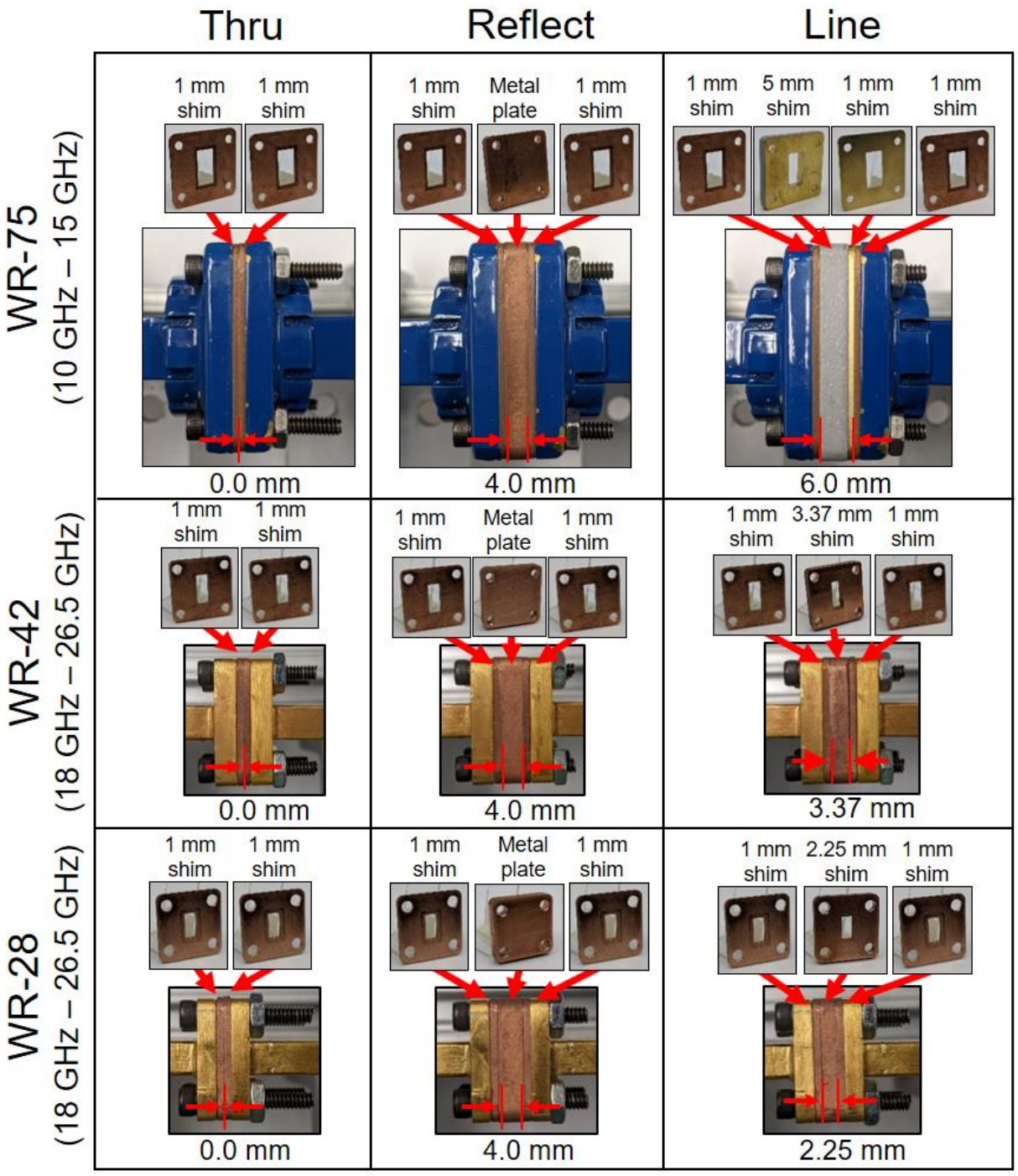

Figure 27. Configurations of the TRL calibration standards applied to all measurements reported herein for each of the three waveguides used for characterization from 10 GHz to 40 GHz.

In a typical measurement scenario, the three standards were assembled and scanned one-by-one for their S-parameters using the built-in calibration wizard of the VNA software. The Thru standard was

scanned last, enabling unloading of the standard and subsequent mounting of samples for measurement without further movement of the waveguides. The calibration is quantitatively evaluated based on the Thru standard, which should ideally exhibit a constant zero attenuation and zero phase shift across the frequency range after calibration. Figure 28 shows the magnitude and phase of S_{21} for the Thru standards of all three waveguides before and after calibration, demonstrating the benchmark used for data acquisition in the present work. As indicated by Figure 28a, the S_{21} magnitude of the Thru standard and all peripheral components of the setup is ~−4 dB and decreasing across the frequency range before calibration, suggesting increasing attenuation; calibration reduces this to a constant 0 dB showing no attenuation. The fluctuation of the S_{21} phase in Figure 28b before calibration is indicative of a large length of travel represented by the coaxial cables and waveguides; calibration eliminates this length from the phase by reducing it to a constant 0°.

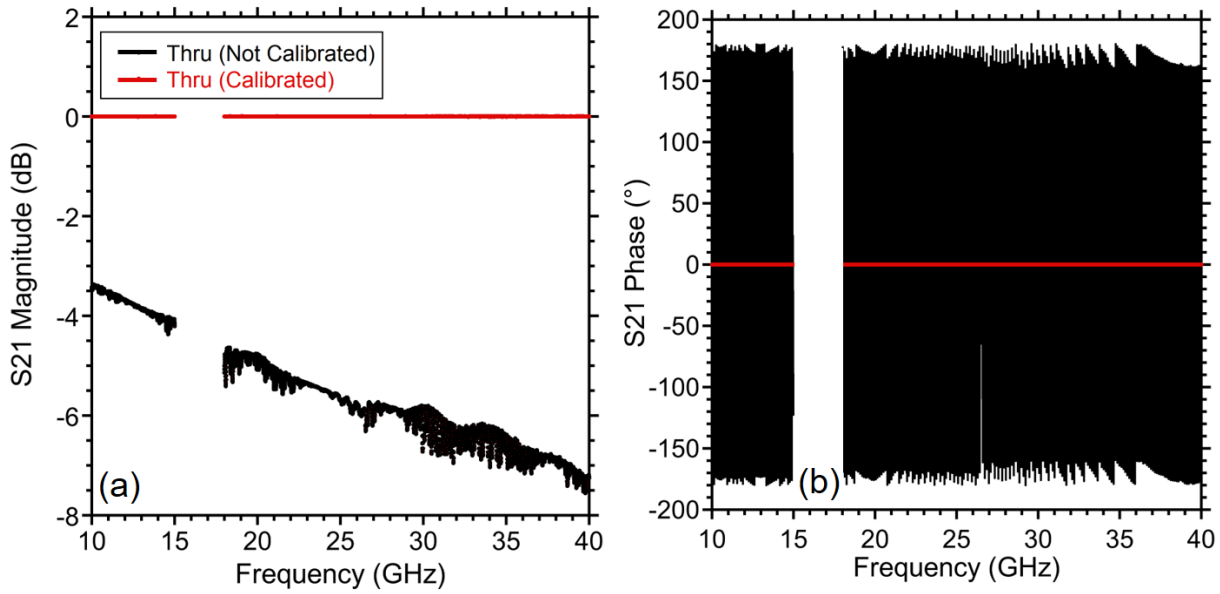

Figure 28. The S_{21} magnitude (a) and phase (b) of the Thru standard with and without calibration using the TRL method.

Measurement

After calibration was complete, the sample to be measured was placed on one of the 1 mm waveguide shims and aligned to cover the waveguide opening. The second shim was then placed on top of the first and the assembled sample mount was screwed into place between the waveguide probes. The calibration order as discussed above enabled this to be done without moving the waveguides or coaxial cables between measurements. After the sample was mounted, five frequency sweeps with 5 s duration, 2001 data points each were performed using an intermediate frequency bandwidth (IFBW) of 1 kHz, for a total of 6003 data points across the whole 10 GHz to 40 GHz frequency range. The frequency sweeps were then averaged and the data were analyzed using calculation algorithms as described in Section 5.2.2, depending on the property of interest. Demounting of the sample proceeded in the opposite order to mounting.

5.3 Testing of the Rectangular Waveguide Setup

5.3.1 Effect of sample dimensions on measured AC conductivity of MWCNT sheet

The overlap of the CNT sheet with the metal surface of the rectangular waveguide flanges might affect the measurement accuracy due to the difference in conductivity between the two materials. To determine if this factor affected results, triplicate samples of as-received Miralon HGR MWCNT sheet were laser cut to dimensions of 12 mm × 22 mm, 16 mm × 25 mm, and 22 mm × 38 mm. These sizes corresponded to 18%, 28% and 58% CNT sheet coverage of the WR-75 waveguide flange (38 mm × 38 mm), respectively, as shown in Figure 29a. The real and imaginary parts of the AC conductivity from 10 GHz to 15 GHz as the average of triplicate samples at the three sizes are presented in Figure 29b and c, respectively. The real part is nominally constant for all samples in this frequency range, while the imaginary part is negative and decreasing, indicating a capacitive response. To analyze the difference between the samples of each set of dimensions, the values of real and imaginary AC conductivity at 12.5 GHz for each was directly compared in Figure 29d. The error bars represent one standard deviation of

the triplicate measurements for samples of each set of dimensions. As the error bars for all three sizes overlap in both real and imaginary AC conductivity, there is no significant difference in the measured values. Based on these results, the smallest sample dimensions of 12 mm × 22 mm were selected for all further testing as they would streamline processing of the CNT sheet using purification, chemical doping, or CVD metallization.

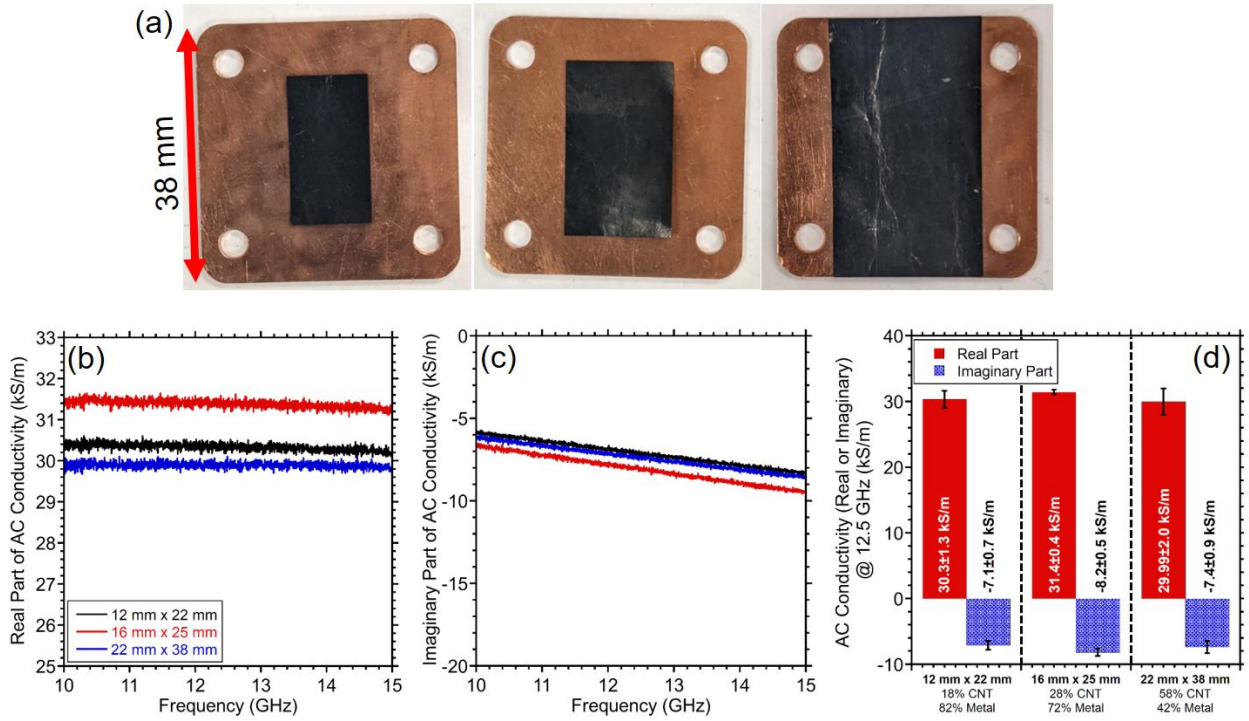

Figure 29. (a) MWCNT sheets of three different sets of dimensions were measured with dimensions (from left to right) of 12 mm × 22 mm, 16 mm × 25 mm, and 22 mm × 38 mm. The real (b) and imaginary (c) parts of the AC conductivity measured for samples of all three sets of dimensions (d) The real and imaginary AC conductivity taken at 12.5 GHz for samples of all three sets of dimensions. The error bars represent experimental error from triplicate measurements.

5.3.2 Effect of time drift on measured AC conductivity of MWCNT sheet

Measurement of a large collection of samples in a single session after one calibration could potentially introduce variability due to instrument drift over time. To assess the extent to which time drift affected the measurement, a single sample of MWCNT sheet was measured repeatedly after an initial calibration without modifying the test setup. This test was performed in 15 min intervals between

scans, from immediately after the calibration until 105 min. The results of this experiment for the real and imaginary parts of AC conductivity are presented in Figure 30a and b, respectively. There is no noticeable drift in the measurement across the entire tested time span, indicating that there should be no detrimental effects from measurements taken over time after calibration.

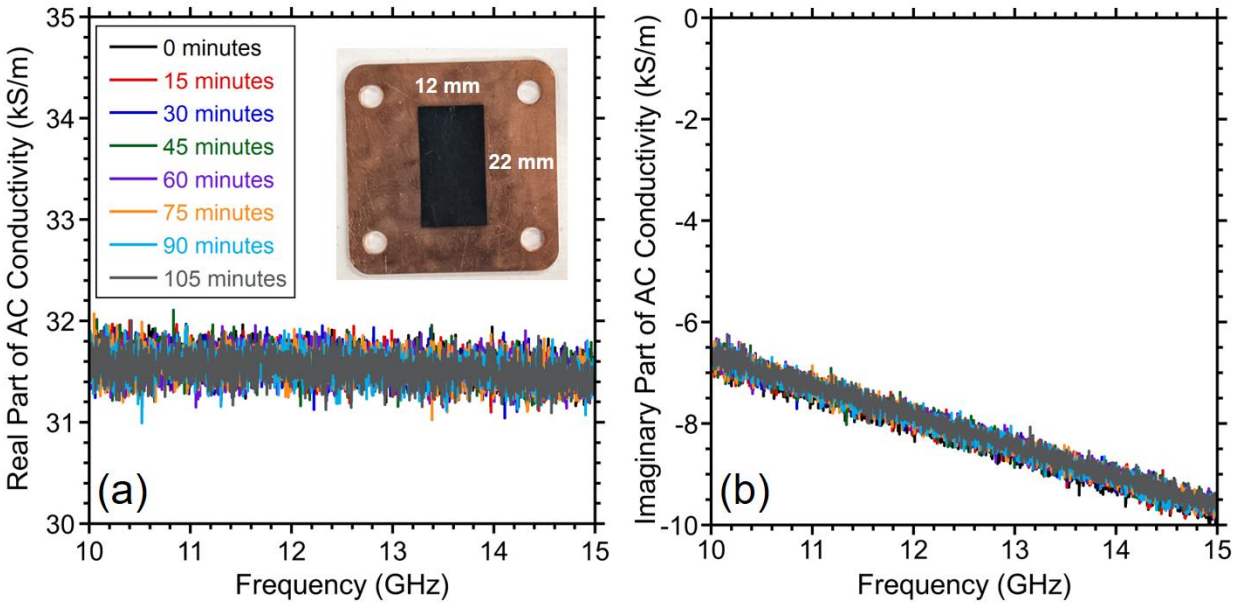

Figure 30. The real (a) and imaginary (b) parts of AC conductivity of a 12 mm × 22 mm MWCNT sheet sample, measured from 10 GHz to 15 GHz at time intervals of 15 min over a time span of 0 min to 105 min after calibration.

5.4 Outcomes

The rectangular waveguide method was selected to perform RF characterization of CNT materials in the present work due to its sample dimensional requirements and facile sample mounting strategy. An experimental setup to perform these measurements from 10 GHz to 40 GHz was successfully implemented. Initial testing of the rectangular waveguide setup showed that sample dimensions and time drift did not have a noticeable effect on the measured results. The successful establishment of this measurement capability enabled the completion of several studies in which the effects of purification, $KAuBr_4$ chemical doping, and platinum deposition on the AC conductivity of MWCNT sheets were investigated.

6 AC Conductivity of Purified & $KAuBr_4$-Doped MWCNT Sheets

Task 2 Objectives

- Understand the effects of impurities and $KAuBr_4$ dopant on the AC conductivity of commercial MWCNT sheet material.
- Understand the effect of sample thickness on AC conductivity measurement of MWCNT sheet with conductivity enhanced by $KAuBr_4$ dopant.

The DC conductivity of CNT networks is affected by amorphous carbon impurities and metallic catalyst remnants from the manufacturing processes used to produce the material. Structures adsorbed or chemically bonded to the CNT surface can act as scattering sites or affect the contact resistance at inter-CNT junctions. Chemical doping using metal halide compounds such as $KAuBr_4$ is known to affect the DC conductivity of CNT networks through electron withdrawal [25]. Published work to date has not explored the high-frequency effects of impurities or chemical doping on CNT properties. The research herein reports the use of a previously published thermal oxidation and acid treatment purification process to remove amorphous carbon and residual iron catalyst impurities from commercial Miralon MWCNT sheet, whereby the effects of these impurities on the AC conductivity from 10 GHz to 40 GHz are investigated. The purified MWCNT material is then subjected to chemical doping with $KAuBr_4$ to determine if dopant enhances the AC conductivity. For supplementary data to this chapter, please refer to Appendix A, Section 11.1. The following work is reprinted with permission from (Boyd, S. J. et al., Chemically doped, purified bulk multi-walled carbon nanotube conductors with enhanced AC conductivity to 40 GHz, *Carbon* 226 (2024): 119209). Copyright (2024) Elsevier https://doi.org/10.1016/j.carbon.2024.119209

Chapter 6 – AC Conductivity of Purified & $KAuBr_4$-Doped MWCNT Sheets

6.1 Purification and $KAuBr_4$ Doping Effects on MWCNT AC Conductivity

6.1.1 Characterization of MWCNT sheet after different purification steps

Previous work has shown that the DC electrical conductivity of CNT materials changes based on morphology and chemical treatments [21], [22], [23], [24], [25], [26], [27], [28], [29], [30], [31], [32], [33], [34]. Samples of the Miralon MWCNT sheet were fabricated to investigate the effect of the purification treatment on real AC conductivity (1) in the as-received state, (2) subjected to HCl treatment for 30 min, (3) thermally oxidized to 500°C, and (4) purified according to the procedure outlined in 2.1.

SEM micrographs of the material in these four states are shown in Figure 31a-d, respectively. Impurities are present in the MWCNT network of the as-received material (Figure 31a). The quantity of bright metal particles is slightly reduced in the HCl-treated material (Figure 31b) while the encapsulating carbon is removed from the metal particles by thermal oxidation (Figure 31c) consistent with previous reports [109]. Both types of impurities are significantly reduced by the complete purification process, exposing the MWCNT network (Figure 31d). Raman spectra measured from the as-received and purified MWCNT materials are shown in Appendix A, Figure 49. The Raman spectra for both materials are typical of MWCNT materials, containing the D-band peak (~1350 cm^{-1}), G-band peak (~1580 cm^{-1}) and G'-band peak (~2700 cm^{-1}) [113], [123], [124], [125]. The ratio of D/G peak intensities is a useful metric to quantify CNT purity [126]. The relative Raman ratios for the as-received and purified samples are nominally equivalent within one standard deviation, indicating that the MWCNT quality is not impacted by the purification processing steps.

TGA plots and EDX spectra are shown in Appendix A, Figures 50a and 51a, respectively. TGA results indicate a residual mass of 43.2% w/w in the as-received material (black line in Appendix A, Figure 51a). The thermally oxidized and HCl treated materials had virtually identical residual mass of

~38% w/w (see red and blue lines, respectively, in Appendix A, Figure 50a), indicating both processes do not significantly affect the iron impurity content when performed individually. This is further supported by the EDX results, in which the $Fe_{L\alpha}$ peak intensity is similar between individual treatments and the as-received material. The purified material exhibits the removal of both carbonaceous and iron catalyst impurities from the MWCNT network, as demonstrated by the residual mass of 1.4% w/w in TGA measurements (green line in Figure 50a) and the lack of a $Fe_{L\alpha}$ peak in the EDX spectrum. This is consistent with previously published results [110].

Table 4 contains the thicknesses and DC conductivities of the MWCNT samples which were fabricated for testing the effect of the purification process on AC conductivity. HCl treatment of the as-received sheet enhances the DC conductivity by ~10%, while the thicknesses of the as-received and HCl treated sheets are equivalent within experimental error. This indicates that the conductivity change is mainly a result of chemical doping by the acid, consistent with previous reports [25]. Thermal oxidation of the as-received material does not produce any significant change in the thickness or DC conductivity, as the experimental errors overlap in both metrics. Purification produces the most noticeable difference in sheet thickness, with a near 40% reduction over the as-received material, likely due to densification of the sheet. However, the DC conductivity remains nominally equivalent between the two cases, suggesting that removal of the iron and/or carbonaceous impurities may produce a resistance increase in the bulk material.

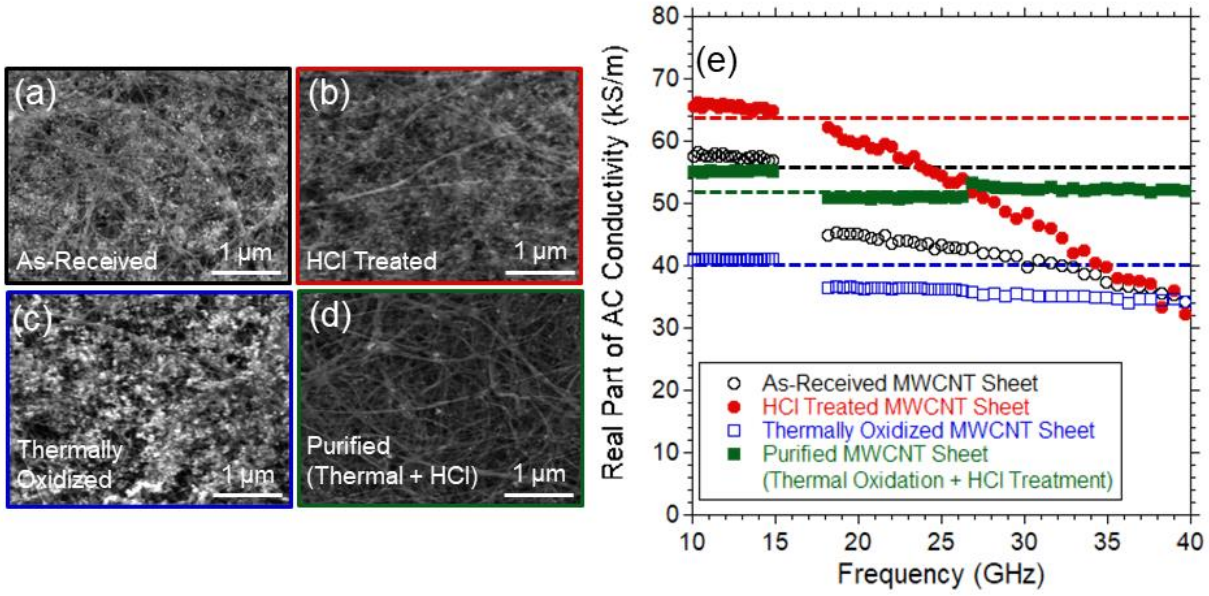

Figure 31. Surface view secondary electron SEM images of (a) as-received, (b) HCl treated, (c) thermally oxidized, and (d) purified MWCNT sheet material, as well as (e) the real part of AC conductivity (markers) and DC conductivity (dashed lines) for the four material preparations measured from 10 GHz to 40 GHz. Plotted values represent the average of triplicate samples, for which the experimental error is 10%. Every 100th data point is shown.

Table 4. Thickness and DC conductivity of as-received, HCl treated, thermally oxidized, and purified MWCNT sheet samples. Error figures represent the error of triplicate samples; the error as a percentage of the average is shown in parentheses.

MWCNT Material Preparation	Thickness (μm)	DC Electrical Conductivity (kS/m)
As-Received	17.6±2.9 (16.7%)	56.7±9.5 (16.8%)
HCl Treated	20.2±1.8 (9.1%)	63.6±6.9 (10.9%)
Thermally Oxidized	14.9±2.6 (17.6%)	40.3±7.2 (17.7%)
Purified	10.8±2.1 (19.5%)	51.9±10.1 (19.5%)

The S_{21} magnitude and phase of the MWCNT sheet in as-received, HCl treated, thermally oxidized, and purified states in three separately measured bands (ranging from 10 GHz to 40 GHz) are shown in Appendix A, Figure 52. The real part of the AC conductivity of the samples is extracted using Equations (5.2-3)-(5.2-4) and is indicated by the markers in Figure 31e; the corresponding DC conductivity values are shown by the dashed lines. The slight offsets in real AC conductivity between the three waveguides are attributed to sample variations due to the differing dimensions of the three

waveguides used. As shown in Figure 31c, the real AC conductivities at 10 GHz for all four material preparations are within 10% of the DC value.

The real part of the AC conductivity of the as-received MWCNT sheet decreases with increasing frequency and diminishes to approximately 65% of the DC value by 40 GHz, as shown by the open black circles in Figure 31e. Metallic iron exhibits a strong magnetic response quantified by high relative permeability[3], thus the high iron content in the as-received MWCNT sheet material would be expected to affect conduction at high frequencies. This response is unlikely to be the result of conventional skin effect because of the nanoscale dimensions of the iron particles. The properties shown in Figure 31e for the Miralon MWCNT sheet are similar to those of randomly oriented MWCNT paper from NanoLab [50] which are also reported to contain iron catalyst nanoparticles[4].

A series of purification treatments were evaluated to understand the effect of MWCNT purity on the AC electrical transport. One sample of the as-received MWCNT material was acid treated with HCl. The DC conductivity of the material increased by approximately 10%, while the real part of the AC conductivity decreased over the measured frequency range to approximately 50% of the DC value obtained at 40 GHz (see the closed red circles in Figure 31e). The improvement in DC conductivity is consistent with that of previous studies that used acids to chemically dope CNTs [25]. Additionally, the TGA results indicated by the red line in Figure 51a suggest that a single step of HCl washing did not remove a significant quantity of iron, likely as a result of the encapsulation of the catalyst particles by shells of carbonaceous material. Therefore, the influence of Fe particles on real AC conductivity is similar to that of the as-received MWCNT sheet.

[3] "Magnetic Properties of Solids." Accessed: Nov. 28, 2023. [Online]. Available: http://hyperphysics.phy-astr.gsu.edu/hbase/Tables/magprop.html#c2

[4] "Buckypaper, carbon nanotube paper." Accessed: Nov. 28, 2023. [Online]. Available: https://www.nano-lab.com/buckypaper.html

Chapter 6 – AC Conductivity of Purified & $KAuBr_4$-Doped MWCNT Sheets

Thermal oxidation was employed to explore the effects of amorphous carbon removal on MWCNT real AC conductivity. Oxidation resulted in a ~25% reduction in the DC conductivity from the as-received material, and the real AC conductivity exhibited a decreasing trend as shown in the open blue squares in Figure 31e. The real AC conductivity of the thermally oxidized MWCNT samples decreases by a smaller amount than the as-received MWCNTs over the measured frequency range. This is attributable to the exposure and oxidation of iron nanoparticles, which is expected to reduce the magnetic response of the impurities as iron oxide has a relative permeability orders of magnitude lower than that of metallic iron [43].

The MWCNT material was purified using both thermal oxidation and HCl treatment steps to examine the intrinsic properties of the MWCNT network. This material had a measured DC conductivity within 10% of that for the as-received material. Due to the removal of a significant percentage of the iron impurities indicated by the TGA and EDXS results, the MWCNTs displayed a nearly constant real AC conductivity with increasing frequency and is consistent with the DC value in the range measured as shown in the closed green squares in Figure 31e.

Overall, the behavior of the MWCNT sheet's real AC conductivity from 10 to 40 GHz is observed to be highly dependent on the residual iron impurity content. The AC conductivity degradation in the as-received and HCl-treated MWCNT sheet samples is attributable to the magnetic properties of the iron interspersed throughout the MWCNT network. The acid treatment does not affect the degradation as the encapsulating amorphous carbon prevents dissolution of the iron. After thermal oxidation, the iron metal is converted to oxide and the reduced degradation in this case may be attributed to the lower magnetic permeability of the oxide particles [127]. The iron content of the samples after treatment in the above cases was nominally equivalent at ~40% w/w. Conversely, purification utilizing both thermal oxidation and HCl treatment steps reduces iron impurity content by approximately an order

of magnitude as indicated by TGA measurements. This resulted in consistent real AC conductivity in the MWCNT sheet within the measured frequency range, and was the process used to investigate the effect of chemical doping with $KAuBr_4$ on the MWCNT AC conductivity.

6.1.2 Characterization of laser-thinned and $KAuBr_4$-doped MWCNT sheets

A rastered laser was used to reduce the thickness of the as-received and purified MWCNT sheets and increase the transmission of the RF signal. See Appendix B for details on the development of the laser thinning process. The thickness and DC conductivity of all samples discussed herein are provided in Table 5, and can be compared with the values listed in Table 4. Laser thinning of the as-received and purified MWCNT sheets was performed until a DC sheet resistance value of 2.5-3 Ω/□ based on increments of 0.75 Ω/□ from the starting value of 1.0 Ω/□ measured for the as-received MWCNT sheet. The as-received and purified MWCNT sheets required ~50 passes and ~7 passes to reach the 2.5-3 Ω/□ value, respectively.

The effect of laser thinning on the as-received MWCNT sheet were 34% and 39% reductions in thickness and DC conductivity, respectively. The properties of the purified material did not significantly change, likely due to the low starting thickness and high starting sheet resistance of the sheet. SEM was used to examine the nanoscale surface morphologies of each sample. Figure 32a-b show that there is a significant reduction in the amount of carbonaceous impurities resulting from laser thinning of the as-received material. The purified material possessed a significantly lower proportion of impurities, and also received fewer laser passes compared with the as-received material, thus leading to similar morphology with and without laser thinning, as shown in Figure 32c-d, respectively. Additionally, a significantly thicker purified MWCNT sheet was produced by layering 16 individual purified sheets using NMP plying according to the procedure discussed in Section 4.2.3, leading to a final thickness of 100.2±5.8 μm (a ~10× increase over a single sheet of purified material as shown in Table 5). This was

done in order to reduce the RF signal transmission and establish a baseline against which the benefits of the laser thinning process could be assessed. The NMP-plied assembly of 16 purified sheets displayed similar surface morphology to the two single sheet purified MWCNT samples (see Figure 32e).

Table 5. Thickness and DC conductivity of as-received & purified MWCNT sheet samples with and without laser thinning and $KAuBr_4$ doping. Error figures represent the error of triplicate samples; the error as a percentage of the average is shown in parentheses.

MWCNT Material Preparation	Thickness (μm)	DC Electrical Conductivity (kS/m)
As-Received, Laser-thinned	11.6±2.7 (22.9%)	34.8±8.0 (23.0%)
Purified, 16 Sheets NMP Plied	100.2±5.8 (5.8%)	57.6±3.6 (6.3%)
Purified, Laser-thinned	8.9±1.3 (14.2%)	45.7±6.5 (14.2%)
Purified, $KAuBr_4$-doped	10.0±1.0 (10%)	300.3±31.6 (10.5%)
Purified, Laser-thinned, $KAuBr_4$-doped	7.3±1.9 (25.7%)	184.9±48.2 (26.1%)

The effect of $KAuBr_4$ doping on DC conductivity was evaluated using the purified samples, where doping of the laser thinned material was performed after the laser process was complete. The $KAuBr_4$-doped MWCNT samples all exhibit a DC conductivity increase in agreement with previously published work [23], [25], [29] as shown in Table 5. The purified and laser-thinned, purified materials exhibited ~5.3× and ~7.9× DC conductivity increases after doping, respectively. Though the purified samples indicated no DC conductivity difference (to within experimental error) with and without laser thinning, the $KAuBr_4$-doped replicates exhibited a difference indicating that laser thinning may change the material response to doping. SEM images of the $KAuBr_4$-doped materials (see Figure 32f-g) showed a similar morphology to the purified material with the addition of bright metal particles in certain regions. EDX mapping of the $KAuBr_4$-doped, purified samples (see Figure 51c) demonstrated that the particles were the result of gold plating, and also showed that there was a coating of bromine over the MWCNT sheet surface.

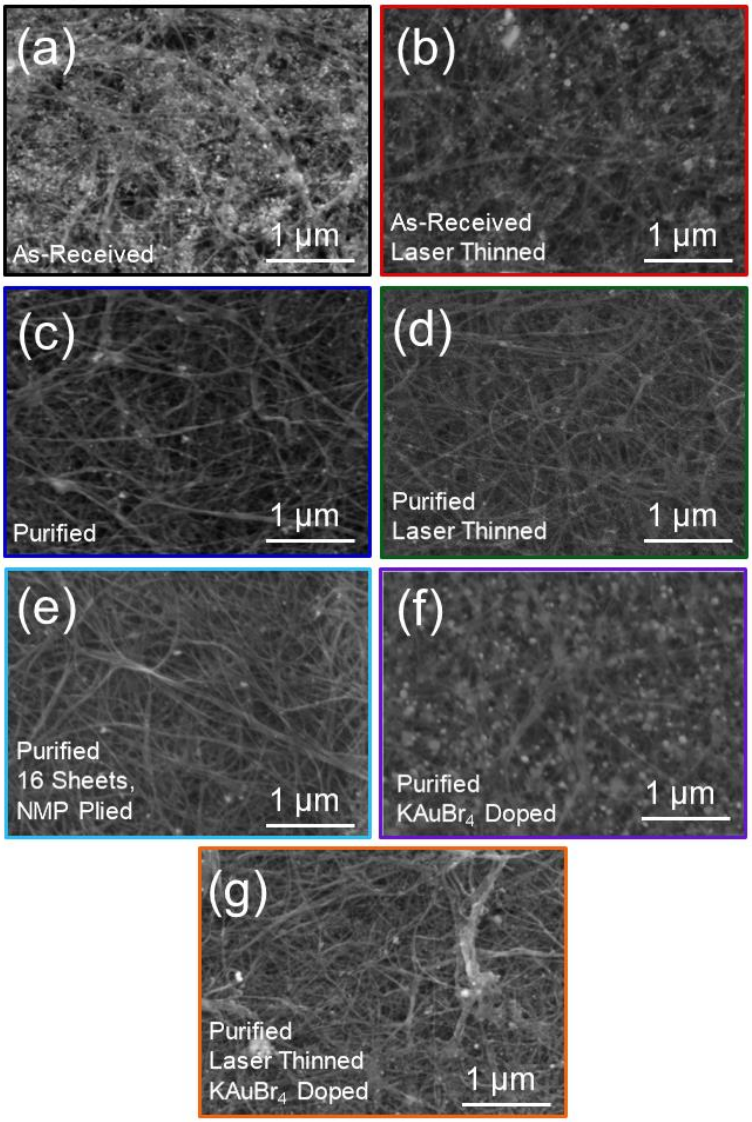

Figure 32. Surface view secondary electron SEM images of (a) as-received, (b) as-received & laser-thinned, (c) purified, (d) purified & laser-thinned, (e) NMP plied, (f) purified & $KAuBr_4$-doped, and (g) purified, laser-thinned & $KAuBr_4$-doped MWCNT sheet material.

Figure 33 shows the real AC conductivity over the range of 10 GHz to 40 GHz for the as-received & purified samples with and without laser thinning, as well as the NMP incorporated purified samples. After laser thinning, the real AC conductivity of the as-received MWCNT sheet were almost constant over the frequency range (compare the open black circles and closed red circles in Figure 33); this matches the DC conductivity (see the red dashed line in Figure 33). The observed behavior is consistent with that for the thermally oxidized and purified samples in Figure 31—and is again

attributed to iron catalyst oxidation. Laser thinning of the purified material resulted in a ~17% reduction in thickness and a ~12% reduction in DC conductivity. The real AC conductivity curves with and without laser thinning for the purified MWCNT sheet are both constant over the full frequency range surveyed (see the open blue squares and closed green squares in Figure 33).

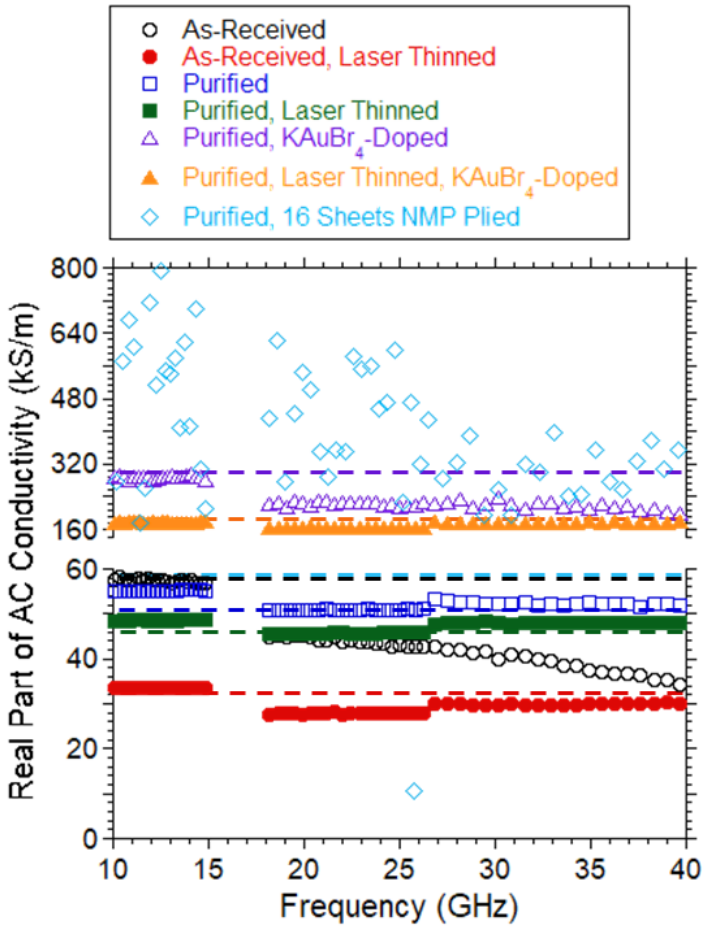

Figure 33. The real part of AC conductivity (markers) and DC conductivity (dashed lines) for as-received, as-received & laser-thinned, purified, purified & laser-thinned, purified & $KAuBr_4$-doped, purified, laser-thinned & $KAuBr_4$-doped, and NMP plied MWCNT sheets in the frequency range of 10 GHz to 40 GHz. Plotted values are the average for triplicate samples, for which the experimental error is 20%. Every 100th data point is shown.

The real AC conductivity of the purified, $KAuBr_4$-doped MWCNT sheet (open purple triangles in Figure 33) is constant from 10 to 15 GHz and matches the DC conductivity (purple dashed line), but deviates from the DC conductivity between 18 and 40 GHz. However, if the material is laser thinned before $KAuBr_4$ doping, the real AC conductivity matches the DC conductivity throughout the full

frequency range of 10 to 40 GHz as shown by the closed orange triangles and orange dashed line in Figure 33. As the material was purified before further processing, the improved matching of the real AC conductivity to the DC value described above is attributed to the laser thinning rather than a change in iron catalyst content. Additionally, the real AC conductivity of the NMP plied purified MWCNT sheet (open, sky blue diamonds in Figure 33) fluctuates significantly and differs from the DC conductivity (sky blue dashed line).The signal transmission was near the ~–100 dB noise floor of the network analyzer for this material[5]. Thus, the effect observed for the $KAuBr_4$-doped materials is hypothesized to be a result of an increased signal-to-noise ratio promoted by laser thinning of the MWCNT sheet. Further supporting evidence for this hypothesis is given in Appendix A, Figure 53, which contains the raw S_{21} magnitude and phase angle for all materials shown in Figure 32 and Figure 33. In summary, laser thinning is an effective approach to increase transmission through the MWCNT sheet. Furthermore, laser thinning improves measurement accuracy of purified, $KAuBr_4$-doped samples which exhibit enhanced frequency-independent real AC conductivity in the measured frequency range (10–40 GHz). To the authors' knowledge, this result is the first demonstration of AC conductivity measurement in chemically doped bulk CNT materials, and shows that the $KAuBr_4$-induced conductivity enhancement in bulk CNTs previously observed through DC electrical measurements [23], [25], [29] is maintained in RF conditions.

6.2 Outcomes

The frequency-dependent AC conductivity of commercially obtained MWCNT sheet material subjected to a multi-step purification process has been measured using the rectangular waveguide

[5] Keysight, "P93xxB Streamline Series Vector Network Analyzer (VNA) | Keysight." Accessed: Jan. 15, 2024. [Online]. Available: https://www.keysight.com/us/en/assets/3121-1262/technical-overviews/P93xxB-Streamline-Series-Vector-Network-Analyzer-VNA.pdf

method. Results show that iron catalyst impurity removal is essential to obtain constant real AC conductivity between 10 and 40 GHz. Laser thinning has been successfully employed to reduce the MWCNT sheet thickness, thereby increasing RF signal transmission; thinning eliminates degradation of the measured real part of AC conductivity with increasing frequency, independent of iron impurity effects, due to improved signal-to-noise ratio. For the first time, the AC conductivity measurement of a $KAuBr_4$-doped bulk CNT material has been demonstrated and shown to exhibit increased absolute conductivity while maintaining frequency independence over the range of 10 GHz to 40 GHz. This demonstrates that $KAuBr_4$-induced conductivity enhancement carries through from DC to AC conditions. Finally, the generalized Drude conduction theory that was previously applied to SWCNTs fits favorably to the experimental data that shows an improvement in the real part of AC conductivity due to elevated carrier density in $KAuBr_4$-doped bulk CNT materials. The theory also indicates the possibility that increases in the real part of AC conductivity may occur at increased frequencies approaching the π-plasmon resonance for doped CNT systems. Overall, the results presented here show that chemical doping of bulk CNT materials can enhance the transport at frequencies in the X and Ka bands, which supports their consideration as an alternative conductor in RF applications.

7 AC Conductivity of Platinum-MWCNT Hybrid Conductors

Task 3 Objectives

- Deposit platinum metal onto ribbons of purified MWCNT material using the previously developed Joule heating-driven CVD method.
- Understand the effect of platinum overcoating on AC conductivity of the MWCNT sheet.

7.1 Review of Joule Heating-Driven CVD of Metals on Miralon MWCNT Roving

The Joule heating-driven CVD technique developed by Leggiero et al. [31], [32] and McIntyre et al. [33], [34], [35] originally stemmed from a desire to utilize the advantageous temperature coefficient of resistivity (TCR) of CNTs in concert with the high conductivity of metals. In this work, it was found that the morphology of MWCNT-metal hybrids depended on the metal used and its wettability to the CNT network surfaces. Copper single-step deposition formed larger discrete particles and resulted in a DC resistance increase, while platinum single step deposition formed smaller, closer packed particles which coalesced into a continuous phase at large deposition masses and caused a DC resistance decrease [31], [32]. Figure 34 shows SEM micrographs of Huntsman MWCNT roving material deposited with Cu (at left) and with Pt (at right). Cu and Pt nanoparticles produced using single-step CVD have been used as seeding sites to facilitate electroplating onto the CNT sample [31]. In addition, deposition of other metals including Ni, Pd, Ru, Rh, and Ir was performed to survey the morphology of the deposited phase, and various particle sizes and arrangements were observed. The metals which produced more uniform coatings with smaller nanoparticles (Pd, Ru, Rh, and Ir) were found to consistently result in improved DC resistance, reinforcing the need for metals with high wettability to the CNT surfaces.

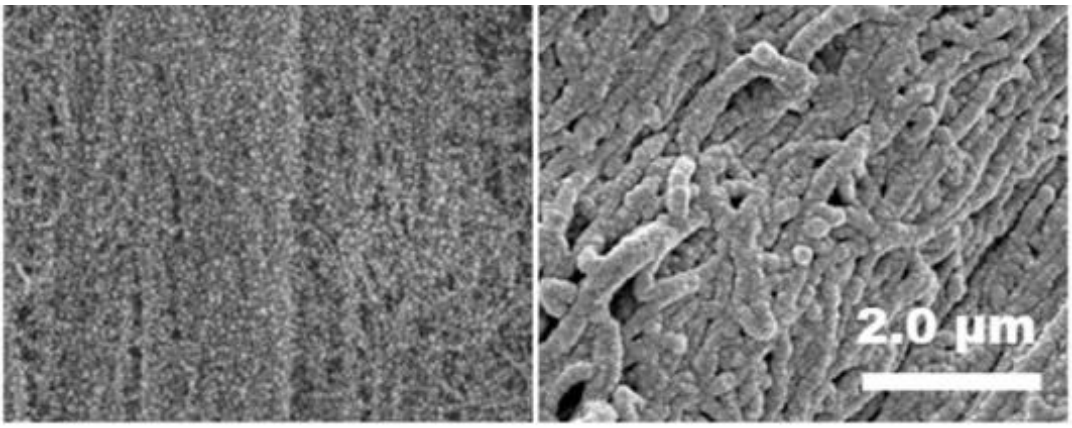

Figure 34. SEM micrographs of MWCNT-Cu (at left) and MWCNT-Pt (at right) hybrids showing the difference in deposited metal morphology depending on wettability. Reprinted with permission from Leggiero et al. [32].

The effect of CVD-derived metal-CNT hybrid morphology on high frequency conductive properties is as yet unstudied in the literature. The primary goal of the research reported herein was to determine whether the benefits of deposited nano-metal with good wettability (e.g. platinum) observed in DC conditions carry through to the AC conductivity of the metal-CNT hybrid materials.

7.2 AC Conductivity Measurement of Platinum-MWCNT Hybrid Conductors

7.2.1 Purified MWCNT sheet sample fabrication

The 8-12 GSM MWCNT sheet material was again used in this study. The material was purified using an extended version of the aforementioned thermal oxidation and HCl treatment-based procedure. The MWCNT sheet was first thermally oxidized to a temperature of 520°C at a rate of 10°C/min under a compressed air flow of 5 SCFM, soaked in a concentrated HCl bath (~37%, CAS#7647-01-0, Sigma-Aldrich) for 30 min, and thermally oxidized with identical conditions to a temperature of 500°C to remove intercalated HCl. To ensure that as much iron catalyst as possible was removed, the MWCNT sheet was soaked in the HCl bath for 30 min and thermally oxidized to 500°C twice more for a total of three purification cycles. Once the purification process was complete, rectangular ribbons with dimensions of 13 mm × 100 mm were laser cut from the MWCNT sheet. The chosen ribbon width was the maximum size capable of sliding freely through the 14/20 ground glass fittings on the three-neck

flask reactor used for CVD, while the ribbon length was chosen to match that previously used in depositions onto MWCNT roving. The ribbons were subjected to laser thinning using the Trotec SpeedMarker 700 fiber laser system according to the procedure described in Appendix B, Section 12.2.3 until a DC resistance per length (R/L) of 250-300 Ω/m which corresponded to a sheet resistance of 2.5-3.0 Ω/□. Copper foil (18 μm thickness) was cut using a Cricut Maker 3 blade cutting tool to create rectangular contacts with dimensions of 10 mm × 26 mm. The copper contacts were placed on each end of the purified MWCNT ribbons with a 5 mm overlap, and the outer tabs were folded over to create a copper-MWCNT-copper stack. Ultrasonic welding of the copper-MWCNT interfaces was performed using a Branson AmTech Ultraweld 40 with conditions of 5 μm amplitude, 30 J energy, and 30 psi pressure to produce the final MWCNT sample geometry used for fabrication of metal-MWCNT hybrid conductors, shown at top in Figure 36.

7.2.2 Physical property characterization of purified MWCNT sheet material

The DC sheet resistance of the purified MWCNT sheet was determined by van der Pauw measurements of samples taken from a ribbon after laser thinning. The thickness of the ribbon was measured at six locations along the center using calipers, and the DC conductivity was calculated using Equation (4.1-3). The thickness and DC conductivity of the purified MWCNT material are shown in Table 6. The DC conductivity of the material in this experiment measured after laser thinning is comparable with that of the laser thinned purified MWCNT sheet discussed in Chapter 6 based on the values in Table 5, indicating that laser thinning had a consistent effect on the purified material in both studies. TGA measurements of the MWCNT sheet over the course of the multiple-cycle purification procedure were performed. The residual mass as a function of temperature for different stages of the process is plotted as shown in Figure 35a. Aliquots of the HCl used for acid treatment during each of the purification cycles are shown in Figure 35b, visually demonstrating the plateau in iron dissolution

between cycles 3 and 4. Differences between the final residual iron content of this purified MWCNT material and that shown in Chapter 6 can be attributed to variation in the properties of the as-received sheet which can be as high as 30%.

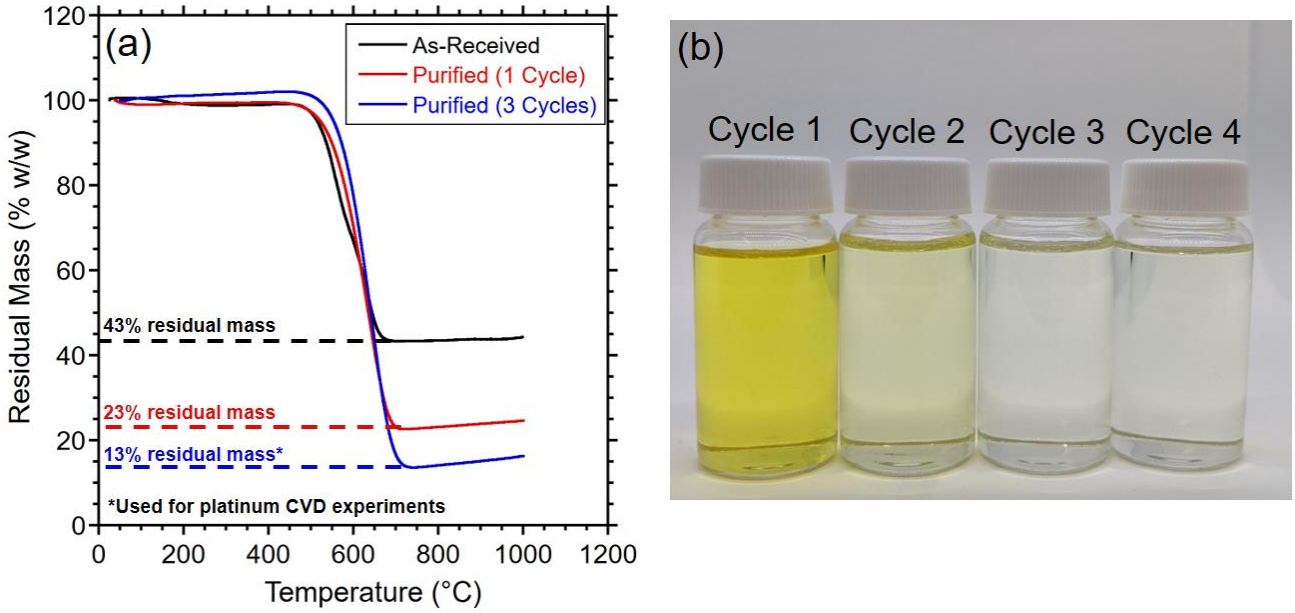

Figure 35. (a) TGA residual mass plots showing the reduction in iron catalyst content of the MWCNT sheet with successive HCl treatment/500°C thermal oxidation cycles. (b) Aliquots taken from the HCl treatment bath after each successive cycle (the HCl bath was replaced for each cycle).

7.2.3 Optimization of Joule heating DC bias for CVD of metal onto MWCNTs

The DC bias used for Joule heating the MWCNT sheet sample is a parameter which must be optimized to ensure the sheet is heated uniformly to a temperature sufficient to decompose the organometallic precursors to their metallic form. Based on previous process optimization using MWCNT roving material [31], a temperature ≥225°C was targeted for heating of the present MWCNT samples. The thermal imaging apparatus described in Section 4.2.5 was used to measure the temperature of the Joule heated MWCNT ribbons. An emissivity value of 0.84, determined by experimental measurement using the procedure also described in Section 4.2.5, was used for all thermal images of the purified MWCNT material. In this optimization process, a MWCNT ribbon prepared as described in

Section 7.2.1 was suspended between two copper clips and subjected to DC biases ranging from 300 to 900 mA with a step size of 200 mA. The collected IR images are presented in Figure 36.

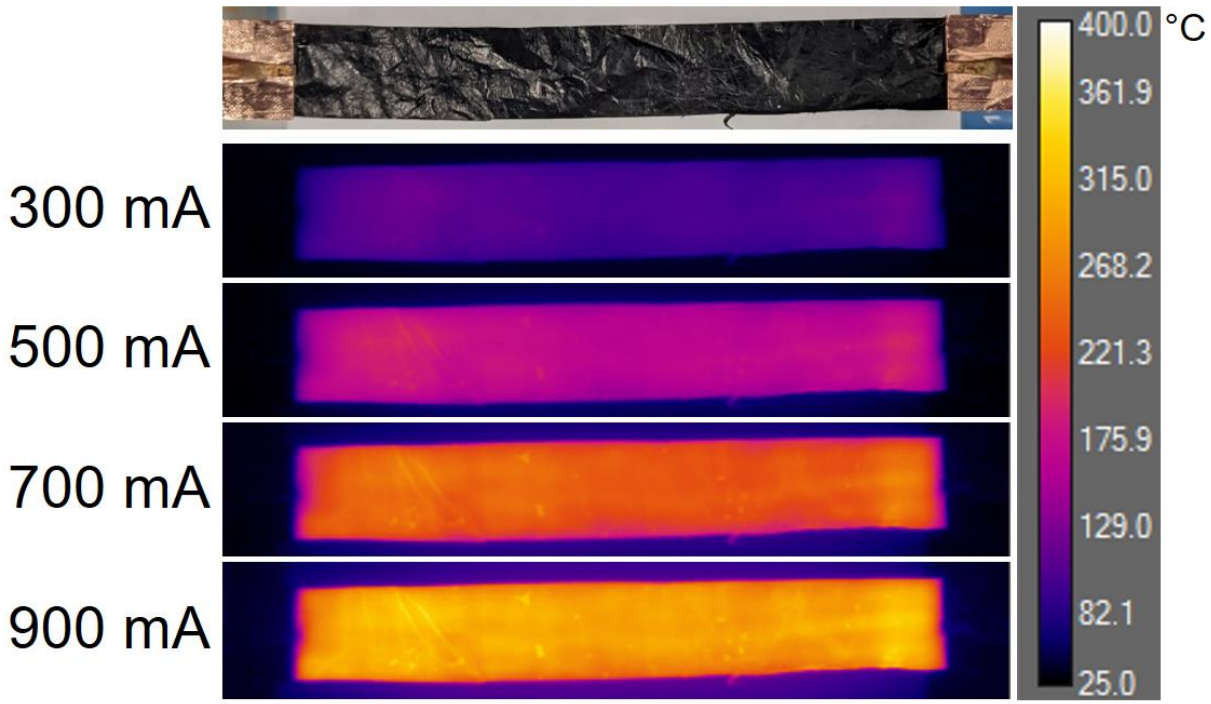

Figure 36. Thermal images of a purified MWCNT ribbon with ultrasonically welded copper contacts (shown at top) when Joule heated with applied biases between 300 and 900 mA. Images were taken using an emissivity value of 0.84.

A DC bias of at least 700 mA was determined to be required for heating the samples to the required temperature of ≥225°C. The uniform heating of the MWCNT ribbon was also evident from visual inspection of the IR images.

7.2.4 Platinum deposition experimental details

Deposition of platinum for the present study was performed using the acetylacetonate complex of the metal as a precursor. This class of organometallic molecule has proven successful for various metals in previous work developing the Joule heating-driven CVD technique [31], [32], [33], [34], [35]. In the molecular structure of these complexes, a cation of the metal to be deposited is bonded to a certain number of acetylacetonate anions, with the number of anions corresponding to the oxidation state of the

metallic cation. The precursor used in the present work was platinum (II) acetylacetonate ($Pt(acac)_2$, 98%, CAS#15170-57-7, Strem Chemicals), whose molecular structure is shown in Figure 37.

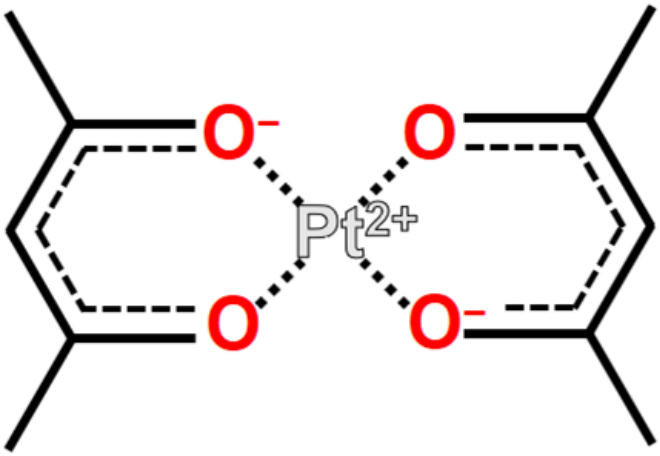

Figure 37. Diagram of the molecular structure of the platinum (II) acetylacetonate precursor. The two organic ligands are driven off of the platinum cation by Joule heating, which is reduced to metallic platinum on the CNT network surface.

7.2.5 Fabrication and characterization of Pt-MWCNT hybrid conductors

The conditions used for deposition of platinum onto the purified MWCNT sheet are presented in Table 6. The effect of varying the $Pt(acac)_2$ mass inserted to the CVD reactor on Pt deposition results was explored. The resulting mass composition (% w/w) for each Pt-MWCNT sample (determined using a microbalance) as well as the thicknesses and DC conductivities of the purified MWCNT sheet and Pt-MWCNT hybrids are presented in Table 6. The Pt content of the MWCNT samples steadily increased as higher $Pt(acac)_2$ masses were used for deposition, while the thicknesses of the sheets remained equivalent within experimental error. The average DC conductivity of the 60 mg $Pt(acac)_2$ (80% w/w Pt) hybrid sample was higher than that of the other samples, but experimental error overlapped between this sample and the 10 mg $Pt(acac)_2$ (56% w/w Pt) sample. This indicates that there is a threshold of deposited Pt mass for conductivity enhancement of the MWCNT sheet located between 70 and 80% w/w.

Table 6. The mass composition of the purified MWCNT sheet and Pt-MWCNT hybrid samples resulting from CVD using the given conditions, as well as the thicknesses and DC conductivities of same. The error in thickness is taken from 6 measurements using calipers on three sheet samples, while the DC conductivity error was obtained by propagation of the thickness and DC sheet resistance error.

$Pt(acac)_2$ mass	Applied DC Bias (mA)	Heating Mantle Temperature (°C)	Composition (% w/w)	Thickness (μm)	DC Conductivity (kS/m)
None	750	200	100% MWCNT (assumed basis)	8.4±0.9	36.1±9.8
10 mg			56% Pt / 44% MWCNT	10.1±2.4	37.7±10.7
30 mg			69% Pt / 31% MWCNT	11.3±1.2	34.6±7.1
60 mg			81% Pt / 19% MWCNT	9.8±2.5	52.2±15.4

The elemental composition of the Pt-MWCNT samples as well as the base purified MWCNT material was analyzed using EDXS. The EDX spectra of the samples as well as the mass composition data are given in Figure 38. The iron content of the material in all cases is low enough to be considered negligible, while traces of copper in the spectrum for the 30 mg sample (blue line) may be a result of material spalling from ultrasonically welding the copper contacts onto the sample. The platinum content of the samples increases from the base purified material to the 30 mg Pt-MWCNT sample, but remains nominally unchanged between the 30 mg and 60 mg Pt-MWCNT samples. The Pt content detected using EDXS did not match the values measured using the microbalance in every case, but this is feasible because the microscale regions probed by EDXS may have higher concentration than the overall value determined from macroscale mass measurements.

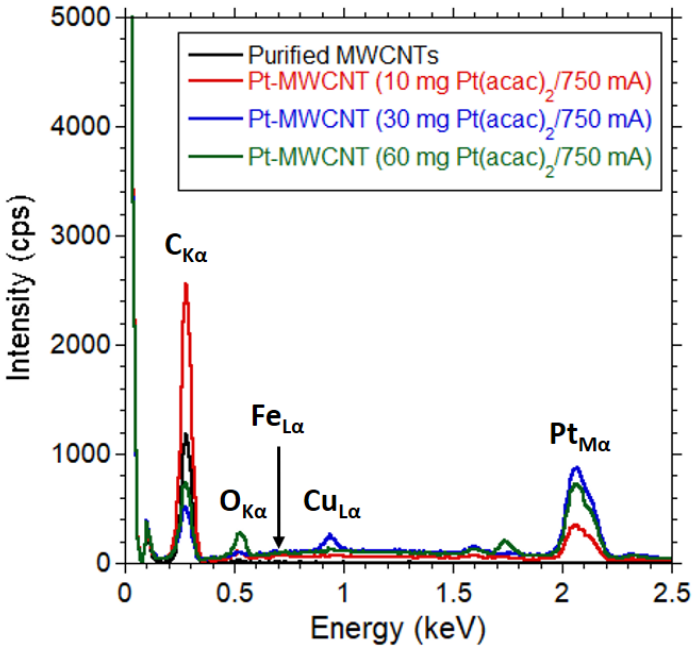

Sample	Composition (% w/w)				
	C	Pt	Fe	O	Cu
Purified MWCNTs	99±1	0±0	0±0	0±0	0±0
Pt-MWCNT (10 mg $Pt(acac)_2$/750 mA)	49±2	48±2	2±0	0±0	0±0
Pt-MWCNT (30 mg $Pt(acac)_2$/750 mA)	8±0	86±0	0±0	0±0	5±0
Pt-MWCNT (60 mg $Pt(acac)_2$/750 mA)	13±0	80±2	0±0	5±2	0±0

Figure 38. EDX spectra showing the elemental constituents of the purified MWCNT sheet and the Pt-MWCNT hybrids deposited using increasing mass of $Pt(acac)_2$. Elemental composition by weight of each sample is presented in the table.

The nanoscale morphology of the deposited material on the MWCNT network was examined using SEM. SEM images of the purified MWCNT sheet and the Pt-MWCNT hybrid conductors produced using increasing $Pt(acac)_2$ mass are shown in Figure 39. As the precursor mass is increased, distinct regions of deposited material form on the MWCNT network, then interconnect into a continuous coating of metal as the precursor mass reaches 60 mg. The morphology of the 30 mg and 60 mg samples is similar, suggesting the primary factor affecting the conductivity change discussed above is the mass of metal deposited.

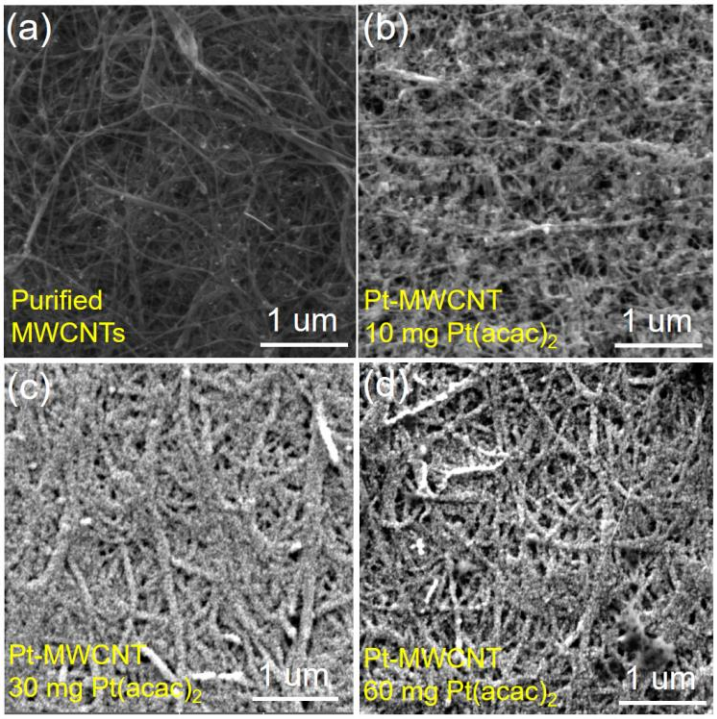

Figure 39. SEM micrographs of the (a) purified MWCNT sheet and Pt-MWCNT hybrid samples produced with (b) 10 mg, (c) 30 mg, and (d) 60 mg of $Pt(acac)_2$.

The AC conductivity of the Pt-MWCNT hybrid conductors was characterized from 10 GHz to 40 GHz using the rectangular waveguide measurement setup to compare with the purified MWCNT sheet. Three samples were taken from each Pt-MWCNT ribbon for these measurements. The real part of the AC conductivity for these samples is shown in Figure 40. The real AC conductivity of the purified MWCNT sheet is constant across the frequency range measured, consistent with the results presented in Chapter 6. As more Pt is deposited onto the MWCNT sheet, the real AC conductivity remains constant and overlaps that of the purified MWCNTs except for the 60 mg $Pt(acac)_2$ (81% w/w Pt) sample (open green circles), whose real AC conductivity is ~1.4x higher. The real AC conductivity of all samples measured matches with their DC conductivity. This indicates that the DC conductivity benefits [32] of Pt deposition onto MWCNTs may carry over into the RF regime without inducing skin effect in the measured frequency range. The conductivity improvement of the Pt-MWCNT hybrid is notably lower than that observed due to $KAuBr_4$ doping.

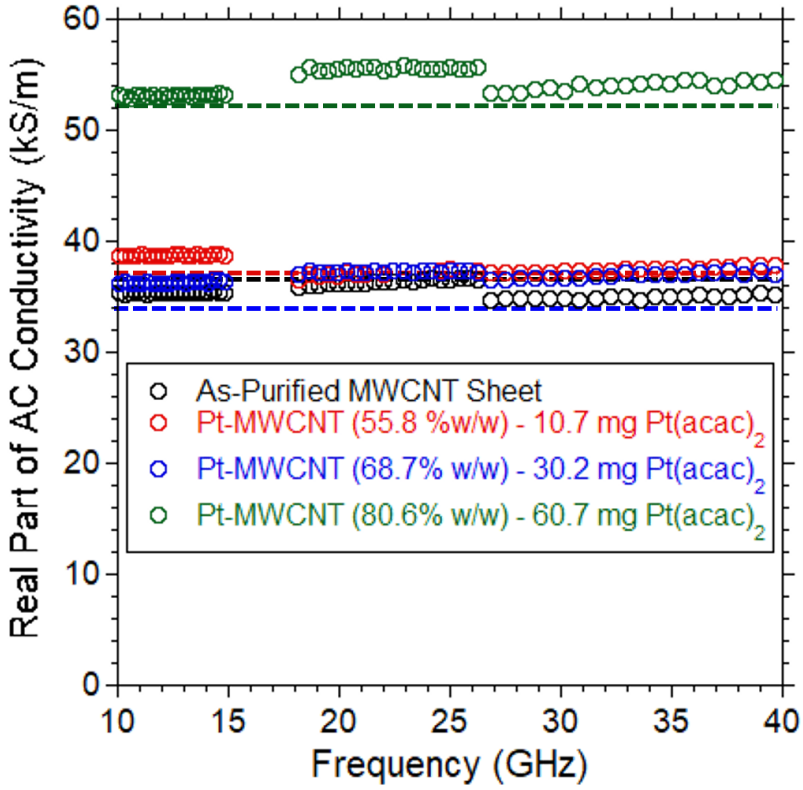

Figure 40. Real AC conductivity (markers) and DC conductivity (dashed lines) of the purified MWCNT sheet and Pt-MWCNT hybrid samples from 10 GHz to 40 GHz. Every 100th data point is shown. Experimental error from triplicate samples is 10%.

7.3 Outcomes

Platinum deposition onto ribbons of purified MWCNT sheet using the previously published Joule heating-driven CVD technique was successfully performed. The Pt-MWCNT samples produced with increasing precursor mass had weight loadings between ~56 and ~80%. The platinum content of the samples was verified by EDXS analysis, and only the 80% w/w Pt-MWCNT samples exhibited a DC conductivity enhancement due to platinum inclusion. The AC conductivity of the Pt-MWCNT hybrid conductors was measured using the rectangular waveguide setup from 10 GHz to 40 GHz and compared with the purified material, and it was shown that the real part of AC conductivity was also only enhanced for the 80% w/w samples. Platinum inclusion did not produce a change in frequency-dependence of the real AC conductivity for any of the samples, indicating that the sole effect of

platinum overcoating of the MWCNT network is to enhance the real AC conductivity at a weight loading between approximately 70 and 80%. The AC conductivity enhancement due to platinum inclusion on the MWCNT samples was significantly less than that caused by $KAuBr_4$ doping, but nonetheless demonstrates that deposition of a metal with suitable wettability to the CNTs is a functional strategy to improve the AC conductivity.

8 Generalized Drude AC Conductivity Modeling

Task 4 Objectives

- Identify a theoretical model for AC conductivity with previous application to bulk CNT materials.
- Apply this model to the measured AC conductivity data from the present work.
- Analyze the resulting fitted model parameters to hypothesize the mechanism(s) of $KAuBr_4$/platinum deposition effects on MWCNT AC conductivity.

8.1 Novel High Frequency Transport in Doped or Metallized Bulk CNT Materials

8.1.1 The generalized Drude model for AC conductivity

Models that derive the frequency-dependent conductivity of materials from a mathematical representation of electron-material interactions or through the use of scaling factors to represent effects of the material nanostructure have been applied to CNTs in literature. One such approach is the Drude model, based on a system of immobile, positively charged particles (ions) surrounded by mobile negatively charged electrons. The proposed mechanism relies on two assumptions: first, electrons undergo collisions that change their velocity with a relaxation time between them of τ, and second, electrons achieve thermal equilibrium with the surroundings solely through these collisions. The result obtained for AC electrical conductivity (σ_{AC}) is as follows,

$$\sigma_{AC}(\omega) = \frac{\sigma_{DC}}{1-j\omega\tau},\ \sigma_{DC} = \frac{ne^2\tau}{m} \tag{8.1-1}$$

where σ_{DC} is the DC conductivity, ω is the angular frequency in rad/s , n is the number of electrons per unit volume, e is the elementary charge, τ is the relaxation time, and m is the mass of an electron. The mathematical form of the Drude AC conductivity clearly suggests a decrease in conductivity with increasing frequency, and it converges to the DC representation at zero frequency. Additions to the Drude theory have been applied in the case of macroscale SWCNT and MWCNT assemblies, such as

the generalized Drude model [45]. This modified approach takes into account localized or weakly confined charge carriers using a "backscattering" term.

The generalized Drude model is a generalization of Drude theory derived by Smith [128] in which electron collision probability follows a Poisson distribution. In this case, the following equation describes the conductivity (to one backscatter term of the expanded series summation),

$$\sigma_{AC}(\omega) = \frac{\varepsilon_0 \omega_p^2 \tau}{(1-j\omega\tau)}\left(1 + \frac{c}{(1-j\omega\tau)}\right) \qquad \omega_p = \sqrt{\frac{ne^2}{\varepsilon_0 m}} \tag{8.1-2}$$

where ε_0 is the permittivity of free space, ω_p is the plasma frequency, and c is the so-called backscatter parameter with $-1 \leq c \leq 0$. The coefficient c represents the amount of the electron's original velocity that is retained after n collisions. With c=0, the typical Drude metallic behavior holds. Bulmer et al. [45] were the first to apply this model to CNT materials in the RF range. They found that the mean free paths (MFP) of 98% metallic, 98% semiconducting, and unsorted SWCNT papers were similar to their mean CNT lengths, based on τ values obtained from generalized Drude fitting to measured AC conductivity. The plasma frequencies of these materials were found to be in the THz range. This dissertation work applied the generalized Drude model to AC conductivity measurements of purified and $KAuBr_4$-doped MWCNT sheets as well as Pt-MWCNT hybrids produced by Joule heating-based CVD.

8.1.2 Generalized Drude modeling of purified, $KAuBr_4$-doped CNTs

The generalized Drude equation as shown in Equation (8.1-2) was analytically solved to obtain the real (σ') and imaginary (σ'') parts of the theoretical AC conductivity as shown by Equations (8.1-3) and (8.1-4).

$$\sigma'(\omega) = \frac{\varepsilon_0 \omega_p^2 \tau}{(1+\omega^2\tau^2)}\left[1 + \frac{c(1-\omega^2\tau^2)}{(1+\omega^2\tau^2)}\right] \tag{8.1-3}$$

$$\sigma''(\omega) = \frac{\varepsilon_0 \omega_p^2 \omega \tau^2}{(1+\omega^2\tau^2)}\left[1 + \frac{2c}{(1+\omega^2\tau^2)}\right] \quad (8.1\text{-}4)$$

Least-squares minimization on the residuals was used to obtain the real and imaginary parts of AC conductivity given by the generalized Drude equation for the two materials. The results of fitting with Equations (8.1-3) and (8.1-4) to the real and imaginary parts of AC conductivity from 10 GHz to 40 GHz as well as extrapolation to 100 GHz are shown in Figure 41a-b.

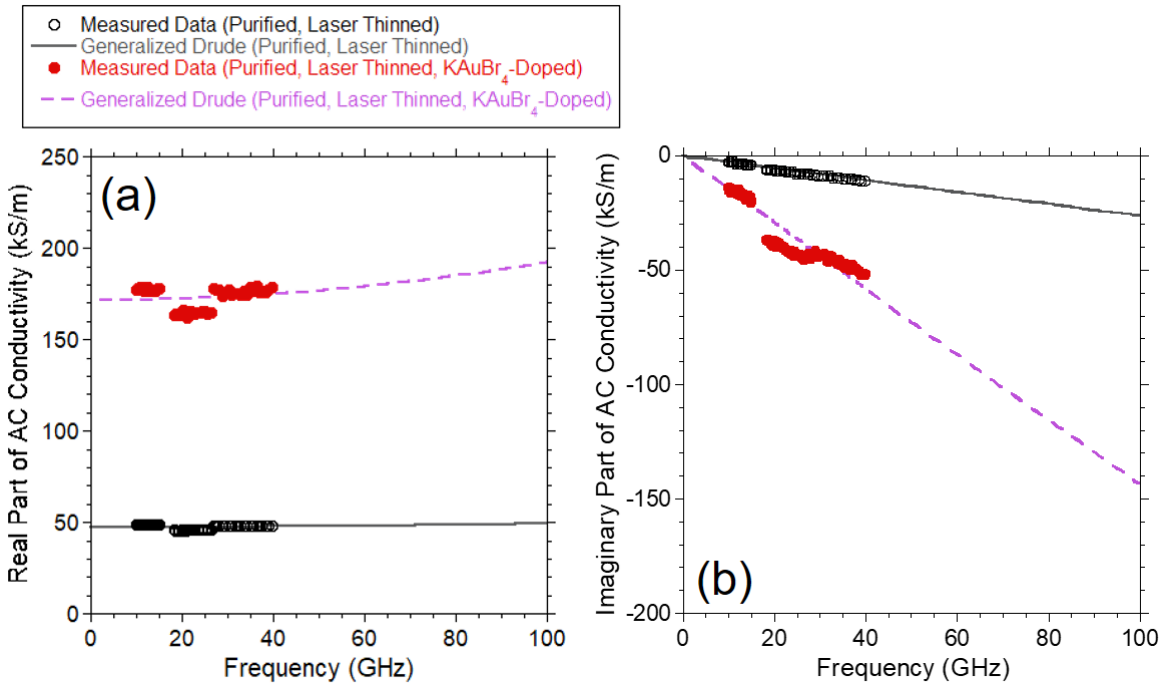

(c)

Material	Parameter			
	ω_p		c	τ (ps)
	THz	eV		
Purified, Laser Thinned	819	3.39	-0.913	0.094
Purified, Laser Thinned, $KAuBr_4$-Doped	1595	6.59	-0.93	0.109

Figure 41. Generalized Drude equation fit to the experimentally measured (a) real part and (b) imaginary part of the AC conductivity for purified, laser-thinned and purified, laser-thinned, $KAuBr_4$-doped MWCNT sheet from 10 GHz to 40 GHz with extrapolation to 100 GHz. (c) The fitted values of the plasma frequency, backscatter parameter, and relaxation time for both materials.

The equations fit favorably to the data for both the purified and laser-thinned as well as the purified, laser-thinned, and $KAuBr_4$-doped MWCNTs as shown in Figure 41a-b. In the frequency band

of the measured data, the real part of the AC conductivity is effectively constant, but begins to increase in the extrapolated region up to 100 GHz. The imaginary part of the AC conductivity is negative and decreasing for the thinned, purified MWCNT sheet with and without $KAuBr_4$ doping. The observed trend in the imaginary part of the generalized Drude model is continuous throughout the extrapolated region up to 100 GHz. The negative values of the imaginary AC conductivity indicate a capacitive response where the induced current leads the electric field, in agreement with the generalized Drude theory which suggests that high backscattering (c approaching –1) will cause the net current to preemptively change direction before the electric field [128]. Appendix A, Figure 54 provides the real AC conductivity curves normalized to their value at zero frequency. The conductivity increase from zero frequency to 100 GHz is 7% for the thinned, purified sample and 12% for the thinned, purified, and $KAuBr_4$-doped sample. The fitted values of plasma frequency, backscatter parameter, and relaxation time for both materials are shown in Figure 41c. The values of c for both materials are approximately equal and indicate a high degree of backscattering. These values are consistent with the fitted *c* values reported previously for sorted and mixed SWCNT papers [45]. The relaxation times for both materials are also approximately equal, and are an order of magnitude smaller than those reported for the SWCNT samples. The plasma frequency for $KAuBr_4$-doped MWCNTs is ~2× that of the as-purified material. This is consistent with the expected increase in carrier density due to $KAuBr_4$ doping [25], as the plasma frequency is directly proportional to the square root of carrier density [129]. Furthermore, the plasma frequencies for both purified MWCNTs and purified, doped MWCNTs are consistent with the π-plasmon resonance energies of SWCNTs [108] after unit conversion to eV. Overall, the generalized Drude theory reasonably describes the frequency-dependent conductive properties of purified MWCNTs over the range from 10 GHz to 40 GHz.

8.1.3 Generalized Drude modeling of Pt-MWCNT hybrid conductors

An identical least-squares procedure was used to fit the generalized Drude equation to the purified MWCNT sheet with and without Pt metallization to produce a hybrid conductor. The resulting fitted curves and experimental data are presented in Figure 42a and b for the real and imaginary AC conductivity. Figure 42c presents the fitted values for the relaxation time, plasma frequency, and backscatter parameter. Similar to the case of $KAuBr_4$ doping, the addition of Pt metal to the MWCNT network caused the plasma frequency to increase, concurrent with improvements to the DC conductivity and real AC conductivity. This is feasible due to the high electron density of the metal, which would increase the carrier density of the composite material. Due to the additional purification cycles applied to this particular sample of the purified MWCNT sheet, its properties are not comparable to the purified material discussed in Section 8.1.2 and it is reasonable that the material could have a different plasma frequency. Additionally, the relaxation time is significantly decreased in the Pt-MWCNT hybrid material over that of the purified MWCNT sheet. This is indicative of a reduction in carrier mobility within the composite Pt-MWCNT material.

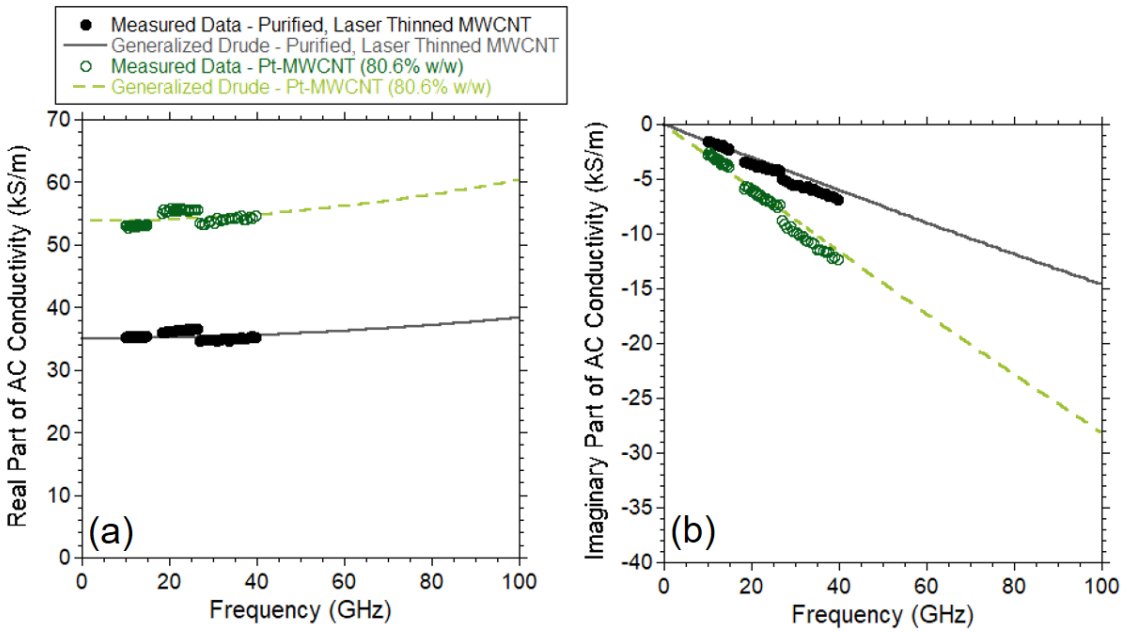

(c)

Material	Parameter			
	ω_p		c	τ (ps)
	THz	eV		
Purified, Laser Thinned MWCNTs	488	2.02	-0.829	0.207
Pt-MWCNT (80.6% w/w)	563	2.33	-0.865	0.168

Figure 42. Generalized Drude equation fit to the experimentally measured (a) real part and (b) imaginary part of the AC conductivity for purified, laser-thinned MWCNT sheet and Pt-MWCNT (80.6% w/w) hybrid sheet from 10 GHz to 40 GHz with extrapolation to 100 GHz. (c) The fitted values of the plasma frequency, backscatter parameter, and relaxation time for both materials.

8.1.4 Mechanistic differences affecting $KAuBr_4$/platinum AC conductivity effects

The experimental results of AC conductivity measurement of $KAuBr_4$-doped MWCNT samples and Pt-MWCNT hybrid samples showed significant differences in the effect of each treatment on the RF properties of the MWCNT material. While $KAuBr_4$ doping produced a 3-4× real AC conductivity increase over the purified MWCNT material, platinum inclusion resulted in a comparatively lower 1.4× increase. Generalized Drude model fitting to the measurement data from both types of samples provided critical information to explain the mechanistic differences between the effects of the two treatments on the MWCNT sheet's AC conductivity. The two most significant differences in the model fitting

parameters between the two cases are the amount of plasma frequency increase and the change in relaxation time. $KAuBr_4$ doping increased the plasma frequency by nearly 2×, while platinum inclusion increased the plasma frequency by a relatively lower amount (~1.2×). However, the relaxation time was nominally equivalent after $KAuBr_4$ doping, but decreased by ~1.2× in the case of platinum inclusion. This suggests that the difference in magnitude of the AC conductivity enhancements due to each treatment occurs due to a tradeoff between carrier density and mobility in the material. $KAuBr_4$ dopant does not noticeably affect carrier mobility, but its electron-withdrawing nature [25] provides an improvement to carrier density at the MWCNT network surfaces themselves. Conversely, the platinum coating deposited through CVD produces an AC conductivity enhancement due to its electron-rich nature, but this enhancement may be primarily due to the metallic layer acting as a conductor in parallel with the MWCNT network [32]. Moreover, the reduction in carrier mobility due to the heavier metal particles (suggested by the reduced relaxation time) likely contributes to the smaller increase in real AC conductivity of the Pt-MWCNT hybrid samples compared with those exposed to $KAuBr_4$ dopant.

8.2 Outcomes

The generalized Drude model was selected as an applicable theory to hypothesize a mechanism for the effects of $KAuBr_4$ doping and platinum nano-metal inclusion on the MWCNT AC conductivity. The equation for the AC conductivity derived from this theory in previous reports was fitted to the measured AC conductivity data, both real and imaginary, for the MWCNT materials modified by each method. The fitting parameters suggested similar mechanisms contributing to AC conductivity enhancement from each modification. Increased carrier density was indicated by higher plasma frequency after $KAuBr_4$ doping/Pt inclusion, where the carriers in question were holes and electrons for the respective treatment methods. However, the decrease in relaxation time in the case of Pt inclusion indicates a reduction in electron mobility, which is a competing effect leading to less overall increase in

the AC conductivity for the Pt-MWCNT hybrid material. The backscatter parameters for each material also indicate a high degree of backscattering, which can be attributed to the capacitive response exhibited in the imaginary part of the AC conductivity. Furthermore, extrapolation of the model to 100 GHz in both cases suggested increasing real AC conductivity at frequencies above the measured range.

9 EMI Shielding Effectiveness of SWCNT and MWCNT Thin Films

Task 5 Objectives

- Fabricate SWCNT and MWCNT thin films, varying processing conditions to produce different film areal densities and thicknesses.
- Employ the rectangular waveguide setup to measure EMI shielding effectiveness of the CNT thin films from 10 GHz to 15 GHz.
- Directly compare experimental results between the SWCNT and MWCNT thin film samples, and also compare with previously published work.

Radar technology is a key aspect of infrastructure worldwide. X-band radar, operating in a frequency range of 8 GHz to 12 GHz, is used for a variety of applications including weather monitoring, air and maritime traffic control, and speed detection in law enforcement [130]. Electromagnetic interference (EMI) shielding materials induce a high degree of attenuation in incident electromagnetic waves, either through reflection, absorption, or a combination thereof. Shielding materials play an essential role in the implementation and efficient function of radar systems; in large-scale operations (e.g. maritime traffic control) they can be used to minimize interference sources affecting radar units [131] or to increase visibility of small targets using highly reflective elements [132].

In smaller scale applications, such as wearable or transparent electronics, materials that maintain their shielding performance with high optical transparency, good flexibility, and/or low weight are attractive. The broad class of transition metal carbides/nitrides/carbonitrides (collectively called MXenes) has previously been identified as promising shielding materials in this field due to their high electrical conductivity, flexibility, low weight, and excellent EMI shielding performance (~46 dB with 94 nm thickness) [133], [134]. In addition, indium tin oxide (ITO) films have received significant attention as transparent shields due to their high electrical conductivity/EMI shielding performance (58 dB with 1 μm thickness) combined with exceptional optical transparency [135], [136], but their

brittleness is a limiting factor in this application which current investigations are seeking to overcome [137], [138], [139]. Previous reports over the past two decades have also identified CNT materials as an attractive shielding material option. The EMI shielding effectiveness of SWCNTs and MWCNTs has been measured in previous reports. In these studies, sample form factors ranged from unsupported CNT papers with thickness in the range of tens of microns [83], [106], [107] to micron/nanometer scale CNT thin films deposited on substrates [83]. These reports have consistently found a strong relationship between film thickness and shielding effectiveness, and have shown competitive shielding effectiveness with the MXene and ITO materials in the thicker CNT films studied (~90 dB for a 24 μm SWCNT film [83] and ~100 dB for a ~15 μm densified MWCNT film [107]).

The current state of the field for CNTs as EMI shielding materials comprises a collection of shielding effectiveness results obtained from various CNT materials, film thicknesses, sample structures, and measurement techniques. Characterization of identically prepared SWCNT and MWCNT samples using the same measurement technique would provide greater confidence in a direct comparison of shielding properties depending on CNT type. Measuring RF material properties of samples mounted on a backing structure relies on accurate characterization of the substrate [75], therefore, it is appealing to utilize unsupported samples. Previous reports have indicated the successful fabrication of free-standing CNT thin films, in which the film is not supported by any substrate or backing structure but is instead mounted on a frame with a central opening [140]. Thus, the present work compared the shielding effectiveness at/near X-band frequencies of high quality, free-standing SWCNT and MWCNT thin films with thicknesses ranging from the micron to sub-micron scale.

Chapter 9 – EMI Shielding Effectiveness of SWCNT and MWCNT Thin Films

9.1 Preparation of Free-Standing SWCNT Thin Films

Please refer to Appendix A, Section 11.2 for supplemental data to this chapter.

The use of vacuum filtration to produce CNT thin films from a dispersion or solution of CNTs is well known [25], [59], [141], [142], [143], [144]. Previous reports have also demonstrated the production of CNT thin films which are free-standing (i.e. mounted so as to support their own weight without any backing structure or substrate) [140]. SWCNT thin films were fabricated via the procedure outlined in Section 4.2.7 targeting initial SWCNT paper masses (synthesized using the procedure described in Section 4.2.6) of 3.0, 2.0, 1.0, 0.5, 0.25, 0.15, 0.05, and 0.025 mg. The resulting circular samples had diameters of 35 mm, leading to calculated areal densities (ρ_A) of 3000, 2000, 1000, 500, 250, 150, 50, and 25 mg/m^2. Each SWCNT thin film was prepared for RF reflectance/transmittance testing and physical characterization. Frames were fabricated from 9 µm thick copper foil using a Cricut Maker 3 blade cutting tool. The initial frame structure had dimensions of 30 mm x 40 mm, with a 9 mm x 19 mm rectangular opening in the center which matched the WR-75 rectangular waveguide used for RF measurements from 10-15 GHz. After transfer onto a glass slide, the CNT thin film was cut with a razor blade into two semicircular sections, one of which was returned to the water bath. The thin film section was drawn out of the bath onto the frame at a ~45° angle to the film surface, with the drawing motion serving to lay the film flat across the rectangular opening with full coverage. A schematic of this process is presented in Appendix A, Figure 55. The resulting copper frame/CNT film assembly was air-dried at room temperature while suspended in mid-air to prevent the film from adhering to other surfaces. The film was dried at 200°C in a vacuum furnace (VWR 1400E) for 3 h (also with the sample suspended in mid-air) to remove any remaining water. Lastly, the frame was trimmed using scissors to leave a ~3 mm wide border around the rectangular opening. The remaining thin film section on a glass slide was dried using identical conditions and used for physical characterization. Photographs of the

free-standing SWCNT thin films stretched across the Cu foil frame are shown in Figure 43a, where the "RIT" logo is placed behind each sample to demonstrate optical transparency as a function of areal density. As the areal density of the SWCNT films decreases, the logo becomes more visible.

9.2 SWCNT Thin Films Characterization

9.2.1 Areal density effects on SWCNT thin film physical properties

The physical properties of the SWCNT thin films were characterized to quantify their relationship with the areal density and investigate the effect on the RF reflectance/transmittance. All CNT film characterization experiments reported herein were carried out using a single sample of each areal density. The three-dimensional surface profile of each glass-slide-backed film was measured using optical profilometry and the thickness of each film was estimated by analyzing three two-dimensional line scans crossing over the clearly defined step in each profile (all profiles shown in Appendix A, Figure 56). The maximum error in the thinnest SWCNT thin film was 10%, with decreasing error as the film thickness increased. Figure 43b shows the average thicknesses (open blue triangles-error bars are within the data point for all samples) of the SWCNT thin films versus the film areal density, while the sheet resistances of the films plotted versus the film areal density are given by the closed red squares in Appendix A, Figure 57. The DC electrical conductivity values for each SWCNT thin film are given in Appendix A, Table 8, along with the volume density and specific DC conductivity (absolute conductivity normalized to volume density).

As the areal density of the film decreases, thickness decreases linearly until ~500 mg/m^2, after which the film thickness abruptly decreases by an order of magnitude between 500 and 250 mg/m^2. Sheet resistance increases asymptotically with decreasing SWCNT areal density, and the behavior of the DC conductivity with areal density changes drastically below a value of 500 mg/m^2 from a steady decrease to a sharp increase for SWCNT samples. This DC conductivity trend is primarily attributed to a

sharp increase in volume density of the SWCNT network as indicated by the thickness trend discussed above. The surface morphology of each film was also examined by SEM imaging of samples taken from the edge of each copper frame, leading to the representative micrographs of the films presented in Appendix A, Figure 58. The films are visible as randomly oriented, interconnecting and crossing bundles of SWCNTs forming a continuous layer. The SWCNT bundle sizes visibly decrease below an areal density of 500 mg/m^2, and increased void space in the surface morphology is observed. This indicates the density increase is primarily in the through-plane direction.

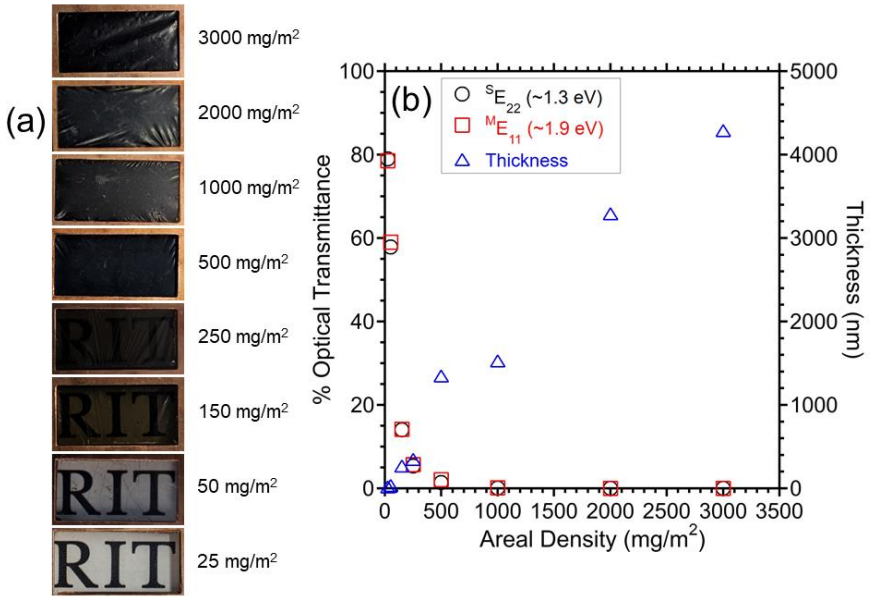

Figure 43. (a) Photographs of the free-standing SWCNT thin films mounted on copper foil frames with areal densities in the range of 3000 mg/m^2 to 25 mg/m^2 (from top to bottom). (b) The optical transmittance of the free-standing SWCNT thin films at the $^{S}E_{22}$ and $^{M}E_{11}$ interband transitions, as well as the film thickness, versus the film areal density.

Optical absorbance spectroscopy was employed to analyze the optical transparency of the copper-frame-mounted free-standing SWCNT thin films. Appendix A, Figure 59b shows the characteristic optical absorbance spectra of the SWCNT thin films over the range of 1.0 to 2.5 eV; the two clearly visible peaks are associated with the electronic transitions from the Van Hove singularities in the density of states for SWCNTs [115]. The respective sources of the peaks located at ~1.3 eV and

~1.9 eV are the second interband transition for semiconducting SWCNTs ($^{S}E_{22}$) and the first interband transition for metallic SWCNTs ($^{M}E_{11}$). These peaks are clearly defined for the thin films with thickness between 25 and 1000 mg/m^2, however, the absorbance measurement for the 2000 and 3000 mg/m^2 thin films is unreliable due to significant opacity resulting from the high SWCNT mass causing very low detected transmittance values. The optical transmittance at the maximum peak intensity for each electronic transition was determined from the relationship between optical absorbance (A_{opt}) and transmittance (T_{opt}), as shown in Equation (4.1-5). These are plotted as a percentage vs. the SWCNT thin film areal density in Figure 43b (open black circles for $^{S}E_{22}$ and open red squares for $^{M}E_{11}$). Optical transmittance is taken to be 0% for the 2000 and 3000 mg/m^2, as these spectra do not have clearly resolved peaks. The optical transmittance of the films begins at ~80% for the 25 mg/m^2 film, then decreases logarithmically to a constant 0% that spans from 1000 mg/m^2 to 3000 mg/m^2. There is not a significant difference between the transmittance at either electronic transition, but the relevance of the $^{S}E_{22}$ transition to the visual appearance of the films should be noted as it occurs within the visible light region. Representative photographs of each SWCNT thin film for each areal density in Figure 43a clearly show that the film transparency decreases in a manner consistent with the decrease in optical transmittance. Further analysis is primarily discussed in terms of the thickness, which corresponds to the areal density as shown in Table 8.

Raman spectroscopy was employed to ensure that the CNT properties of the SWCNT thin film samples were consistent across different film thicknesses. Appendix A, Figure 60a shows the averaged Raman spectra for the SWCNT thin films scanned from 100 to 3000 cm^{-1} at three randomly selected spots on each thin film. The characteristic D-band (~1350 cm^{-1}), G-band (~1580 cm^{-1}), and G'-band (~2700 cm^{-1}) peaks, as well as the radial breathing mode (RBM) of SWCNTs (100-300 cm^{-1}) are present in the spectra for all SWCNT thin films. The ratio of D-band to G-band peak intensities is a

well-known metric to quantify the CNT quality, as it represents the amount of defects present in the typical sp^2 bonding structure of CNTs [126]. As shown in Figure 60c, the D/G peak ratio values as a function of film thickness indicate that the variation of processing conditions leading to different thicknesses does not impact CNT quality.

9.2.2 Effect of SWCNT thin film sheet resistance on RF reflectance and transmittance

RF reflectance and RF transmittance of the SWCNT thin films with varying thickness were measured using the rectangular waveguide setup according to the procedure outlined in Section 5.2. The resulting RF reflectance as a function of frequency from 10 GHz to 15 GHz for each SWCNT film thickness are presented in Figure 44a. The corresponding RF transmittance curves are given in Appendix A, Figure 61a. The reflectance of each film as a function of frequency is nominally constant across the measured band, regardless of thickness. However, the reflectance is observed to decrease with decreasing film thickness. The reflectances of the films with thicknesses of 4287 nm and 3292 nm are approximately 99% (black and red curves), while reflectance begins to decrease at 1529 nm and reaches 40% for the 18 nm film (sky blue curve). To enable clearer examination of these trends, the all samples were compared at 12 GHz to assess the sample performance at the highest X-band frequency (near the mid-point of the measured frequency range). The RF reflectance and RF transmittance of the SWCNT thin films at this frequency are plotted versus film thickness in Figure 44c, represented by the closed red circles and open red circles, respectively. Transmittance of the films follows an opposite trend to reflectance, but the sum of reflectance and transmittance at each thickness is not unity, indicating a portion of the incident RF signal is also absorbed by the SWCNT films.

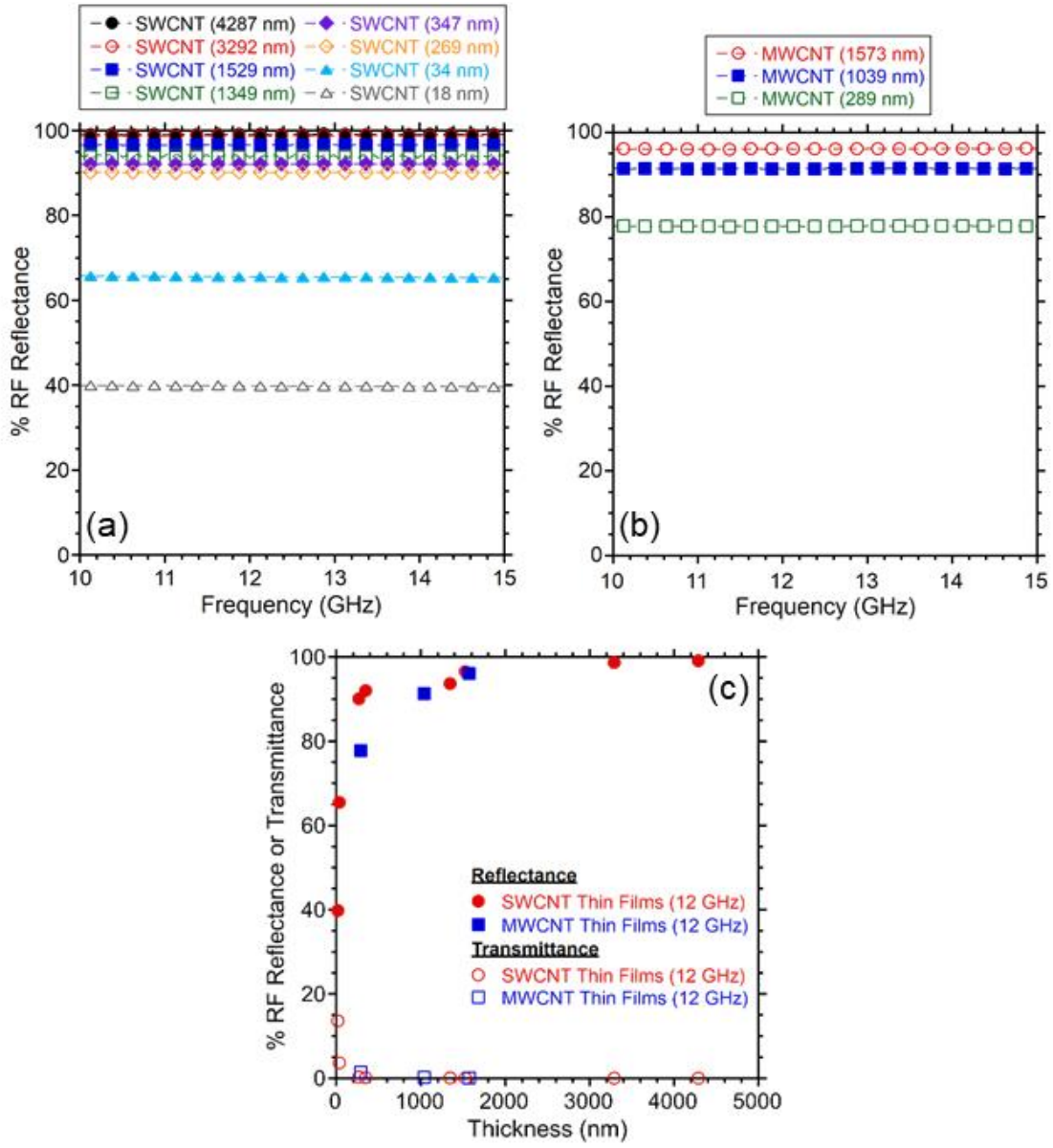

Figure 44. Frequency sweeps of RF reflectance for (a) the SWCNT thin films, and (b) the MWCNT thin films. (c) The relationship of RF reflectance and RF transmittance to SWCNT and MWCNT film thickness.

To demonstrate the differences between optical and RF properties of the SWCNT thin films, the optical transmittance and RF reflectance were compared. Figure 45a shows the optical transmittance at the $^{S}E_{22}$ interband transition and RF transmittance at 12 GHz as a percentage (closed and open red circles, respectively), plotted vs. the thickness of the SWCNT thin films. The values given by both

measurements show similar logarithmic trends, with the optical transmittance decreasing as the RF reflectance increases. The data shown here indicate that an RF reflectance of ~60% can be achieved while maintaining greater than 50% optical transparency, demonstrating the merit of the SWCNT thin films as transparent shielding materials. Overall, the very high RF reflectance values of the SWCNT films demonstrate that the present material can effectively redirect electromagnetic waves even at micron or sub-micron thicknesses.

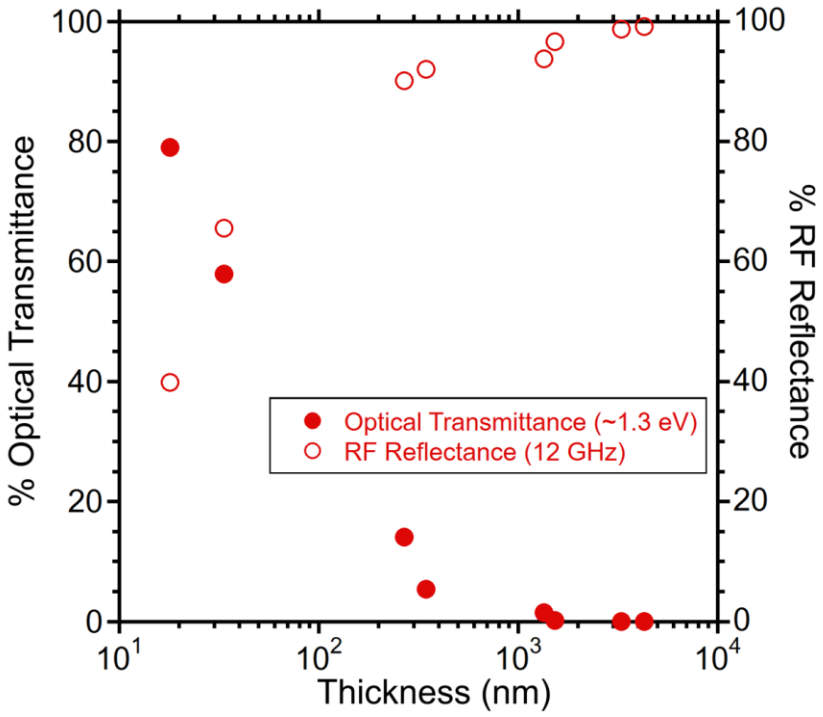

Figure 45. The relationships between optical transmittance at 1.3 eV and RF reflectance at 12 GHz and the SWCNT film thickness.

9.3 Comparison Between SWCNTs and MWCNTs

9.3.1 MWCNT thin film fabrication and physical characterization

MWCNT thin films with areal density of 2000, 1000, and 500 mg/m^2 were fabricated from Huntsman commercial MWCNT sheet material (purified as described in Section 4.2.1) using the same procedure as the SWCNT films in order to compare CNT types within the range of SWCNT film areal density specifications that produced an RF reflectance greater than 90% in the experiments described in

the previous section. The thicknesses (closed blue triangles) and sheet resistances (closed green diamonds) of the MWCNT thin films can be compared with the SWCNT samples in Figure 57. The MWCNT thin films are thinner than the corresponding SWCNT samples, and increase in sheet resistance at a higher rate with decreasing areal density. The thickness, sheet resistance, and DC electrical conductivity values for the MWCNT thin films are given in Appendix A, Table 8. The surface morphology of the MWCNT thin films was examined using SEM and compared to that of the SWCNT thin films. Representative SEM images of each MWCNT thin film are presented in Appendix A, Figure 58i-k. The network density of the MWCNT samples is visibly higher than that of the SWCNT samples made with equivalent thin film areal densities; this result is consistent with the higher volume density of the MWCNT samples. Despite this, the higher physical densities of the MWCNT films do not result in higher electrical conductivity than the SWCNT samples, which may be a result of current flow being restricted to only the outer layers of the MWCNTs.

Raman spectra for the MWCNT thin films are presented in Figure 60b. The radial breathing mode is prominently absent from the MWCNT Raman spectra, confirming these samples are composed entirely of MWCNTs, consistent with existing literature [126]. Consistency in relative Raman D/G ratios reported in Figure 60c indicate that the processing conditions do not affect CNT quality, similar to the SWCNT thin films.

9.3.2 Effect of CNT type on RF reflectance and transmittance

The RF reflectance and transmittance of the fabricated MWCNT thin films was measured from 10 to 15 GHz using the rectangular waveguide setup. The RF reflectance is presented versus frequency for each thickness in Figure 44b. The corresponding RF transmittance curves are given in Appendix A, Figure 61b. To compare trends between the two CNT types, the RF reflectance (closed blue squares) and RF transmittance (open blue squares) at 12 GHz for the MWCNT thin films are plotted versus thickness

in Figure 44c, and can be compared with the values for the SWCNT thin films. The RF reflectance and transmittance trends with thickness for the SWCNT and MWCNT thin films are in family, indicating that the free-standing MWCNT thin films can also act as functional shielding materials.

9.4 Shielding Effectiveness of Free-Standing SWCNT and MWCNT Thin Films

Shielding effectiveness has been previously used as the figure of merit for assessing the RF shielding capabilities of CNT thin films [83], [104], [105], [107]. The shielding effectiveness of the free-standing SWCNT and MWCNT thin films fabricated in the present work was calculated from the measured RF reflectance and transmittance. Shielding effectiveness is conventionally taken as the sum of reflection, absorption, and multiple internal reflection (MIR) components. The MIR shielding effectiveness component was assumed to be negligible as the absorption component is ≥10 dB for the large majority of samples measured (see Table 8) [145]. Thus, the shielding effectiveness was calculated as the sum of the reflective and absorptive components in accordance with Equations (5.2-11) to (5.2-13) as described in Section 5.2.2. The shielding effectiveness of the SWCNT and MWCNT thin films are plotted versus frequency in Figure 46a and 46b, respectively. Due to the smaller thickness of the MWCNT films compared to their SWCNT counterparts at equivalent starting CNT mass, the shielding effectiveness of the MWCNT films is lower. Furthermore, this lower shielding effectiveness may be attributed to only the outer walls of each MWCNT contributing to the shielding effect, in agreement with the results of previous AC electrical characterization performed on isolated MWCNTs [78]. When the shielding effectiveness at 12 GHz is plotted versus film thickness as shown in Figure 46c, the trends for MWCNT (solid blue squares) and SWCNT (solid red circles) thin films are in family with one another, and demonstrate greater shielding effectiveness with increasing thickness.

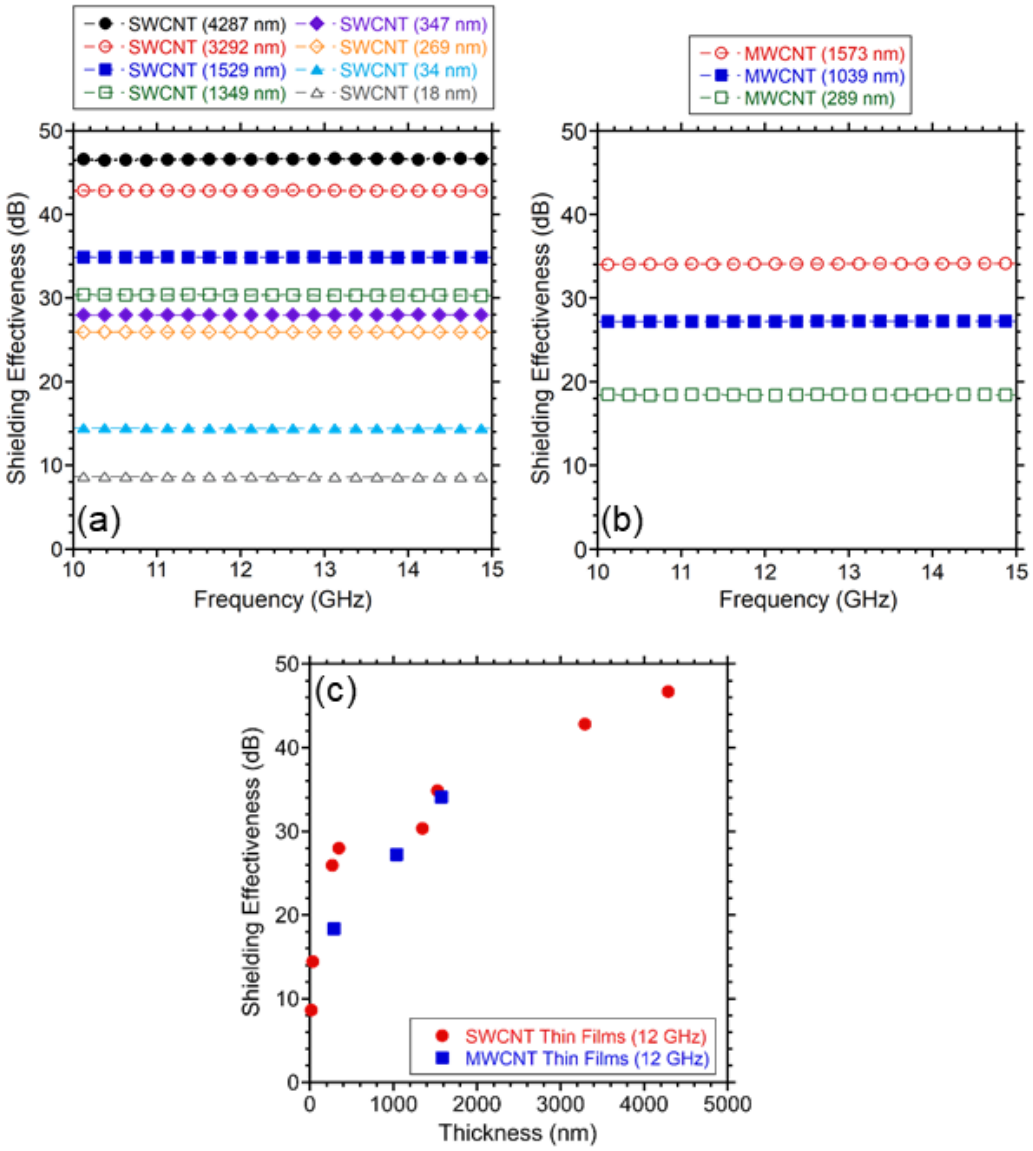

Figure 46. (a) Shielding effectiveness as a function of frequency for the (a) SWCNT and (b) MWCNT thin films from 10 GHz to 15 GHz. (c) The shielding effectiveness of the SWCNT and MWCNT thin films taken at 12 GHz versus film thickness.

9.5 Comparison to Surveyed Shielding Materials

The EMI shielding effectiveness measurements presented herein represent a new development in the characterization of free-standing SWCNT and MWCNT thin films. To better understand the developments of the present study in the broader field of thin RF shielding materials, these measured values were compared directly to published results on the shielding effectiveness of SWCNT/MWCNT and graphene films, non-CNT/graphene carbon materials, metal foils, transition metal

carbides/carbonitrides (MXenes), and ITO. MXenes possess electrical conductivity on par with the CNT films studied in the present work and are a promising option for conformal, flexible shielding materials [146], while ITO represents the state of the art for transparent shielding materials [135], [136]. To benefit this comparison, all shielding effectiveness values from the present work and referenced publications were normalized to the volume density and thickness of the films, resulting in a specific shielding effectiveness/thickness (SSE/t). The SSE/t values for the present and referenced shielding materials versus film thickness are represented by a scatter plot in Figure 47. A summary of the materials and values used to produce this plot, as well as their respective sources, is presented in Appendix A, Table 9.

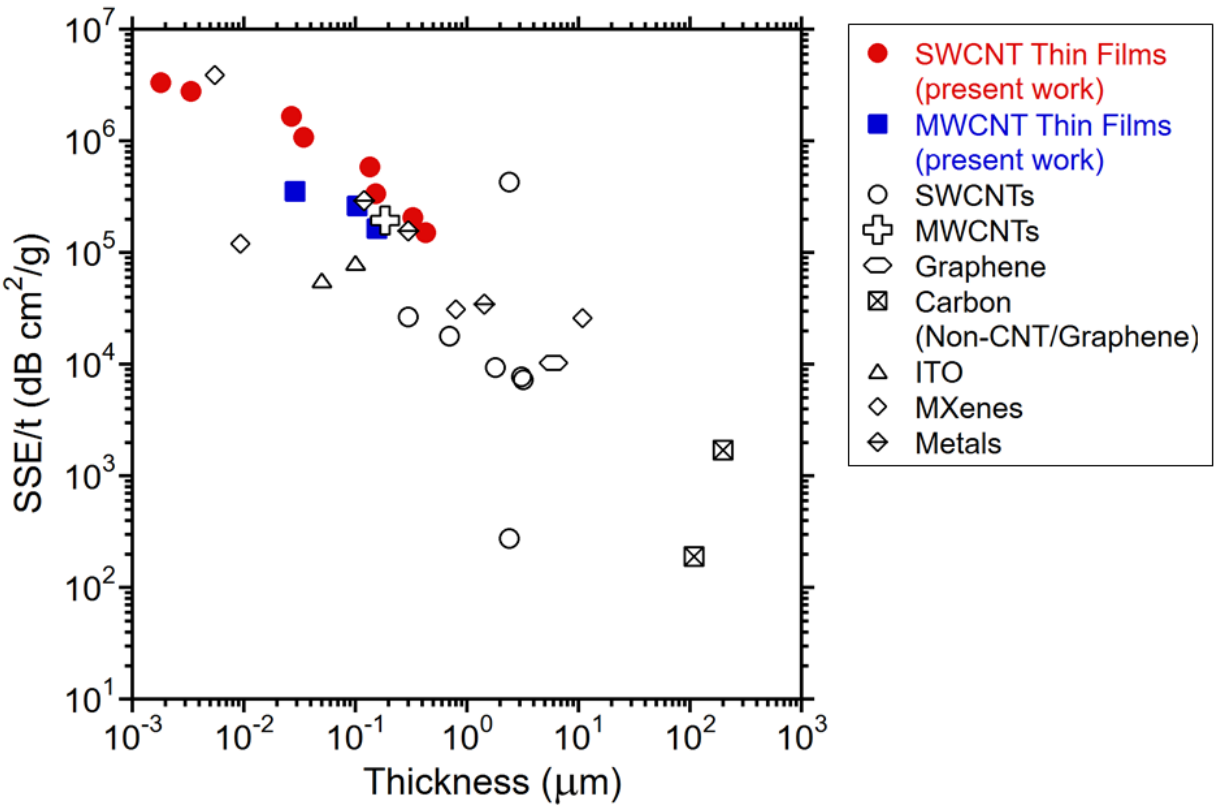

Figure 47. Scatter plot of thickness-normalized specific shielding effectiveness (SSE/t) versus thickness for samples over a range of 1-18 GHz (with specific values provided in Table 9) to compare the presently studied SWCNT and MWCNT thin films with surveyed CNT, graphene, non-CNT/graphene carbon, indium tin oxide (ITO), transition metal carbides/carbonitrides (MXenes), and metal shielding materials.

The collection of materials surveyed for comparison encompasses a wide range of film thicknesses and conductivities, leading to a variety of shielding effectiveness values. As the specific SE is normalized to the thickness of the film, there is a strong linear relation between the two values, with the thinnest films having the highest SSE/t as shown in Figure 47. The SWCNT and MWCNT thin films studied in the present work (solid circles and squares, respectively) fall at the lower end of the thickness range (micro to sub-micron thickness). They are the thinnest CNT films among the surveyed samples, and are the first reported shielding effectiveness measurement of free-standing micron and submicron thickness CNT films. Worthy of note is that the presently studied SWCNT thin films outperform the other SWCNT materials surveyed (open circles), and the values for the MWCNT thin films in the present work agree with the surveyed MWCNT materials (open crosses).

The present SWCNT and MWCNT thin films also outperform the metal films (open diamonds with horizontal stroke) in the metric of SSE/t due to their much lower density, and have values in family with the MXenes (open diamonds). The present CNT films also have merit as transparent shielding materials with decreased material mass, possessing higher SSE/t than ITO (triangles) at a given thickness. In summary, the tunable optical properties of the presently studied CNT films along with their adaptability to various substrate shapes make them an attractive shielding material with the combined benefits of surface conformability, optical transparency, and high shielding effectiveness relative to their CNT mass content and thickness.

9.6 Demonstration of Bluetooth Signal Attenuation Using Free-Standing SWCNT Thin Films

A relevant practical application which utilizes RF signals for inter-device communication is Bluetooth, operating at a frequency of 2.4 GHz. A setup (shown in Figure 48a) consisting of a cell phone and a Bluetooth speaker placed ~4 m apart was used to demonstrate the capability of the free-standing CNT thin films to attenuate RF signals. To ensure that the cell phone could only transmit to the

speaker within line-of-sight, it was placed atop a ~3 mm thick aluminum plate and sealed inside of a box which was shielded using a layer of copper foil and three layers of aluminum tape. A 60 mm diameter circular hole was left open in the side of the box facing the Bluetooth speaker. As-produced, 35 mm diameter SWCNT thin films (500 mg/m^2 and 3000 mg/m^2) were suspended across 25 mm diameter holes in the center of annular copper/aluminum sample holders of 70 mm outer diameter; an identical holder was left uncovered. Additionally, a circular, solid copper/aluminum shield of 70 mm diameter was also prepared for comparison to the SWCNT thin film shields. Photographs of the three shields prepared for testing are shown in Figure 48b. Aluminum tape was used to secure the box and sample holders in place and seal any potential sources of leakage.

To perform the demonstration, the uncovered sample holder was placed onto the shielding box for a step of 20 s, and was subsequently replaced with one of the three tested shield samples for another 20 s step. This process was repeated until all three shield samples had been tested. The transmitted power in dB over time was measured using a Bluetooth performance tracking mobile application to compare the results with and without each of the shields placed over the 25 mm hole. Simultaneously, music was played through the Bluetooth speaker to observe the effect of attenuation on the speaker's reception. As shown in Figure 48c, the copper/aluminum shield (solid black line) attenuated the Bluetooth signal to a level of −20 dB over the signal strength which passed through the open sample holder. All of the CNT shield samples attenuated the Bluetooth signal to a similar level to the metal shield, causing the speaker to disconnect from the phone. Shortly after each shield had been placed over the hole in the box, the music playing over the Bluetooth speaker broke up into static. Overall, this demonstration showed that CNT thin films are functional EMI shielding materials that can perform competitively with conventional metal shields.

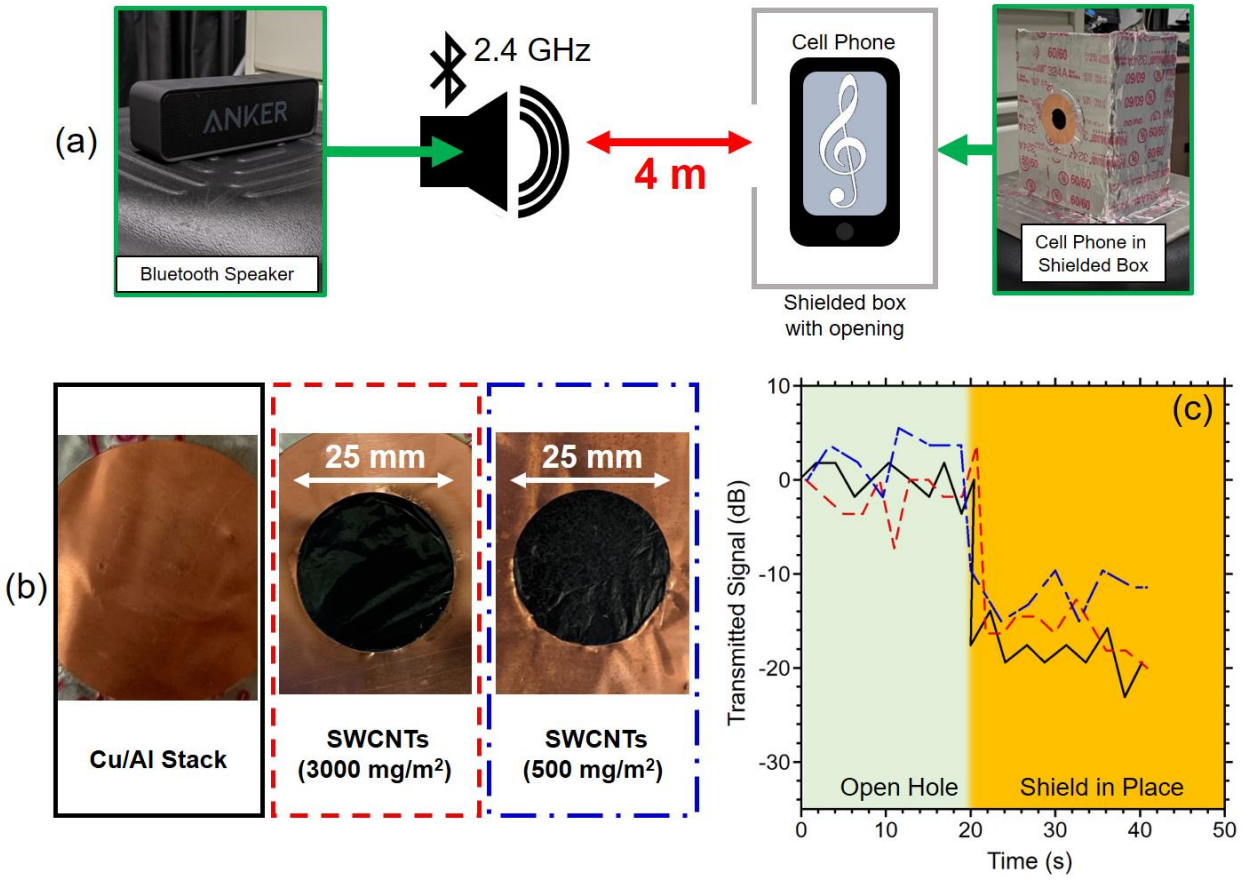

Figure 48. (a) The layout of components used to perform the Bluetooth signal attenuation demonstration with free-standing SWCNT thin films. (b) Photos of the copper/aluminum shield and the two SWCNT thin film shields used for the demonstration. (c) The transmitted signal over time showing the attenuation of the Bluetooth signal before and after each shield is placed in its path (color and dashed lines correspond to the border of each photo in (b)).

9.7 Outcomes

Free-standing SWCNT and MWCNT thin films have been successfully fabricated on copper foil frames. The RF reflectance, RF transmittance, and shielding effectiveness of the SWCNT and MWCNT thin films were measured using a rectangular waveguide setup from 10 GHz to 15 GHz, marking the first RF characterization of CNT thin films in the absence of any substrate or backing structure. Increasing RF reflectance was observed with increasing SWCNT film thickness, accompanied by a decrease in optical transmittance. An RF reflectance of 60% was maintained with optical transmittance

≥50%, demonstrating the merit of the free-standing CNT thin films as transparent conductors. The EMI shielding effectiveness of the CNT thin films was then calculated from the measured RF reflectance and transmittance. The CNT thin films exhibited shielding effectiveness in the range of 10 to 50 dB and increased with film thickness, independent of SWCNT or MWCNT type. These shielding effectiveness results were consistent with previous measurements of substrate mounted CNT thin films. The present CNT thin films were then compared with other previously studied shielding materials based on their specific shielding effectiveness, normalized to the film thickness. This comparison indicated that the present CNT thin films possessed near the highest shielding effectiveness relative to their density and thickness among the collection of surveyed materials. In particular, the present CNT thin films distinguished themselves as having superior specific shielding effectiveness/thickness to state-of-the-art transparent ITO films and highly conformal transition metal carbide films. This makes them valuable as alternative shielding materials in flexible, wearable electronics, aerospace, or any other applications in which transparency, conformability, and low weight are required.

10 Dissertation Conclusions and Impact

This dissertation explored the effects of strategies to modify the inter-tube junction properties in bulk CNT materials on their AC electrical conductivity, which was characterized from 10 GHz to 40 GHz using a rectangular waveguide measurement system that was designed and implemented for use in this work. In particular, sample processing methods such as purification, $KAuBr_4$ doping, and platinum nano-metal deposition were applied to a commercial MWCNT sheet material in order to explore their effects on the AC conductivity. The MWCNT samples were interrogated via four-point probe measurements, TGA, Raman spectroscopy, and SEM/EDXS analysis to determine the effect of processing on their DC electrical properties, structural quality, surface morphology, and composition. Laser- and solvent-based techniques were employed to produce MWCNT samples of various thicknesses so that the effect on AC conductivity measurements could be explored. The experimental efforts were buttressed by application of theoretical AC conductivity modeling to inform hypotheses regarding the mechanisms behind the observed responses due to material processing. Finally, the EMI shielding capabilities of the CNT materials in a free-standing thin film format were explored to provide a demonstration of their multi-functional optical and mechanical properties in tandem with their advantageous characteristics in the RF field. The outcomes of each chapter are summarized in the following paragraphs, culminating in an outline of the dissertation impacts.

Chapter 5 assessed the four most prominent AC conductivity characterization methods in the existing literature based on the criteria of probe consistency, sample dimensional requirements, sample mounting requirements, and operable frequency range within the available capability (100 kHz – 44 GHz) offered by the Keysight P9377b vector network analyzer utilized for this work. The microstrip line method was the first method considered, and was rejected based on the inconsistency of contact geometry with the CNT samples and the frequency limitations arising from radiation losses and

geometric effects. The free space method was removed from consideration based on its sample dimensional requirements, which were too large to enable its use with metal-CNT hybrids (size limited due to the CVD reactor dimensions). Between the remaining two candidates, the rectangular waveguide method was selected due to the simplicity of sample preparation and mounting compared with the gold contact geometry needed for the coaxial probe method, though both methods were acceptable in terms of their sample dimensional requirements, frequency capabilities, and probe consistency. The rectangular waveguide method was successfully implemented and established the capability to perform consistent measurements of AC conductivity, RF reflectance/transmittance, and shielding effectiveness. Three sets of rectangular waveguides with the required specifications to measure these properties between 10 GHz and 40 GHz were obtained. A standardized method was established including a TRL calibration to subtract waveguide and VNA component effects from the measured S-parameters and also utilizing calculation algorithms to obtain the aforementioned material properties from said measurements. Preliminary testing was performed on the commercial MWCNT sheet, in which it was determined that the effects of sample dimensions and time drift on the AC conductivity measurement were negligible.

In Chapter 6, acid treatment and thermal oxidation-based purification of the MWCNT sheet was performed to remove iron catalyst impurities and investigate the effect of different purification process steps on the measured real part of AC conductivity. Specifically, the MWCNT sheet was measured in its as-received state, as well as after a 30 min acid treatment in concentrated HCl, after thermal oxidation to 500°C, and after the complete purification process combining both steps. TGA and SEM/EDXS analysis demonstrated that HCl treatment and thermal oxidation did not affect the ~43% w/w starting iron content of the as-received MWCNT material, though significant oxide formation after thermal oxidation was observed. The complete purification process greatly reduced the iron content, consistent with previously published work. The real AC conductivity of the MWCNT sheet in each of the tested states

matched the DC values near 10 GHz, but exhibited different responses with increasing frequency which were attributed to the varying iron content reduction after different purification steps. The iron catalyst, with its high magnetic permeability, was hypothesized to contribute to the decreasing AC conductivity with frequency of the as-received MWCNT material. The lack of iron removal by the HCl treatment step alone led to a similar response, but the initial value was enhanced by the known acid doping effect. Most importantly, oxidation or removal of the iron catalyst by thermal oxidation or the complete purification resulted in quenching and complete elimination of the decreasing trend, respectively, demonstrating that purification plays a key role in avoiding the detrimental effect of the iron catalyst on AC conductivity of the MWCNT sheet.

Chapter 7 demonstrated the successful preparation of ribbon-form platinum-MWCNT hybrid samples through Joule heating-driven CVD onto the purified MWCNT sheet. Weight loadings ranging from ~56% w/w to ~80% w/w were achieved, and surface morphology analysis via SEM demonstrated Pt overcoating of the MWCNT network consistent with previous reports using MWCNT roving material. It was determined through DC electrical characterization that conductivity enhancement occurred at a threshold lying between 70 and 80% w/w. The measured real AC conductivity of the 80% w/w Pt-MWCNT sample exhibited a 1.4× improvement over the starting material, showing that platinum nano-metal overcoating via Joule-heating driven CVD is also an effective strategy to enhance the AC conductivity of CNT materials.

Chapter 8 utilized the generalized Drude conduction theory to inform hypotheses regarding the mechanisms producing the AC conductivity responses of $KAuBr_4$-doped MWCNT sheets and Pt-MWCNT hybrids discussed in Chapters 6 and 7. The model equation was fitted by least-squares minimization to the real and imaginary parts of the measured AC conductivity for these samples as well as their purified MWCNT base materials. Elevated plasma frequency of the modified material relative to

the starting material was demonstrated by the fitting parameters in both cases, suggesting that both $KAuBr_4$ doping and platinum inclusion enhance the AC conductivity by increasing the material's carrier density. The lesser enhancement in AC conductivity by Pt inclusion was attributed to a competing reduction in carrier mobility of the Pt-MWCNT sample indicated by decreasing relaxation time. Moreover, the fitted backscatter parameters for all analyzed samples were indicative of high degrees of backscattering, in agreement with the capacitive response of the imaginary part of AC conductivity. Extrapolation of the model up to 100 GHz was performed for all samples, and showed the potential for the real part of AC conductivity to increase with frequency above the experimentally measured range.

In Chapter 9, the practical application of bulk CNTs as shielding materials was demonstrated from 10 GHz to 15 GHz, utilizing a thin film form factor to leverage their multi-functional properties of optical transparency, surface conformability, and favorable DC and AC electrical properties. The shielding effectiveness of SWCNT and MWCNT thin films was directly compared, and showed that both types of CNTs are effective shielding materials, consistent with previous work. MWCNT films of equivalent CNT mass had lower shielding effectiveness despite their higher density relative to their SWCNT counterparts, suggesting that only the outer layers of the MWCNTs interact with the incident electromagnetic radiation. A comparison was then made to surveyed CNT and non-CNT shielding materials from previous literature, demonstrating that the currently investigated CNT thin films are among the thinnest studied to date and exhibit exceptional shielding effectiveness relative to their thickness and density in the current state of the field. Finally, the utility of the CNT thin film shields was demonstrated through the attenuation of signal between a cell phone and a Bluetooth device.

Overall, this work has shown the capability to consistently measure the AC electrical properties of bulk CNT conductors in a sheet form factor over a broad frequency range of 10 GHz to 40 GHz using rectangular waveguides. This dissertation validated the effectiveness of $KAuBr_4$ dopant or conformal Pt

coatings to enhance the AC electrical conductivity of an MWCNT conductor through increased carrier density. These proven strategies address the challenges posed by inter-CNT junction resistance in bulk CNT materials to their application as RF conductors and advance their potential as an alternative to conventional metals. Furthermore, the necessity of iron impurity removal to promote a more pristine MWCNT network surface morphology in order to take advantage of the CNTs' favorable AC electrical properties was elucidated. A practical perspective on these advancements to the field of CNT AC conductors was then given through their demonstration as EMI shielding materials in a thin film form factor, which leveraged their low density, high optical transparency, surface conformability, and favorable AC conductive properties in tandem. Future developments to the body of knowledge surrounding CNTs in RF applications could benefit from investigation into how the AC electrical properties of doped or metallized CNT conductors respond at even higher frequencies. Additionally, determining the effects of inter-CNT void spaces on the AC conductivity response could inform the application of bulk CNT materials as RF conductors in different form factors that necessitate changes to the CNT network density, such as the central wire of a coaxial cable. Ultimately, the successful demonstration of enhanced AC conductivity in $KAuBr_4$-doped MWCNT conductors and Pt-MWCNT hybrid conductors has provided a significant contribution to the growing field of CNT RF electronics.

11 Appendix A: Supplemental Data

Data sets included here are supplemental to the results discussed in Chapters 6 and 9 and should be referred to in assistance to the reader's understanding of those chapters; they do not necessarily form a cohesive story by themselves.

11.1 Supplemental data to study of purification/$KAuBr_4$-doped MWCNT sheet AC conductivity

The following is reprinted with permission from (Boyd, S. J. et al., Chemically doped, purified bulk multi-walled carbon nanotube conductors with enhanced AC conductivity to 40 GHz, *Carbon* 226 (2024): 119209). Copyright (2024) Elsevier https://doi.org/10.1016/j.carbon.2024.119209

The Raman spectra of the as-received and purified MWCNT sheet material used in this study are shown in Figure 49a, with the respective peak locations and intensity ratios provided in Figure 49b-c. Three peaks are expected to occur in the Raman spectra of MWCNT materials, which are all present in the measured spectra of the as-received and purified MWCNT sheets. The G-band peak (~1580 cm^{-1}) arises from the pristine graphitic bonding structure of the MWCNTs, while the intensity of the D-band peak (~1350 cm^{-1}) increases with the amount of defects in said bonding structure. Lastly, the G'-band peak (~2700 cm^{-1}) is a result of long range, double-phonon scattering [113].

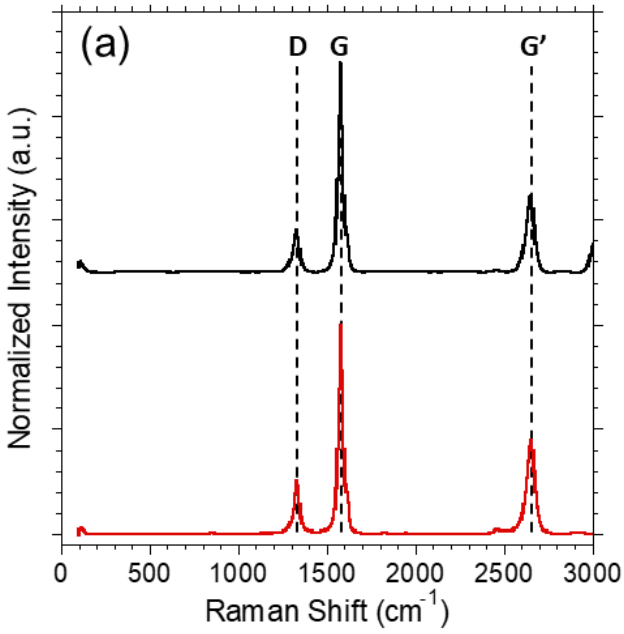

(b)

	D	G	G'
Abs. Intensity (counts)	1841±627	9084±552	3320±818
Peak Location (cm^{-1})	1329±1.12	1579±0.829	2650±2.18
	D/G	G'/G	D/G'
	0.204±0.0712	0.405±0.174	0.554±0.141

(c)

	D	G	G'
Abs. Intensity (counts)	2225±668	8693±826	3881±619
Peak Location (cm^{-1})	1332±0.517	1580±0.907	2654±1.76
	D/G	G'/G	D/G'
	0.256±0.0706	0.447±0.0664	0.578±0.158

Figure 49. (a) Raman spectra and peak location/intensity as well as peak locations and intensity ratios for (b) the as-received MWCNT sheet and (c) the purified MWCNT sheet. The spectra and associated peak locations/intensity ratios are the average of 10 spots taken across the area of the MWCNT samples.

Thermogravimetric analysis (TGA) plots of the as-received, HCl treated, thermally oxidized, and purified MWCNT sheets are presented in Figure 50a. The residual catalyst amounts shown in Figure 50b were determined by finding the minimum of the dataset, as the metal is the only constituent of the material not expected to decompose or evaporate in the temperature range scanned. It should be noted that since the TGA experiments were carried out in air, the percentages shown represent quantities of iron oxide and the true metallic iron content is likely smaller to some degree. Determination of the exact amount is outside the scope of this work.

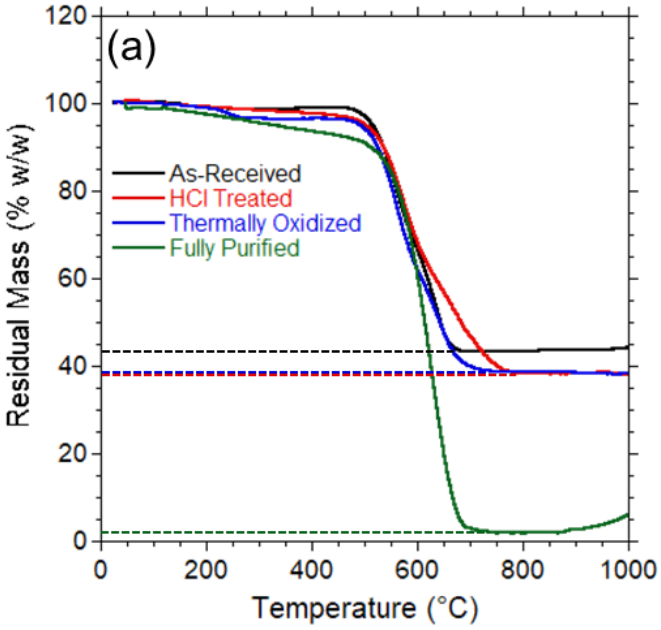

(b)

Material Type	Residual Catalyst
As-Received	43.2%
HCl Treated	37.9%
Thermally Oxidized	38.1%
Fully Purified	1.4%

Figure 50. (a) TGA residual mass plots of the as-received, HCl treated, thermally oxidized, and fully purified MWCNT sheet. The dotted lines show the approximate level considered to be the residual catalyst amount for each material. (b) The residual catalyst % w/w for each material treatment.

Energy-dispersive X-ray (EDX) spectra of all MWCNT materials measured in this work are presented in Figure 51a-b. Elemental maps of carbon (C), iron (Fe), bromine (Br), and gold (Au) in the purified, laser thinned, $KAuBr_4$-doped MWCNT sheet are presented in Figure 51c. Acquisition of the EDX spectra and elemental maps shown was performed using Quantax ESPRIT analysis software.

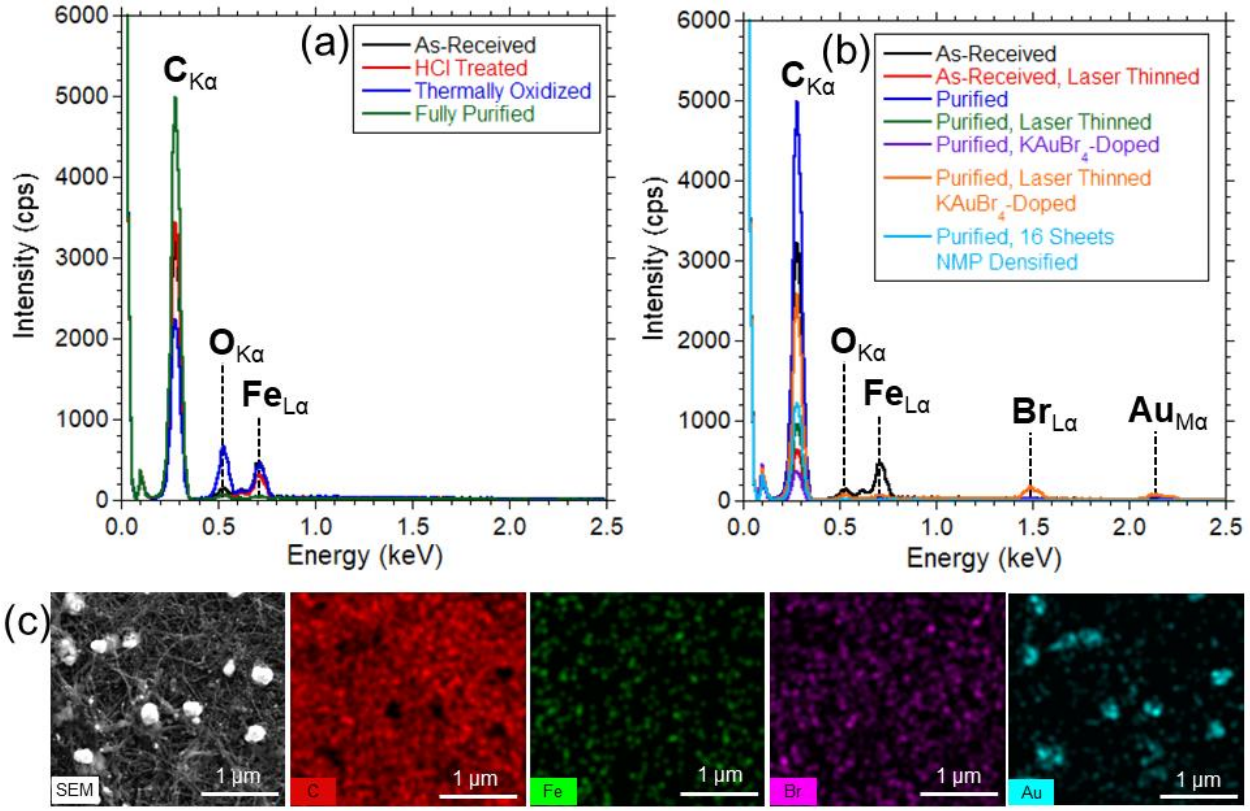

Figure 51. (a) EDX spectra for the MWCNT sheet with different purification steps. (b) EDX spectra for the as-received and purified MWCNT sheet with and without laser thinning and $KAuBr_4$ doping, as well as the NMP incorporated purified MWCNT sheet. (c) EDX elemental maps showing the distributions of C, Fe, Br, and Au in the purified, laser-thinned, $KAuBr_4$-doped material.

Table 7 contains specifications for the waveguide parts which were purchased from Pasternack for this work.

Table 7. Operating frequency ranges, cutoff frequencies, and part information of the rectangular waveguides used.

Rectangular Waveguide	Operating Frequency Range	Cutoff Frequency*	Waveguide Section Pasternack Part ID	Coaxial Adapter Pasternack Part ID
WR-75	10 GHz – 15 GHz	7.869 GHz	PE-W75S001-3	PEWCA1004
WR-42	18 GHz – 26.5 GHz	14.051 GHz	PE-W42S002-3	PEWCA1018
WR-28	26.5 GHz – 40 GHz	21.077 GHz	PEW28S010-3	PEWCA1000

*Cutoff frequency values[6] were verified based on the internal dimensions of the waveguides.

[6] "Waveguide Sizes | Dimensions & Cutoff Frequency - everything RF." Accessed: Dec. 20, 2023. [Online]. Available: https://www.everythingrf.com/tech-resources/waveguides-sizes

Chapter 11 – Appendix A: Supplemental Data

The S-parameter data comparing the different purification process step effects on the MWCNT sheets are presented in Figure 52. The S-parameter magnitude is reported in units of dB, representing the number of decades by which the received power compares to the incident power. Thus, a more negative S_{21} magnitude represents a lower transmission amount. The curve of the magnitude data in each frequency band is due to the changing wave impedance in the waveguide, which follows a similar trend as it asymptotically approaches the impedance of free space. As seen in Figure 52 and comparing with values reported in Table 4, the HCl-treated material (red) is the most conductive and has the lowest transmission, and the less conductive as-received sheet transmits slightly more. The materials with the highest transmission are the thermally oxidized (blue) and purified material (green), which have nearly identical transmission; their conductivities and thicknesses are also nominally equal within experimental error. The phase delay is consistent with expectations for these properties.

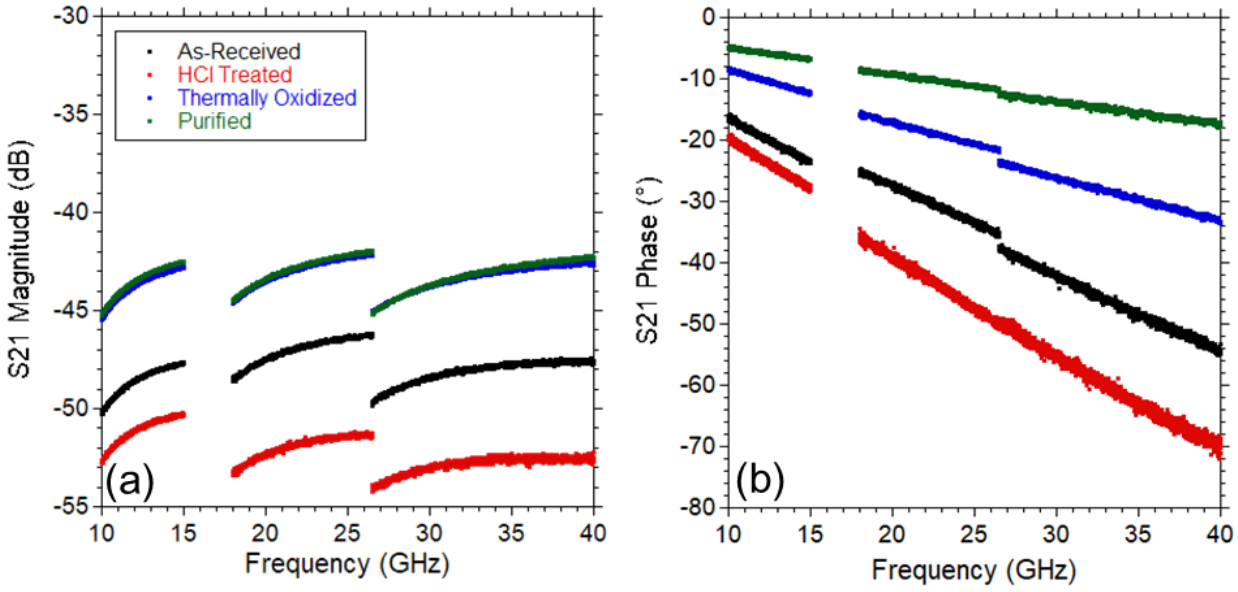

Figure 52. (a) S_{21} magnitude and (b) S_{21} phase from 10 to 40 GHz for the MWCNT sheet after different purification steps.

Chapter 11 – Appendix A: Supplemental Data

The S-parameter data comparing sample thickness and $KAuBr_4$ doping of the MWCNT sheets are presented in Figure 53. As with the data shown in Figure 52 and Table 4, the data shown in Figure 53 and Table 5 are consistent from a thickness/DC conductivity standpoint to the amount of transmitted signal indicated by the S_{21} magnitude. Laser thinning accordingly increases the transmission of the as-received (compare black to red), purified (compare blue to green), and purified/$KAuBr_4$-doped (compare purple to orange) materials. For the NMP plied MWCNT sheet (sky blue), the magnitude of the transmitted signal is eight decades smaller than that of the incident signal. This is feasible due to the large thickness of the material. A strong indication that the transmitted signal for this material is approaching or below the noise floor of the instrument is the disappearance of the typical curve shape in the S_{21} magnitude as well as the incoherent phase angle.

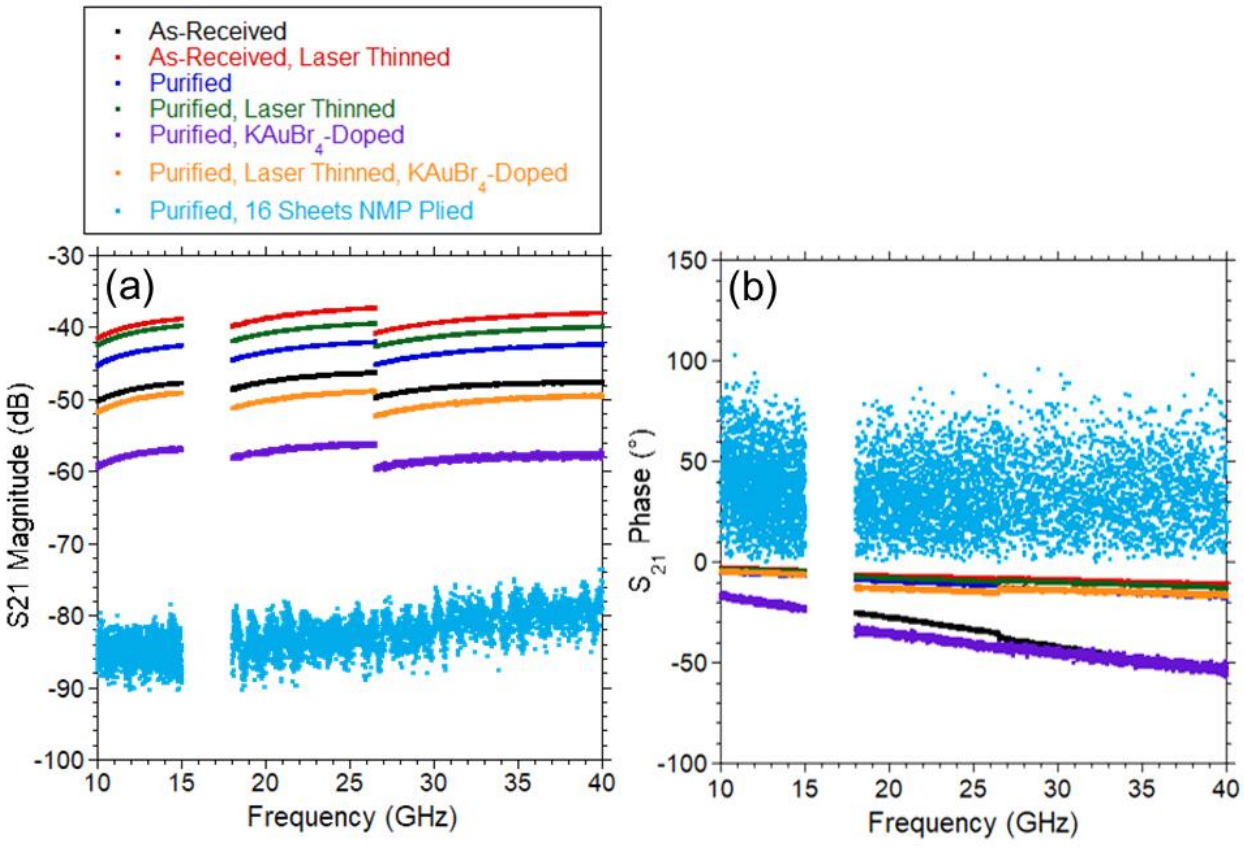

Figure 53. (a) S_{21} magnitude and (b) S_{21} phase from 10 to 40 GHz for the as-received and purified MWCNT sheet with and without laser thinning and $KAuBr_4$ doping, as well as the thicker NMP plied, purified MWCNT sheet.

Chapter 11 – Appendix A: Supplemental Data

The generalized Drude model curves for the real part of AC conductivity purified MWCNT sheet before and after treatment by $KAuBr_4$ doping or CVD of platinum were normalized to their value at 0 Hz to compare the amount of increase observed when the model was extrapolated to 100 GHz. The resulting normalized curves are presented in Figure 54. The values of AC conductivity at 100 GHz are 7% and 12% greater than the 0 Hz value for the purified MWCNT sheet with and without $KAuBr_4$ doping, respectively. The values of AC conductivity at 100 GHz are 9% and 12% greater than the 0 Hz value for

the purified MWCNT sheet with and without CVD of platinum, respectively.

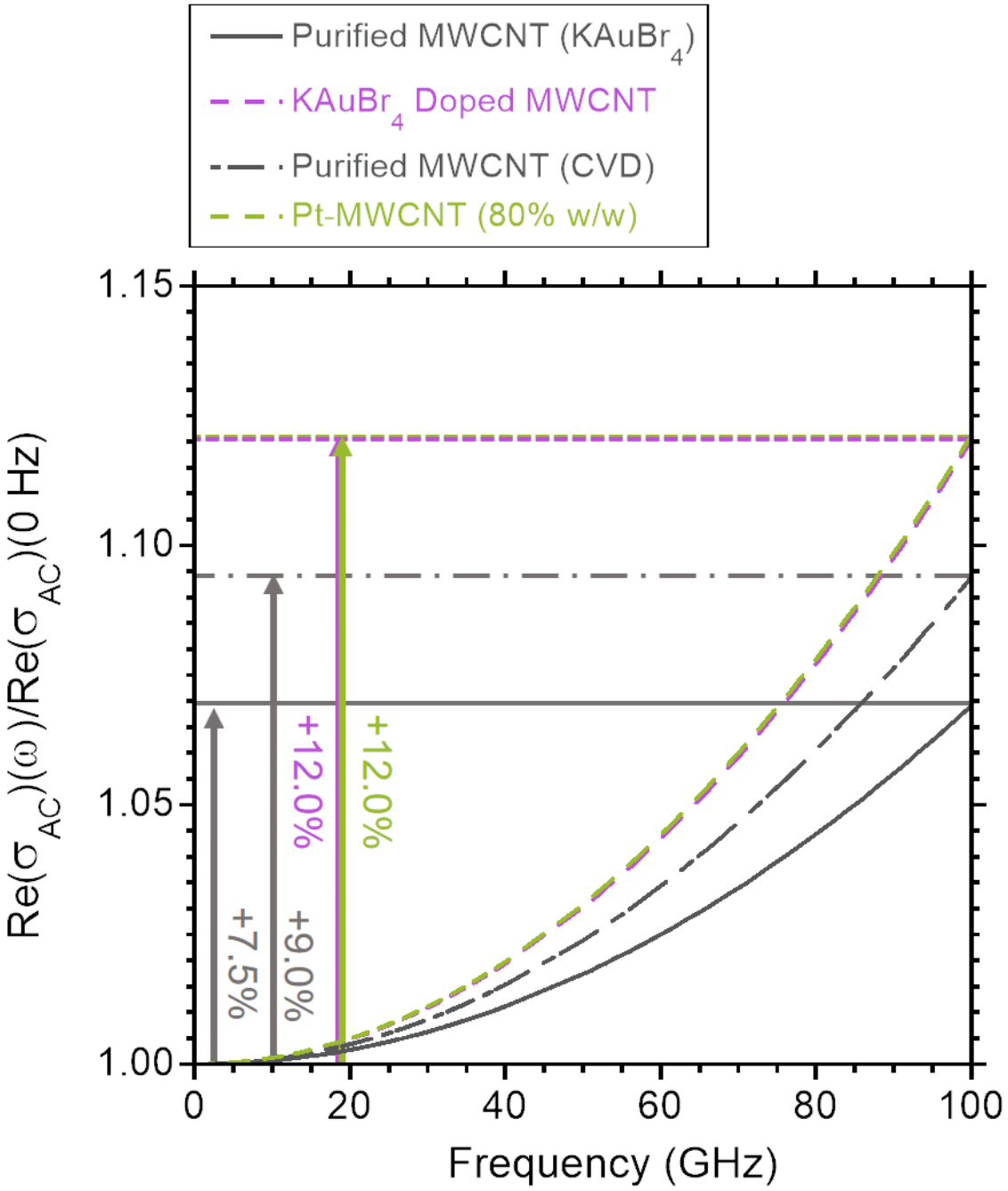

Figure 54. Real part of AC conductivity normalized to the 0 Hz value from 0 to 100 GHz for the purified MWCNT materials before and after modification by $KAuBr_4$ doping or CVD to create a Pt-MWCNT hybrid with 80% w/w Pt.**,**

11.2 Supplemental data to study of SWCNT/MWCNT thin film shielding effectiveness

Figure 55a shows the process used to mount the CNT thin films onto the copper frames by lifting the film diagonally off the surface of the DI water bath in a drawing motion. The dimensions of the rectangular opening were 9 mm × 19 mm to match the WR-75 rectangular waveguide, while the outer dimensions of the copper sheet were arbitrary as long as they were large enough to fit the semicircular CNT film section. In this study, a 3 cm × 4 cm sheet was used for each sample, which was then trimmed using scissors to a ~3 mm border surrounding the opening. The framed CNT thin film samples were then aligned with the rectangular waveguide opening and secured between two waveguide shims as shown in Figure 55b for RF characterization.

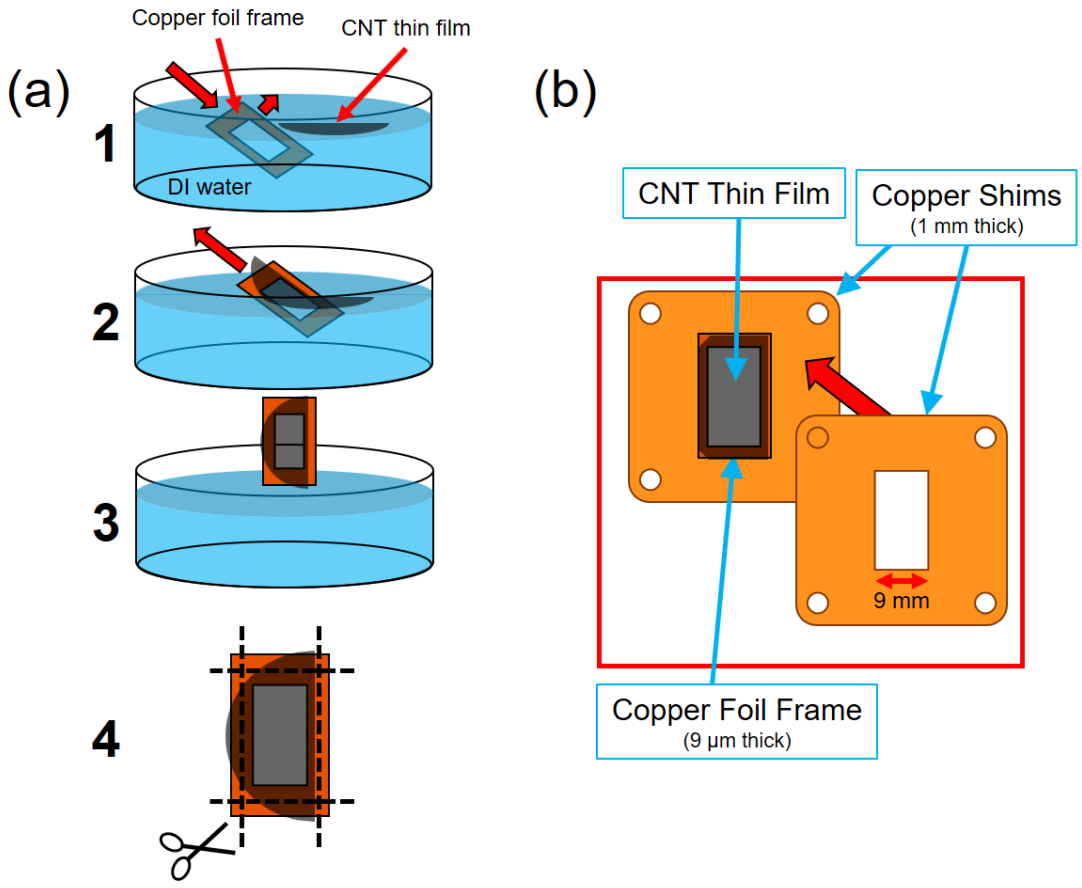

Figure 55. (a) Schematic representation of the procedure used to draw the floating CNT thin film samples from a DI water bath onto the copper foil frames used for RF characterization. (b) Diagram of the mounting strategy for the CNT thin films using a copper foil frame in between two 1.0 mm thick copper waveguide shims.

Chapter 11 – Appendix A: Supplemental Data

Optical profilometry was used to measure the thickness of the SWCNT and MWCNT thin film samples which were mounted on glass slides. Thickness measurement required a clearly defined step into the CNT material region to be created. This was done by masking a portion of the slide before transferring the CNT thin film on top and drying the sample; the tape was subsequently removed, leaving behind a straight edge of CNT material. Three line scans were obtained from optical profilometry measurements of this step for each SWCNT and MWCNT sample, and plotted as shown in Figure 56. The surface z-values of the glass slide and the CNT film (denoted as pre- and post-step, respectively), were determined by taking the average of only the values that were within one standard deviation calculated from all values in that respective region of the data. This eliminated clear outliers represented by the sharp spikes in Figure 56. The film thickness (average ± standard deviation) was calculated from the differences between the post-step and pre-step z-values for each line scan. Film thicknesses for the SWCNT (solid black circles) and MWCNT thin films (solid blue triangles) are plotted versus areal density in Figure 57. The thicknesses of both the SWCNT and MWCNT thin films decreased with decreasing areal density. In particular, this trend experienced a sharp step down between 500 mg/m^2 and 250 mg/m^2 for the SWCNT thin films.

The sheet resistances of the SWCNT and MWCNT thin films were measured using the van der Pauw method with a four-point probe station. I-V sweeps were performed using a maximum voltage of 10 V and maximum current of 50 mA. A 1 cm-diameter clover geometry produced by laser ablation of the surrounding film (Trotec SpeedMarker 700 30 W 1064 nm fiber laser, 20% power, 12000 mm/s, 100 kHz pulse frequency, 3 passes) was employed for sheet resistance measurements. Colloidal silver paint was used to create electrical contacts to each of the clover “petals”. The sheet resistances of the SWCNT (solid red squares) and MWCNT (solid green diamonds) thin films are plotted versus areal density in

Figure 57. Sheet resistance decreased asymptotically with increasing areal density for both CNT types, with higher sheet resistances for the MWCNT thin films below 1000 mg/m^2.

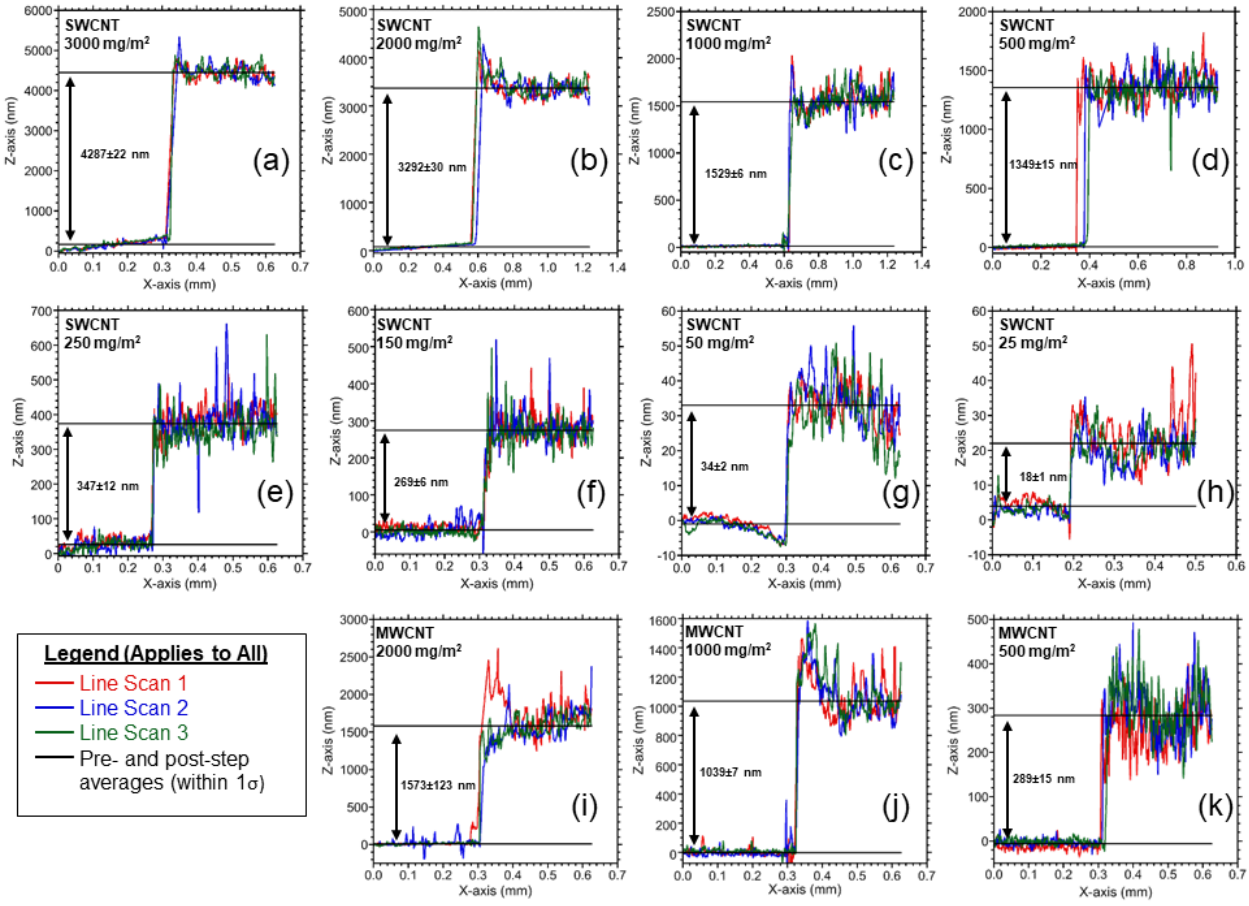

Figure 56. Optical profilometry thickness measurements of the SWCNT and MWCNT thin films mounted on glass slides. Three line scans are presented for each case: (a) SWCNT – 3000 mg/m^2, (b) SWCNT – 2000 mg/m^2, (c) SWCNT – 1000 mg/m^2, (d) SWCNT – 500 mg/m^2, (e) SWCNT – 250 mg/m^2, (f) SWCNT – 150 mg/m^2, (g) SWCNT – 50 mg/m^2, (h) SWCNT – 25 mg/m^2, (i) MWCNT – 2000 mg/m^2, (j) MWCNT – 1000 mg/m^2, (k) MWCNT – 500 mg/m^2.

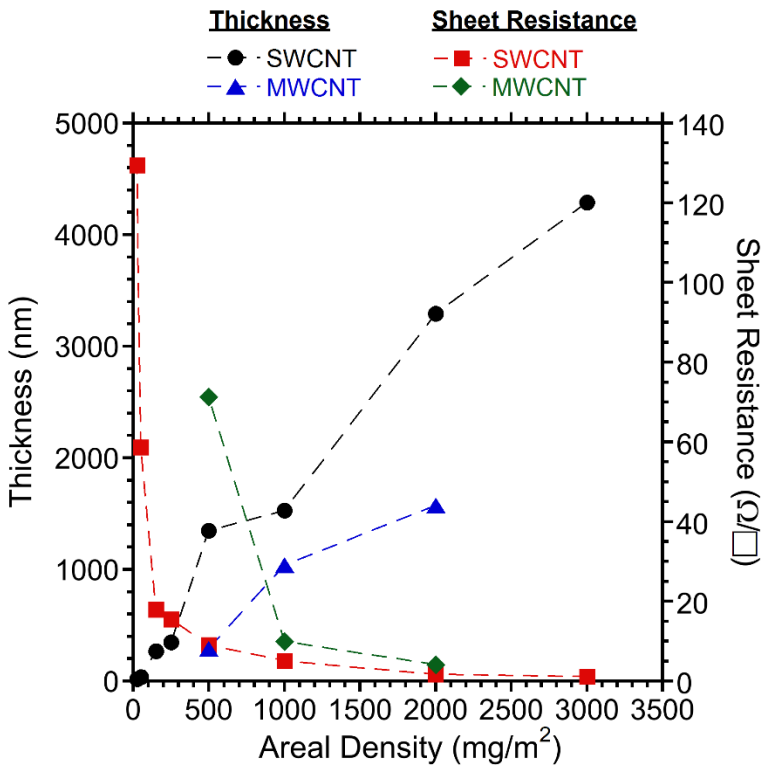

Figure 57. Relationship between thickness, sheet resistance, and areal density of the SWCNT and MWCNT thin films.

The volume density of the SWCNT and MWCNT thin films was calculated from the CNT mass, the radius of the as-produced thin film samples (17.5 mm) and the measured average thicknesses of the thin films. The DC electrical conductivity was calculated from the measured sheet resistances and thicknesses of the CNT thin films according to Equation (1.2-1). Additionally, the reflection and absorption components of the shielding effectiveness for each thin film preparation taken at a frequency of 12 GHz are tabulated for comparison. All of these measured and calculated values are summarized in Table 8.

Chapter 11 – Appendix A: Supplemental Data

Table 8. Areal density (ρ_A), thickness (t), volume density (ρ), sheet resistance (R_s), DC electrical conductivity (σ), and shielding effectiveness reflection (SE_R) and absorption (SE_A) components at 12 GHz of the free-standing SWCNT and MWCNT thin films.

Material	ρ_A (mg/m^2)	t (nm)	ρ (g/cm^3)	R_s ($\Omega/\square$)	σ (kS/m)	SE_R @ 12 GHz (dB)	SE_A @ 12 GHz (dB)
SWCNT	3000	4287±22	0.69	1.08	215.9±1.1	20	27
	2000	3292±30	0.61	1.69	179.7±1.6	19	24
	1000	1529±6	0.65	5.01	130.6±0.5	15	20
	500	1349±15	0.37	9.01	74.1±0.9	12	18
	250	347±12	0.72	15.5	185.8±6.4	11	17
	150	269±6	0.56	17.9	207.4±4.6	10	16
	50	34±2	1.49	58.6	507.2±28.3	5	10
	25	18±1	1.38	129.4	427.7±22.9	2	7
MWCNT	2000	1573±123	1.27	4.09	155.5±12.1	14	20
	1000	1039±7	0.96	9.89	97.4±0.7	11	17
	500	289±15	1.73	71.3	48.6±2.6	7	12

The microscale morphology of the SWCNT and MWCNT thin films was examined using SEM. Representative SEM images of each film are presented in Figure 58. As the film areal density of the SWCNT thin films decreases (Figure 58a-h) the apparent thickness of the sample also decreases, as indicated by the increasing transparency of the film showing the copper substrate underneath. Notably, between 500 and 250 mg/m^2, the bundles of SWCNTs decrease significantly in size. The sharp decrease in film thickness observed between these same CNT masses indicates a denser thin film through-plane. This suggests that the increasing density of the SWCNT films at this threshold leads to improved conductivity.

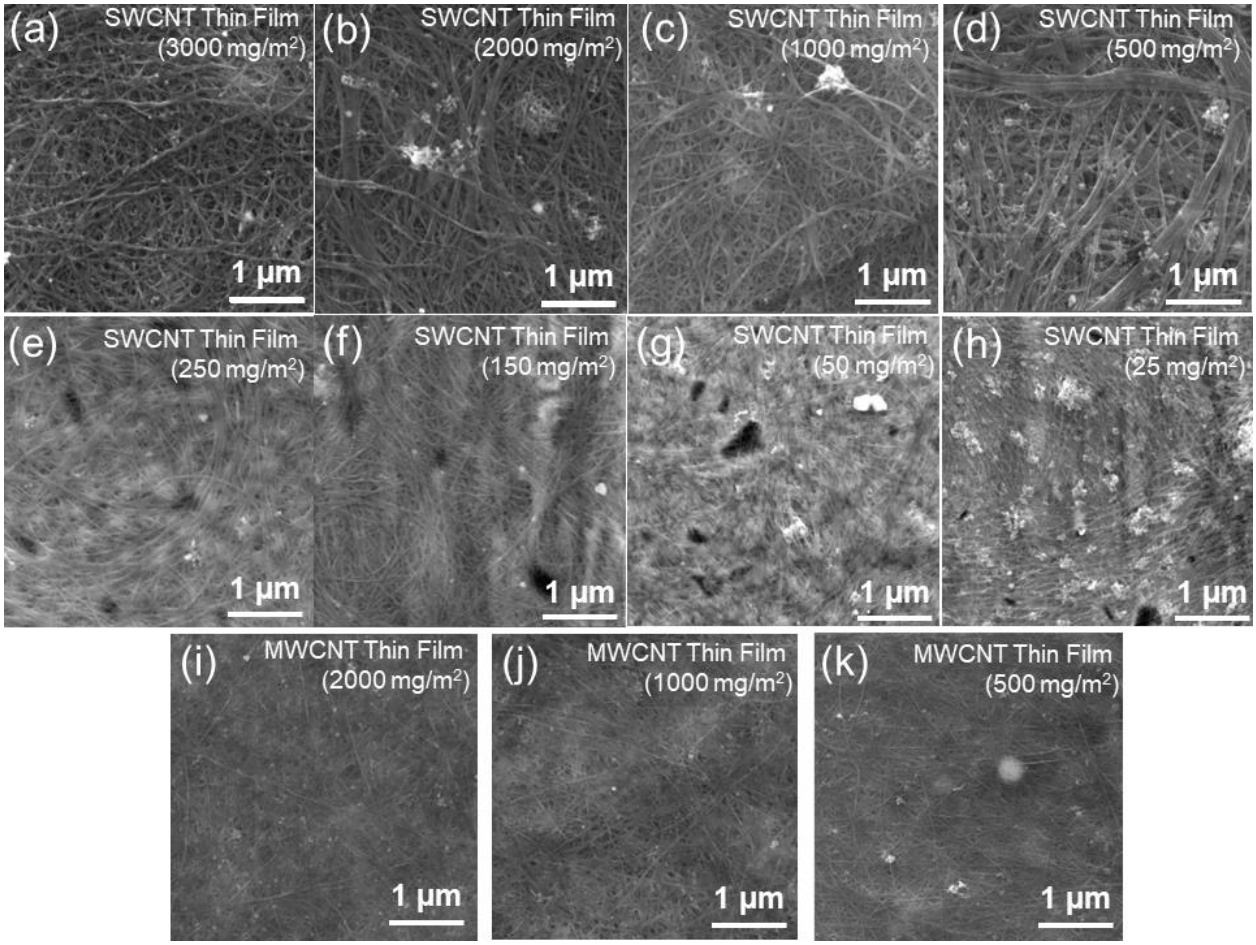

Figure 58. SEM micrographs of the SWCNT and MWCNT thin films mounted on copper foil. (a) SWCNT – 3000 mg/m^2, (b) SWCNT – 2000 mg/m^2, (c) SWCNT – 1000 mg/m^2, (d) SWCNT – 500 mg/m^2, (e) SWCNT – 250 mg/m^2, (f) SWCNT – 150 mg/m^2, (g) SWCNT – 50 mg/m^2, (h) SWCNT – 25 mg/m^2, (i) MWCNT – 2000 mg/m^2, (j) MWCNT – 1000 mg/m^2, (k) MWCNT – 500 mg/m^2.

The effect of film areal density/thickness on optical transparency of the SWCNT thin films was investigated using optical absorbance spectroscopy. This was not done for the MWCNT thin films as the characteristics of their optical absorbance spectra would not enable direct comparison of the absorbance at the electronic interband transitions [147]. To perform these measurements, the copper frames with attached free-standing SWCNT thin films were inserted into the thin film holder of the spectrometer as shown in Figure 59a. Optical absorbance spectra were collected in a photon energy range of 1.1 to 2.5 eV after a 1 A absorbance baseline correction, and are plotted in Figure 59b. The $^{S}E_{22}$ (~1.3 eV) and $^{M}E_{11}$ (~1.9 eV) peaks represent the interband transitions relating to the van Hove singularities in the

SWCNT electronic density of states. The $^{S}E_{22}$ and $^{M}E_{11}$ peaks correspond to semiconducting and metallic SWCNTs, respectively, and their presence indicates the SWCNT samples contain both electronic types of SWCNTs. The increase in optical absorbance, and therefore the decrease in optical transparency, is evident as the film thickness/areal density increases. Due to the high CNT mass/film thickness in the 2000 and 3000 mg/m^2 samples, the collected absorbance spectra for these samples contained significant noise. For purposes of optical transparency comparison, these spectra were taken to represent a 0% optical transmittance.

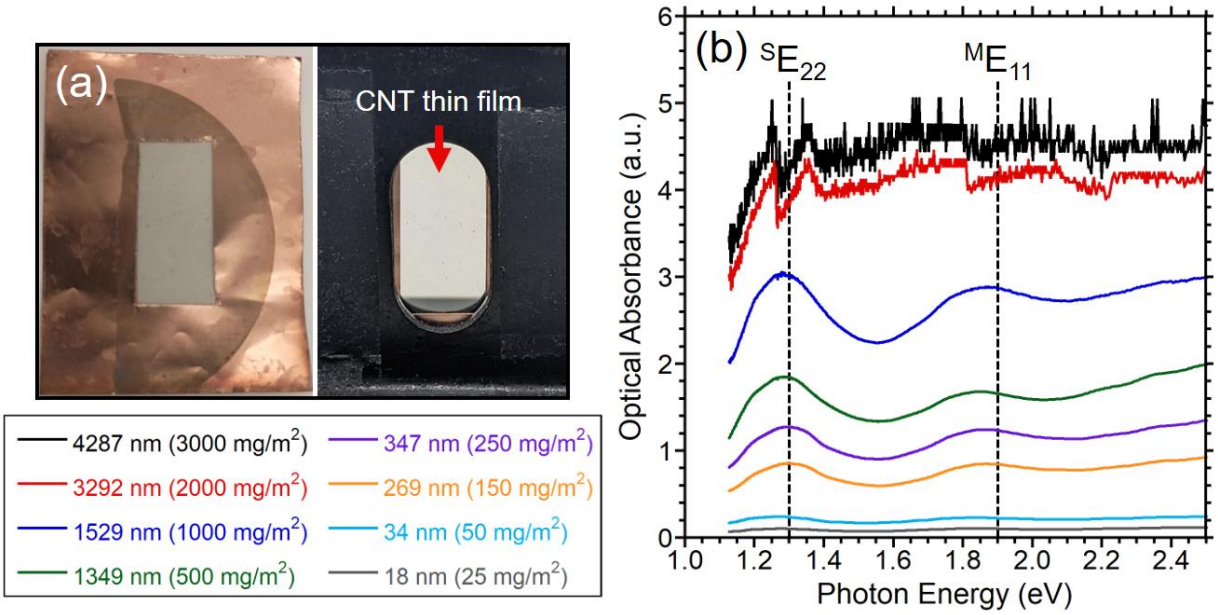

Figure 59. (a) A free-standing CNT thin film (25 mg/m^2) mounted on a copper foil frame and placed in the thin film holder of the optical absorbance spectrometer. (b) Optical absorbance spectra measured from each of the free-standing SWCNT thin films within an energy range of 1.0 to 2.5 eV, showing the absorbance peaks corresponding to the semiconducting ($^{S}E_{22}$) and metallic ($^{M}E_{11}$) interband transitions from the van Hove singularities in the SWCNT density of states at ~1.3 and ~1.9 eV, respectively.

Raman spectroscopy was employed to verify the presence of SWCNTs and MWCNTs in each thin film sample set, respectively, as well as to assess the consistency of CNT quality across the various areal densities/thicknesses produced for the SWCNT and MWCNT thin films. Raman spectra were

collected at three randomly selected spots on each thin film sample (mounted on glass slides) in a Raman shift range of 100 to 3000 cm^{-1} with an excitation wavelength of 633 nm. Figure 60a and 60b exhibit the averaged Raman spectra from each of the samples for the SWCNT and MWCNT thin films, respectively. Visible in the spectra for all CNT samples are the D-band (~1350 cm^{-1}), G-band (1580 cm^{-1}), and G'-band (2700 cm^{-1}) peaks. The G-band peak represents the sp^2-bonded carbon structure of CNTs and confirms the presence of CNTs in all of the thin films. An additional spectral feature which is valuable for distinguishing SWCNTs and MWCNTs is the radial breathing mode (RBM) peak, located between 100 and 300 cm^{-1}.The RBM is unique to SWCNTs and represents the characteristic phonon mode of SWCNTs as an in-phase radial vibration of all carbon atoms in the tube [148]. This feature confirms the presence of the specified CNT type in both sets of thin films.

The D-band peak provides information pertaining to the defect concentration of a CNT sample, as it arises from defects in the sp^2 bonding structure of the CNTs. The D/G ratio, comparing peak intensities of the D- and G-bands, is a commonly used metric to assess this. The D/G ratios for the SWCNT and MWCNT thin films are compared as a column plot in Figure 60c. It can be clearly seen that the D/G ratios for both SWCNT and MWCNT thin films are not significantly impacted by the film's areal density or thickness, indicating that the CNT quality is not affected by differences in the film properties.

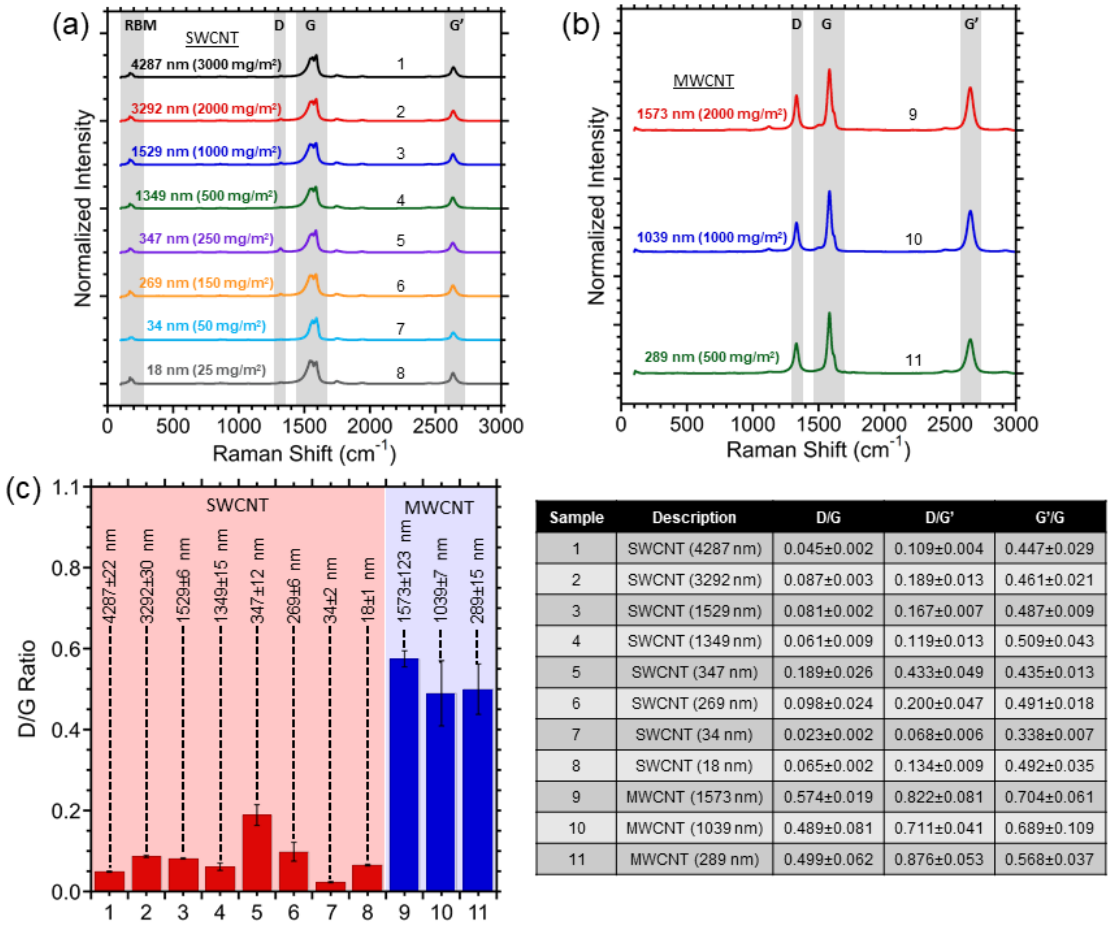

Sample	Description	D/G	D/G'	G'/G
1	SWCNT (4287 nm)	0.045±0.002	0.109±0.004	0.447±0.029
2	SWCNT (3292 nm)	0.087±0.003	0.189±0.013	0.461±0.021
3	SWCNT (1529 nm)	0.081±0.002	0.167±0.007	0.487±0.009
4	SWCNT (1349 nm)	0.061±0.009	0.119±0.013	0.509±0.043
5	SWCNT (347 nm)	0.189±0.026	0.433±0.049	0.435±0.013
6	SWCNT (269 nm)	0.098±0.024	0.200±0.047	0.491±0.018
7	SWCNT (34 nm)	0.023±0.002	0.068±0.006	0.338±0.007
8	SWCNT (18 nm)	0.065±0.002	0.134±0.009	0.492±0.035
9	MWCNT (1573 nm)	0.574±0.019	0.822±0.081	0.704±0.061
10	MWCNT (1039 nm)	0.489±0.081	0.711±0.041	0.689±0.109
11	MWCNT (289 nm)	0.499±0.062	0.876±0.053	0.568±0.037

Figure 60. Averaged Raman spectra taken from three spots on each of the (a) SWCNT and (b) MWCNT films mounted on glass slides. (c) The D/G ratios of all films are compared in the column plot, while all Raman peak ratios are given in the table. Error bars represent the standard deviation of the measurement at three spots on each film.

Figure 61a and b show the measured RF transmittance as a function of frequency for the SWCNT and MWCNT thin films, respectively. Their values can be compared with the RF reflectance curves shown in Figure 44a. Values taken at 12 GHz were used to produce Figure 44c.

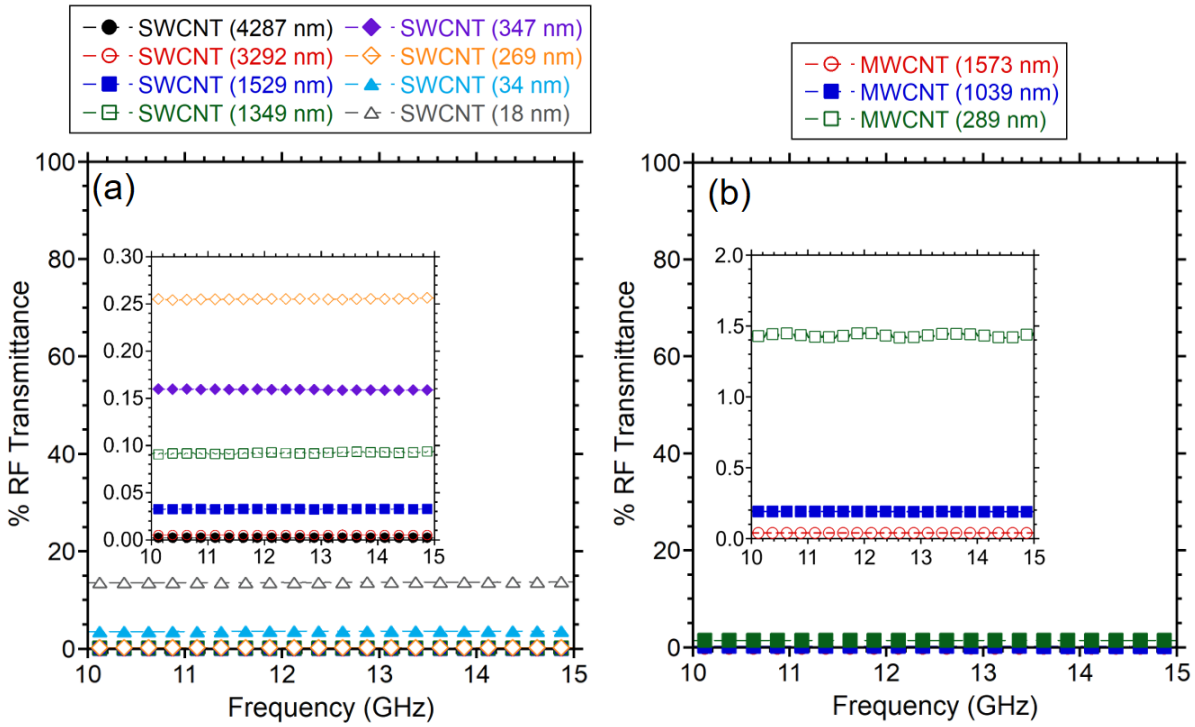

Figure 61. Frequency sweeps of RF transmittance for (a) the SWCNT thin films, and (b) the MWCNT thin films. Insets show zoomed in views of the frequency sweeps at very low transmittance to enable better comparison of individual samples.

The SWCNT and MWCNT thin films were compared with a survey of other shielding materials from the literature. The shielding effectiveness of each material was normalized to the volume density and the thickness to produce specific shielding effectiveness over thickness (SSE/t). These values were used to produce the scatter plot shown in Figure 47, and a full summary of the values and their respective sources is given in Table 9.

Chapter 11 – Appendix A: Supplemental Data

Table 9. Thickness, absolute shielding effectiveness (SE), and specific shielding effectiveness/thickness (SSE/t) values from the present SWCNT and MWCNT thin films as well as surveyed shielding materials including SWCNTs, MWCNTs, graphene, non-CNT/graphene carbon, indium tin oxide (ITO), transition metal carbides/carbonitrides (MXenes), and metals. References for all values are included.

Material Category	Material	t (μm)	SE (dB)	SSE/t (dB cm^2/g)	Measurement Frequency	Reference
SWCNT Thin Films (present work)	SWCNT	4.287	46.6	149587	12 GHz	This Work
		3.292	42.8	206131		
		1.529	34.9	335850		
		1.349	30.4	584716		
		0.347	28.0	1076850		
		0.269	25.9	1663691		
		0.034	14.4	2780378		
		0.018	8.7	3329768		
MWCNT Thin Films (present work)	MWCNT	1.573	34.1	164108	12 GHz	This Work
		1.038	27.2	261939		
		0.289	18.5	355452		
SWCNTs	SWCNTs (bulk)	24	90.0	428222	8-12 GHz	[106]
	SWCNT/PS	1200	18.5	275	8-12 GHz	[105]
	SWCNT/cellulose	30.8	35.0	7678	12-18 GHz	[104]
	SWCNT/Cu	3	29.5	26441	2-10 GHz	[149]
		7	42.8	17941		
		18	50.1	9378		
		32	71.7	7308		
MWCNTs	MWCNT (bulk)	1.85	50.0	193798	8-12 GHz	[107]
Graphene	Graphene (bulk)	60	61.0	10218	8-12 GHz	[150]
Carbon (Non-CNT/Graphene)	Carbon Black/ABS	1100	20.0	190	8-12 GHz	[151]
	Carbon/PN resin	2000	51.2	1705	8-12 GHz	[152]
MXenes	Ti3C2Tx	0.055	20.0	3890000	8-12 GHz	[133]
		0.94	46.1	120000	8-12 GHz	[134]
		110	68	25863	8-12 GHz	[153]
		8	57	30830	8-12 GHz	
ITO	ITO	1	58.0	81232	1 GHz	[136]
	ITO	0.5	20.0	56022	1-4.5 GHz	[135]
Metals	Copper nanosheets	1.2	49.6	292000	12-18 GHz	[154]
		3	62.6	156500		
		14.3	103.2	34387		

12 Appendix B: Additional Experiments

Data discussed here concerns experiments carried out to develop the capability of laser thinning. Experimentally rigorous tests were performed, but are included here in detail so as to inform the reader without disturbing the continuity of related main text chapters.

12.1 Rationale for CNT Sheet Thinning

12.1.1 Initial measurement of $KAuBr_4$-doped MWCNT sheet AC conductivity

Initial AC conductivity measurements of Huntsman Miralon MWCNT sheet samples which were doped with $KAuBr_4$ indicated the measurement may have been affected by complications arising from the conductivity enhancement induced by the dopant. Figure 62a and b show the real part of AC conductivity and the raw S_{21} magnitude, respectively (black lines), measured using the rectangular waveguide setup described in Chapter 5 from 10 GHz to 40 GHz of an as-received MWCNT sheet doped with $KAuBr_4$. The real AC conductivity as a function of frequency predicted by the skin effect model was determined using the following equations[7]:

$$R_{AC} = \begin{cases} \frac{A}{\sigma_{DC}Bt}, & 2\delta \geq B \text{ or } 2\delta \geq t \\ \frac{A}{\delta\sigma_{DC}(2t-4\delta+2B)} & 2\delta < B \text{ and } 2\delta < t \end{cases} \quad (12.1\text{-}1)$$

$$Re(\sigma_{AC,skin}) = \frac{A}{R_{AC}Bt} \quad (12.1\text{-}2)$$

where R_{AC} is the AC resistance, $\sigma_{AC,skin}$ is the AC conductivity predicted by the skin effect model, A, B, and t are the sample dimensions as shown in Figure 62a, σ_{DC} is the material's DC electrical conductivity measured via four-point probe, and δ is the skin depth calculated using Equation (1.2-2). The skin effect prediction for the $KAuBr_4$-doped MWCNT sheet sample is shown by the red line in Figure 62a. The

[7] https://www.emisoftware.com/calculator/resistance-rectangular-wire/

measured real AC conductivity of the doped MWCNT sheet rapidly degrades into negative values by 18 GHz, and becomes progressively noisier as the frequency approaches 40 GHz. The measured curve not only exhibits nonphysical, negative real AC conductivity values, but is significantly different from the modeled curve through the measured frequency range.

As can be concluded from the experiments discussed in Section 6.1.1, some part of this observed result may be attributed to the presence of iron catalyst in the starting, as-received MWCNT material. However, the degradation to negative values was not observed in the Section 6.1.1 experiments which extended fully to 40 GHz, and so the effect shown here was also hypothesized to be a result of the DC conductivity increase caused by chemical doping. This can be attributed to the reduced signal transmission as the higher conductivity of the doped sample results in increased signal absorption, supported by comparing the S_{21} magnitude as shown in Figure 62b with that of the as-received MWCNT sheet shown in Figure 52a (black line). The value of S_{21} magnitude for the as-received MWCNT sheet lies at approximately −50 dB at 10 GHz and remains in that regime to 40 GHz, while that of the $KAuBr_4$-doped MWCNT sheet is −64 dB at 10 GHz and reduces to −70 dB by 40 GHz. This indicates a ~0.25% reduction in the transmitted signal at 10 GHz due to $KAuBr_4$ doping, which can be significant when near the −100 dB reported noise floor of the VNA. The increased noise in the measurement of the doped MWCNT sample approaching 40 GHz is also a strong indication of this effect. Based on this experiment, it was hypothesized that an increase in the sample's resistance induced by thickness reduction would counteract the transmission loss and improve measurement of the $KAuBr_4$-doped material.

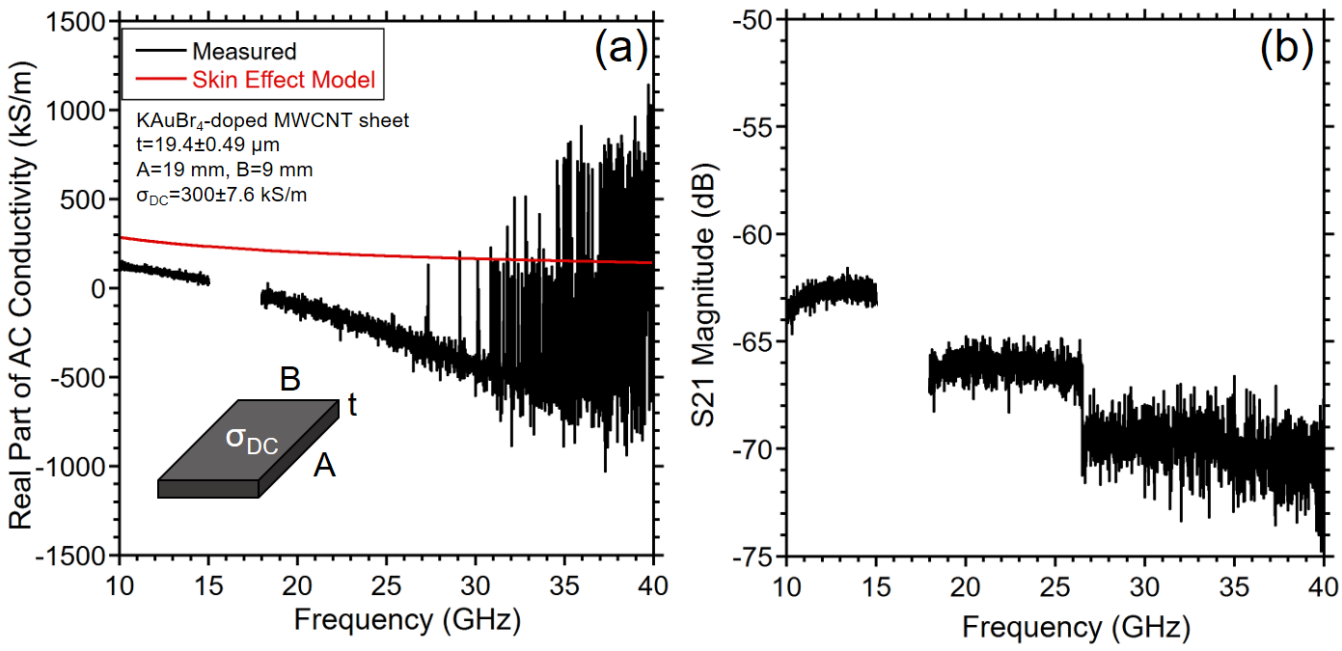

Figure 62. (a) Real part of AC conductivity and (b) S_{21} magnitude measured from a $KAuBr_4$-doped MWCNT sheet from 10 GHz to 40 GHz. The real AC conductivity is compared with the skin effect model.

12.1.2 Thinning method selection

In preliminary testing, three thinning methods were considered to potentially undergo experimental development for use in AC conductivity measurement studies. The first method considered was the tape delamination method (Figure 63a), in which a sample of the MWCNT sheet is adhered to a glass slide using double sided tape. Tweezers are used to take hold of the upper layers of the MWCNT sheet and peel away the sample, leaving behind a delaminated, sacrificial layer of material. This is then repeated as needed to further reduce the sheet's thickness. It was immediately evident that this method would not produce the uniformity or thickness control desired for the studies requiring a thinning process, and the tape delamination method was discontinued. The second method was CSA dispersion and filtration (Figure 63b). The technique is performed using an identical procedure to the CNT thin film fabrication process described in Section 4.2.7 with larger CNT masses to create thicker sheets. Initial testing showed that the method could produce cohesive samples such as the one shown, but this

method posed a number of issues. Producing clean samples required purified MWCNT sheet as the starting material, which meant the method could not be used to explore the effect of sheet thickness on the as-received material. Additionally, the filtration apparatus was limited to 35 mm diameter samples which led to small available ribbon lengths to perform CVD deposition of metals. For these reasons, it was decided to focus development efforts on the laser ablation-based thinning method (Figure 63c), as it could be performed on any starting materials or sample dimensions within the laser's cutting footprint and offered a wide range of customization due to the versatile laser cutting conditions available.

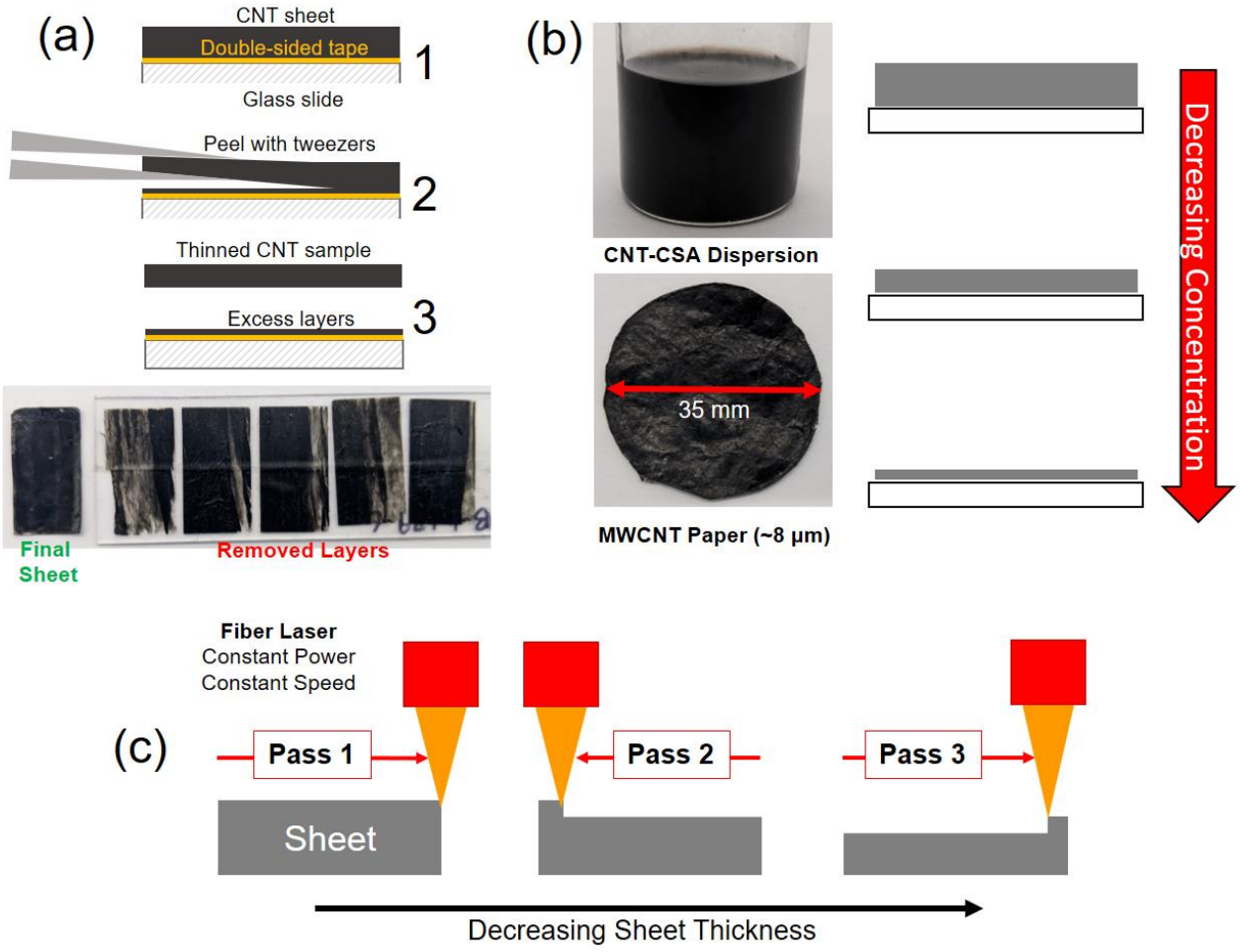

Figure 63. Schematic representations of the (a) tape delamination, (b) chlorosulfonic acid dispersion, and (c) laser thinning methods.

Chapter 12 – Appendix B: Additional Experiments

12.2 Laser Thinning Development

12.2.1 Optimizing applied laser power and pass count

The starting point for laser conditions optimization to be used for laser thinning with the Trotec SpeedMarker 700 fiber laser system was 6% power, 500 mm/s, 100 kHz pulse frequency, 5 passes. This was determined from cutting conditions for CNT mesh reflector structures, which were systematically optimized to just barely cut fully through the MWCNT sheet. Preliminary conditions for laser thinning were selected based on a grid of 1 cm squares to which different combinations of laser power (1% to 6%) and number of passes were applied (1 pass to 5 passes) at a constant 500 mm/s speed as shown in Figure 64a. Each grid square was cut using a cross-hatching pattern in which the laser rasters horizontally from bottom to top, followed by vertically from right to left, with the raster lines separated by a user-defined pitch. A diagram of this pattern is given in Figure 64b; for initial testing the pitch used was 50 μm. Qualitative analysis of the optimization grid shows that laser powers ≥3% will burn fully through the MWCNT sheet for the majority of the tested pass counts. SEM imaging of selected grid squares was performed to assess the effect of different laser thinning conditions on the MWCNT sheet's surface morphology. Figure 64c presents SEM images of the MWCNT sheet without thinning and with thinning using 1% and 6% power at constant 500 mm/s and 1 pass. The surface morphology of the 1% power sample does not show significant change due to the laser, while at 6% there is significant agglomeration of the iron catalyst (beads of metal along each MWCNT bundle). Thus, all subsequent experiments were conducted using 1% power. Additional macroscale observations about the process were made at this stage. It was determined that the airflow within the laser cutting chamber when the fume extraction system was active affected the uniformity of laser thinning (see Figure 65), and so subsequent testing was performed with the fume extraction inactive. For good measure, the cross-hatching pattern was also rotated by 90° after every quarter of the total pass quantity applied, moving the

starting point of the thinning process sequentially to each corner of the sample for equivalent portions of the overall thinning run.

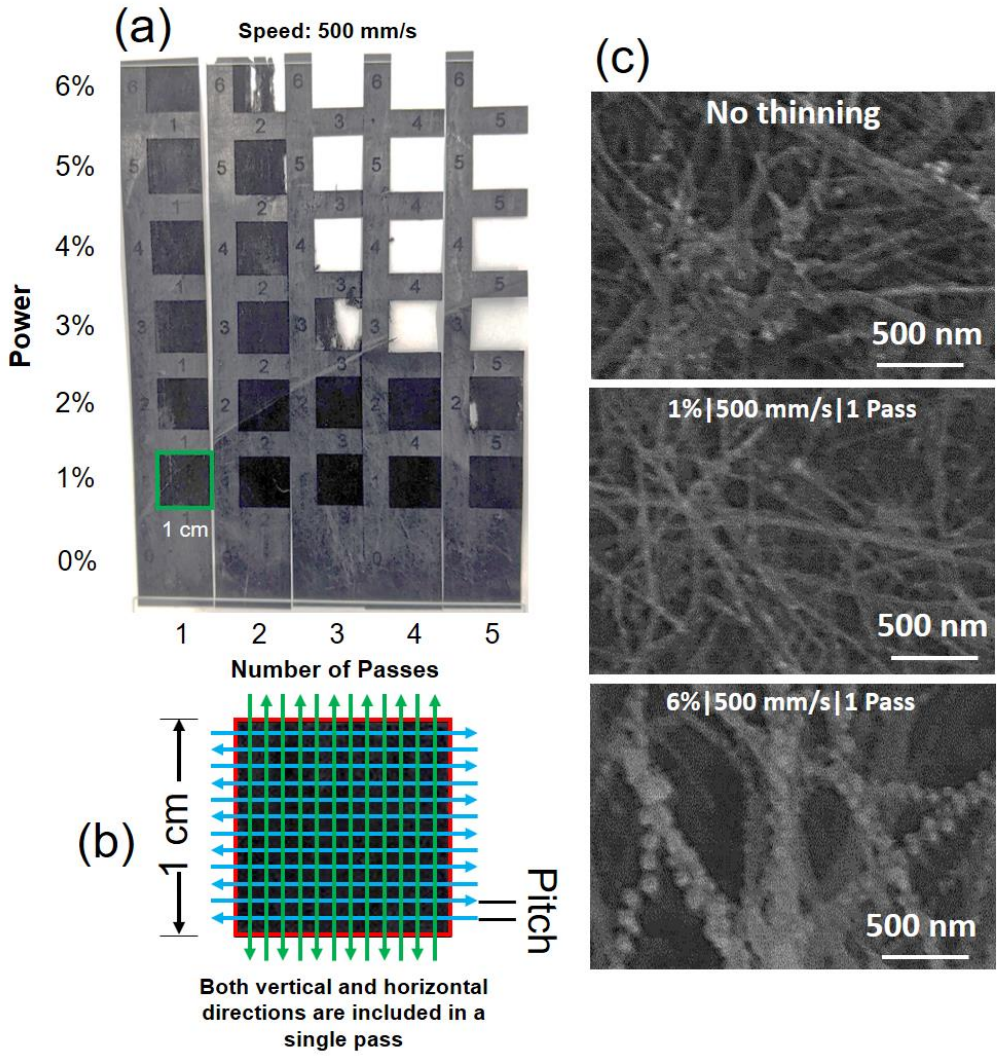

Figure 64. (a) The sample grid used for preliminary optimization of the laser thinning conditions. (b) Schematic of the cross-hatching pattern used for laser thinning. (c) SEM images showing the effect of different laser power on the MWCNT sheet surface morphology with a constant speed of 500 mm/s at 1 pass.

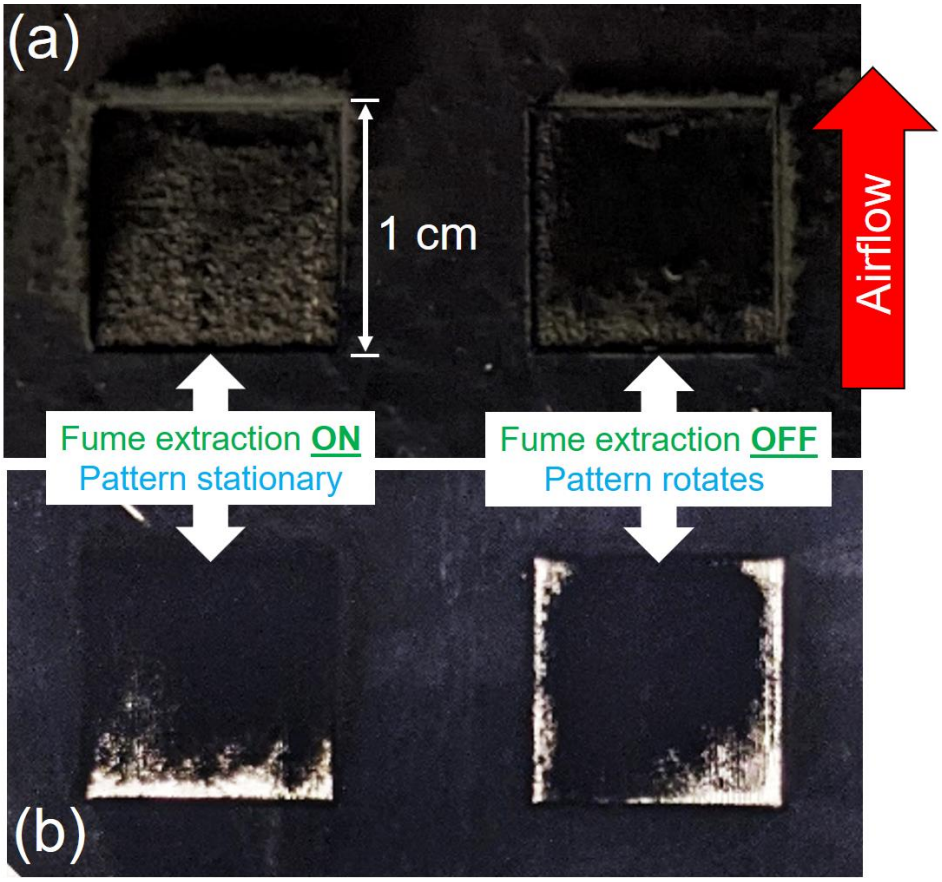

Figure 65. The results of laser thinning with the fume extraction of the laser active/using a stationary cross-hatching pattern (at left) and with the fume extraction inactive/rotating the cross-hatching pattern (at right). (a) Immediately after laser thinning, the difference in distribution of the ablated material depending on the airflow should be noted. (b) The difference in uniformity of laser thinning depending on the airflow from the fume extraction is clear when the samples are viewed with backlighting.

12.2.2 Optimizing cross-hatching pattern pitch

SEM imaging revealed that the initial pattern pitch of 50 μm produced an uneven geometry on the MWCNT sheet surface compared with the sheet before thinning (see Figure 66a-b) as the pitch was too wide for the beam to achieve full coverage of the sheet. To correct this issue while minimizing the effect on the results of the thinning process, the pitch was tested at reduced values of 25 μm and 10 μm with the laser speed increased by an equivalent factor to the pitch reduction (1000 and 2500 mm/s, respectively). This would in theory maintain an equivalent laser energy flux, as the increased speed would lead to the same dwell time at a given spot. The effect of four-pass laser thinning at 1% power with these conditions on the MWCNT sheet surface morphology is shown in Figure 66c-d; the

disappearance of the surface patterning effect with reduced cross-hatching pitch is evident, though there is still some surface fraying present. Most importantly, the thickness of the sheet after thinning with each pitch value was nominally equivalent, validating the need to increase the laser speed equivalently to the pitch reduction. It was decided to use a pitch of 0.01 mm for all subsequent experiments.

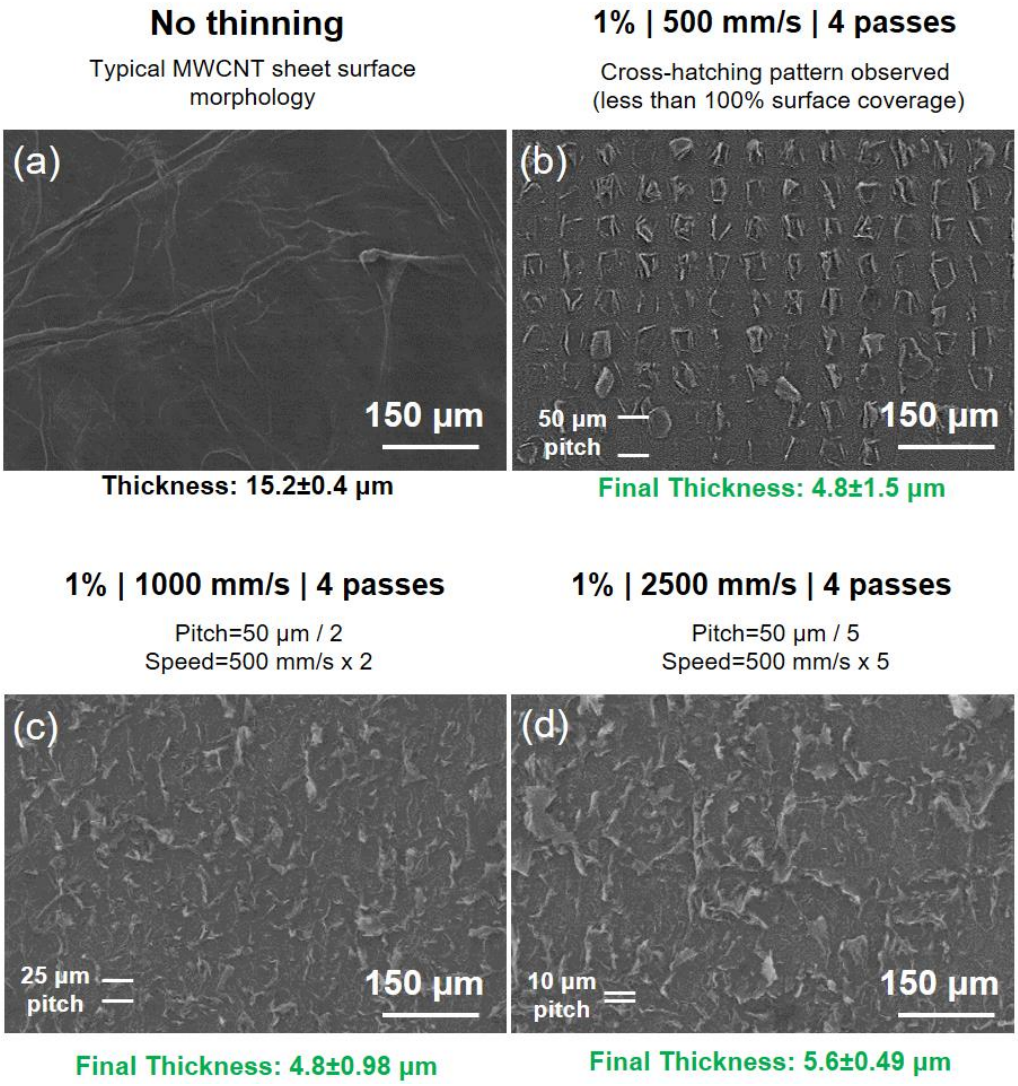

Figure 66. Surface morphology of the MWCNT sheet (a) before laser thinning, and after thinning with 1% power, 500 mm/s, and 4 passes using a pitch of (b) 50 µm, (c) 25 µm, and (d) 10 µm.

12.2.3 Effect of laser thinning on sample thickness and electrical properties

The conditions of 1% power, 2500 mm/s speed, and 100 kHz pulse frequency were used to investigate how the number of applied laser passes affected the thickness and electrical properties of the sample. This was done using 1 cm squares of material, with three samples being tested to account for variation across the MWCNT sheet. Progressively more passes were applied to the samples at the above conditions, and the thickness and sheet resistance of the samples was measured at each increment. The thickness was measured using calipers at 5 spots on each square (all corners and center). The DC conductivity was then calculated from the measured values. The relationships between thickness/DC sheet resistance/DC conductivity and pass count are shown in Figure 67. The thickness (black circles) decreased steadily from an initial value of 20 μm to 9 μm at 7 passes, while the DC sheet resistance (red squares) increases from ~0.5 Ω/□ to ~2.5 Ω/□. Calculating the DC conductivity from these values gives the values in blue triangles (refer to the blue third y-axis, not scaled to the first two y-axes). The DC conductivity does not steadily change with the applied pass count, but appears to decrease overall. This indicates that although thinning produces the desired thickness reduction and resistance increase, it may not completely preserve the initial properties of the MWCNT sheet.

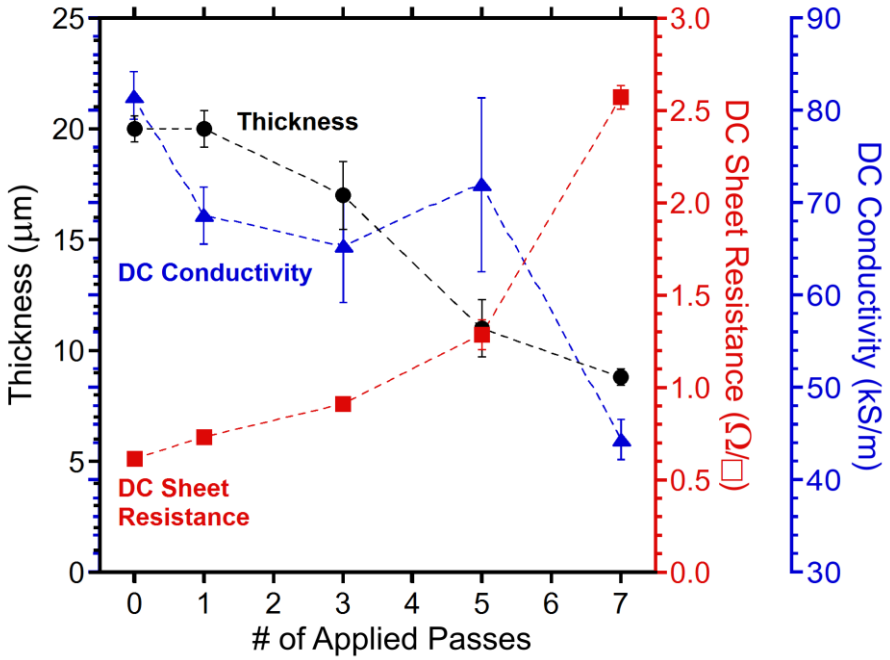

Figure 67. The relationship between the MWCNT sheet thickness/DC sheet resistance/DC conductivity and the applied laser pass count used for laser thinning with constant conditions of 1% power, 2500 mm/s speed, 100 kHz pulse frequency.

To determine if the consistency of the MWCNT sheet properties with increased laser thinning could be improved, the laser speed was increased to the maximum available value of 12000 mm/s. This, combined with the minimum 1% power which was already in use, minimized the laser power delivered per pass to the MWCNT sheet. The test of MWCNT sheet thickness and electrical properties as a function of applied pass count was repeated with the expectation that significantly more passes would be required to match or exceed the results achieved with 2500 mm/s. Influenced by the experiments on purified material described in Section 6.1.1, these relationships were also investigated for the purified MWCNT sheet with laser thinning using identical conditions. The relationship between thickness/DC sheet resistance and applied pass count at 12000 mm/s for the as-received and purified MWCNT sheet materials is shown in Figure 68a, while the same for the calculated DC conductivity is shown in

Figure 68b. Figure 68c shows the progress of material removal with increasing applied pass count using these conditions for laser thinning.

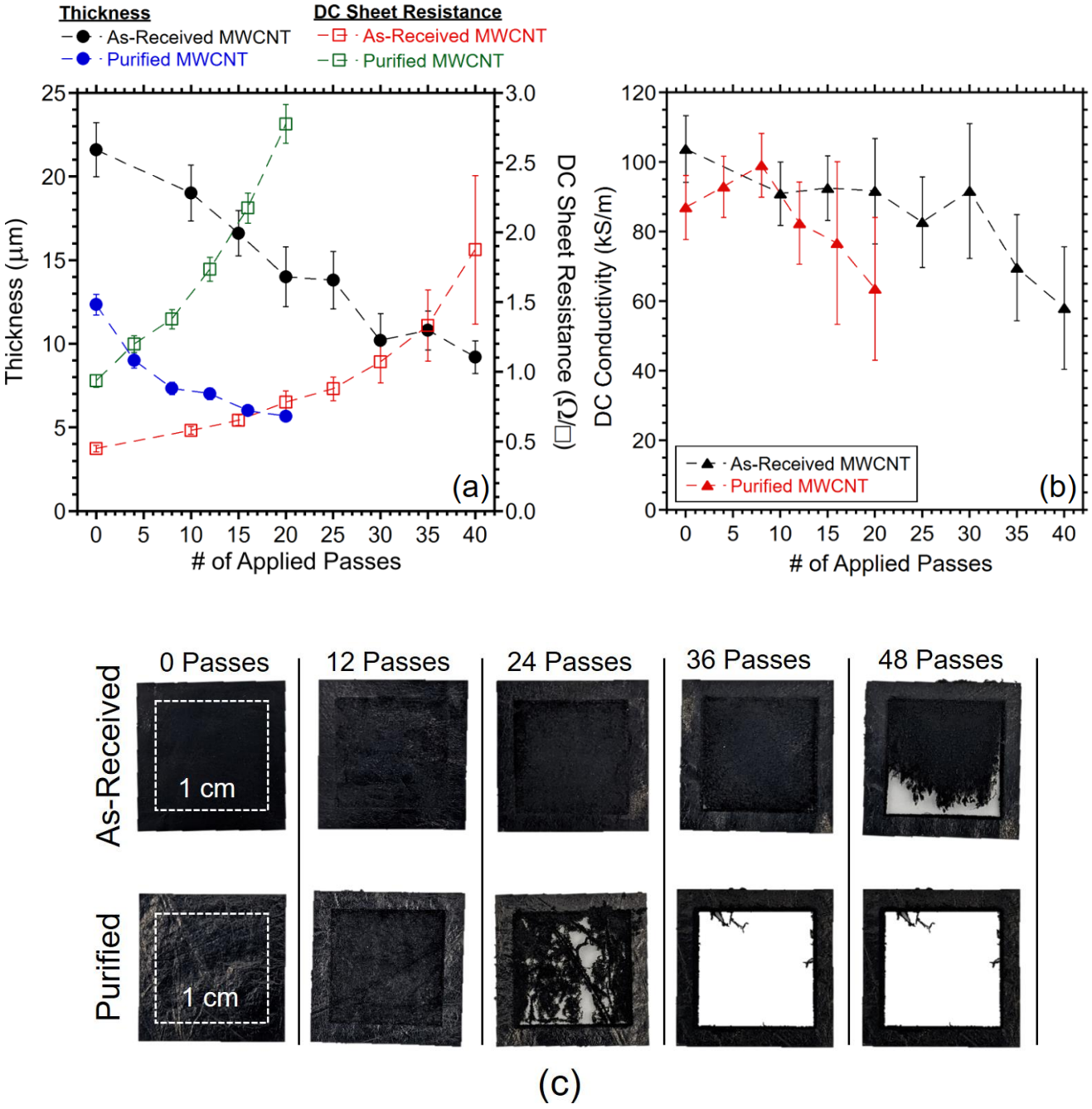

Figure 68. The relationship between the MWCNT sheet thickness/DC sheet resistance (a) or DC electrical conductivity (b) and the applied laser pass count used for laser thinning with constant conditions of 1% power, 12000 mm/s speed, 100 kHz pulse frequency. (c) Photographic progression showing the material loss of the as-received and purified MWCNT sheets with increasing number of laser passes using these conditions.

The thicknesses of the as-received (solid black circles) and purified (solid blue circles) MWCNT sheets decrease at similar rates, but the purified material's initial thickness is approximately half that of the as-received material due to densification and material loss during the purification process. Therefore, the purified MWCNT sheet loses structural integrity at ~20 passes while the as-received sheet can withstand 40+ passes. Accordingly, the DC sheet resistances of both materials increase with greater pass count, and the initial value for the purified material (open green squares) is just under double that of the as-received material (open red squares). Calculating the DC conductivity from these measured values gives the relationships shown in Figure 68b for the as-received (solid black triangles) and purified (solid red triangles) MWCNT sheet. Both materials exhibit a region of nominally constant conductivity, indicated by overlapping error bars, with the conductivity values of the materials being comparable. The conductivity then decreases for both materials at elevated pass counts; this regime occurs at a lower pass count for the purified material, again due to its smaller initial thickness leading to earlier breakdown of the material. Unfortunately, these results did not indicate a significant improvement in material consistency over the thinning process using a speed of 2500 mm/s, but did present an advantage in terms of reduced processing time.

12.2.4 Laser thinning conclusions

The results using conditions of 1% power, 12000 mm/s speed, and 100 kHz pulse frequency represent the current stage of development for the laser thinning process, and were deemed suitable for experimental use in the study of AC conductivity in the MWCNT sheet. The thinning of samples for these studies was carried out using the rotating cross-hatching pattern and no fume extraction during processing, and the measured DC sheet resistance or resistance-per-unit-length of the samples was used as the metric for the targeted sample properties.

Chapter 12 – Appendix B: Additional Experiments

12.3 Microstrip Line AC Resistance Measurements

For this dissertation work, preliminary testing to measure the AC resistance of CNT sheet materials was performed using a microstrip line geometry, similar to that used by Bulmer et al. [45]. For this test method, samples were placed into an opening in the trace conductor of the microstrip line, which was otherwise constructed from standard FR4 and deposited copper.

12.3.1 Microstrip line sample fabrication

For this work, a microstrip line with a target characteristic impedance of Z_0=50 Ω was designed according to the following equations from Pozar [36]:

$$Z_0 = \frac{120\pi}{\sqrt{\varepsilon_{eff}}\left[\frac{W}{h}+1.393+\frac{2}{3}\ln\left(\frac{W}{h}+1.444\right)\right]} \quad for\ \frac{W}{h} \geq 1 \tag{12.3-1}$$

$$\varepsilon_{eff} = \frac{\varepsilon_r+1}{2} + \frac{\varepsilon_r-1}{2}\frac{1}{\sqrt{1+12h/W}} \quad for\ \frac{W}{h} \geq 1 \tag{12.3-2}$$

where W is the width of the microstrip trace conductor, h is the thickness of the dielectric substrate, ε_r is the relative permittivity of the substrate, and ε_{eff} is the effective dielectric constant which describes the combined medium of air and dielectric substrate within the electromagnetic field region of the microstrip line. The resulting microstrip line design (W=2.8 mm, h=1.57 mm) was fabricated commercially by AdvancedPCB using their standard FR4 substrate (ε_r=4.34 [155]) with 1 oz copper deposition (35 μm thickness). The individual microstrip coupons had lengths of 40 mm parallel to the trace conductor and clearance of 10 mm from either edge of the trace conductor. A 20 mm long gap in the trace conductor was used to mount strips of material-under-test with identical width to the trace. Representative photos (front and back) of one of the microstrip line test coupons with soldered SMA board-edge connectors and an inserted 18 μm thick copper foil strip is shown in Figure 69a.

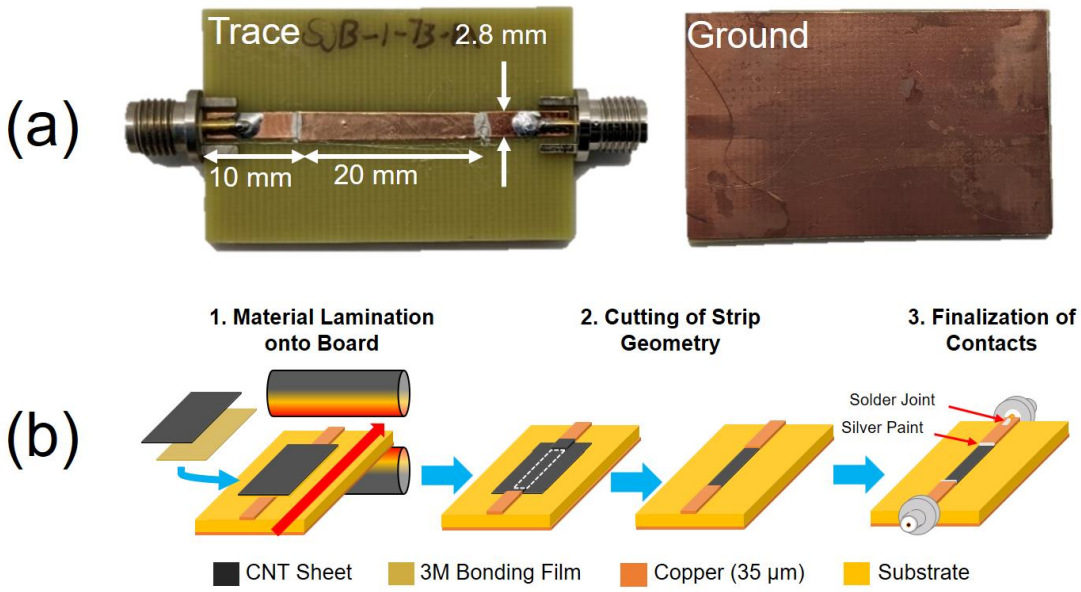

Figure 69. (a) Front and back views of the microstrip line test coupons, showing the trace and ground conductors, inserted sample in the center of the trace, and electrical contacting of the sample/trace interfaces and SMA board-edge coaxial connectors. (b) The procedure used to secure materials-under-test onto the board and cut them to match the width of the microstrip trace.

Microstrip line test coupons were prepared for measurement by the procedure shown in a schematic in Figure 69b. A sample of material to be tested, larger than the size of the intended sample geometry, was laminated into place on the board using 3M thermal bonding film 588 with a heated laminator running at 140°C. Depending on the material to be tested, the excess material was then removed using a razor blade (for metals) or a laser cutter (for CNT materials). Lastly, silver paint was used to electrically connect the junction between the material-under-test and the deposited copper strips on either end, and board-edge SMA coaxial connectors were soldered in place to both the trace and ground conductors.

12.3.2 AC resistance measurement of copper foil in a microstrip line

For this work, the AC resistance of the trace conductor in the microstrip line was obtained from the Telegrapher's equations, conventionally derived from the equivalent circuit representation of a transmission line (shown in Figure 11a). The trace resistance per unit length (R') is the desired parameter to be determined, while additional parameters on a per unit length basis include the

inductance (*L'*) in series with *R'* as well as the shunt conductance (*G'*) and the shunt capacitance (*C'*) between the trace and ground conductors. The Telegrapher's equations are given by Equations (2.2-1) and (2.2-2), and are reprinted below for convenience.

$$-\frac{\partial}{\partial x}V(x) = (R' + j\omega L')I(x)$$

$$-\frac{\partial}{\partial x}I(x) = (G' + j\omega C')V(x)$$

V(x) and *I(x)* are the length dependent voltage and current, and ω is the angular frequency in radians/s. The values of R', L', G', and C' can be calculated from the measured S-parameters of the microstrip line. For the purposes of this dissertation work, this was done according to the procedure published by Orloff et al. (see reference [156] for details).

An AC resistance measurement of a copper sample in a microstrip line coupon was performed as a control. In order to ensure that the measurement consisted only of the copper foil section, a TRL calibration procedure was used. The standards employed were designed for a frequency range of 1-3 GHz and commercially fabricated on a test board by AdvancedPCB as shown in Figure 70a. All standards used the same cross-sectional dimensions as the sample measurement coupons, with the Thru consisting of a continuous 20 mm microstrip line section, the Reflect consisting of a single-port 10 mm long section that was shorted to the ground plane at its end through two plated vias, and the Line consisting of a ~48 mm long continuous microstrip line section which represented a ~28 mm extension of the Thru. This was equivalent to 90° phase shift at the center frequency of 2 GHz.

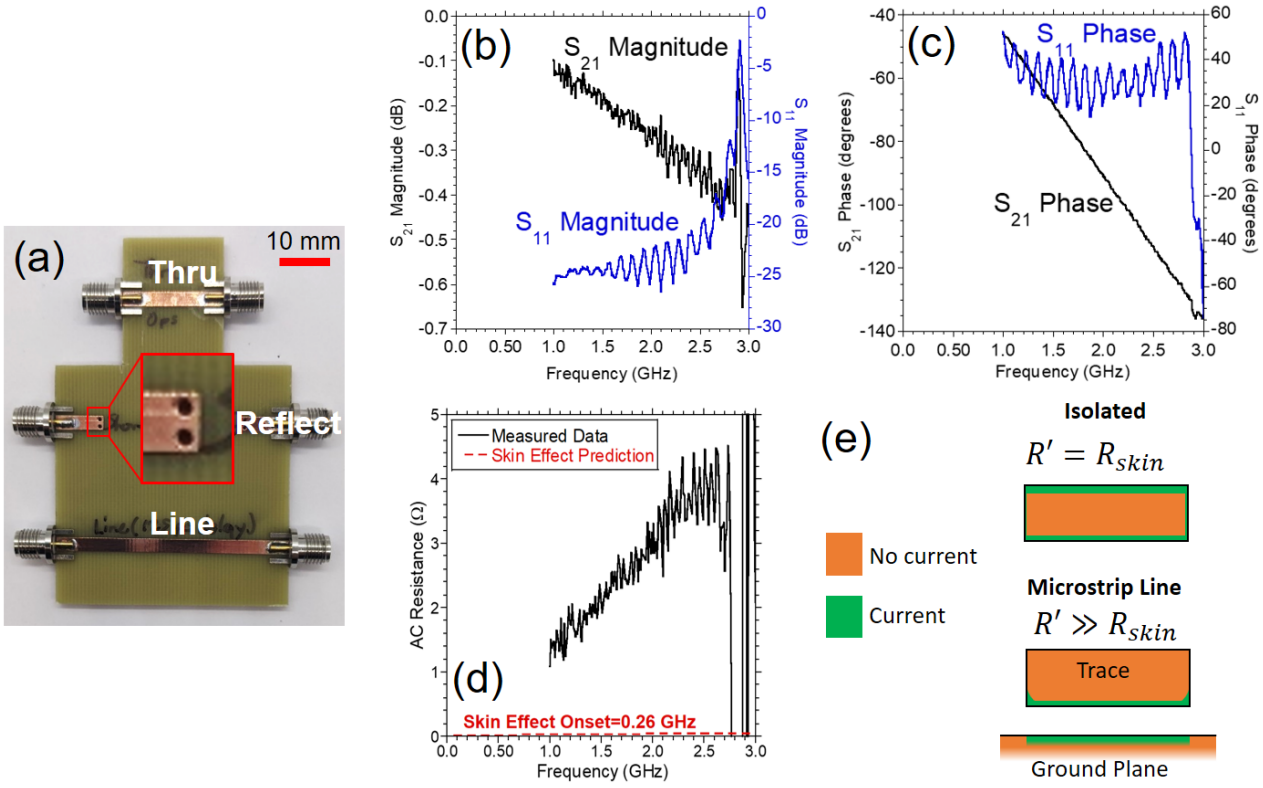

Figure 70. (a) The microstrip line-based TRL calibration board used for characterization of microstrip line samples. (b) S_{11} and S_{21} magnitude and (c) S_{11} and S_{21} phase of a copper foil sample measured in a microstrip line test coupon from 1-3 GHz (representative of S_{22} and S_{12} measurements). (d) The AC resistance of the copper foil sample calculated from the S-parameter measurements. (e) Diagrams showing the hypothesized current distribution in the rectangular conductor with and without the proximity of the ground plane.

S_{11}, S_{21}, S_{12}, and S_{22} of a copper foil sample were measured from 1-3 GHz using an Agilent E8363b VNA, access to which was provided by Dr. Jayanti Venkataraman. Representative S_{11}/S_{21} magnitude and phase data are given in Figure 70b and c. The AC resistance calculated using the method based on the Telegrapher's equations is compared with the modeled AC resistance due to skin effect determined from Equations (1.2-2), (1.2-4), and (1.2-6) in Figure 70d. The S_{21} magnitude indicates between −0.1 and −0.4 dB of attenuation across the measured frequency range, and the attenuation is increasing with frequency. The S_{11} magnitude indicates ~5% reflection at 1 GHz, and reflection increases with frequency. This could be attributed to the mismatch resulting from the silver paint connection, the twofold difference in thickness between the copper foil and the deposited copper forming the microstrip geometry, or from slight impedance mismatch between the VNA and the

microstrip coupon. Ultimately, the calculated AC resistance of the copper foil sample is several orders of magnitude higher than the skin effect model predicts. In addition to the issues posed by the sample mounting geometry, the differences between measurement and prediction can also be attributed to known characteristics of the cross-sectional current distribution in the microstrip trace. The so-called "edge-singularity" effect occurs when current is concentrated into the corners of a rectangular conductor [73]. Furthermore, the proximity effect plays a significant role in the current distribution of adjacent conductors regardless of shape; in the case of a microstrip line [72], the presence of the ground plane results in the current within the trace being drawn towards the surface nearest to the ground plane (i.e. the bottom of the trace). The diagrams in Figure 70e illustrate the hypothetical current distribution in the trace cross section with and without the ground plane, which could be the reason for differences observed in the AC resistance measurement of the copper foil from skin effect. Due to the variety of complications experienced in initial testing of the microstrip line method for AC resistance measurement, it was decided to prioritize development of the rectangular waveguide setup for the experiments reported in this dissertation.

12.3.3 Signal attenuation in CNT microstrip lines

Although the aforementioned complications prevented the determination of AC resistance from measurements of the microstrip lines in order to compare metal and CNT samples with the predicted skin effect response, the attenuation of the signal across the microstrip with different CNT materials was still observable. To this end, samples of Huntsman Corporation MWCNT sheet subjected to purification and $KAuBr_4$ doping were placed into microstrip line test coupons. Additionally, samples of Galvorn CNT film with a high degree of CNT alignment (see Figure 71a) were prepared with the CNTs oriented either parallel or perpendicular to the direction of propagation down the length of the trace. Figure 71b shows the S_{21} magnitude of the CNT and copper foil microstrip line samples from 1 to 3 GHz. The

attenuation for all samples increases with frequency, but clear differences can be observed in the level of attenuation depending on CNT material type and treatment. Attenuation in the as-received and purified MWCNT microstrip lines shown by the red data both fall around −1 dB, and $KAuBr_4$ doping improved the attenuation levels for both MWCNT materials to around −0.5 dB (blue data). The green data show that the attenuation in the microstrip lines made with DexMat Galvorn CNT sheet is significantly lower when the CNTs are oriented parallel to the direction of propagation (compare solid to dashed lines), in agreement with previous study into the impedance of aligned MWCNT networks [88]. These attenuation measurements produced encouraging results that drove further development of the rectangular waveguide method in order to directly compare the AC conductivity of the MWCNT sheet with different treatments as discussed in Chapters 5, 6, and 7. The results shown in this section were included in a poster presentation to representatives of the U.S. Air Force Research Laboratory (AFRL) at RIT in October 2022.

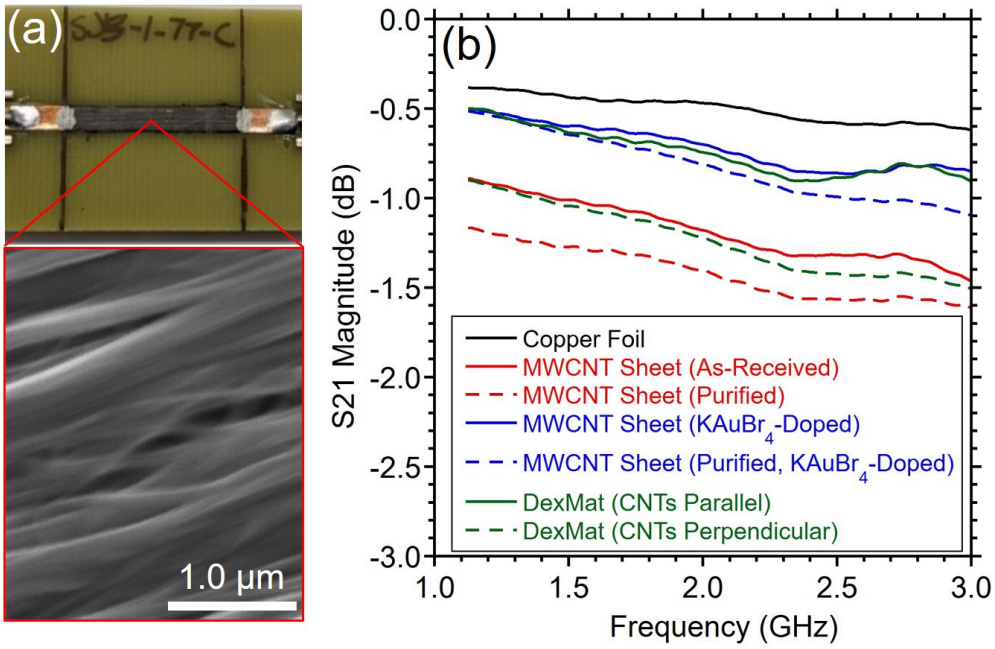

Figure 71. (a) SEM view of the CNT alignment within the trace of a microstrip line fabricated with DexMat Galvorn CNT film, in which the CNTs are aligned parallel to the propagation direction. (b) S_{21} magnitude measured from the copper foil and CNT microstrip line samples from 1-3 GHz.

Chapter 12 – Appendix B: Additional Experiments

12.4 CNT Patch Antennas

12.4.1 Design and fabrication of CNT patch antennas

The patch antenna provides a suitable component geometry to test a variety of different CNT sheet materials as alternative conductor materials. In the present work, a variety of patch antennas were fabricated in which all or some of the metal conductors were replaced with CNT materials. The S_{11} magnitude of CNT patch antennas was measured to verify that the antennas resonated at the targeted frequency, and the effects of $KAuBr_4$ doping and CNT alignment were tested through specially prepared patch antenna coupons. To determine the design length of the antennas for a given resonance frequency, the following equation was used [157].

$$f \approx \frac{c}{2L\sqrt{\varepsilon_r}} \tag{12.4-1}$$

L is the length of the antenna patch, ε_r is the relative permittivity of the dielectric substrate, and c is the speed of light in a vacuum. This equation specifies that the length of the antenna should be equal to half the wavelength in the dielectric medium. The microstrip line feed for the antennas was routed into one edge of the patch in all cases, and was designed using Equations (12.3-1) and (12.3-2).

In the present work, several CNT patch antennas were fabricated as shown in Figure 72, using Rogers RT/duroid® 5880 laminate as the dielectric substrate (ε_r=2.2 [158]). In all cases, the conductor materials were laminated at 140°C onto both sides of the substrate using 3M thermal bonding film 588, and laser cutting was used to cut and remove excess material on one side in order to produce the patch and feedline geometry. An SMA board-edge coaxial connector was placed at the end of the feedline and electrically contacted to the feedline and ground plane using silver paint for CNT materials and solder for copper.

Chapter 12 – Appendix B: Additional Experiments

A set of antennas were designed for resonance frequencies of 1, 2, and 3 GHz. This corresponded to lengths of ~3.37, ~5.05, and ~10.1 cm as shown in Figure 72a; the width of the patches was kept constant at ~3.37 cm. These antennas were fabricated using Huntsman Corporation MWCNT sheet for the patch, feedline, and ground plane, and all three were doped with $KAuBr_4$ to enhance their electrical conductivity. Two antennas were also fabricated with all conductors consisting of MWCNT sheet for a resonance frequency of 1.5 GHz (shown in Figure 72b), where one antenna was $KAuBr_4$ doped in order to observe the effect on power absorption through S_{11} measurements. Additionally, two antennas were fabricated for a resonance frequency of 2 GHz with copper foil feedlines and ground planes. The patches of the antennas were made from DexMat Galvorn aligned CNT film and electrically contacted to the feedlines using silver paint. The CNTs were oriented parallel or perpendicular to the patch length in their respective antennas as shown in Figure 72c. The patch width in the latter two sets of antennas was made equal to the patch length.

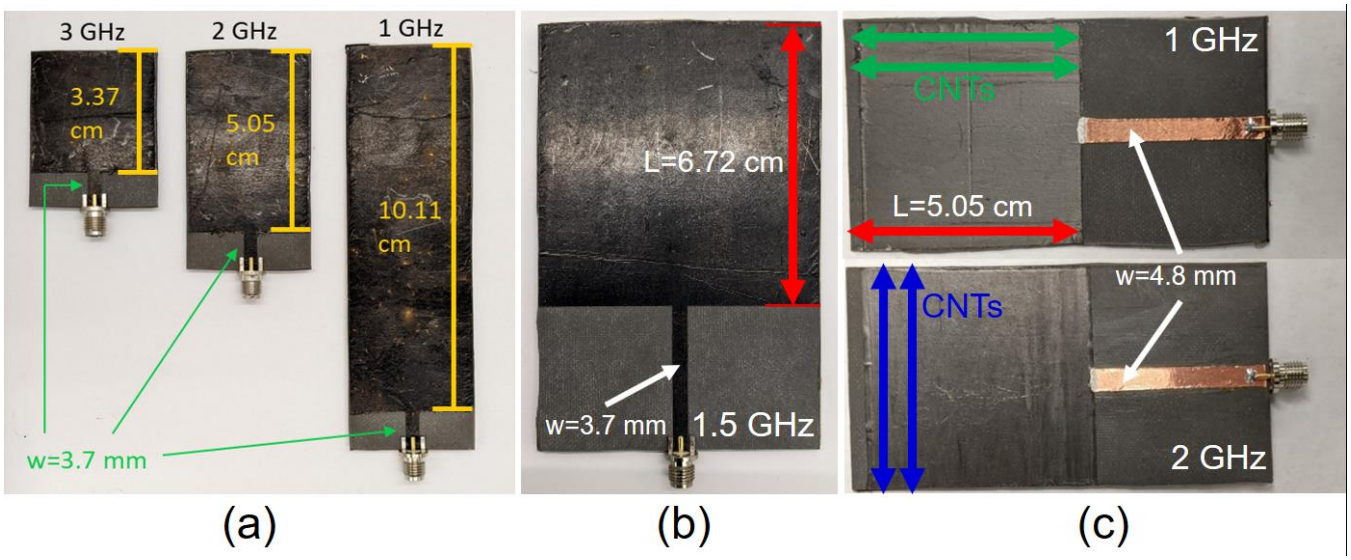

Figure 72. (a) CNT patch antennas fabricated to test the capability to target different resonance frequencies between 1 and 3 GHz. (b) One of the 1.5 GHz CNT patch antennas fabricated to test the effect of $KAuBr_4$ doping on absorbed power. (c) The 2 GHz CNT-Cu patch antennas fabricated to test the effect of CNT orientation within the patch.

12.4.2 S_{11} measurements of CNT patch antennas

S_{11} measurements of the antennas described above were taken up to 3 GHz, in which the position and amplitude of the resulting resonance peak were used to assess the resonance frequency and power absorption of the antenna. As these were single-port measurements of isolated antennas in a non-controlled environment, no conclusions were made as to the radiated signal intensity or radiation pattern of the antennas from the presently reported data. The resulting S_{11} magnitude data for each of the three cases shown in Figure 72 are presented in Figure 73a, b, and c, respectively. Figure 73a shows that the MWCNT patch antennas each resonated at their designed frequencies of 1, 2, and 3 GHz. The 2nd and 3rd harmonics of the 1 GHz antenna can also be seen within this frequency range at 2 and 3 GHz, respectively. Figure 73b shows that the S_{11} magnitude at resonance of the 1.5 GHz MWCNT patch antennas is ~−10 dB without $KAuBr_4$ doping and ~−22 dB with $KAuBr_4$ doping, suggesting that $KAuBr_4$ doping increases the power absorption by the antenna patch. Figure 73c shows the difference in S_{11} magnitude at resonance between CNT orientations within the patches of the tested 2 GHz antennas. The absorbed power is higher when the CNTs are perpendicular to the length of the patch, but there is a slight downward shift in resonance frequency.

More extensive testing with improved designs and replicate samples is needed to determine the significance of certain results shown here, such as those relating to CNT orientation. Overall, the capability to design CNT patch antennas to resonate at targeted frequencies has been demonstrated, and the benefits of $KAuBr_4$ doping for the power absorption have been shown. Specific improvements that should be made for future testing include standardization of the electrical contacting methods, patch impedance control through the feedline attachment location and patch width, as well as increased substrate and ground plane footprint compared with the patch size.

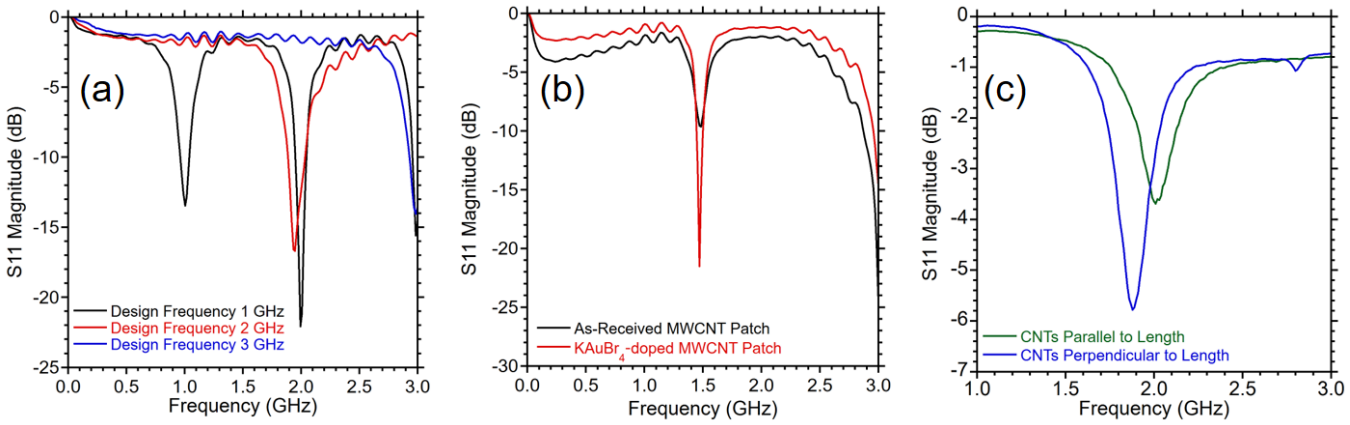

Figure 73. S_{11} magnitude data up to 3 GHz for the CNT patch antennas fabricated for testing of (a) different resonance frequencies, (b) $KAuBr_4$ doping effect on absorbed power, and (c) CNT orientation within the patch.

References

[1] S. Ellingson, *Electromagnetics*, vol. 2. Blacksburg, VA: Virginia Tech, 2018.

[2] J. F. Shackelford and W. Alexander, Eds., *CRC materials science and engineering handbook*, 3rd ed. Boca Raton, FL: CRC Press, 2001.

[3] *Metals Handbook*, 10th ed., vol. 2. ASM International, 1990.

[4] "Permeability," The Engineering Toolbox. Accessed: May 22, 2023. [Online]. Available: https://www.engineeringtoolbox.com/permeability-d_1923.html

[5] C. R. Paul, *Analysis of Multiconductor Transmission Lines*, 2nd ed. Wiley, 2008.

[6] H. B. Dwight, "Skin effect and proximity effect in tubular conductors," *Trans. Am. Inst. Electr. Eng.*, vol. 41, pp. 189–198, 1922, doi: 10.1109/T-AIEE.1922.5060774.

[7] A. E. Kennelly and H. A. Affel, "Skin-effect resistance measurements of conductors at radio–frequencies up to 100,000 cycles per second," *Proc. Inst. Radio Eng.*, vol. 4, no. 6, pp. 523–574, 1916, doi: 10.1109/JRPROC.1916.217281.

[8] F. E. Terman, "Radio Engineering Fundamentals of Radio Measurements in Radio Engineering," *Mcgraw Hill Book Company*. pp. 1–1036, 1943.

[9] S. Iijima, "Helical microtubules of graphitic carbon," *Nature*, vol. 354, no. 6348, pp. 56–58, 1991, doi: 10.1038/354056a0.

[10] J. Kong *et al.*, "Synthesis, integration, and electrical properties of individual single-walled carbon nanotubes," *Appl. Phys. Mater. Sci. Process.*, vol. 69, no. 3, pp. 305–308, 1999, doi: 10.1007/s003390051005.

[11] H. Ajiki and T. Ando, "Electronic states of carbon nanotubes," *J. Phys. Soc. Jpn.*, vol. 62, no. 4, pp. 1255–1266, 1993, doi: https://doi.org/10.1143/JPSJ.62.1255.

[12] M. Ouyang, J.-L. Huang, C. L. Cheung, and C. M. Lieber, "Energy gaps in 'metallic' single-walled carbon nanotubes," *Science*, vol. 292, no. 5517, pp. 702–705, 2001, doi: 10.1126/science.1058853.

[13] C. H. Sun, L. C. Yin, F. Li, G. Q. Lu, and H. M. Cheng, "Van der Waals interactions between two parallel infinitely long single-walled nanotubes," *Chem. Phys. Lett.*, vol. 403, no. 4–6, pp. 343–346, 2005, doi: 10.1016/j.cplett.2005.01.030.

[14] C. H. Sun, G. Q. Lu, and H. M. Cheng, "Simple approach to estimating the van der Waals interaction between carbon nanotubes," *Phys. Rev. B - Condens. Matter Mater. Phys.*, vol. 73, no. 19, pp. 1–5, 2006, doi: 10.1103/PhysRevB.73.195414.

[15] M. S. Purewal, B. H. Hong, A. Ravi, B. Chandra, J. Hone, and P. Kim, "Scaling of resistance and electron mean free path of single-walled carbon nanotubes," *Phys. Rev. Lett.*, vol. 98, no. 18, pp. 2–5, 2007, doi: 10.1103/PhysRevLett.98.186808.

[16] S. Li, Z. Yu, C. Rutherglen, and P. J. Burke, "Electrical properties of 0.4 cm long single-walled carbon nanotubes," *Nano Lett.*, vol. 4, no. 10, pp. 2003–2007, 2004, doi: 10.1021/nl048687z.

[17] M. Stadermann *et al.*, "Nanoscale study of conduction through carbon nanotube networks," *Phys. Rev. B - Condens. Matter Mater. Phys.*, vol. 69, no. 20, pp. 10–12, 2004, doi: 10.1103/PhysRevB.69.201402.

[18] S. V. Kalinin, S. Jesse, J. Shin, A. P. Baddorf, M. A. Guillorn, and D. B. Geohegan, "Scanning probe microscopy imaging of frequency dependent electrical transport through carbon nanotube networks in polymers," *Nanotechnology*, vol. 15, no. 8, pp. 907–912, 2004, doi: 10.1088/0957-4484/15/8/006.

[19] Y. Kodama *et al.*, "Field-effect modulation of contact resistance between carbon nanotubes," *Appl. Phys. Lett.*, vol. 91, no. 13, pp. 3–6, 2007, doi: 10.1063/1.2790805.

References

[20] P. N. Nirmalraj, P. E. Lyons, S. De, J. N. Coleman, and J. J. Boland, "Electrical connectivity in single-walled carbon nanotube networks," *Nano Lett.*, vol. 9, no. 11, pp. 3890–3895, 2009, doi: 10.1021/nl9020914.

[21] R. D. Downes *et al.*, "Geometrically constrained self-assembly and crystal packing of flattened and aligned carbon nanotubes," *Carbon*, vol. 93, pp. 953–966, 2015, doi: 10.1016/j.carbon.2015.06.012.

[22] A. R. Bucossi, C. D. Cress, C. M. Schauerman, J. E. Rossi, I. Puchades, and B. J. Landi, "Enhanced Electrical Conductivity in Extruded Single-Wall Carbon Nanotube Wires from Modified Coagulation Parameters and Mechanical Processing," *ACS Appl. Mater. Interfaces*, vol. 7, no. 49, pp. 27299–27305, Dec. 2015, doi: 10.1021/acsami.5b08668.

[23] J. Alvarenga *et al.*, "High conductivity carbon nanotube wires from radial densification and ionic doping," *Appl. Phys. Lett.*, vol. 97, no. 18, p. 182106, 2010, doi: 10.1063/1.3506703.

[24] Y. Zhao, J. Wei, R. Vajtai, P. M. Ajayan, and E. V. Barrera, "Iodine doped carbon nanotube cables exceeding specific electrical conductivity of metals," *Sci. Rep.*, vol. 1, no. c, pp. 1–5, 2011, doi: 10.1038/srep00083.

[25] I. Puchades *et al.*, "Mechanism of chemical doping in electronic-type-separated single wall carbon nanotubes towards high electrical conductivity," *J. Mater. Chem. C*, vol. 3, no. 39, pp. 10256–10266, 2015, doi: 10.1039/c5tc02053k.

[26] D. Janas, K. Z. Milowska, P. D. Bristowe, and K. K. K. Koziol, "Improving the electrical properties of carbon nanotubes with interhalogen compounds," *Nanoscale*, vol. 9, no. 9, pp. 3212–3221, 2017, doi: 10.1039/c7nr00224f.

[27] S. Li *et al.*, "Enhancement of carbon nanotube fibres using different solvents and polymers," *Compos. Sci. Technol.*, vol. 72, no. 12, pp. 1402–1407, 2012, doi: 10.1016/j.compscitech.2012.05.013.

[28] P. Liu, D. C. M. Hu, T. Q. Tran, D. Jewell, and H. M. Duong, "Electrical property enhancement of carbon nanotube fibers from post treatments," *Colloids Surf. Physicochem. Eng. Asp.*, vol. 509, pp. 384–389, 2016, doi: 10.1016/j.colsurfa.2016.09.036.

[29] C. D. Cress *et al.*, "Carbon nanotube wires with continuous current rating exceeding 20 Amperes," *J. Appl. Phys.*, vol. 122, no. 2, 2017, doi: 10.1063/1.4990981.

[30] J. Di *et al.*, "Strong, Twist-Stable Carbon Nanotube Yarns and Muscles by Tension Annealing at Extreme Temperatures," *Adv. Mater.*, vol. 28, no. 31, pp. 6598–6605, 2016, doi: 10.1002/adma.201600628.

[31] A. P. Leggiero *et al.*, "High Conductivity Copper-Carbon Nanotube Hybrids via Site-Specific Chemical Vapor Deposition," *ACS Appl. Nano Mater.*, vol. 2, no. 1, pp. 118–126, 2019, doi: 10.1021/acsanm.8b01740.

[32] A. P. Leggiero *et al.*, "Platinum nanometal interconnection of copper–carbon nanotube hybrid electrical conductors," *Carbon*, vol. 168, pp. 290–301, 2020, doi: 10.1016/j.carbon.2020.07.009.

[33] D. J. McIntyre, A. P. Leggiero, R. K. Hailstone, I. Puchades, C. D. Cress, and B. J. Landi, "Integrated Titanium-Carbon Nanotube Conductors via Joule-Heating Driven Chemical Vapor Deposition," *ECS Trans.*, vol. 97, no. 7, pp. 321–327, 2020, doi: 10.1149/09707.0321ecst.

[34] D. J. McIntyre, R. K. Hirschman, I. Puchades, and B. J. Landi, "Enhanced copper–carbon nanotube hybrid conductors with titanium adhesion layer," *J. Mater. Sci.*, vol. 55, no. 15, pp. 6610–6622, 2020, doi: 10.1007/s10853-020-04457-1.

[35] D. J. McIntyre, "Titanium Interconnection in Metallized Carbon Nanotube Conductors," Ph.D. Dissertation, Rochester Institute of Technology, 2021.

[36] D. M. Pozar, *Microwave Engineering*, 4th ed. Hoboken, NJ: Wiley, 2012.

References

[37] Y. Zhang, K. Suenaga, C. Colliex, and S. Iijima, "Coaxial nanocable: Silicon carbide and silicon oxide sheathed with boron nitride and carbon," *Science*, vol. 281, no. 5379, pp. 973–975, 1998, doi: 10.1126/science.281.5379.973.

[38] Y. Li, Y. Bando, and D. Golberg, "SiC-SiO2-C Coaxial Nanocables and Chains of Carbon Nanotube-SiC Heterojunctions," *Adv. Mater.*, vol. 16, no. 1, pp. 93–96, 2004, doi: 10.1002/adma.200306117.

[39] C. F. Herrmann, F. H. Fabreguette, D. S. Finch, R. Geiss, and S. M. George, "Multilayer and functional coatings on carbon nanotubes using atomic layer deposition," *Appl. Phys. Lett.*, vol. 87, no. 12, p. 123110, Sep. 2005, doi: 10.1063/1.2053358.

[40] S. P. Turano, J. D. Flicker, and W. J. Ready, "Nanoscale coaxial cables produced from vertically aligned carbon nanotube arrays grown via chemical vapor deposition and coated with indium tin oxide via ion assisted deposition," *Carbon*, vol. 46, no. 5, pp. 723–728, 2008, doi: 10.1016/j.carbon.2008.01.025.

[41] P. Jarosz *et al.*, "Carbon nanotube wires and cables: Near-term applications and future perspectives," *Nanoscale*, vol. 3, no. 11, pp. 4542–4553, 2011, doi: 10.1039/c1nr10814j.

[42] P. R. Jarosz, A. Shaukat, T. Mastrangelo, C. M. Schauerman, C. D. Cress, and R. D. Ridgley, "Coaxial cables with single-wall carbon nanotube outer conductors exhibiting attenuation/length within specification," *IET Micro Nano Lett.*, vol. 7, no. 9, pp. 959–961, 2012, doi: 10.1049/mnl.2012.0502.

[43] P. R. Jarosz *et al.*, "High-performance, lightweight coaxial cable from carbon nanotube conductors," *ACS Appl. Mater. Interfaces*, vol. 4, no. 2, pp. 1103–1109, 2012, doi: 10.1021/am201729g.

[44] F. Mirri *et al.*, "Lightweight, Flexible, High-Performance Carbon Nanotube Cables Made by Scalable Flow Coating," *ACS Appl. Mater. Interfaces*, vol. 8, no. 7, pp. 4903–4910, 2016, doi: 10.1021/acsami.5b11600.

[45] J. S. Bulmer *et al.*, "Microwave conductivity of sorted CNT assemblies," *Sci. Rep.*, vol. 4, pp. 1–8, 2014, doi: 10.1038/srep03762.

[46] M. A. El-Sabbagh, S. M. El-ghazaly, and H. A. Naseem, "Carbon Nanotube-Based Planar Transmission Lines," pp. 353–356, 2009.

[47] J. J. Karakash, *Transmission Lines and Filter Networks*. Macmillan, 1950.

[48] M. Cometto *et al.*, "Theoretical study of CNT based waveguide," *2018 IEEE MTT- Int. Conf. Numer. Electromagn. Multiphysics Model. Optim. NEMO 2018*, pp. 18–20, 2018, doi: 10.1109/NEMO.2018.8503140.

[49] G. Gradoni, D. Micheli, V. Mariani Primiani, F. Moglie, and M. Marchetti, "Determination of the electrical conductivity of carbon/carbon at high microwave frequencies," *Carbon*, vol. 54, pp. 76–85, 2013, doi: 10.1016/j.carbon.2012.11.005.

[50] L. Wang, R. Zhou, and H. Xin, "Microwave (8-50 GHz) Characterization of Multiwalled Carbon Nanotube Papers Using Rectangular Waveguides," *Carbon*, vol. 56, no. 2, pp. 499–506, 2008.

[51] A. Katsounaros, K. Z. Rajab, Y. Hao, M. Mann, and W. I. Milne, "Microwave characterization of vertically aligned multiwalled carbon nanotube arrays," *Appl. Phys. Lett.*, vol. 98, no. 20, pp. 1–4, 2011, doi: 10.1063/1.3592263.

[52] S. Li, Q. Zhu, and H. Xin, "Experimental research on the microwave properties of carbon nanotube array," *2012 IEEE Int. Workshop Antenna Technol. IWAT 2012*, pp. 331–334, 2012, doi: 10.1109/IWAT.2012.6178679.

[53] J. J. Carr, *Practical Antenna Handbook*, 4th ed. McGraw-Hill, 2001.

References

[54] S. Prashar, K. Sharma, S. Anand, and D. Engles, “Carbon Nanotube Based Flexible Antennas,” vol. 3, no. 1, pp. 129–132, 2012, doi: 10.9735/0976-8742.

[55] Y. M. Wu, X. Lv, B. K. Tay, and H. Wang, “Carbon nanotube-based printed antenna for conformal applications,” *2013 Int. Conf. Optoelectron. Microelectron. ICOM 2013*, pp. 91–93, 2013, doi: 10.1109/ICoOM.2013.6626498.

[56] J. Zhou, X. Xu, Y. Xin, and G. Lubineau, “Coaxial Thermoplastic Elastomer-Wrapped Carbon Nanotube Fibers for Deformable and Wearable Strain Sensors,” *Adv. Funct. Mater.*, vol. 28, no. 16, pp. 1–8, 2018, doi: 10.1002/adfm.201705591.

[57] S. D. Keller, A. I. Zaghloul, V. Shanov, M. J. Schulz, D. B. Mast, and N. T. Alvarez, “Radiation performance of polarization selective carbon nanotube sheet patch antennas,” *IEEE Trans. Antennas Propag.*, vol. 62, no. 1, pp. 48–55, 2014, doi: 10.1109/TAP.2013.2287272.

[58] N. Fichtner, X. Zhou, and P. Russer, “Investigation of carbon nanotube antennas using thin wire integral equations,” *Adv. Radio Sci.*, vol. 6, no. 2, pp. 209–211, 2008, doi: 10.5194/ars-6-209-2008.

[59] I. Puchades, J. E. Rossi, C. D. Cress, E. Naglich, and B. J. Landi, “Carbon Nanotube Thin-Film Antennas,” *ACS Appl. Mater. Interfaces*, vol. 8, no. 32, pp. 20986–20992, 2016, doi: 10.1021/acsami.6b05146.

[60] J. C. Maxwell, *A Treatise on Electricity and Magnetism*, vol. I. Oxford, 1873.

[61] O. Heaviside, “Effective resistance and inductance of a round wire,” *Electr. Pap.*, pp. 353–429, 1884.

[62] J. H. Poynting, “On the transfer of energy in the electromagnetic field,” *Philos. Trans. R. Soc. Lond.*, p. 277, 1884.

[63] Lord Rayleigh, “On the self-induction and resistance of straight conductors,” *Lond. Edinb. Dublin Philos. Mag. J. Sci.*, vol. 21, no. 132, pp. 381–394, 1886, doi: 10.1080/14786448608627863.

[64] H. F. Weber, “Remarks on the Second Paper of Mr. Hughes Regarding Self-Induction,” 1886.

[65] J. Stefan, “Über veränderliche elektrische Ströme in dicken Leitungsdrähten,” *Kk Hof-Staatsdruckerei*, 1887.

[66] O. J. Lodge, “On the theory of lightning-conductors,” *Lond. Edinb. Dublin Philos. Mag. J. Sci.*, vol. 26, no. 159, pp. 217–230, 1888, doi: 10.1080/14786448808628252.

[67] Lord Kelvin, “Ether, Electricity, and Ponderable Matter,” *Math. Phys. Pap.*, vol. 3, pp. 484–515, 1890.

[68] H. Hertz, “On the propagation of electric waves by means of wires,” *Electr. Waves*, pp. 160–171, 1893.

[69] J. J. Thomson, *Notes on Recent Researches in Electricity and Magnetism*. Oxford, 1893.

[70] L. Heinzle, “Measurement of Skin Effects using the Bode 100.” Omicron Lab, 2011. [Online]. Available: https://www.omicron-lab.com/applications/detail/news/measure-skin-effects#

[71] K.-T. Kim *et al.*, “Skin Effect-Related AC Resistance Study in Macroscopic Scale Carbon Nanotube Yarn Applicable to High-Power Converter,” *IEEE Trans. Nanotechnol.*, vol. 20, pp. 417–424, 2021, doi: 10.1109/TNANO.2021.3076472.

[72] R. Faraji-Dana and Y. L. Chow, “The AC resistance of a microstripline and its ground plane,” in *IEEE MTT-S International Microwave Symposium Digest*, Long Beach, CA, USA: IEEE, 1989, pp. 325–327. doi: 10.1109/MWSYM.1989.38730.

[73] J. C. Rautio, “An investigation of microstrip conductor loss,” *IEEE Microw. Mag.*, vol. 1, no. 4, pp. 60–67, Dec. 2000, doi: 10.1109/6668.893247.

[74] Y. Poo, R. Wu, X. Fan, and J. Q. Xiao, “Measurement of ac conductivity of gold nanofilms at microwave frequencies,” *Rev. Sci. Instrum.*, vol. 81, no. 6, p. 064701, Jun. 2010, doi: 10.1063/1.3436450.

[75] J. W. Schultz, *Focused Beam Methods: Measuring Microwave Materials in Free Space*. Createspace Independent Publishing Platform, 2012.

[76] Z. Yu and P. J. Burke, “Microwave Transport in Metallic Single-Walled Carbon Nanotubes,” *Nano Lett.*, vol. 5, no. 7, pp. 1403–1406, Jul. 2005, doi: 10.1021/nl050738k.

[77] J. J. Plombon, K. P. O’Brien, F. Gstrein, V. M. Dubin, and Y. Jiao, “High-frequency electrical properties of individual and bundled carbon nanotubes,” *Appl. Phys. Lett.*, vol. 90, no. 6, p. 063106, Feb. 2007, doi: 10.1063/1.2437724.

[78] S. C. Jun *et al.*, “Passive electrical properties of multi-walled carbon nanotubes up to 0.1 THz,” *New J. Phys.*, vol. 9, no. 8, pp. 265–265, Aug. 2007, doi: 10.1088/1367-2630/9/8/265.

[79] P. J. Burke, “An RF circuit model for carbon nanotubes,” *IEEE Trans. Nanotechnol.*, vol. 2, no. 1, pp. 55–58, Mar. 2003, doi: 10.1109/TNANO.2003.808503.

[80] Y. Massoud and A. Nieuwoudt, “Modeling and design challenges and solutions for carbon nanotube-based interconnect in future high performance integrated circuits,” *ACM J. Emerg. Technol. Comput. Syst.*, vol. 2, no. 3, pp. 155–196, Jul. 2006, doi: 10.1145/1167943.1167944.

[81] O. Hilt, H. B. Brom, and M. Ahlskog, “Localized and delocalized charge transport in single-wall carbon-nanotube mats,” *Phys. Rev. B*, vol. 61, no. 8, pp. R5129–R5132, Feb. 2000, doi: 10.1103/PhysRevB.61.R5129.

[82] C. Highstrete, E. A. Shaner, M. Lee, F. E. Jones, P. M. Dentinger, and A. Alec Talin, “Microwave dissipation in arrays of single-wall carbon nanotubes,” *Appl. Phys. Lett.*, vol. 89, no. 17, p. 173105, Oct. 2006, doi: 10.1063/1.2364061.

[83] H. Xu, S. M. Anlage, L. Hu, and G. Gruner, “Microwave shielding of transparent and conducting single-walled carbon nanotube films,” *Appl. Phys. Lett.*, vol. 90, no. 18, p. 183119, Apr. 2007, doi: 10.1063/1.2734897.

[84] H. Xu, S. Zhang, S. M. Anlage, L. Hu, and G. Grüner, “Frequency- and electric-field-dependent conductivity of single-walled carbon nanotube networks of varying density,” *Phys. Rev. B*, vol. 77, no. 7, p. 075418, Feb. 2008, doi: 10.1103/PhysRevB.77.075418.

[85] C. Highstrete, M. Lee, A. A. Talin, and A. L. Vance, “Microwave conductance spectra of single-walled carbon nanotube arrays,” *Appl. Phys. Lett.*, vol. 95, no. 20, p. 203111, Nov. 2009, doi: 10.1063/1.3263708.

[86] M. Z. Iqbal, M. W. Iqbal, J. Eom, M. Ahmad, and N. Ferrer-Anglada, “Capacitive tunnels in single-walled carbon nanotube networks on flexible substrate,” *J. Appl. Phys.*, vol. 111, no. 6, p. 063712, Mar. 2012, doi: 10.1063/1.3695992.

[87] M. Z. Iqbal, J. Pérez-Puigdemont, J. Eom, and N. Ferrer-Anglada, “High-frequency impedance of single-walled carbon nanotube networks on transparent flexible substrate: HF impedance of SWCNT networks on transparent flexible substrate,” *Phys. Status Solidi B*, vol. 251, no. 12, pp. 2461–2465, Dec. 2014, doi: 10.1002/pssb.201451233.

[88] B. L. Brown, J. S. Bykova, A. R. Howard, A. A. Zakhidov, E. A. Shaner, and M. Lee, “Microwave conductance of aligned multiwall carbon nanotube textile sheets,” *Appl. Phys. Lett.*, vol. 105, no. 26, p. 263105, Dec. 2014, doi: 10.1063/1.4905220.

[89] R. L. Muhlbauer and R. A. Gerhardt, “Impedance spectroscopy of short multiwalled carbon nanotube networks deposited on a paper substrate: tracking the evolution of in-plane and thru-plane electronic properties,” *J. Mater. Sci.*, vol. 56, no. 4, pp. 3256–3267, Feb. 2021, doi: 10.1007/s10853-020-05498-2.

[90] B. E. Kilbride *et al.*, "Experimental observation of scaling laws for alternating current and direct current conductivity in polymer-carbon nanotube composite thin films," *J. Appl. Phys.*, vol. 92, no. 7, pp. 4024–4030, Oct. 2002, doi: 10.1063/1.1506397.

[91] K. Keramatnejad *et al.*, "Skin effect mitigation in laser processed multi-walled carbon nanotube/copper conductors," *J. Appl. Phys.*, vol. 118, no. 15, p. 154311, Oct. 2015, doi: 10.1063/1.4934255.

[92] S. Barrau, P. Demont, A. Peigney, C. Laurent, and C. Lacabanne, "DC and AC Conductivity of Carbon Nanotubes−Polyepoxy Composites," *Macromolecules*, vol. 36, no. 14, pp. 5187–5194, Jul. 2003, doi: 10.1021/ma021263b.

[93] Z. Ounaies, "Electrical properties of single wall carbon nanotube reinforced polyimide composites," *Compos. Sci. Technol.*, vol. 63, no. 11, pp. 1637–1646, Aug. 2003, doi: 10.1016/S0266-3538(03)00067-8.

[94] J. K. W. Sandler, J. E. Kirk, I. A. Kinloch, M. S. P. Shaffer, and A. H. Windle, "Ultra-low electrical percolation threshold in carbon-nanotube-epoxy composites," *Polymer*, vol. 44, no. 19, pp. 5893–5899, Sep. 2003, doi: 10.1016/S0032-3861(03)00539-1.

[95] Y. J. Kim, T. S. Shin, H. D. Choi, J. H. Kwon, Y.-C. Chung, and H. G. Yoon, "Electrical conductivity of chemically modified multiwalled carbon nanotube/epoxy composites," *Carbon*, vol. 43, no. 1, pp. 23–30, 2005, doi: 10.1016/j.carbon.2004.08.015.

[96] D. S. McLachlan *et al.*, "AC and DC percolative conductivity of single wall carbon nanotube polymer composites," *J. Polym. Sci. Part B Polym. Phys.*, vol. 43, no. 22, pp. 3273–3287, Nov. 2005, doi: 10.1002/polb.20597.

[97] P. V. Kodgire, A. R. Bhattacharyya, S. Bose, N. Gupta, A. R. Kulkarni, and A. Misra, "Control of multiwall carbon nanotubes dispersion in polyamide6 matrix: An assessment through electrical conductivity," *Chem. Phys. Lett.*, vol. 432, no. 4–6, pp. 480–485, Dec. 2006, doi: 10.1016/j.cplett.2006.10.088.

[98] A. Linares *et al.*, "Broad-Band Electrical Conductivity of High Density Polyethylene Nanocomposites with Carbon Nanoadditives: Multiwall Carbon Nanotubes and Carbon Nanofibers," *Macromolecules*, vol. 41, no. 19, pp. 7090–7097, Oct. 2008, doi: 10.1021/ma801410j.

[99] P.-C. Ma *et al.*, "Enhanced Electrical Conductivity of Nanocomposites Containing Hybrid Fillers of Carbon Nanotubes and Carbon Black," *ACS Appl. Mater. Interfaces*, vol. 1, no. 5, pp. 1090–1096, May 2009, doi: 10.1021/am9000503.

[100] Ye. P. Mamunya *et al.*, "Electrical and thermomechanical properties of segregated nanocomposites based on PVC and multiwalled carbon nanotubes," *J. Non-Cryst. Solids*, vol. 356, no. 11–17, pp. 635–641, Apr. 2010, doi: 10.1016/j.jnoncrysol.2009.09.038.

[101] A. Vavouliotis, E. Fiamegou, P. Karapappas, G. C. Psarras, and V. Kostopoulos, "DC and AC conductivity in epoxy resin/multiwall carbon nanotubes percolative system," *Polym. Compos.*, vol. 31, no. 11, pp. 1874–1880, Nov. 2010, doi: 10.1002/pc.20981.

[102] Z. Samir, Y. El Merabet, M. P. F. Graça, S. S. Teixeira, M. E. Achour, and L. C. Costa, "Impedance spectroscopy study of polyester/carbon nanotube composites," *Polym. Compos.*, vol. 39, no. 4, pp. 1297–1302, Apr. 2018, doi: 10.1002/pc.24067.

[103] P. Verma, T. Bansala, S. S. Chauhan, D. Kumar, S. Deveci, and S. Kumar, "Electromagnetic interference shielding performance of carbon nanostructure reinforced, 3D printed polymer composites," *J. Mater. Sci.*, vol. 56, no. 20, pp. 11769–11788, Jul. 2021, doi: 10.1007/s10853-021-05985-0.

References

[104] X. Feng *et al.*, "High Electromagnetic Interference Shielding Effectiveness of Carbon Nanotube–Cellulose Composite Films with Layered Structures," *Macromol. Mater. Eng.*, vol. 303, no. 11, p. 1800377, Nov. 2018, doi: 10.1002/mame.201800377.

[105] Y. Yang, M. C. Gupta, K. L. Dudley, and R. W. Lawrence, "Novel Carbon Nanotube−Polystyrene Foam Composites for Electromagnetic Interference Shielding," *Nano Lett.*, vol. 5, no. 11, pp. 2131–2134, Nov. 2005, doi: 10.1021/nl051375r.

[106] Z. Zeng *et al.*, "Printable Aligned Single-Walled Carbon Nanotube Film with Outstanding Thermal Conductivity and Electromagnetic Interference Shielding Performance," *Nano-Micro Lett.*, vol. 14, no. 1, p. 179, Dec. 2022, doi: 10.1007/s40820-022-00883-9.

[107] Y.-J. Wan *et al.*, "Ultrathin Densified Carbon Nanotube Film with 'Metal-like' Conductivity, Superior Mechanical Strength, and Ultrahigh Electromagnetic Interference Shielding Effectiveness," *ACS Nano*, vol. 14, no. 10, pp. 14134–14145, Oct. 2020, doi: 10.1021/acsnano.0c06971.

[108] B. J. Landi, H. J. Ruf, C. M. Evans, C. D. Cress, and R. P. Raffaelle, "Purity Assessment of Single-Wall Carbon Nanotubes, Using Optical Absorption Spectroscopy," *J. Phys. Chem. B*, vol. 109, no. 20, pp. 9952–9965, May 2005, doi: 10.1021/jp044990c.

[109] B. J. Landi, C. D. Cress, C. M. Evans, and R. P. Raffaelle, "Thermal Oxidation Profiling of Single-Walled Carbon Nanotubes," *Chem. Mater.*, vol. 17, no. 26, pp. 6819–6834, Dec. 2005, doi: 10.1021/cm052002u.

[110] C. M. Schauerman, J. Alvarenga, J. Staub, M. W. Forney, R. Foringer, and B. J. Landi, "Ultrasonic Welding of Bulk Carbon Nanotube Conductors," *Adv. Eng. Mater.*, vol. 17, no. 1, pp. 76–83, Jan. 2015, doi: 10.1002/adem.201400117.

[111] A. R. Bucossi, Q. Campbell, J. E. Rossi, and B. J. Landi, "Effects of Solution Properties on Iodine Monobromide Doping for Enhanced Bulk Carbon Nanotube Electrical Conductivity," *ACS Appl. Nano Mater.*, vol. 1, no. 5, pp. 2088–2094, May 2018, doi: 10.1021/acsanm.8b00041.

[112] L. van der Pauw, "A method of measuring specific resistivity and Hall effect of discs of arbitrary shape," *Philips Res. Rep.*, vol. 13, no. 1, pp. 1–9, Feb. 1958.

[113] R. Saito *et al.*, "Double resonance Raman spectroscopy of single-wall carbon nanotubes," *New J. Phys.*, vol. 5, pp. 157–157, Dec. 2003, doi: 10.1088/1367-2630/5/1/157.

[114] P. T. Araujo, P. B. C. Pesce, M. S. Dresselhaus, K. Sato, R. Saito, and A. Jorio, "Resonance Raman spectroscopy of the radial breathing modes in carbon nanotubes," *Phys. E Low-Dimens. Syst. Nanostructures*, vol. 42, no. 5, pp. 1251–1261, Mar. 2010, doi: 10.1016/j.physe.2010.01.015.

[115] H. Kataura *et al.*, "Optical properties of single-wall carbon nanotubes," *Synth. Met.*, vol. 103, no. 1–3, pp. 2555–2558, Jun. 1999, doi: 10.1016/S0379-6779(98)00278-1.

[116] K. D. Ausman, R. Piner, O. Lourie, R. S. Ruoff, and M. Korobov, "Organic Solvent Dispersions of Single-Walled Carbon Nanotubes: Toward Solutions of Pristine Nanotubes," *J. Phys. Chem. B*, vol. 104, no. 38, pp. 8911–8915, Sep. 2000, doi: 10.1021/jp002555m.

[117] T. Hasan, V. Scardaci, P. Tan, A. G. Rozhin, W. I. Milne, and A. C. Ferrari, "Stabilization and 'Debundling' of Single-Wall Carbon Nanotube Dispersions in *N* -Methyl-2-pyrrolidone (NMP) by Polyvinylpyrrolidone (PVP)," *J. Phys. Chem. C*, vol. 111, no. 34, pp. 12594–12602, Aug. 2007, doi: 10.1021/jp0723012.

[118] American Society for Testing and Materials, "ASTM E1933-99a - Standard Test Methods For Measuring And Compensating For Emissivity Using Infrared Imaging Radiometers." American Society for Testing and Materials, 2005.

References

[119] D. L. Broderick, S. J. Boyd, J. E. Rossi, and B. J. Landi, "Selective chemical doping of carbon nanotube conductors to reduce contact resistance with copper in ultrasonic welds," *Carbon*, vol. 227, p. 119222, Jun. 2024, doi: 10.1016/j.carbon.2024.119222.

[120] Keysight, "Network Analysis," Keysight. Accessed: Apr. 24, 2023. [Online]. Available: https://www.keysight.com/us/en/solutions/measurement-fundamentals/network-analysis.html

[121] G. Engen and C. Hoer, "Thru-Reflect-Line: An Improved Technique for Calibrating the Dual Six-Port Automatic Network Analyzer," *IEEE Trans. Microw. Theory Tech.*, vol. 27, no. 12, pp. 987–993, Dec. 1979, doi: 10.1109/TMTT.1979.1129778.

[122] R. B. Marks, "A multiline method of network analyzer calibration," *IEEE Trans. Microw. Theory Tech.*, vol. 39, no. 7, pp. 1205–1215, Jul. 1991, doi: 10.1109/22.85388.

[123] X. Zhao, Y. Ando, L.-C. Qin, H. Kataura, Y. Maniwa, and R. Saito, "Characteristic Raman spectra of multiwalled carbon nanotubes," *Phys. B Condens. Matter*, vol. 323, no. 1–4, pp. 265–266, Oct. 2002, doi: 10.1016/S0921-4526(02)00986-9.

[124] J. M. Benoit, J. P. Buisson, O. Chauvet, C. Godon, and S. Lefrant, "Low-frequency Raman studies of multiwalled carbon nanotubes: Experiments and theory," *Phys. Rev. B*, vol. 66, no. 7, p. 073417, Aug. 2002, doi: 10.1103/PhysRevB.66.073417.

[125] G. S. B. McKee and K. S. Vecchio, "Thermogravimetric Analysis of Synthesis Variation Effects on CVD Generated Multiwalled Carbon Nanotubes," *J. Phys. Chem. B*, vol. 110, no. 3, pp. 1179–1186, Jan. 2006, doi: 10.1021/jp054265h.

[126] R. A. DiLeo, B. J. Landi, and R. P. Raffaelle, "Purity assessment of multiwalled carbon nanotubes by Raman spectroscopy," *J. Appl. Phys.*, vol. 101, no. 6, p. 064307, Mar. 2007, doi: 10.1063/1.2712152.

[127] H. Yun *et al.*, "Size- and Composition-Dependent Radio Frequency Magnetic Permeability of Iron Oxide Nanocrystals," *ACS Nano*, vol. 8, no. 12, pp. 12323–12337, Dec. 2014, doi: 10.1021/nn504711g.

[128] N. Smith, "Classical generalization of the Drude formula for the optical conductivity," *Phys. Rev. B*, vol. 64, no. 15, p. 155106, Sep. 2001, doi: 10.1103/PhysRevB.64.155106.

[129] P. Gibbon, "Introduction to Plasma Physics," *CERN Yellow Rep.*, pp. 51–65, Feb. 2016, doi: 10.5170/CERN-2016-001.51.

[130] "What are S- and X-Band Radar and How Are They Used Today?," Leonardo DRS. Accessed: Jun. 17, 2024. [Online]. Available: https://www.leonardodrs.com/news/thought-leadership/what-are-s-and-x-band-radar-and-how-are-they-used-today/

[131] C. Stergiou, M. Koledintseva, and K. Rozanov, "Hybrid polymer composites for electromagnetic absorption in electronic industry," in *Hybrid Polymer Composite Materials: Applications*, Elsevier, 2017, pp. 53–96.

[132] A. Bole, A. Wall, and A. Norris, "Target Detection," in *Radar and ARPA Manual: Radar, AIS and Target Tracking for Marine Radar Users*, 3rd ed., Elsevier, 2014, pp. 139–210.

[133] T. Yun *et al.*, "Electromagnetic Shielding of Monolayer MXene Assemblies," *Adv. Mater.*, vol. 32, no. 9, p. 1906769, Mar. 2020, doi: 10.1002/adma.201906769.

[134] J. Zhang *et al.*, "Scalable Manufacturing of Free-Standing, Strong $Ti_3C_2T_x$ MXene Films with Outstanding Conductivity," *Adv. Mater.*, vol. 32, no. 23, p. 2001093, Jun. 2020, doi: 10.1002/adma.202001093.

[135] S. Greco, M. S. Sarto, and A. Tamburrano, "Shielding performances of ITO transparent windows: Theoretical and experimental characterization," in *2008 International Symposium on Electromagnetic Compatibility - EMC Europe*, Hamburg, Germany: IEEE, Sep. 2008, pp. 1–6. doi: 10.1109/EMCEUROPE.2008.4786870.

References

[136] J. L. Huang, B. S. Yau, C. Y. Chen, W. T. Lo, and D. F. Lii, "The electromagnetic shielding effectiveness of indium tin oxide films," *Ceram. Int.*, 2001.

[137] R. Datta *et al.*, "Flexible two-dimensional indium tin oxide fabricated using a liquid metal printing technique," *Nat. Electron.*, vol. 3, pp. 51–58, 2020, doi: https://doi.org/10.1038/s41928-019-0353-8.

[138] S.-K. Lu, J.-T. Huang, T.-H. Lee, J.-J. Wang, and D.-S. Liu, "Flexibility of the Indium Tin Oxide Transparent Conductive Film Deposited Onto the Plastic Substrate," *Smart Sci.*, vol. 2, no. 1, pp. 7–12, Jan. 2014, doi: 10.1080/23080477.2014.11665597.

[139] H. Wang *et al.*, "Highly Flexible Indium Tin Oxide Nanofiber Transparent Electrodes by Blow Spinning," *ACS Appl. Mater. Interfaces*, vol. 8, no. 48, pp. 32661–32666, Dec. 2016, doi: 10.1021/acsami.6b13255.

[140] A. G. Nasibulin *et al.*, "Multifunctional Free-Standing Single-Walled Carbon Nanotube Films," *ACS Nano*, vol. 5, no. 4, pp. 3214–3221, Apr. 2011, doi: 10.1021/nn200338r.

[141] P. Aldeanueva-Potel, M. A. Correa-Duarte, R. A. Alvarez-Puebla, and L. M. Liz-Marzán, "Free-Standing Carbon Nanotube Films as Optical Accumulators for Multiplex SERRS Attomolar Detection," *ACS Appl. Mater. Interfaces*, vol. 2, no. 1, pp. 19–22, Jan. 2010, doi: 10.1021/am9008715.

[142] H. Gu and T. M. Swager, "Fabrication of Free-standing, Conductive, and Transparent Carbon Nanotube Films," *Adv. Mater.*, vol. 20, no. 23, pp. 4433–4437, Dec. 2008, doi: 10.1002/adma.200801062.

[143] Y. Zhou, L. Hu, and G. Grüner, "A method of printing carbon nanotube thin films," *Appl. Phys. Lett.*, vol. 88, no. 12, p. 123109, Mar. 2006, doi: 10.1063/1.2187945.

[144] C. Lim, D.-H. Min, and S.-B. Lee, "Direct patterning of carbon nanotube network devices by selective vacuum filtration," *Appl. Phys. Lett.*, vol. 91, no. 24, p. 243117, Dec. 2007, doi: 10.1063/1.2824575.

[145] P. Saini and M. Aror, "Microwave absorption and EMI shielding behavior of nanocomposites based on intrinsically conducting polymers, graphene and carbon nanotubes," in *New Polymers for Special Applications*, IntechOpen, 2012, pp. 71–112.

[146] F. Shahzad, A. Iqbal, H. Kim, and C. M. Koo, "2D Transition Metal Carbides (MXenes): Applications as an Electrically Conducting Material," *Adv. Mater.*, vol. 32, no. 51, p. 2002159, Dec. 2020, doi: 10.1002/adma.202002159.

[147] L. Minati *et al.*, "Investigation on the Electronic and Optical Properties of Short Oxidized Multiwalled Carbon Nanotubes," *J. Phys. Chem. C*, vol. 114, no. 25, pp. 11068–11073, Jul. 2010, doi: 10.1021/jp101868s.

[148] S. Reich, J. Maultzsch, and C. Thomsen, *Carbon Nanotubes: Basic Concepts and Physical Properties*. Wiley, 2008.

[149] M.-J. Kim *et al.*, "Molecular-level hybridization of single-walled carbon nanotubes and a copper complex with counterbalanced electrostatic interactions," *Commun. Mater.*, vol. 5, no. 1, p. 111, Jun. 2024, doi: 10.1038/s43246-024-00548-7.

[150] L. Zhang *et al.*, "Preparation and characterization of graphene paper for electromagnetic interference shielding," *Carbon*, vol. 82, pp. 353–359, Feb. 2015, doi: 10.1016/j.carbon.2014.10.080.

[151] M. H. Al-Saleh, W. H. Saadeh, and U. Sundararaj, "EMI shielding effectiveness of carbon based nanostructured polymeric materials: A comparative study," *Carbon*, vol. 60, pp. 146–156, Aug. 2013, doi: 10.1016/j.carbon.2013.04.008.

[152] L. Zhang, M. Liu, S. Roy, E. K. Chu, K. Y. See, and X. Hu, "Phthalonitrile-Based Carbon Foam with High Specific Mechanical Strength and Superior Electromagnetic Interference Shielding Performance," *ACS Appl. Mater. Interfaces*, vol. 8, no. 11, pp. 7422–7430, Mar. 2016, doi: 10.1021/acsami.5b12072.

[153] F. Shahzad *et al.*, "Electromagnetic interference shielding with 2D transition metal carbides (MXenes)," *Science*, vol. 353, no. 6304, pp. 1137–1140, 2016, doi: https://doi.org/10.1126/science.aag2421.

[154] H. K. Choi *et al.*, "Hierarchical Porous Film with Layer-by-Layer Assembly of 2D Copper Nanosheets for Ultimate Electromagnetic Interference Shielding," *ACS Nano*, vol. 15, no. 1, pp. 829–839, Jan. 2021, doi: 10.1021/acsnano.0c07352.

[155] "PCB Design & Assembly, Standard PCBs, and Global Services." Accessed: Jul. 22, 2024. [Online]. Available: https://www.advancedpcb.com/en-us/services/standard-pcbs/

[156] N. D. Orloff *et al.*, "How to extract distributed circuit parameters from the scattering parameters of a transmission line," in *2017 90th ARFTG Microwave Measurement Symposium (ARFTG)*, Boulder, CO: IEEE, Nov. 2017, pp. 1–5. doi: 10.1109/ARFTG.2017.8255872.

[157] "Microstrip Antennas: The Patch Antenna." Accessed: Jul. 23, 2024. [Online]. Available: https://www.antenna-theory.com/antennas/patches/antenna.php

[158] "RT/duroid® 5870/5880 High Frequency Laminates." Rogers Corporation, 2022. Accessed: Jul. 23, 2024. [Online]. Available: https://www.rogerscorp.com/advanced-electronics-solutions/rt-duroid-laminates/rt-duroid-5880-laminates